UNIVERSITÀ
DEGLI STUDI
DI PADOVA

Università degli Studi di Padova

DIPARTIMENTO DI FISICA E ASTRONOMIA G. GALILEI
Corso di Dottorato di ricerca in Astronomia
Ciclo XXXVI

PHD THESIS
5th APRIL 2024

Multi-wavelength and multi-messenger studies of blazars as candidate neutrino emitters

Candidato:
Ilaria Viale

Relatore:
Prof. Elisa Bernardini

Overview

Even after a century from their discovery, the origin of high-energy cosmic rays is still an open issue. Cosmic rays are charged particles able to reach Earth at energies up to 10^{20} eV, requiring their sources to be cosmic accelerators. However, the identification of such acceleration sites remains puzzling. Due to their electric charge, cosmic rays undergo deflection by intergalactic magnetic fields before reaching Earth, preventing a direct association with their emitting sources. A promising approach in establishing this association is represented by multi-messenger astrophysics, a relatively recent field exploiting the diverse information carried by different messengers originating from the same cosmic sources.

In this context, the detection of high-energy astrophysical neutrinos and photons from the same objects represents an important step towards the identification of genuine cosmic ray accelerators. While photons can originate in both leptonic and hadronic processes, neutrinos are direct tracers of hadronic interactions, since they are thought to be produced by cosmic rays interacting with ambient matter or radiation fields during their acceleration or propagation. From the same interactions, also $\gamma-$rays are expected to be produced, making a joint observation of high-energy photons and neutrinos a stronger indication of hadronic processes from the emitting source.

Neutrino astronomy has seen significant advancements in the last decade. In 2013 the discovery of an astrophysical neutrino flux was announced by the IceCube Neutrino Telescope [1, 2], confirming the existence of high-energy neutrinos of cosmic origin, while in more recent years the first potential neutrino sources were detected [3–5]. The first evidence for a neutrino source came in 2017, when a high-energy neutrino event detected by IceCube was found to be in spatial and temporal coincidence with the flaring blazar TXS 0506+056 [3]. Observatories from all around the world operated a prompt follow-up of the neutrino event, pointing in its direction and finding it consistent with the location of the blazar. The source was detected in both high energy (HE, $0.5\,\mathrm{MeV} < E < 100\,\mathrm{GeV}$) and very high energy (VHE, $E > 100$ GeV) $\gamma-$rays and the chance coincidence probability of the photon-neutrino association was rejected at the $\sim 3\sigma$ level.

Two more recent studies performed by the IceCube Collaboration found evidence of neutrino emission from the Seyfert-II galaxy NGC 1068 (4.2σ) [4] and from the Galactic plane (4.5σ) [5], involving an analysis of the integral neutrino signal recorded with the IceCube detector in 9 and 10 years of data respectively. The former identified galaxy

is an active galaxy as TXS 0506+056. However, differently from the blazar, it does not show a relativistic jet of particles. The latter result implies that a contribution to the astrophysical neutrino flux is given also by nearby sources in our galaxy. The variety of identified objects suggests different processes and astrophysical environments contributing to the neutrino background.

This thesis comprises different works dealing with two relevant open problems in this field: the investigation of emission processes at work in astrophysical sources and the search for new neutrino (and hence cosmic-ray) sources. Although an unbiased follow-up of neutrino events is performed in one of these projects, the main focus of the thesis is the study of blazars as possible neutrino emitters.

Such studies require a comprehensive analysis, exploiting information from several instruments. This includes information associated with events detected by neutrino observatories, as well as data collected by multiple telescopes operating in different bands of the electromagnetic spectrum. The instruments and cosmic messengers relevant for this thesis work are presented in Chapter 1, with a special focus on the MAGIC telescopes, operating in the VHE $\gamma-$ray regime. Chapter 2 concentrates on AGNs and, especially, blazars, describing their subclasses and the radiative processes commonly invoked to characterize their emission from both a leptonic and a hadronic point of view. The following chapters illustrate my contributions to the field. Chapter 3 presents the first long-term monitoring of TXS 0506+056, performed with the MAGIC telescopes and multi-wavelength partners. Chapter 4 focuses on a selection of blazars with similar observational properties to TXS 0506+056, aiming at investigating their multi-messenger role. To do this, we firstly explored their nature through the study of their accretion mechanism, secondly we exploited the obtained results to build lepto-hadronic emission models on publicly available data, interpreting their emission and estimating their detectability from Imaging Air Cherenkov Telescopes (IACT) and the IceCube Neutrino Observatory. Chapter 5 describes the main results of the follow-up observations of IceCube neutrino events performed by the MAGIC telescopes and the other currently operating IACT collaborations after the 2017 multi-messenger association. Additionally, this chapter also comprises the investigation of the detection chances of the sources monitored by IceCube for neutrino cluster events with MAGIC, based on the variability of their emission. Chapter 6 shows the implementation of hadronic processes relevant in blazars emission into the open source python package `agnpy`, a software developed for the interpretation of AGNs broadband emission. Finally, Chapter 7 discusses the main results of this thesis and prospects for the future.

Contents

Chapter 1

Multi-wavelength and multi-messenger astrophysics

Multi-messenger astrophysics is a relatively new and exciting research field of astronomy which rapidly evolved in the last decade. It aims at enhancing our understanding of the most extreme phenomena in the univierse by combining information provided by different messengers coming from the same astrophysical environments. These messengers are *photons, cosmic-rays (CR), neutrinos,* and *gravitational waves (GW)*. Traditionally, electromagnetic radiation in all its wavelengths, from radio waves to $\gamma-$rays, was the main source of information for astrophysicists to study the universe. However, many processes involved in the sources environment remain hidden or poorly understood if investigated with electromagnetic radiation alone. Since the different messengers carry different kind of information, the multi-messenger approach is essential in order to have a complete picture of the phenomena occurring in the emitting objects.

This thesis concentrates on the possible emission of photons, with a special focus on Very High Energy (VHE, $E > 100$ GeV) $\gamma-$rays, and high-energy neutrinos from the same astrophysical sources. These two messengers are both expected to originate in the interactions of accelerated CRs with ambient matter or radiation fields, but only neutrinos provide a unique signature of hadronic interactions, since VHE $\gamma-$rays can also be produced in leptonic processes. Therefore, the joint detection of these messengers can lead us to the still unresolved sources of CRs. In this context, synergies between the detectors and observatories specialized in the observation of each messenger are needed in order to have a simultaneous picture of the state of the emitting source.

The following sections provide a description of the messengers involved in this work and the instruments needed to detect them.

1.1 Cosmic messengers: cosmic-rays, photons and neutrinos

As already mentioned, the two messengers involved in this thesis are *photons* and *neutrinos*, which are directly connected to *cosmic-rays*.

Cosmic-rays (CR) are charged particles produced in astrophysical environments that can reach the Earth atmosphere and interact with the nuclei composing it [6]. They are mostly composed of protons ($\simeq 90\,\%$), helium nuclei ($\lesssim 10\,\%$) and a small fraction of electrons, positrons and heavier nuclei. They are expected to have both a Galactic and an extragalactic origin but the precise sources producing them are still unknown. The energy spectrum of CRs, shown in Fig. 1.1, is characterized by steep falling fluxes and spans several orders of magnitude, from GeV energies to hundreds of EeV, with fluxes going from thousands of particles per square meter per second at low energies down to one particle per square kilometer per century at the highest ones. It can be well described by a power-law $\mathrm{d}N/\mathrm{d}E \propto E^{-\alpha}$, with a different spectral index α depending on the energy range considered. It shows two features at 10^{15} eV and 10^{18} eV, called *knee* and *ankle* respectively. The former marks a transition of the spectral index from $\simeq 2.7$ to $\simeq 3.1$ and, possibly, a transition from CRs of Galactic origin to an extragalactic one. The latter marks a hardening of the spectrum, with the spectral index going from $\simeq 3.1$ to $\simeq 2.6$, the nature of which is still debated. CRs above the ankle energy are usually referred to as Ultra High Energy Cosmic Rays (UHECR). They have a relevant role in high-energy astroparticle physics because they can travel undeflected by inter- and intra-galactic magnetic fields thanks to their extremely high energy, being thus able to carry information on the sources producing them. Finally above an energy of 5×10^{19} eV, the spectrum undergoes a severe cut-off, due to the interaction of CRs with the Cosmic Microwave Background (CMB), the so-called GZK cut-off [8, 9].

CRs can give origin to neutrinos through their interactions with low energy photons or target matter and the following decay of the products, which are mainly pions ($\pi^{\pm,0}$) and muons ($\mu^{\pm}$). The main interaction channels are:

$$\text{Photo} - \text{meson interactions :} \qquad p + \gamma \to \Delta^+ \to \begin{cases} p + \pi^0 \\ n + \pi^+ \end{cases} \tag{1.1}$$

$$\text{Bethe} - \text{Heitler pair production :} \qquad p + \gamma \to p + e^+ + e^- \tag{1.2}$$

$$\text{Proton} - \text{proton interactions :} \qquad p + p \to \text{hadrons} \to \pi^{\pm,0} + X, \tag{1.3}$$

where Δ^+ is a quickly decaying resonance, e^- is the electron, e^+ is the positron, and X are other products from $p - p$ interactions. These reactions are followed by the decays:

$$\pi^+ \to \mu^+ + \nu_\mu \tag{1.4}$$
$$\hookrightarrow e^+ + \nu_e + \bar{\nu}_\mu \tag{1.5}$$
$$\pi^- \to \mu^- + \bar{\nu}_\mu \tag{1.6}$$
$$\hookrightarrow e^- + \bar{\nu}_e + \nu_\mu \tag{1.7}$$
$$\pi^0 \to \gamma + \gamma, \tag{1.8}$$

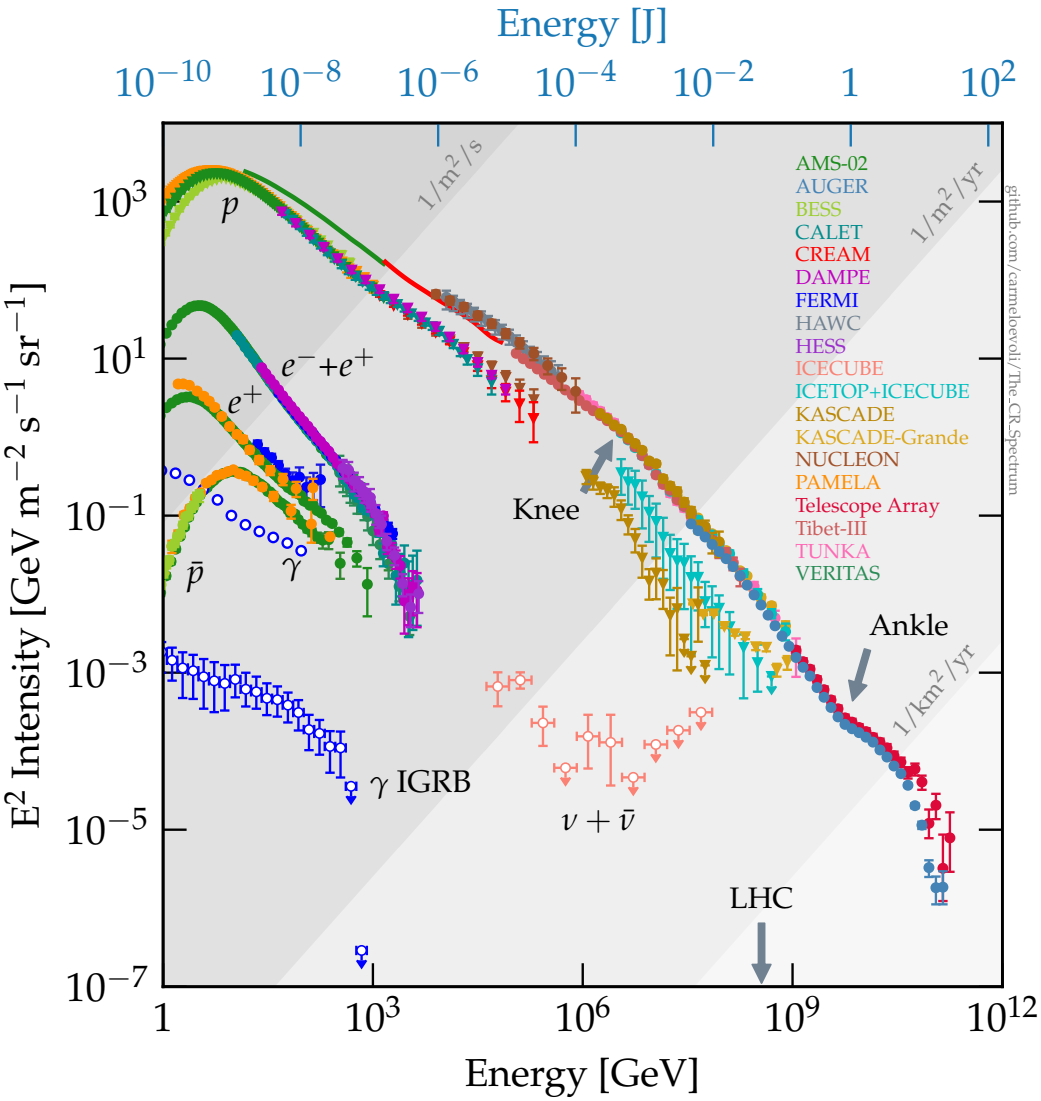

Figure 1.1: Spectrum of cosmic-rays with data from several different instruments. The grey shaded areas denote the expected detection rates. The two features *knee* and *ankle* are highlighted, together with the maximum achievable energy by the LHC experiment. The spectrum of the leptonic component of CRs, anti-protons, neutrinos, antineutrinos, $\gamma-$rays and isotropic diffuse $\gamma-$ray background (IGRB) are also shown. Credits: [7]

where neutrinos and anti-neutrons of different flavours are produced together with $\gamma-$rays.

Neutrinos are uncharged weakly-interacting particles that can be produced in three flavours (electron neutrinos ν_e, muon neutrinos ν_μ, tau neutrinos ν_τ) and oscillate between them during their propagation. Thanks to their neutral charge they can travel undeflected by cosmic magnetic fields, pointing back to the source that produced them. Moreover, their weakly-interacting nature and, consequently, very small cross section, allows them to travel unimpeded for long distances and escape dense environments, bringing information on the core of the astrophysical objects producing them. However this feature also represents a disadvantage since it makes neutrino detection very challenging. In addition, neutrinos of astrophysical origin have energies in the TeV$-$PeV range, and, as for the case of CRs, their flux is much lower with respect to events of lower energy. This can be observed in the neutrino spectrum displayed in Fig. 1.2, showing the flux of neutrinos coming from different sources. In this work, we are interested in astrophysical neutrinos, namely those denoted as "ν from AGN", where AGN refer to particular extragalactic sources called Active Galactic Nuclei (see Chapter 2 for more details). They are candidate neutrino emitters, but to date we know that they are just one of the potential neutrino sources. Because of the small interaction rate and low flux at high energies, detectors of huge volumes are needed to detect astrophysical neutrinos. To date, the largest working neutrino telescope is the IceCube Neutrino Observatory[1], with a volume of 1 km^3. It is deployed in the antarctic ice, which is used as part of the detector. Indeed, the higher density of ice with respect to air increases the interaction rate of neutrinos with the medium they are traveling in, leading to the production of charged particles (like for example muons or electrons), detectable by the instrument. Thanks to IceCube observations, neutrino astronomy officially began in 2013, when the instrument announced the discovery of a high-energy neutrino flux [1], which was well established in the following years through additional measurements [2]. More details on IceCube and neutrino detection principles are given in Sec. 1.2.

The last messenger relevant for this work is the photon. **Photons** are massless uncharged particles used for centuries as the only source of information on the objects producing them. Like neutrinos they can travel towards Earth undeflected by cosmic magnetic fields, pointing back at their sources of origin. However, they have a larger cross-section than neutrinos, so they can get absorbed in the source environment if it is of high density or interact more likely with matter (e. g., gas clouds) or electromagnetic radiation during their travel to Earth. This is particularly relevant at high energies. Indeed VHE $\gamma-$rays are very likely to interact with the Extragalactic Background Light (EBL) [11], namely the radiation created during star formation processes through the whole cosmic history. It is mainly composed of star light and absorbed/re-processed star light by dust in the near-infrared to ultraviolet (UV) band. The interaction between photons of very high energy and the EBL gives origin to an electron-positron pair, thus reducing the VHE $\gamma-$ray flux at Earth, with the effect of changing the source observed spectral shape with respect to the intrinsic one. This effect is relevant especially for dis-

[1] https://icecube.wisc.edu/

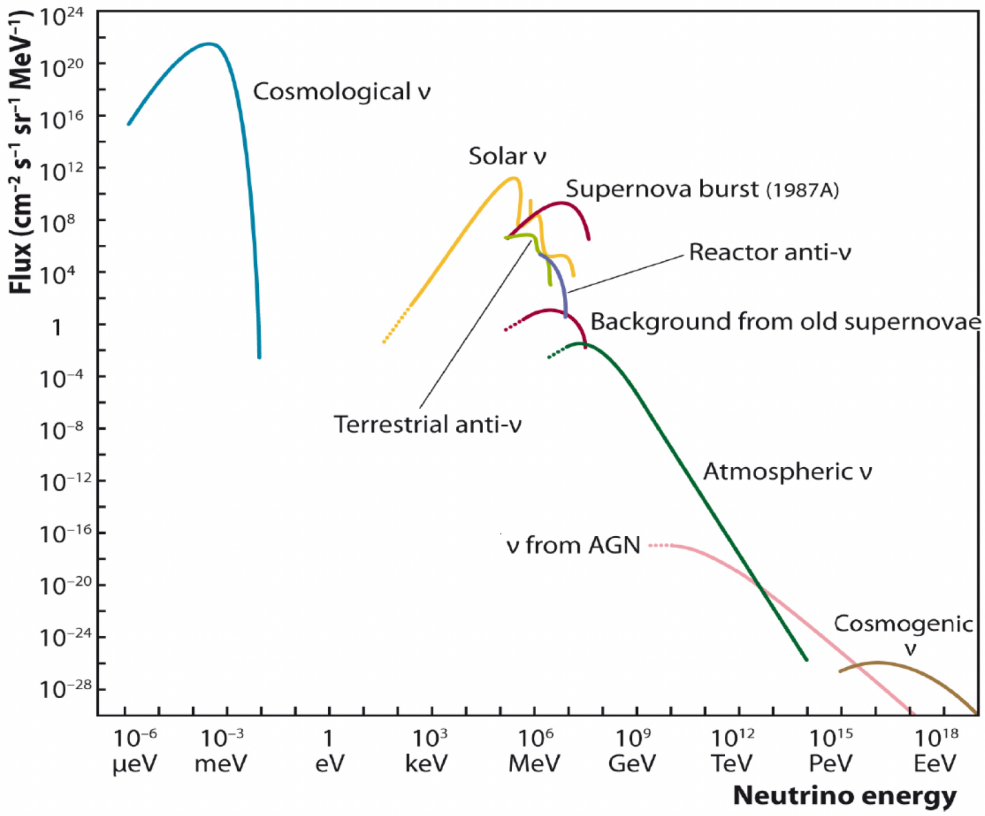

Figure 1.2: Spectrum of neutrinos originated in different sources and environments. Credits: [10]

tant sources, since the effect of EBL absorption increases with the distance. To date, the farthest source ever detected in VHE $\gamma-$rays is the Gamma-Ray Burst GRB 201216C, located at a redshift of $z = 1.1$ [12].

In the context of multi-messenger and neutrino astrophysics the detection of high-energy neutrinos and VHE $\gamma-$rays from the same object is relevant since they can be produced together in CR interactions as shown in Eqs. 1.1$-$1.8 and thus pinpoint to the long-sought CR sources. However, also information provided by other wavelengths are necessary in order to build a complete picture of the emitting objects. Indeed, photons of lower energy can arise from particle cascades initiated by interactions of the emitted hadrons in their way to Earth. In this thesis we exploit data in optical/UV range, X$-$rays, high energy (HE, 0.5 MeV $-$ 100 GeV) $\gamma-$rays and VHE $\gamma-$rays. These kind of radiation have different properties, so different instruments and detection techniques are needed. For example, the penetration depth of photons in the Earth atmosphere is wavelength-dependent, as shown in Fig. 1.3, so only the radio, near infrared and optical bands can be directly observed with telescopes built on Earth. The far infrared

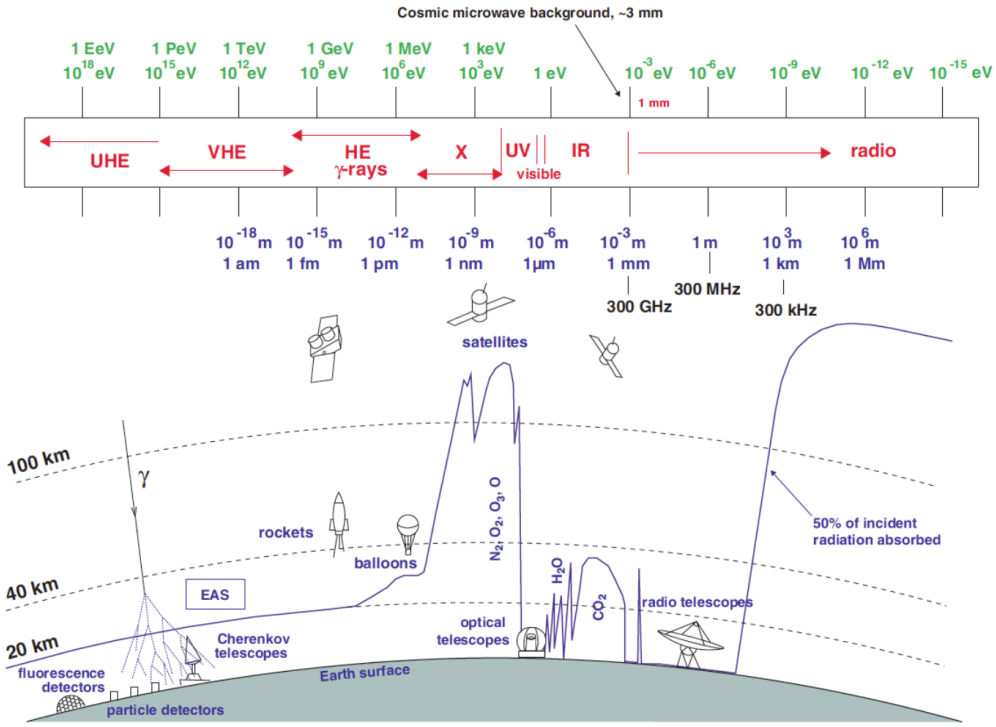

Figure 1.3: Spectrum of electromagnetic radiation. The top bar reports the different wavebands and respective energies, while the bottom illustration shows the height at which photons of different energies are fully absorbed by the Earth atmosphere and the different instruments used for the detection. On the left, VHE $\gamma-$rays and Extensive Air Showers (EAS) are shown. Credits: [13]

and the higher energy bands can be directly detected only through satellite-based experiments. However, as shown in the same Figure, VHE $\gamma-$rays are detected from Earth by *Imaging Atmospheric Cherenkov telescopes* (IACT), through an indirect method called *Imaging Atmospheric Cherenkov Technique* (see Sec. 1.3.1 for more details), which exploits the interaction of $\gamma-$rays with the Earth atmosphere and the production of the so-called **Extensive Air Showers** (EAS). EAS are cascades of particles originated from the interaction of high-energy $\gamma-$rays or hadrons with the nuclei of the air molecules composing the Earth atmosphere. They can be divided into *electromagnetic showers* and *hadronic showers* based on the primary particle initiating the cascade. Fig. 1.4 shows a schematic representation of the development of these types of showers.

In electromagnetic showers the progenitor is a $\gamma-$ray of very high energy. When it reaches the Earth atmosphere, it interacts with the atmospheric nuclei, typically at an altitude of about 20 km above sea level, undergoing the pair production process and producing an $e^- e^+$ pair. Then, while traveling, the produced particles interact with

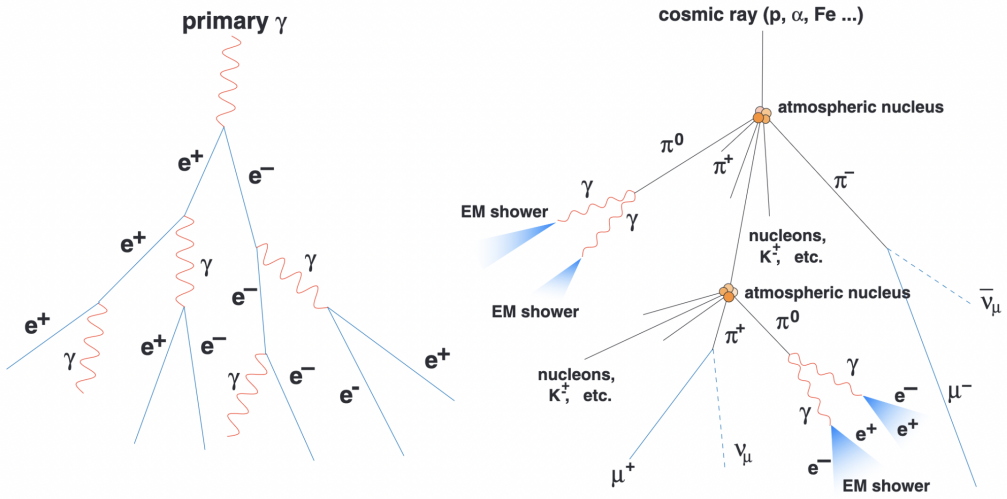

Figure 1.4: Schematic representation of electromagnetic (left) and hadronic (right) showers. The particles produced at each interaction step are shown. Credits: [14]

the electric field of the nuclei, losing energy via bremsstrahlung and producing further high-energy photons, which give origin to additional e^-e^+ pairs and so on, generating a cascade of secondary particles. The energy of the primary $\gamma-$ray is distributed to the produced particles, which have a lower energy at each interaction step. The process stops when a critical energy is reached. It is the energy at which the energy losses through bremsstrahlung and ionization are equal for the pairs. This energy corresponds to about 80 MeV in air at standard conditions ($T = 20\,^{\circ}\mathrm{C}$, $P = 1\,\mathrm{atm}$).

Hadronic showers are initiated by high-energy protons and nuclei, which are the main components of CRs. In their first interaction with atmosphere these particles mostly produce pions ($\sim 90\%$), kaons ($\sim 10\%$), and a small amount of nucleons, which in turn generate photons, electrons, positrons, muons and neutrinos through further interactions or decay. These processes stop when nucleons reach the minimum energy required for pion production, which is about 1 GeV. Compared to electromagnetic showers, hadronic ones penetrate deeper in atmosphere, since hadrons have a larger mean free path than electrons, and, consequently, develop in a longer time ($\sim$ 10 ns compared to $\sim$ 3 ns). Considering the secondary particles generated in hadronic showers, neutrinos are produced by the decay of charged pions, kaons and muons, while $\gamma-$rays by the decay of neutral pions. The produced $\gamma-$rays can then initiate electromagnetic showers. Neutrinos and $\gamma-$rays produced in hadronic showers represent a source of background for neutrino observatories and Cherenkov telescopes, since they do not come from astrophysical sources. Thus, methods for background rejection have to be implemented in the instruments observation strategies and analyses in order to filter out these sources of noise.

1.2 The IceCube Neutrino Observatory

The IceCube Neutrino Observatory [15] is a neutrino detector located at the geographic South Pole and immersed in the antarctic ice, starting at a depth of about 1450 m. It covers a total volume of approximately 1 km^3 of ice. Its construction began in 2004 and the instrument started taking data in its final configuration in 2011. It is composed of 86 strings, which were buried into ice through the use of hot water drills. Each string is equipped with 60 Digital Optical Modules (DOM), for a total of 5160 modules, located between 1450 and 2450 m below the surface. A DOM is a glass sphere split in half at the equator containing a Photomultiplier Tube (PMT), needed to detect the signatures left by neutrinos in ice, and the support electronics, needed to transmit the acquired information to the Laboratory, placed on the surface. IceCube consists of the main *large-scale detector* and *DeepCore*, as shown in Fig. 1.5. The former embeds 78 strings located 125 m apart and containing DOMs at a distance of 17 m each other. This configuration is optimized for high-energy, and thus astrophysical, neutrinos. It has a minimum detectable energy of the order of 100 GeV. The latter involves 8 central strings deployed at a distance of 72 m each other and DOMs placed at a distance from 7 to 10 m apart. This configuration allows the instrument to reach lower energies, so DeepCore is mainly used for the study of atmospheric neutrinos and neutrino oscillations. The minimum detectable energy of the DeepCore is about 10 GeV. Finally, on the surface, IceCube is equipped with an array of 162 tanks, each one containing two DOMs, divided into 81 stations. This array is called *IceTop*. It is able to detect particles produced in extensive air showers initiated by cosmic-rays and is mainly used as a veto for the underground detector, since atmospheric neutrinos represent a source a background. Its energy threshold is approximately 300 TeV; this means that it is more sensitive to showers produced by cosmic-rays in the PeV−EeV energy range. Besides IceTop, on the surface, at the center of the array, the *IceCube Laboratory* is located. It is the central operations building for the experiment. It includes two cable towers, which connect the array surface cables to readout computers in order to collect the data acquired by the DOMs.

As already mentioned, the DOMs have the role of detecting neutrino signatures in ice and send the registered information to the Laboratory. The detection method is based on the observation of the *Cherenkov light* produced by relativistic charged particles created in neutrino interactions with the atomic nuclei of the medium they are traveling in [16, 17]. The interaction happens via deep inelastic scattering with the quarks of the target nucleus. It involves the exchange of a $W^{\pm}$ or Z^0 bosons. In the first case we refer to *Charged Current* (CC) interaction, while in the second one to *Neutral Current* (NC) interaction. The CC interaction leads to the production of a charged lepton sharing the initial neutrino flavor, while the NC interaction leaves the neutrino state intact. The reactions can be described as:

$$\text{CC}: \quad \nu_l + N \rightarrow l + X \tag{1.9}$$

$$\text{NC}: \quad \nu_l + N \rightarrow \nu_l + X, \tag{1.10}$$

where l denotes the type of lepton (e, μ, τ), while N and X are the target and produced

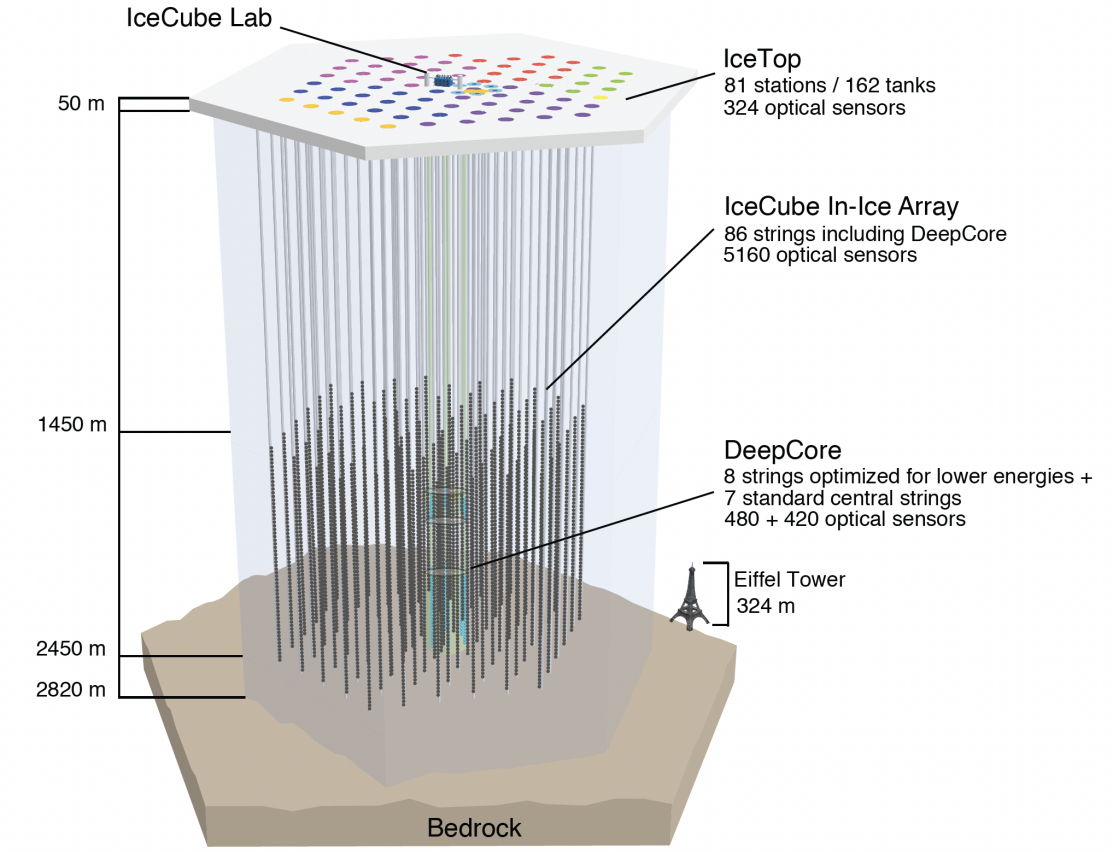

Figure 1.5: Schematic representation of the IceCube Neutrino Observatory. Large-scale detector, DeepCore, IceTop and the IceCube Laboratory are highlighted. The Eiffel tower is also shown for comparison. Credits: [15]

nuclei. The output lepton and the hadronic cascades initiated by the output nucleus X can undergo the *Cherenkov effect* [18], through which they can be detected by the DOMs. This effect happens when a charged particle moves in a dielectric medium with a velocity v greater than the velocity of light in that medium, causing the emission of an electromagnetic shock wave, called Cherenkov light, in the direction of the moving particle. The emitted light has an opening angle given by $\cos\theta_c = [\beta n]^{-1}$, with $\beta = v/c$ and n the refractive index of the medium (for ice $n \approx 1.32$). The Cherenkov light consists of very short flashes of few ns and is emitted in the blue/ultraviolet band. Thus, it can be detected by optical sensors with a very fast electronics, like PMTs. Moreover, in order to increase the neutrino interaction probability and allow detection of the Cherenkov light, a dense and transparent medium is needed. This is the reason why ice was chosen. Another possible choice is water. Examples of neutrino telescopes under water are ANTARES [19], which was in operation until 2022, and KM3Net [20], still

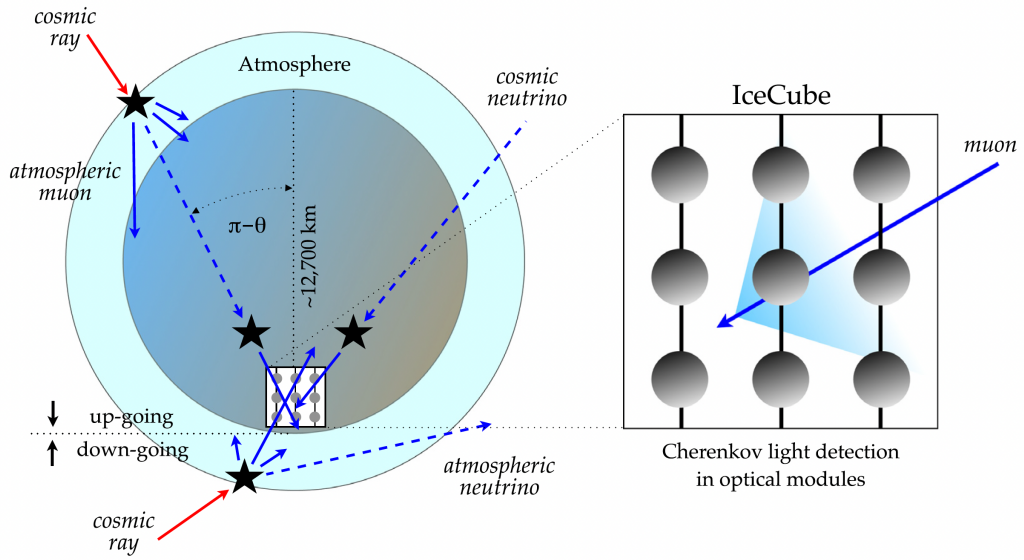

Figure 1.6: Path of up-going and down-going tracks detected by IceCube. The blue solid arrows refer to background high-energy muon tracks generated by CR interaction in the atmosphere, blue dashed arrows refer to up-going tracks produced by both atmospheric and astrophysical muon neutrinos, stars indicate the interaction points. On the right, the Cherenkov light pattern left by a muon track in the detector is shown. Credits: [16]

under construction, both located in the Mediterranean sea.

Within the neutrino signatures detected by IceCube, a huge amount of background events are present, the rejection of which represents one of the main challenges for each neutrino telescope. These events consist of muons and muon neutrinos generated by CR air showers in the Earth atmosphere and they represent a source of noise for the identification of astrophysical events. In order to reduce the atmospheric background for such events, IceCube can select only up-going events, namely those events originating below the horizon. In this way, particles are required to pass through Earth in order to reach the detector. A drawback is the reduction of the sky coverage, since with this approach only the Northern Hemisphere can be observed. A schematic representation of this method is shown in Fig. 1.6, together with an illustration of the Cherenkov light emission inside the instrument. The remaining background from atmospheric up-going tracks can then be further reduced with the application of energy cuts. Indeed, the spectrum of atmospheric neutrinos, described by a power-law $\mathrm{d}N/\mathrm{d}E \propto E^{-3.7}$ was found to be much softer compared to the astrophysical neutrino flux, described by $\mathrm{d}N/\mathrm{d}E \propto E^{-2.19}$. At energies $E > 100$ TeV the astrophysical neutrino flux is dominant over the background, so the chance of an event to be of astrophysical origin increases

with energy. Cuts on energy are used also to observe signals from the Southern Hemisphere. In this case, since the Earth cannot be used to reduce the background, cuts are harder in order to remove atmospheric muons.

1.2.1 IceCube alert streams

IceCube has the remarkable capability of observing the whole sky almost continuously, with an up-time exceeding 99.8% during an ordinary week. This quality makes it an ideal platform for conducting real-time studies, which are really important in neutrino astronomy given the transient nature of neutrino events and, possibly, of the astrophysical phenomena related to them. For this reason, since 2016 [21], IceCube provides a real-time system which promptly notifies the astrophysical community for follow-up observations when astrophysical neutrino candidates are identified. There are two main analyses, which identify different kinds of events and alert streams [22]. On the one hand, IceCube operates a search for single high-energy astrophysical neutrino candidates events with the goal of identifying possible electromagnetic counterparts. This search is based on the harder spectrum of astrophysical events with respect to background ones, so it is more sensitive for events with energies $E > 100$ TeV. On the other hand, an approach for the identification of clusters of neutrino events was also implemented. This search is performed on both the location of known sources and the whole sky, with the goal of determining changes in the emission state of the candidate in the first case, and discovering new sources in the second one. The cluster identification technique is based on the fact that the neutrino background is isotropic, temporally and spatially, so a significant excess would indicate an astrophysical event. In the following a description of these analyses and related alert channels is reported.

Single high-energy tracks and cascades

The single high-energy alert events are due to the interaction of a single neutrino through the CC or NC interactions described above.

In particular, **tracks** are predominantly produced by the CC interactions of muon neutrinos with nucleons, namely $\nu_\mu + N \rightarrow \mu^- + X$. Given the low interaction rate of muons, the majority of these tracks pass fully through the detector, allowing a precise reconstruction of their arrival direction ($< 1^\circ$ for neutrinos with energies above few TeV[2]), at the expense, however, of the energy resolution. Indeed, muons lose energy gradually through ionization, bremsstrahlung, pair production and photo-nuclear interactions during their travel, part of which lies outside the detector. The energy reconstruction is then limited by the length of the muon track inside the instrumented volume.

Differently from tracks, **cascades** can be produced by both CC and NC interactions (see Eqs. 1.9−1.10), where hadronic cascades can be initiated by the output nuclei X

[2]Note that the average scattering angle between the interacting muon neutrino and the produced muon decreases with increasing energy, following the relation $\psi_{\nu\to\mu} \sim 0.7^\circ (E_\nu/\mathrm{TeV})^{-0.7}$ [23], hence the angular resolution of an event improves at higher energies.

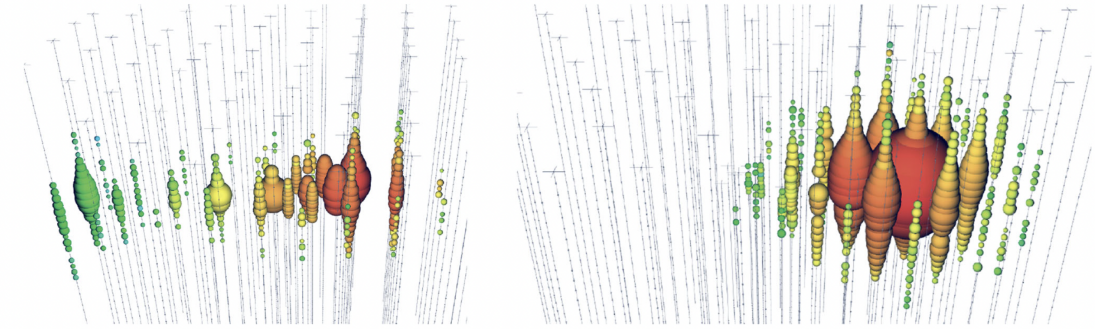

Figure 1.7: Examples of track-like (left) and cascade-like (right) events. The coloured dots represent the hit DOMs, their dimensions the quantity of Cherenkov light detected, and the colors the arrival time of the Cherenkov flashes (earlier times in red and later in green). Credits: [17]

and detected through the Cherenkov light emitted by the secondary charged particles produced. However, in CC interactions involving electron and tau neutrinos, namely $\nu_e + N \rightarrow e^- + X$ and $\nu_\tau + N \rightarrow \tau^- + X$, cascades can also originate from the outgoing leptons, which cannot produce elongated tracks in the detector because of their rapid scattering (electrons) and decay (taus). The energy deposited in the medium by cascades has a rather spherical distribution, so the angular uncertainty is much worse than for tracks ($\sim 10^\circ - 15^\circ$). On the contrary, the energy reconstruction is much more precise since cascades can often be fully contained in the detector volume.

In Fig. 1.7 examples of a muon track crossing the detector and a cascade originated by a ν_e or ν_τ CC or any flavour NC interaction are shown. Basically, the number of photo-electrons detected by each PMT correlates with the energy deposited by the event, while the arrival time of the Cherenkov photons is linked to its direction, allowing the reconstruction of the two quantities.

Starting from 2016, IceCube broadcasts the events it detects to the astrophysical community. Initially, two alert streams were defined, based on specific cuts related to the properties of each event. Both of them considered track-like events only, best suited for multi-messenger studies given their precise angular resolution. Alerts for cascade events were then issued starting from 2020. The two original alert streams are **High-Energy Starting Events (HESE)** and **Extreme High-Energy (EHE) events** [21]. HESE alerts include only starting tracks, namely tracks with a neutrino interaction vertex inside the detector. Since the probability for an event to be of astrophysical origin increases with energy, only events depositing > 6000 photo-electrons are taken. EHE alerts mainly consist of muon tracks fully contained in the detector volume. The selection is more sensitive to events with energies between 500 TeV and 10 PeV, targeting tracks with an angular resolution $< 1^\circ$ [21]. These selections were operated separately until May 2019, when the real-time infrastructure was updated with the implementation of a unified algorithm which combines EHE alerts, an improved version of HESE

ones[3] and a stream based on an already existing selection called **Gamma-ray follow-up (GFU)**, in operation since 2012 and originally designed for follow-ups in VHE $\gamma-$rays [24, 25]. It exploits statistical methods called boosted decision trees to treat up-going and down-going events in a different way in order to reduce the background. Most of the alerts issued by IceCube fall under the GFU selection. Moreover the updated infrastructure introduces a new, key, parameter called signalness, which is applied to all the aforementioned alert types. It is defined as

$$\text{Signalness}(E,\delta) = \frac{N_{\text{signal}}(E,\delta)}{N_{\text{signal}}(E,\delta) + N_{\text{background}}(E,\delta)}, \tag{1.11}$$

where E is the reconstructed neutrino energy, δ is the declination of the event, $N_{\text{signal}}(E,\delta)$ and $N_{\text{background}}(E,\delta)$ are the number of signal and background events expected at a declination δ and above an energy E. They are computed through simulations. This quantity is a measure of the probability for an event to be of astrophysical origin and introduces the new **GOLD** and **BRONZE** streams, which classify the alerts based on their signalness value: if an event has a signalness value between 30% and 50% it is classified as a BRONZE alert, while if the value is $>$ 50% it is classified as a GOLD alert. Fig. 1.8 reports all the GOLD and BRONZE alerts issued by IceCube between 2011 and 2020 in a sky-map in equatorial coordinated.

Track and cascade alerts are publicly distributed through the NASA General Coordinates Network[4] (GCN) in the form of circulars containing information on their sky coordinate, angular uncertainty, energy and signalness in order for other observatories to start follow-up observations promptly.

Neutrino clusters from known $\gamma-$ray sources and the whole sky

These alert streams were specifically tailored for follow-up observations by partner IACTs in VHE $\gamma-$rays, which are thought to be produced together with high-energy neutrinos in the same hadronic interactions , as already mentioned in Sec. 1.1. Thus, a joint program between IceCube and IACTs would be beneficial in the search for neutrino sources. These streams are part of the GFU selection, which includes the partnership of MAGIC (see Sec. 1.3 for more details) and VERITAS [26] since 2012, and H.E.S.S. [27] since 2019. In its most recent version[5], this channel looks for flares of lower-energy astrophysical neutrino events over the background . The search is operated on a predefined list of sources, with the aim of alerting IACTs about neutrino multiplets in the direction of known $\gamma-$ray emitters as well as on the whole sky, with the aim of discovering new potential neutrino candidates or targeting sources not yet observed in $\gamma-$rays.

The monitored sources are blazars, a subclass of Active Galactic Nuclei (AGN, see 2 for more details) showing a highly variable behaviour in $\gamma-$rays and for which it is

[3]The new HESE stream places, as an additional cut, the selection of only those events with a length of at least 200 m inside the detector, with the aim of reducing the amount of poorly reconstructed tracks.

[4]https://gcn.nasa.gov/

[5]The GFU selection was upgraded in May 2019.

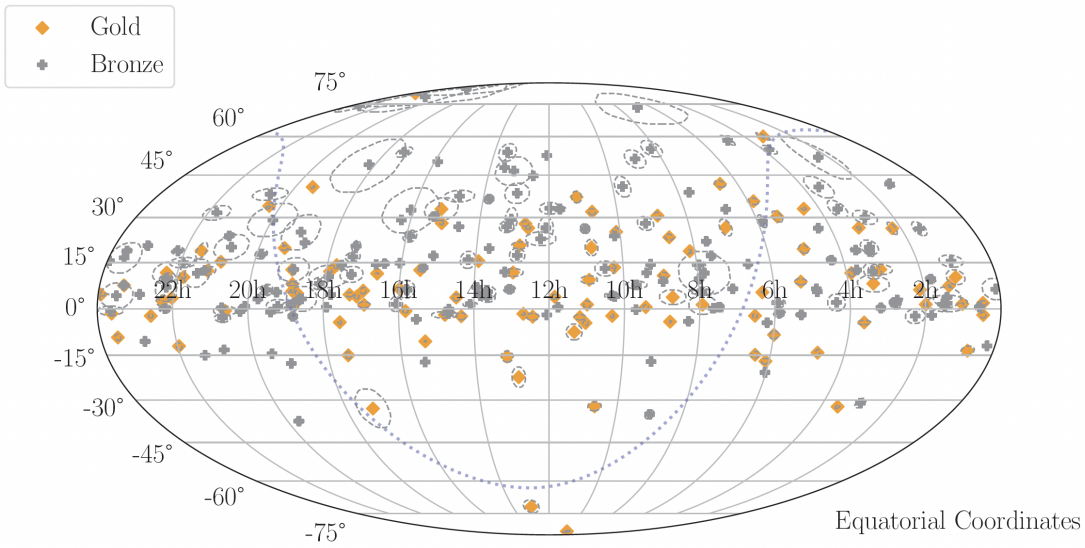

Figure 1.8: Distribution of GOLD and BRONZE alerts issued by IceCube between 2011 and 2020. The orange diamonds refer to GOLD alerts, while the grey crosses refer to BRONZE ones. The dashed contours denote the angular uncertainty of each alert at the 90% confidence level. Credits: [25]

expected to have a detectable neutrino signal in coincidence with $\gamma-$ray flares. The selection was made starting from the Third Fermi catalog of active galactic nuclei (3LAC) [28], and the third Fermi catalog of hard spectrum sources (3FHL), [29] released by the Fermi/LAT Collaboration[6]. The selection criteria are [22]:

- Visibility from the sites of IACTs, with elevation above horizon $> 50^\circ$ for MAGIC and VERITAS, and $> 60^\circ$ for H.E.S.S.,
- Extragalactic origin, with redshift $z \leq 1$, where the chosen threshold corresponds to the most distant object observed in VHE $\gamma-$rays,
- Variability at 99% confidence level[7]
- Detectability prospects for IACTs, which is evaluated as follows: starting from the average Fermi flux a flare is simulated by multiplying it by a factor 10, then the flux at $E > 100$ GeV is extrapolated taking into account the EBL effect. Only those

[6] https://glast.sites.stanford.edu/

[7] The criteria to evaluate the variability are different in the 3LAC and 3FHL catalogs. In the first case a likelihood test on the monthly averaged lightcurves is used to compare the hypothesis of variability against the one of steady emission. The sources are considered to be variable if they show a variability index > 18.47. In the second case a bayesian blocks algorithm is used to divide the lightcurve into blocks of constant flux. A source is considered to be variable if it shows two or more blocks.

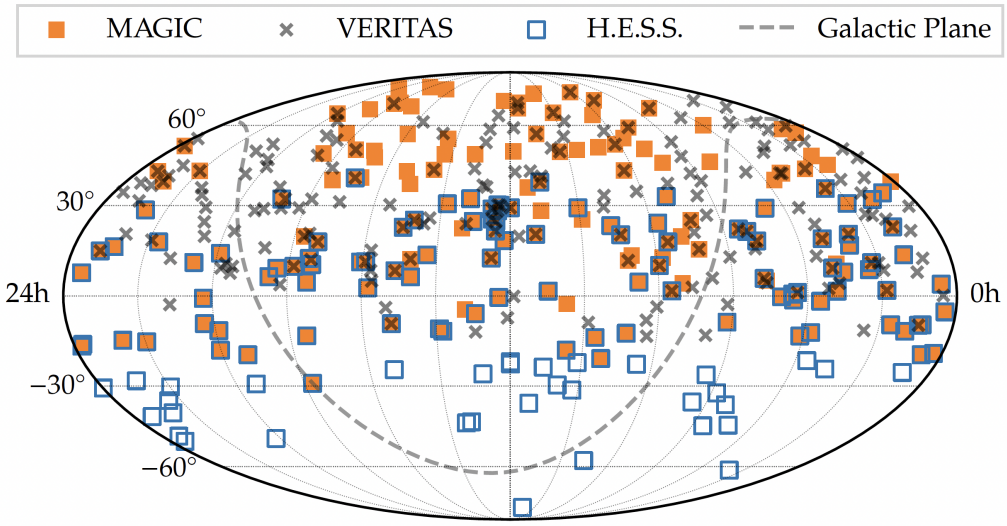

Figure 1.9: Sky-map showing the sources monitored by IceCube for neutrino clusters for each IACT. Orange filled boxes refer to MAGIC selected sources, grey crosses to VERITAS ones, and blue empty boxes to H.E.S.S. ones. Credits: [22]

sources showing a flux above 100 GeV exceeding the 5σ sensitivity of the IACT for 2 hours (MAGIC , VERITAS) or 3 hours (H.E.S.S.) of observation are taken.

The final selection includes 179 sources for MAGIC, 190 for VERITAS, and 139 for H.E.S.S., for a total of 339 objects, since some of them are in common between two or more lists. Fig. 1.9 shows the location of the sources monitored for each IACT.

The search for **neutrino clusters from monitored sources** is thus restricted to these pre-defined locations, required to be within 1σ ($\sim 1^\circ - 2^\circ$) of the neutrino event angular uncertainty. When an event satisfying this requirement is detected, its signal-to-noise ratio $\mathcal{S}/\mathcal{B}$ is evaluated and only those events with $\mathcal{S}/\mathcal{B} > 1$ trigger the analysis. The analysis operates a likelihood maximization on time windows defined by the detected event and earlier events with $\mathcal{S}/\mathcal{B} > 1$, for a maximum length of 180 days [22]. After that, the best-fit time window is chosen. If the significance of the likelihood analysis exceeds a threshold of 3σ, then an alert is issued to the partner telescopes. Once an alert is released, the system is muted. This requires the previous event to be below the threshold and means that following events above the threshold do not imply the issuing of new alerts since they are thought to belong to the on-going flare. In this way the behaviour of significance over time is not known. However, a subsequent offline analysis can reveal the global best-fit of the flare as the most significant cluster of events. It is typically following an earlier alert. Simplified schemes of the analysis method and the alert issuing are shown in Fig. 1.10.

The same analysis is applied also in an **unbiased search on the whole sky**, with an

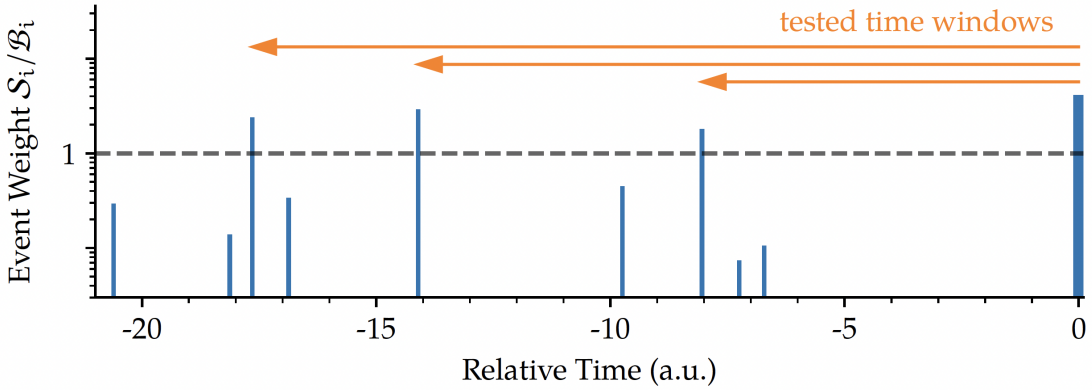

(a) Scheme of the algorithm used in the search for neutrino clusters. The blue bars show the signal-to-noise ratio $\mathcal{S}/\mathcal{B}$ of the neutrino event, while the orange arrows represent the time windows considered to the likelihood analysis. The time windows start with an event having $\mathcal{S}/\mathcal{B} > 1$ and end with the triggering event.

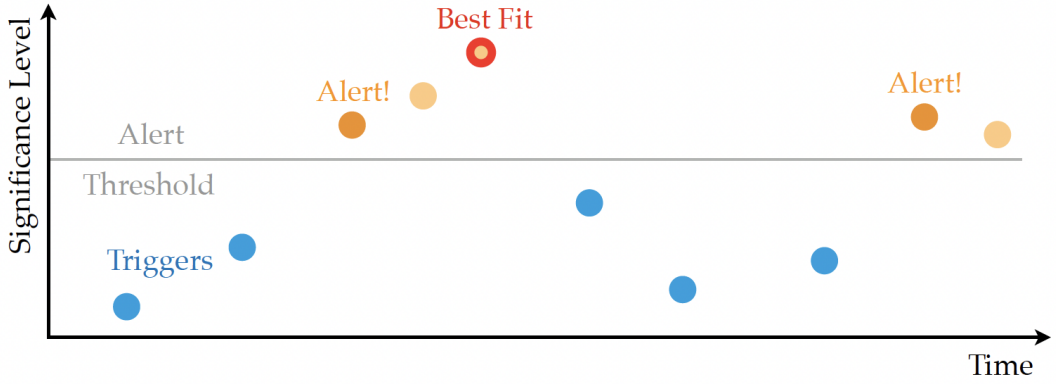

(b) Scheme of alert issuing after the analysis algorithm has run on a neutrino event with $\mathcal{S}/\mathcal{B} > 1$. If the significance of the best-fit time window likelihood is below the alert threshold of 3σ, then no alert is distributed (light blue points), otherwise if it crosses the threshold, an alert is issued (dark orange). Following triggers above the threshold are considered part of the same flare and not qualify as independent alerts (light orange). The flare can continue until a peak is reached (red), which usually represents the outcome of a following offline analysis.

Figure 1.10: Simplified schemes of the analysis used in the search for neutrino clusters. The top panel shows the algorithm used to select interesting events, while the bottom one shows the alert issuing given the outcome of the above algorithm. Credits: [22]

additional algorithm defining the direction of the excess through a grid scanning. In this scan, the celestial sphere is pixelized in square bins of side 0.92° and each bin is treated as a source hypothesis. When an event with $\mathcal{S}/\mathcal{B} > 1$ is observed in a specific bin, the time clustering algorithm described above (and shown in Fig. 1.10) is triggered on the target bin and the nearby ones, taking into account the event angular uncertainty and constraining the search to a maximum radius of 2°. The algorithm operates the

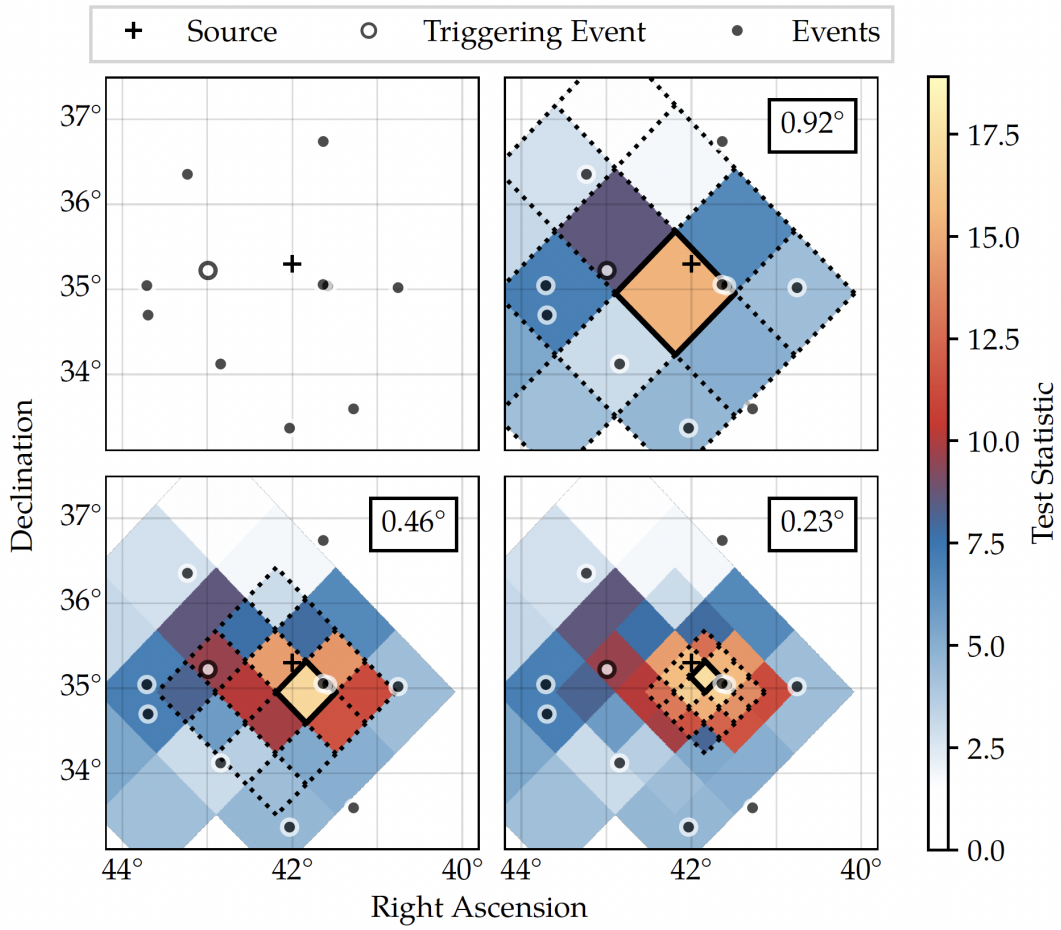

Figure 1.11: Scheme of the all-sky search method. Once a triggering event is observed, the sky is divided into spatial bins (upper plots). The dotted contours indicate the scanned bins, the solid contour selects the most significant one, which is divided into sub-bins at each step (lower plots). The colors give the value of the significance in each bin. Remember that for each bin scanned in space, the time clustering algorithm, looking for the best-fit time window, is triggered. Credits: [22]

likelihood maximization in each considered bin and the most significant one is taken. Then, it is divided into sub-bins, the likelihood is maximized in each sub-bin and so on, until the best-fit grid size is reached. An example of the spatial scanning method is shown in Fig. 1.11. Given that this search is unconstrained in space, the number of tested source locations is huge. Hence, the sensitivity of the all-sky search is lower and it is more likely to select background overfluctuations with respect to the source monitoring. For this reason, the alert threshold is set higher, to 5σ, in order to select only the events most likely to be real signals.

With the set thresholds the expected alert rate is of ~ 10 events/year for the source monitoring and of ~ 0.5 alerts/year for the all-sky search. The emitted alerts are distributed privately to the partner IACTs and contain information about the source candidate (if the source monitoring is performed), the significance, and the flare duration.

1.3 The MAGIC telescopes

The Major Atmospheric Gamma-ray Imaging Cherenkov (MAGIC) telescopes are a system of Imaging Atmospheric Cherenkov Telescopes (IACT) located at the Observatorio Roque de los Muchachos (ORM, 28° 45.70′ N, 17° 53.42′ W) in the Canary Island of La Palma, Spain, at 2225 m above sea level. They are placed at a distance of 85 m from each other and have a reflector with a diameter of 17 m, which allows to reach an energy threshold of 50 GeV, which can be lowered to 30 GeV if a particular type of trigger system, called Sum-Trigger-II analog trigger and described in Sec. 1.3.2, is used. The first telescope, MAGIC-I, started operating in 2004. It operated in mono-mode until 2009, when the second telescope, MAGIC-II, started its commissioning phase. Since then the two telescopes work in stereoscopic mode. As already introduced in Sec. 1.1, these kind of telescopes is designed to indirectly detect VHE $\gamma-$rays through the products of the EAS they produce when reaching the Earth atmosphere. The technique they use for such purpose is explained in the next section. Thanks to this technique and their joint observations in stereo mode, they are able to reach an integral flux sensitivity of $(0.66 \pm 0.03)\%$ of the Crab Nebula (usually taken as a reference source in $\gamma-$ray astronomy) flux above 220 GeV for 50 hours of observation [30]. A picture of the MAGIC telescopes is reported in Fig. 1.12.

1.3.1 Imaging Atmospheric Cherenkov Technique

The Imaging Atmospheric Cherenkov Technique is the method used by IACTs to observe VHE $\gamma-$rays. It is an indirect technique combining the information provided by the products of EAS initiated by a VHE $\gamma-$ray interacting with the Earth atmosphere. Thus, the atmosphere acts as a fundamental part of the detector. The aim of this technique is the extraction of the spatial and temporal information of the detected light and the reconstruction of the energy and direction of the primary particle. As for the case of neutrinos, the Cherenkov effect is exploited: as already mentioned in Sec. 1.1, the atmospheric electromagnetic showers produce a cascade of electrons and positrons (together with $\gamma-$rays), which emit Cherenkov radiation when moving with a velocity greater than the speed of light in air. The emitted light has an opening angle which varies from $\sim 0.2^\circ$ at a height of ~ 30 km, to 1.5° at sea level, due to the changes of the atmospheric density with altitude. This results in the formation of a light circle with a typical radius of $120 - 150$ m on the ground, called *Cherenkov light pool*. If an IACT lies inside this ring, then it can detect the Cherenkov flashes.

Given the properties of the Cherenkov light, some specific requirements on the structure of such telescopes have to be satisfied. IACTs need to have large reflectors,

Figure 1.12: Picture of the two MAGIC telescopes during an observing night. Credits: C. Righi

composed by mirrors, with a diameter of several meters, in order to collect the maximum number possible of Cherenkov photons and focus them to the camera[8]. Given the short duration of the Cherenkov flashes, the camera needs fast electronics. It is usually composed of an array of PMTs placed on the focal plane. Moreover, in order to ensure a detailed reconstruction of the shower image, the number of PMTs must be large. As an example, MAGIC camera has 1039 PMTs. Differently from neutrino telescopes, IACTs can operate only at night and have a small Field of View (FoV, usually $< 5^{\circ}$), so their duty cycle[9] is limited ($\leq$ 20%) and sources must be directly pointed in order to be observed. Once the Cherenkov light is collected by the reflector and focused on the camera, the shower image can be recorded. The image produced by a $\gamma-$ray signal has an elliptical and narrow shape. The intensity of the image signal is proportional to the amount of Cherenkov radiation produced, in turn linked to the energy of the primary $\gamma-$ray. An example of the Imaging Atmospheric Cherenkov Technique and the recorded $\gamma-$ray images is shown in Fig. 1.13.

However, a big challenge in the application of this technique lies in the discrimi-

[8]Note that IACTs are essentially optical telescopes, since they detect the Cherenkov light, which is in the optical/UV band.

[9]The duty cycle is defined as the fraction of time in which the telescope can perform observations compared to the total available time. Given that Cherenkov telescopes can work only at night, the fraction of time they can use to perform observations is limited.

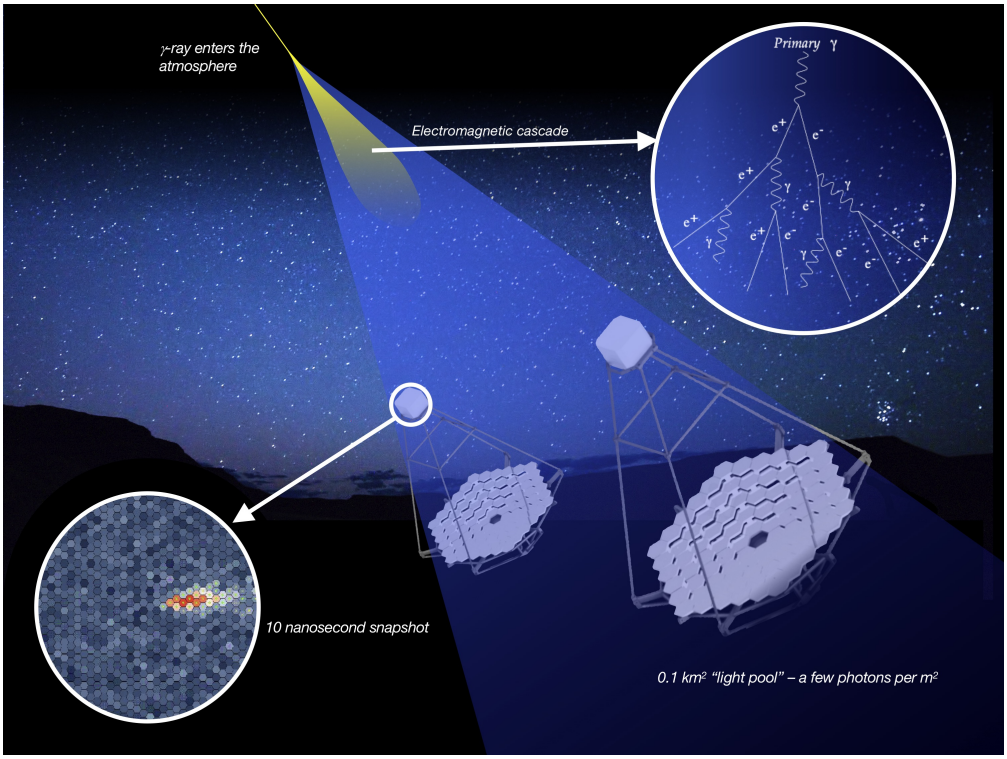

Figure 1.13: Scheme of the Imaging Atmospheric Cherenkov Technique. The Cherenkov light from electromagnetic cascades initiated by a VHE $\gamma-$ray is collected by the mirrors and reflected into the camera. PMTs in the camera record the signal and generate the $\gamma-$ray image. Credits: CTA Observatory

nation between $\gamma-$ray signals and the background. The main source of background is given by hadronic showers, the contribution of which is about three orders of magnitude larger than electromagnetic ones. In order to recognize and suppress this source of background, the different geometry and temporal features of the images produced by the two types of showers are exploited during the data analysis phase. Indeed, hadronic cascades give origin to wide images of irregular shape, which are quite different from the $\gamma-$ray ones. Also atmospheric muons produced in hadronic cascades contribute to the background, but their effect can be easily recognized and rejected thanks to the ring-like images they produce. Another source of background is represented by the isotropically distributed photons composing the Night Sky Background (NSB). The NSB basically represents the brightness of the sky and is the result of the contribution of several components like scattered light from stars and galactic sources, airglow, zodiacal light, artificial lights and the Moon [31]. It depends on the time of the observation and the location. La Palma island was chosen as the site of the MAGIC telescopes because it has very good NSB values. The NSB effect on $\gamma-$ray images is removed during the data analysis in a step called *Image cleaning* (see Sec. 1.3.4), while

its random fluctuations are directly discarded thanks to trigger system.

Finally, the use of two or more telescopes in stereoscopic mode, like the MAGIC system, improves the event selection and the geometrical reconstruction of the shower. With such a configuration an event is registered only if it is observed in both telescopes. Moreover, it provides a view of the same shower from different perspectives, so the direction of the primary particle can be recovered more precisely.

1.3.2 Hardware and trigger systems

The hardware of the MAGIC telescopes consists of several components, including the alt-azimuthal supporting structure and the drive system, the mirrors and the reflector, the camera, the readout and trigger system, and other auxiliary and online subsystems facilitating effective telescope operations [30, 32]. All these systems are handled by a **Central Control software** called SuperArehucas, which receives reports on the status of the subsystems every second and sends updates to the telescope operators through a graphical interface.

Telescope structure, mirrors and camera

One of the main science goals of the MAGIC telescopes is the prompt follow-up of transient events like, for example, the aforementioned neutrinos, Gamma-Ray Bursts (GRB), or Gravitational Waves (GW). In order to achieve this objective, a fast repositioning of the telescopes during the occurrence of such events is needed. The telescope **structure** has thus to be both rigid and light-weight; requirements that are satisfied by the use of reinforced carbon fiber tubes. Thanks to the use of such materials, the overall weight of the MAGIC telescopes is < 70 tons, with the structure alone weighting < 20 tons. This allows the telescopes to move with an angular speed of $4^\circ/\mathrm{s}$ during standard observations. It can be increased up to $7^\circ/\mathrm{s}$ in case of fast repositioning, used to track transient sources. In this way, the telescopes are able to re-point to each location in the sky in less than 30 s. Moreover, the mount of the telescopes is alt-azimuthal, so that they can be moved in a wide range of positions both in zenith and azimuth. Specifically, they can be moved from -90° to 318° in azimuth and from -70° to $+105^\circ$ in zenith.

The movement of the telescopes is controlled by a hardware component called **drive system** [33]. The drive monitors the pointing and tracking of the sources, which can be affected by the gravitational load of the structure and thus needs to be corrected. This is done through the use of two Charged-Coupled Device (CCD) cameras placed in the center of the reflector. The first one, called **TPoint camera**, takes pictures of the catalogued bright stars in the telescope FoV spanning the whole zenith and azimuth ranges. It compares the observed stars with the catalog in order to find possible mispointings so that the drive can correct them. This is important in order to update the so-called *bending model* of the structure, which allows to have a pointing precision of $\sim 0.01^\circ$. The second camera, called **Starguider camera**, is aligned with the telescope axis and continuously compares the position of the PMT camera, signaled by a ring of 6 Light-

Emitting Diodes (LEDs) at its edge, with the position of reference stars in the FoV, in order to correct possible misalignment.

The structure weight can introduce deformations also in the **mirror dish** during the telescope movement, worsening the focus of the instrument. The mirror dish is a parabolic reflector with a diameter and a focal length of 17 m. The parabolic shape is chosen because of its isochronicity. In this way the arrival times of the Cherenkov photons on the dish are conserved on the camera. The reflector is composed of 247, $1\,\mathrm{m} \times 1\,\mathrm{m}$, small mirrors which can be moved through the **Active Mirror Control system (AMC)** [34], consisting of actuators acting on the individual mirrors in order to correct for the weight loading effect and obtain a focused image on the camera. The quantity determining the angular resolution of a telescope is the Point Spread Function (PSF), defined as the 39% containment radius of the light spot generated by a point-like source in the focal point. With the mirrors focused, the PSF of the MAGIC telescopes is smaller than 10 mm. The PSF of the single mirrors and the complete reflector is measured by a CCD camera, called **SBIG camera**, located in the center of the mirror dish as the aforementioned ones.

In the focal point of the reflector, the **PMT camera** is placed, which collects the Cherenkov photons reflected by the mirrors. The MAGIC camera has a total weight of 850 kg and is sustained by an aluminum arc. It is composed of 1039 PMTs of 2.54 cm diameter arranged in a circular shape and grouped in 169 clusters of 7 pixels as shown in Fig. 1.14 (black thick contours). Each PMT has a FoV of 0.1°, and the whole camera has a total FoV of 3.5°. The PMTs are sensitive in the blue band, with a high quantum efficiency of 34% for wavelengths of ~ 350 nm and a response time of ~ 1 ns. Moreover they have a low gain, of $\sim 3 \times 10^4$, managed by setting their High Voltage (HV). The low-gain configuration is designed to reduce the amount of charge hitting the PMT anode, thus preventing their rapid deterioration, but it is also useful in increasing the telescope duty cycle. Indeed IACTs ideally should work in dark conditions only, but, given that the anode current flowing into the PMTs is proportional to the NSB level, by reducing the PMT gain it is possible to observe also under moderate moon light conditions [35]. For MAGIC the PMT gain is reduced by a factor of 1.7 and the configuration is called *reduced HV*. In order to observe under higher moon levels, MAGIC camera is equipped with UV-pass filters.

Moreover, since the PMT gain and readout undergo fluctuations due to external factors like temperature variations, a **calibration system** [36] is needed in order to obtain a uniform gain in the whole camera. This system is located in the center of the reflector as the mentioned CCD cameras and consists of a calibration box containing a laser with light properties as close as possible to the Cherenkov light (MAGIC calibration box laser has a wavelength of 355 nm and duration of pulses of 0.4 ns). The laser is used to uniformly illuminate the camera plane thanks to a sphere placed in front of it and evenly diffusing the laser light. A controlled illumination of the camera allows the adjustment of the HV settings of each PMT in order to have the same gain in each pixel (the so called *flat fielding*) and to obtain the conversion factor between analog-to-digital counts (ADC) and number of photoelectrons (phe).

In order to focus the coming light into the PMT window and thus increase the collection efficiency, each PMT is coupled with a light concentrator called Winston cone, which also avoids NSB light from large zenith angles to enter the PMTs. Once photons reach the camera, the PMTs convert them into phe in order to register the signal, then this electric signal is converted into an optical one through vertical cavity surface emitting lasers (VCSEL) and sent to a data acquisition (DAQ) building, called counting house (CH), through 160 m long optical fibers. Here, the signal is converted back into an electric one and split into two branches, one of which is sent to the readout system and the other one to the trigger system. Both are installed in the CH and separated from the camera body in order to achieve a light-weight design and allow fast movement of the instrument.

The **trigger system** is composed of three levels considering single pixels, clusters of pixels in the same camera, and coincidences in the two telescopes. Only if the signal passes all the levels it can be recognized as a $\gamma-$ray event and not, for example, as a background fluctuation. Details on the trigger systems are given in the next sections.

The **readout system** consists of a memory chip, called Domino Ring Sampler 4 (DRS4), where the signal is host, waiting for the trigger decision. It is composed of an array of 24 capacitors, which are charged with the signal. When the trigger conditions are fulfilled, the charge accumulated in the capacitors is converted into a digital signal through an Analog-to-Digital Converter (ADC) and the signal in each pixel is recorded into waveforms of 30 s in the form of ADC counts.

Finally, the signal passing the trigger levels and processed by the readout system, is sent to a **Data AcQuisition system (DAQ)**, consisting of a dedicated computer per telescope which stores the events in .raw data files and performs a first online data analysis. Each raw file contains about 14000 events and has a size of about 2 GB.

Standard trigger system

The trigger is a fundamental system with the role of selecting the Cherenkov signal from $\gamma-$ray induced showers, discriminating it from the background noise of hadronic showers and NSB. Thanks to its selection it is also possible to significantly reduce the total number of events stored by the readout system and the DAQ.

The trigger system of the MAGIC telescopes [30, 37] is composed of three levels. The lowest level, called **Level 0 (L0)**, is an amplitude discriminator operating on individual PMTs. It performs a selection of those pixels with signal exceeding a specific amplitude threshold, called Discriminator Threshold (DT), by issuing a digital 1 if this condition is satisfied. In order to optimize the sensitivity of the telescopes, the DT level changes based on the sky brightness and the type of source observed. For the observation of extragalactic sources it is lower than for galactic ones, because of the higher luminosity of the galactic plane region. In the same way, a lower level is used during dark nights, and it is increased in presence of the Moon in order to avoid contamination from the higher NSB. In general, the DT is kept as low as allowed by the trigger rate in order to select also faint events. Moreover, the DT is continuously monitored and modified during the same night according to the variations of the light conditions in order to

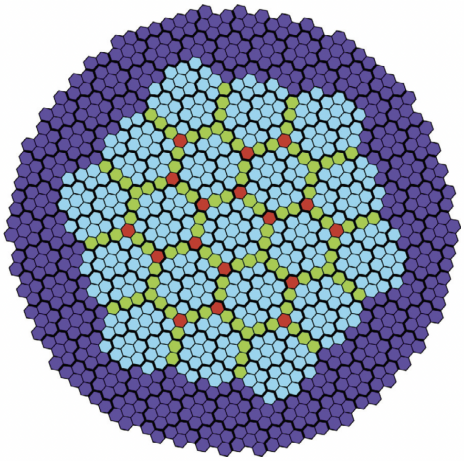

Figure 1.14: Scheme of the MAGIC camera showing the 1039 PMTs composing it. The cyan hexagons mark the 19 L1 macrocells. Pixels belonging to two or three macrocells are shown in green and red repsectively. Purple pixels do not belong to the trigger region. Black thick contours denote the 169 PMT clusters. Credits: [30]

keep stable rates in each pixel. During standard observations (i. e. dark time) the L0 rate is $\sim$ 800 kHz, with a DT value of 4.25 phe for extragalactic sources and 15% higher for galactic ones.

The signal passing the L0 trigger is sent to the **Level 1 (L1)** trigger, which searches for spatial and temporal coincidences of adjacent pixels in the same camera with a signal above the DT. It is useful to reject pixels which underwent individual fluctuations due to the background. In particular, the L1 trigger searches for a minimum number n of Next Neighbour (NN) pixels within a temporal gate of $8 - 9$ ns. There are different NN configurations implemented, with n varying from 2 to 5. During standard stereo observations the 3NN configuration is used. The L1 trigger operates on 19 overlapping hexagonal cells of 37 pixels each, called macrocells (see Fig. 1.14). In each macrocell the boundary pixels are in common with the adjacent cells and in total they cover the innermost 547 pixels of the camera. The typical L1 rate is $\sim$ 15 kHz.

The output of each macrocell is processed and sent to the last trigger stage, the stereo trigger, also named **Level 3 (L3)** trigger. It searches for time coincidence between the signals in the two telescopes and works at a trigger rate of $\sim 250 - 350$ Hz. Since the MAGIC telescopes are placed at a distance of about 80 m, the shower signal reaches them at different times. Thus, the L1 trigger signals are delayed by an amount depending on the specific pointing direction of the telescopes. If the signals are within a coincidence window of 180 ns, then the event is accepted as an astrophysical one and the readout starts.

Sum-Trigger-II system

Besides the standard MAGIC trigger, an alternative trigger system is installed at the L1 level, named Sum-Trigger-II [38, 39]. When observations are performed with this kind of trigger, the L0 output is sent to the Sum-Trigger-II system rather than to L1 and its output is sent to the stereo trigger as in the standard case. The Sum-Trigger-II system is specifically designed to improve the telescopes performance in the low energy domain

($E < 80$ GeV) and is driven by different science cases like galactic sources (e. g. pulsars), distant AGNs, and GRBs, for which the bulk of $\gamma-$ray emission is expected to happen at low energies, with a cutoff at tens to hundreds of GeV.

The detection of $\gamma-$rays at these energies is challenging due to the lower energy of the primary particles, which interact with the Earth's atmosphere at a greater height. This results in less energy being transferred to secondary particles in the EAS. As a consequence, the shower develops at higher altitudes, and the emitted Cherenkov light is partly absorbed on its way to the ground, reducing the amount of light reaching the telescopes and resulting in very faint flashes on the camera, close to the noise level[10]. Moreover, at that altitude, the air is more rarefied, hence the air refraction index is lower. This results in a strongly collimated Cherenkov emission producing images with the photon distribution confined in a small region of the camera. Finally, given that the shower develops higher in the atmosphere, its interaction with the geomagnetic field becomes non negligible. Therefore, the trajectories of particles in the EAS are bent and, as a result, the Cherenkov image is distorted, complicating the direction reconstruction. The features of these images are clearly different from the ones produced by higher-energy $\gamma-$rays, which typically exhibit an elliptical shape, with the majority of the charge concentrated at the peak of the shower development. At low energies, the accumulated charge in the single PMTs is generally not enough to generate signals passing the L1 trigger previously described, which was designed for high-energy $\gamma-$rays. Thus its performance is not effective in these cases and the need of a different type of trigger system emerges.

For this reason the Sum-Trigger-II system was developed. The basic principle of Sum-Trigger-II involves the sum of the signals from single PMTs belonging to the same predefined camera patches (similar to the previously mentioned macrocells) and the application of the threshold to the resulting output. In particular, the camera is divided into 3 layers of patches partly overlapping, for a total of 55 patches and 529 pixel used (see Fig. 1.15). Each patch contains 19 PMTs, except 12 patches in the external region, which contain 4 blind pixels not used for the triggers (filled coloured pixels in the image). They are excluded in order to fill the same trigger area used in the standard trigger. The FoV of the patches is about 0.5° and their size is chosen in order to match the size of the images produces by low-energy $\gamma-$rays. The exact number of PMTs in each patch is the result of Monte Carlo (MC) simulations aiming at optimizing the trigger efficiency around $25 - 30$ GeV. A smaller size would imply the loss of part of the Cherenkov signal, while a larger one would increase the accidental number of spurious triggers due to the NSB.

For each telescope, the signal registered by each PMT within a certain amount of time is collected. The time interval is set to 3 ns. Since electromagnetic showers emit Cherenkov light of about $2 - 3$ ns duration, the chosen value reults to be wide enough to maximize the detection of Cherenkov photons in the EAS and sufficiently narrow to minimize the rate of spurious triggers produced by the NSB. Then the signal in each

[10]Note that the Cherenkov light produced by an EAS initiated by a primary $\gamma-$ray with $E \lesssim 80$ GeV is emitted at a height of $\sim 10 - 12$ km.

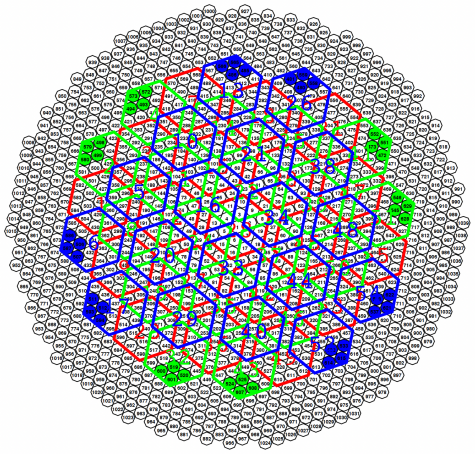

Figure 1.15: Scheme showing the three layers of camera patches used in the Sum-Trigger-II system. Patches belonging to each level are shown in red, blue, and green. The blue and green layers have the same shape but a different orientation on the camera. The fully coloured pixels do not contribute to the trigger decision. Credits: [38]

PMT in the same patch is summed. In this way all pixels in a patch contribute to the trigger, making non negligible also faint signals generally below the sensitivity of the standard trigger on the one hand, and signals dominated by the fluctuations of the NSB on the other hand. However, given that low energy $\gamma-$rays produce small confined images on the camera, the principle of integrating over regions of the camera where the $\gamma-$ray image may be confined increases the signal-to-noise (S/N) ratio. Indeed the PMT signals coming from a shower are correlated, so they stack up linearly, while the signals originating from the noise in each PMT are completely independent and hence don't add together. Therefore, in a camera patch, the summed signal results in an increase of the S/N ratio, making Sum-Trigger-II particularly suitable for detecting low-energy $\gamma-$rays. The patches summed signals exceeding a defined threshold are sent to the L3 trigger previously described, which searches for coincidences in the two telescopes. The DT for Sum-Trigger-II is set in the range $16 - 24$ phe per patch [39], the specific value of which depends on the light condition of the night sky in each camera patch. The total trigger rate of the single telescopes with Sum-Trigger-II is $\sim$ 30 kHz, while the stereo trigger rate is about $500 - 600$ Hz.

Finally, the performance of Sum-Trigger-II was determined by simulating 64 million $\gamma-$ray events from a source with a power-law spectral index of -2.6. As shown in Fig. 1.16, performance at energies lower than 80 GeV is considerably better compared to the standard trigger, with a resulting energy threshold[11] of 21 GeV, significantly lower than that of the standard trigger (41 GeV) and a capability to trigger 6 times larger at 20 GeV [39].

Weather monitoring instruments

The monitoring of the atmospheric conditions is of great importance for the telescope operators to determine the feasibility of the observations and for the data analyzers to

[11]The energy threshold is defined as the peak of the event rate energy distribution, computed from simulated MC $\gamma-$rays. It increases with increasng zenith angle or NSB level.

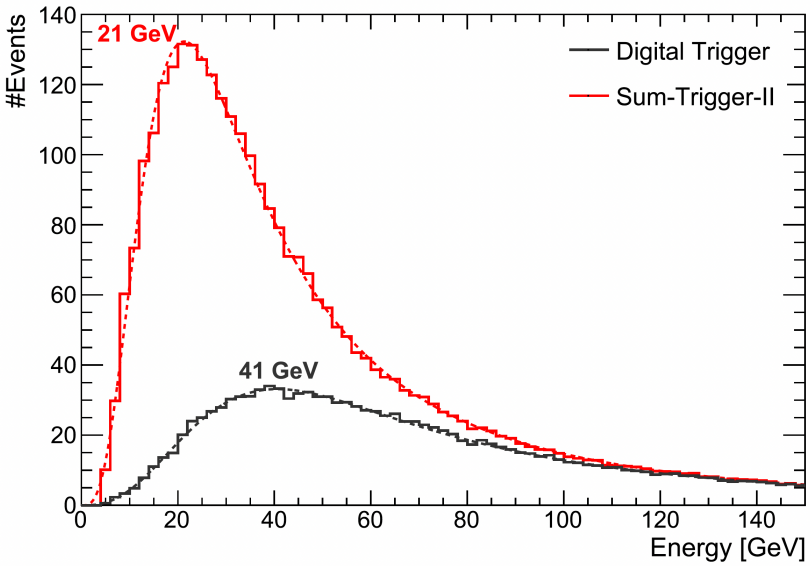

Figure 1.16: Energy threshold for the Sum-Trigger-II system assuming a source spectrum with a -2.6 power-law index. The number of stereo events close to the threshold (peak of the distribution) is shown for both the standard trigger (black line) and the Sum-Trigger-II system (red line). Credits: [39]

inspect the quality of the taken data. The MAGIC site is equipped with several auxiliary instruments with the role of continuously checking the weather.

Within them there is a **weather station**, which provides information about pressure, temperature, relative humidity, wind speed and wind direction every two seconds. This monitoring is crucial to maintain safe telescope operations by adhering to predefined limits. If these limits are exceeded, alerts are issued and automatic reactions ensure the safety of the telescopes. On the roof of the CH also a **rain sensor** and an **all-sky camera** are installed, the latter having a FoV of 150° and taking images of the sky every two minutes.

In addition, there are two systems used to monitor the transparency of the atmosphere. The information they provide is really helpful during the analysis phase because it allows to distinguish good-quality data and select them. The former, called **LIght Detection And Ranging (LIDAR)** [40], consists of a laser shooting light pulses in the atmosphere at a position distant 4° from the target location in order not to interfere with MAGIC observations. It exploits the backscattering of the laser light by clouds and aerosols to give a value of the atmosphere transmission. This value is linked to the arrival time of the backscattered photons. The latter, called **pyrometer**, is an instrument pointing at the same direction of the telescopes aiming at evaluating the presence of clouds. In order to do this, it measures the sky temperature, which increases in presence of clouds because they reflect the thermal radiation from the Earth. Each MAGIC ob-

servation is complemented by a transmission parameter and a cloudiness value, given by the LIDAR and pyrometer outputs respectively, generally in good agreement, indicating the quality of the sky during the observation.

Other subsystems

Telescope operations are finally complemented by additional subsystems hosted in the CH and linked to the MAGIC CC. They receive information from external facilities and perform a first preliminary data reduction. These include:

- The **Automatic alert system** [32]: It is a system processing the alerts sent from the General Coordinates Network (GCN), where a number of missions report the detection of transient events, like GRBs, GWs or neutrinos, soliciting follow-up observations. The system evaluates the alerts in terms of observability from the MAGIC site and, if some pre-defined criteria are met, it takes control of the telescope, automatically pointing it to the target position. The observational strategy and criteria defined for the follow-up of neutrino events are described in Sec. 5.2.

- The **MAGIC OnLine Analysis (MOLA)** [41]: It is a program performing a real-time analysis of MAGIC data from calibration to high level products, with the aim of giving a first estimation of the significance and flux of the observed sources. This is particularly important in case of flaring sources or transient events, since it allows telescope operators and schedulers to extend the observation and issue alerts towards other observatories in case of an interesting signal is detected;

- The **On-Site Analysis (OSA)** [42]: It is a program performing the first steps of the standard analysis chain while data are produced. After the end of the observations, in the morning, the raw and processed data are transferred from La Palma to an external cluster, called Port d'Informació Cientifica (PIC) and located in Barcelona, where they are available to analyzers to perform the high level analysis. Thanks to this system, the data size, of $\sim 1-2$ GB for raw data, is reduced by a factor of ~ 500 before being transferred making the transfer faster. However, OSA works only in case of dark nights and data taken with the standard trigger. When such conditions are not met, the analyzers have to start the analysis from raw data or explicitly request the processing at PIC, based on the type of analysis they have to perform.

- The **Data check system**: It is a program automatically running at the end of each observation night which provides different outputs allowing to inspect the quality of the data taking both in terms of atmospheric conditions and electronics performance. One of the outputs mostly used by analyzers is the so-called Superplot which contains the evolution of source zenith, M2 camera current, L3 trigger rate, transmission and cloudiness over the whole observation.

1.3.3 Data taking

The MAGIC telescopes, as IACTs, can operate only at night and the best conditions for them to observe are given by moonless nights, the so-called dark time. The total amount of dark time in one year is $\sim$ 1600 hours, resulting in a duty cycle of about 18%. This time is further reduced in case of bad weather or technical problems. It was noted that, on average, the fraction of dark time really used by the MAGIC telescopes to take data is $\sim$ 65%. In this regard, the moderate gain of the camera PMTs is of great help in increasing the observation time, allowing to observe in moon conditions with NSB level up to 12 times higher than in dark time. The observation time can be further increased by lowering the gain of the PMTs and applying UV-pass filters, allowing observations under NSB levels respectively 20 and 100 times higher than the dark time one. With these adjustments the telescopes are able to observe under moonlight conditions up to 75% of the Moon phase and need to stop observations only for $3 - 4$ days during full Moon nights, resulting in an increase of the duty cycle from 18% up to 40% [35].

During every observation night, the MAGIC telescopes take different types of data, each of which has a specific role in the calibration and extraction of scientific information from the source data. Before observations start, once per night, the **pedestal subtraction run (pedsub)** is taken. It consists of an observation of few minutes performed with the camera lids closed. It is needed to calibrate the baseline of the DRS4 capacitors in the readout system. After the pedsub is taken, observations start. For each observation, before pointing to the target source, other two types of data are taken. The former is the **pedestal run**, which is taken with the camera open and has the purpose of evaluating the number of background events caused by the NSB and the readout noise. It contains events with random triggers and, so, without any pulse, which are then subtracted from the scientific data during data calibration. The latter is the **calibration run**, consisting of a uniform and artificial illumination of the camera with a known light pulse from the calibration box laser. It is used to compute the conversion factor between digital counts and number of phe. After these preliminary data acquisitions are performed, the actual observations start. The related data type is called **data run** and contains the signal (triggered events) from the target source. The data run usually has a duration of 15 or 20 minutes and is divided into subruns of 2 minutes each and containing about $1 - 2$ GB of data. Moreover, in between the data acquisition, interleaved pedestal and calibration events are recorded in order to monitor possible changes in the detector and electronic noise.

Pointing modes

The MAGIC data taking can be performed with two types of pointing configurations. The former is the **ON/OFF mode**, in turn requiring two different observations to be performed: a ON observation and a OFF one. In the former the telescope directly points at the source coordinates, so that the source lies in the center of the camera; while the latter points to a position in the sky without VHE sources and is used for the estimation of the background. The OFF pointing should be performed under similar zenith and

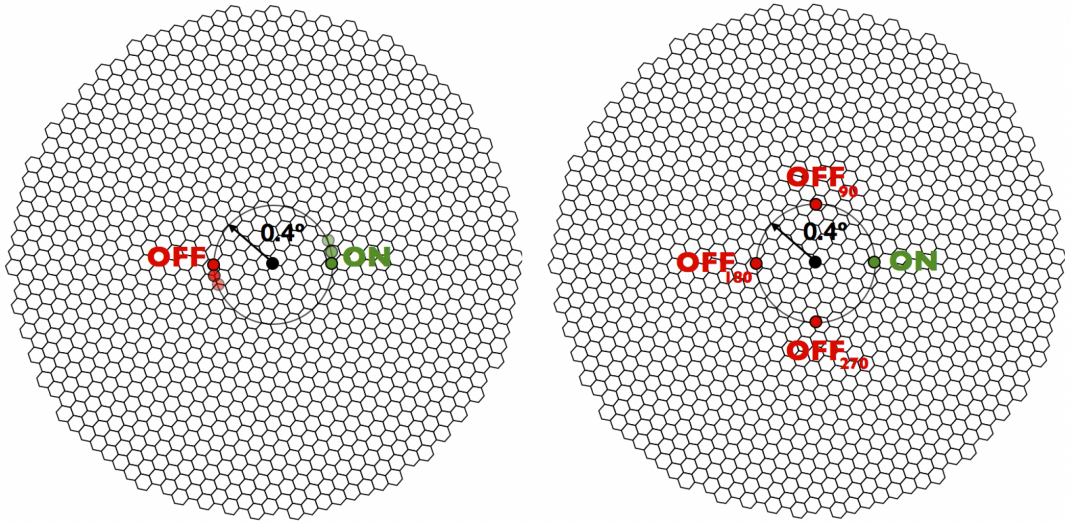

Figure 1.17: Schematic representation of the wobble observation mode for one (left) and three (right) OFF positions. The black dot marks the camera center, the green one the location of the source in the camera, and the red ones the location of the selected OFF positions. Credits: [44]

azimuth conditions to the ON one and for the same amount of time. With this mode, part of the dark observation time is lost due to OFF runs, while it could be used to point scientific targets. For this reason another pointing mode was developed, called **wobble mode** [43]. In this configuration the telescopes do not point directly at the target but at a coordinate offset with respect to the nominal source position. The MAGIC telescopes use a standard offset of 0.4° for point-like sources. The background is estimated during the observation thanks to the selection of one or more OFF positions symmetric to the pointing position with respect to the camera center. An example is shown in Fig. 1.17, where the green point represents the position of the target and the red one(s) the position of the OFF region(s). Selecting more than one OFF region allows to better estimate the background since systematic effects due to the position in the FoV or the PMT response can be reduced. Moreover, in order to remove possible inhomogeneities in the camera, after every $15 - 20$ min (namely after each data run) the wobble pointing is changed, so that the following run is taken with the same offset and with a rotation angle of 90° or 180° based on the number of wobbles needed. Recalling Fig. 1.17, the next wobble would point at one of the regions marked as OFF. In this way the region that now is the target position becomes a OFF region. The process is then repeated, covering the other symmetric positions, until the allocated observation time for the given target is over. Currently, the wobble tracking is the default pointing mode for MAGIC, while the ON configuration is used only in very specific science cases.

1.3.4 Standard data analysis chain

The .raw files from DAQ, containing information on charge and arrival time, represent the starting point for MAGIC data analysis. The software used to analyze MAGIC data is a proprietary software called **MAGIC Analysis and Reconstruction Software (MARS)** [45], consisting of a collection of `C++` scripts built on the `ROOT` framework[12] [46]. The data analysis chain spans from the calibration of the taken data and up to the production of high level scientific results, like spectra and lightcurves. It can be split into three main levels of data processing:

- **Low-level analysis**: Stage consisting in the conversion of the taken data from .raw to .root format (using the program `merpp`), calibration and signal extraction (`sorcerer`), and image cleaning and parametrization (`star`);
- **Intermediate-level analysis**: Stage where data from the two single telescopes are combined and stereo parameters are estimated (`superstar`), a Random Forest (RF) is trained starting from Monte Carlo (MC) simulations (`coach`) and applied to data (`melibea`) in order to estimate how $\gamma-$like is the event and reconstruct its energy and direction;
- **High-level analysis**: Stage consisting in the computation of scientific quantities like significance (`odie`), skymaps (`caspar`), spectrum and lightcurve (`flute`).

In addition, an auxiliary program, called `quate`, is usually used by analyzers to select good-quality data, namely data not affected by bad weather or hardware problems. A schematic representation of the data analysis flow is shown in Fig. 1.18. As shown in the image, the analysis is applied on three different types of data: ON data are those coming from the source we are observing, OFF data are those coming from observations with no evidence of $\gamma-$ray signal. They are selected in order to have a sample of data dominated by the background and estimate it. They usually come from faint sources which were not detected during the observations. Finally, MC $\gamma-$rays are $\gamma-$ray data coming from MC simulations. The simulations are generated by a modified version of the `CORSIKA` (COsmic Ray SImulations for KAscade) code [48], called `mmcs`, specifically customized for the MAGIC telescopes [49]. The MC data have to closely reproduce the observational and technical conditions of the telescopes in order to optimize the analysis, so different MC periods are defined based on seasonal variations (e. g. the calima sand storm, mainly acting in summer, which worsens the reflectivity of the mirrors) and hardware changes. The periods are named ST.XX.YY, where ST means stereo, XX indicated the major hardware change, and YY is the analysis period corresponding to the minor hardware changes. For each period, different files satisfying specific observational settings are created, in order to account for their different influence on the observations. In particular, they simulate the pointing observational mode (wobble or ON mode), the source type (point-like of extended), and the source zenith, reason for which the MAGIC MC data are divided into zenith ranges ($5^\circ - 35^\circ$, $35^\circ - 50^\circ$,

[12] https://root.cern.ch/

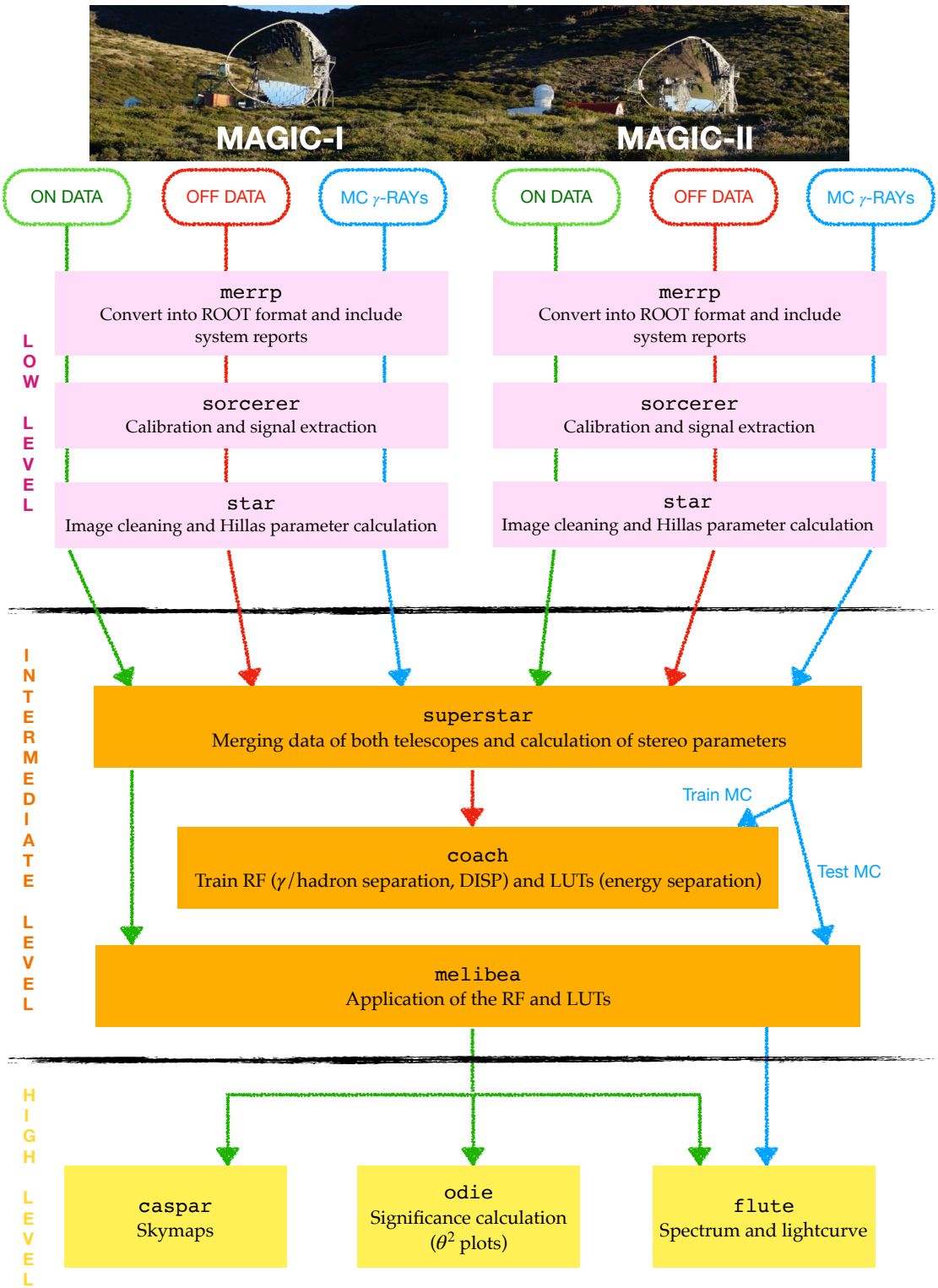

Figure 1.18: Flowchart of MAGIC data analysis chain. Both ON, OFF and MC $\gamma-$ray data have to pass the different analysis steps in order to obtain high-level scientific results about the source emission. Adapted from [47].

$50^\circ - 62^\circ$, $62^\circ - 70^\circ$). In the same way, also real data (i. e. ON and OFF) are divided according to the same observational conditions. In this thesis real and MC data from point-like sources observed in wobble mode at low/mid zenith ($z_d < 50^\circ$) are used. In the analysis, both OFF and MC $\gamma-$ray data are used in the intermediate-level stage to instruct the system to distinguish γ-like showers from hadron-like ones.

Low-level analysis

The signal is registered by the DAQ in the form of digital counts in 30 ns waveforms. The very first step of the analysis relies on the conversion of the raw data given by the DAQ output in .raw format, into the .root format. This task is performed by the program `merpp` (MERging and Preprocessing Program). This program also makes a merge of the data files with the reports from all the MAGIC subsystems, in order to complement the data with additional information necessary for further analysis. This information comprises for example telescope pointing, status of the various subsystems, wobble used, etc.

Done this, the **signal extraction and calibration** is performed. The program used here is `sorcerer` (Simple, Outright Raw Calibration; Easy, Reliable Extraction Routines), which acts on each individual pixel to extract the stored intensity and arrival time of the Cherenkov light. The signal of each pixel is initially stored in time slices of 0.5 ns each, and each waveform is composed by the sum of the actual signal and the baseline of the capacitors in the readout system. For the estimation of the baseline, all the recorded time slices stored in the *pedestal run* are binned into a histogram and fitted with a Gaussian, the mean value of which is taken as baseline and will be removed from the real signal. After that, the signal is extracted from the DAQ waveform through an algorithm looking for the largest value registered in 6 consecutive time slices (i.e. 3 ns) and sliding over the windows repeating the search. If no signal is present, the largest noise fluctuation is taken. The arrival time of the window is computed as the weighted average of the time slices in the selected window with the digital counts registered in each of them. Once the signal is extracted, it can be calibrated, meaning that the digital counts are converted into number of phe. In order to do this, the so-called F-factor method [50] is used on the *calibration run*. The number of phe emitted in the calibration pulses are assumed to have a Poisson distribution with mean N and standard deviation $\sqrt{N}$. The same assumption is made for the digital counts registered. Considering Q counts, we define $\langle Q \rangle$ their mean and σ_Q their standard deviation, which is expected to be wider than the pure Poissonian expectation because of the PMT noise. These quantities can be related in the following way: $F\frac{\sqrt{N}}{N} = \frac{\sigma_Q}{\langle Q \rangle}$, where F is the so-called F-factor and is different for each PMT. From this relation, the conversion factor between digital counts and phe can be derived as: $C = \frac{N}{Q} = F^2 \frac{\langle Q \rangle}{\sigma_Q^2}$. The homogeneous illumination provided by the calibration run is also exploited for a flat-fielding procedure, aimed at adjusting the HV of each pixel in order to have the same response, which is needed since PMTs have a different gain. In this way the calibration can be done on the average number of phe rather than on a per-pixel basis.

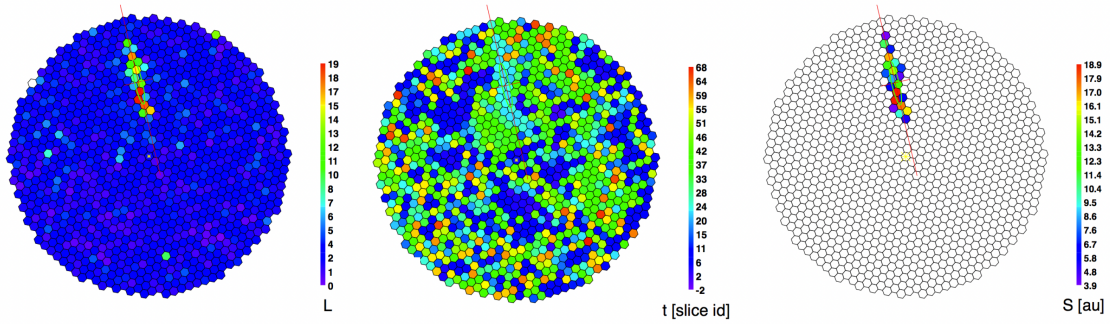

Figure 1.19: Example of a $\gamma-$ray induced shower recorded in MAGIC camera. Left: recorded signal charge before image cleaning; center: distribution of arrival times; right: cleaned image. Credits: [44]

The calibrated signal has then to undergo an **image cleaning** [51] in order to remove the pixels that most likely do not belong the the $\gamma-$ray signal. Indeed, Cherenkov images are mostly dominated by noise, given by the contribution of the NSB or fluctuations of the electronics, which has to be removed in order to genuinely identify the real signal. The program performing this task is `star` (STandard Analysis and image Reconstruction), which also does the following parametrization of the cleaned image. Firstly, the signals are clipped in amplitude in order to reduce the effect of possible strong fluctuations due to the NSB or the PMT noise. Then, a sum is computed over the signals of each possible combination of 2, 3, or 4 (i. e. 2NN, 3NN, 4NN) neighbouring pixels. The groups of pixels are accepted to belong to the image if the sum exceeds a certain threshold value within a certain time interval (around $\sim$ 1 ns). Those pixels surviving the sum selection undergo an individual cleaning aimed at identifying the core and boundary pixels of the image. The core pixels are selected as those with a charge above a certain threshold Q_c and a minimum number of neighbouring pixels exceeding the same threshold. This is needed in order to remove random pixels which have a high charge value but are not part of the shower. The mean arrival time of the selected pixels is computed, a time window Δt_c is set, and all those core pixels with arrival time outside the window are rejected. After that, a lower threshold Q_b is set in order to select boundary pixels within those having at least one core pixel as direct neighbour. The boundary pixels are accepted only if they have arrival times within a second time window Δt_b. In this way the shower image is identified. An example of a $\gamma-$ray initiated shower image is shown in Fig. 1.19. The values Q_c and Q_b have to be optimized in order to suppress the background and, at the same time, keep important information about the shower. The values used in standard conditions, namely in dark time, are: $Q_c = 6$ phe, $Q_b = 3.5$ phe, $\Delta t_c = 4.5$ ns, $\Delta t_b = 1.5$ ns.

The cleaned image from a $\gamma-$ray shower has an elliptical shape in the camera. The following step of the analysis is the **image parametrization**, which describes the obtained image through a number of parameters, known as *Hillas parameters* [52]. They

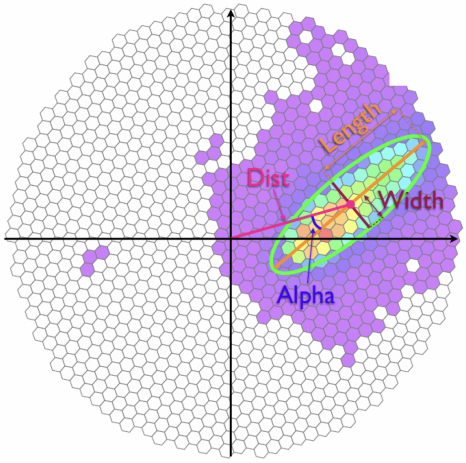

Figure 1.20: Representation of some Hillas parameters in a camera image from an electromagnetic shower. For simplicity an ON-mode observation is shown, where the expected source position lies at the center of the camera. Credits: [53]

can be divided in different subclasses based on their role:

- *Source-independent parameters*: They are properties typical of the recorded image, irrespective of the source location;
- *Source-dependent parameter*: They depend on the position of the source on the camera;
- *Timing parameters*: They take into account the arrival time of the Cherenkov photons in the camera and are useful to distinguish between hadronic and electronic showers given their different temporal development ($\sim$ 3 ns for electromagnetc showers versus $\sim$ 10 ns for hadronic ones);
- *Directional parameters*: They discriminate between the head and the tail of the shower, taking into account that typical showers have higher charge concentration in the head.
- *Image quality parameters*: They evaluate how much signal or noise characterizes the image or if the image is well contained in the camera.

The main parameters of these subclasses are reported in Table 1.1 and some of them are shown in Fig. 1.20. These parameters are a key tool in the analysis chain since they allow to recover properties of the shower in further analysis steps. For example, an image can be tagged as hadron-like or γ-like based on the parameters values. This procedure is called γ/hadron separation and will be described in the next section.

Intermediate-level analysis

In the low-level analysis, the telescopes data are treated separately. At this point, a **stereoscopic reconstruction** is performed to merge the information from the two telescopes in a single file and find the so-called *stereo parameters*. The program performing

Table 1.1: List of the main image parameters implemented in the `star` program and divided by subclass.

Source-independent parameters	
`Size`	Total number of phe in the image. It is related to the energy of the primary particle.
`Width`	Length of the semi-minor axis of the ellipse. It is related to the lateral development of the shower.
`Length`	length of the semi-major axis of the ellipse. It is related to the longitudinal development of the shower.
`Center of Gravity (CoG)`	Coordinates of the weighted average signal along the the X and Y axis in the camera plane.
`Conc(N)`	Fraction on phe contained in the N brightest pixels. It tends to be higher for $\gamma-$ray images since in electromagnetic showers the image core is very compact.
Source-dependent parameters	
`Dist`	Expected distance between the expected position of the source in the camera and the position of the image CoG.
`Alpha`	Angle between the ellipse major axis and the line connecting the expected source position in the camera with the CoG. It is small in $\gamma-$ray showers, since the shower should point at the source position in the camera.
Timing parameters	
`TimeRMS`	Root Mean Square (RMS) of the arrival times of the pixel surviving the image cleaning. It is smaller in $\gamma-$ray showers.
`Time gradient`	Slope of a linear function used to fit the arrival time distribution of the pixels, after projecting the pixels coordinates along the major axis of the ellipse
Directional parameters	
`Asymmetry`	Sign of the difference between the position of the brightest pixel (i. e pixel with highest charge) and the CoG.
`M3Long`	Third longitudinal momentum of the shower image along its major axis. It measures the asymmetry in the signal distribution along the axis and has the same sign of the `Asymmetry` parameter.
Image quality parameters	
`LeakageN`	Fraction of the size of the image contained in the N outermost pixel rings of the camera. It estimates the fraction of signal loss and rejects showers that cannot be reconstructed correctly.
`Number of islands`	Number of non-connected pixel groups that survived image cleaning. It is larger for hadronic showers since they usually are more fragmentated.

this task in the MAGIC analysis software is called `superstar`, which performs a 3-dimensional geometrical reconstruction of the shower starting from the parameters of the single images. Some of the main stereo parameters are reported in Table 1.2.

In the standard MAGIC analysis chain, data up to the superstar level are processed at the MAGIC site by OSA. From this level, data are analyzed off-site by analyzers. Usually, the first step performed by analyzers is the **data-quality check** in order to inspect the presence of data affected by bad weather, hardware problems or various sources of

Table 1.2: List of the main stereo parameters.

Stereo parameters	
`Shower axis`	Direction of the shower. It is given by the intersection of the two major axes of MAGIC-I and MAGIC-II ellipses, combined with telescopes position and pointing.
`Impact parameter`	Distance between the shower axis and the pointing direction of the telescope.
`Impact point`	Impact position of the shower on the ground. It is given by the intersection of the two major axes of MAGIC-I and MAGIC-II ellipses.
`Height of shower maximum`	Height at which the number of particles in the EAS is maximum. It depends on the energy of the primary particle.
`Cherenkov radius`	Radius of the Cherenkov light pool on the ground produced by an electron of energy 86 MeV at the height of the shower maximum.

noise (like e. g. car flashes in the camera during data-taking) and eventually discard them. The program responsible for the selection of good-quality data is called `quate` (QUAlity TEster). It computes the values of a set of parameters over time slices of data and selects only those data with values lying in a given range. Some of the parameters that can be checked are the zenith and azimuth, the rate during the observation, the PMT current, the transmission, and the cloudiness. The latter two are relevant in the data selection because they are related to the quality of the atmosphere where the shower develops (see Sec. 1.3.2). In particular, a low value of the transmission (and, similarly, a high value of the cloudiness) implies a degradation of the shower image and, consequently, a less precise parameter estimation, while a high value (low value in the case of cloudiness) indicates transparent air and thus a better reconstructed shower image. A good compromise for the selection of data not affected by bad atmospheric condition is transmission > 0.75 and cloudiness < 25.

Once good-quality data are selected, a separation between the $\gamma-$ray and hadronic signals is performed (also called γ/hadron separation), together with the reconstruction of the arrival direction and energy of the primary particle. For this purpose, the analysis chain makes use of *Random Forest* (RF) and *Look-Up Table* (LUT) algorithms. The program responsible for the creation of RFs and LUTs is called `coach` (Compressed Osteria Alias Computation of the Hadronness parameter). Given that even in the brightest sources the number of background events surviving the image cleaning is $\sim 10^3$ times larger than the $\gamma-$ray signal, a powerful discrimination method is necessary to correctly identify the $\gamma-$rays coming from the observed source. In MARS the **γ/hadron separation** is performed through the RF, a multi-dimensional classification algorithm based on the construction of *decision trees* [54]. The RF is trained using a sample of simulated MC $\gamma-$ray data and a sample of hadronic events (the OFF data). At this stage the MC sample is divided into two sub-samples: the train MCs, used here in the RF generation, and the test MCs, used in the following steps of the analysis. This separation is applied in order to have two statistically independent samples. Moreover, both the MC and OFF data have to match as much as possible the observational conditions of the source data (i. e. the ON data) in terms of, for example, zenith angle, dark/moon

nights, extragalactic/galactic observations. The RF trees are generated using the set of parameters previously computed in the image parametrization and stereo reconstruction steps, since they reflect the differences between hadronic and and $\gamma-$ray induced showers. The algorithm starts by randomly selecting the first parameter and searching the parameter value that better separates hadrons from $\gamma-$rays, also called cut value. Then, it splits the initial sample into two sub-samples, called branches, based on the cut value used. The best cut value is obtained through the minimization of the so-called Gini index [55], given by $Q_{Gini} = \frac{4N_\gamma N_h}{(N_\gamma+N_h)^2}$, where N_γ and N_h are the number of $\gamma-$ray and hadron events respectively. At this point, a new random parameter is selected and the procedure is repeated, creating new branches. The algorithm stops when one of the branches contains only $\gamma-$rays or hadrons or if the number of events in a sub-branch is below a predefined value. At the ending sub-samples a value called *hadronness* assigned. It is 0 or 1 depending if the sub-sample contains $\gamma-$rays or hadronic events. The trained RF is then applied to real data through a program called `melibea`, which takes as input the ON data from the observed source and the aforementioned MC test data. These data have to pass all the decision trees created in the RF training. At the end, a hadronness value of 0 or 1 is assigned to the ending sub-samples of each tree. The final hadronnes value h of the event is given by the average[13] of all the obtained values h_i over N trees: $h = \frac{1}{N}\sum_{i=1}^{N} h_i$. It is a measure of how γ-like is the observed event. The final background rejection is performed by placing a cut on the hadronness.

The **direction reconstruction** is performed through the training of a RF algorithm exploiting a method called *DispRF* [56, 57]. Since the major axis of the ellipse represents the incoming direction of the primary $\gamma-$ray, the source position should lie in this direction, at a certain distance from the image CoG. This distance is called *disp* and can be estimated from the elongation of the ellipse itself. The method is based on the reconstruction of the disp quantity. As before, the RF is trained using MC $\gamma-$ray data, for which the disp parameter is known, with the aim of finding a relation between the disp and a defined set of parameters. The trained RF is then applied to real data to estimate the disp value for a real shower image. The programs used in these steps are the same used for the γ/hadron separation: `coach` for RF training, and `melibea` for the application to real data, with the same input files. For each telescope image, there are two possible disp values, one in each side of the ellipse major axis with respect to the ellipse image itself, as shown in the left panel of Fig. 1.21. Since MAGIC is a system of two telescopes, four possible source locations are found. They are paired in all possible combinations, the angular distance of each pair is computed, and the pair with the smaller distance is selected. The final source position is estimated by averaging the locations of the points in the selected pair, weighted with the number of pixels in each image. The reconstruction based on two or more telescope images is thus more precise than having a single telescope. A graphical representation of this method is shown in the right panel of Fig. 1.21.

The final step of the intermediate analysis level is **energy estimation**. It can be

[13] In order to reduce the error on the hadronness the default number of created trees is 100.

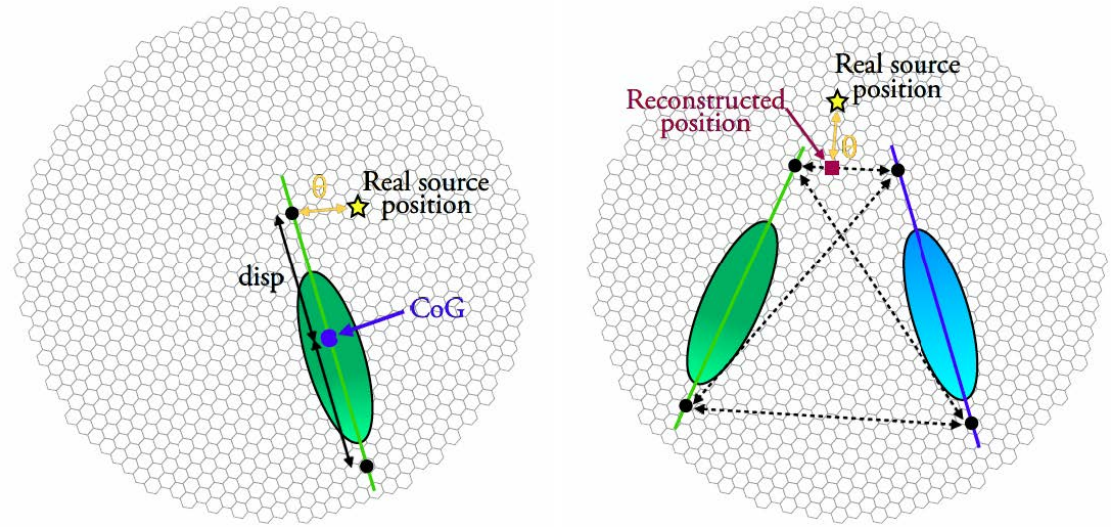

Figure 1.21: Reconstruction of the shower direction through the disp parameter for a single (left panel) and two (right panel) telescope images. In both panels the real source position is also displayed. In the right panel all possible pairs are shown, together with the chosen pair and the reconstructed source position. Credits: [53]

performed using both RF and LUT algorithms, but the current standard method for MAGIC is based on LUTs [58]. As before, the LUTs are built with `coach` using simulated MC $\gamma-$rays. Then they are applied to real data through `melibea`. The method used to build the LUTs assumes that the energy of the incident $\gamma-$ray is almost proportional to the amount of photons populating the Cherenkov image and, as a consequence, to the size parameter (see Table 1.1 for the definition). Moreover, the true energy (E_{true}) of the MC $\gamma-$rays is known. Thus, the LUTs are built by binning E_{true} and the RMS of each event into bins of size and impact parameter (see Table 1.2 for the definition). The estimated energy (E_{est}) of a real event is then computed by applying the LUTs to real data. In this procedure, E_{est} is estimated by averaging the values of E_{true} in the corresponding bins, properly weighted with the RMS of each energy bin, for each telescope image.

High-level analysis

At this point of the analysis, each event has been assigned a hadronness value and a reconstructed energy and direction. In this last stage the high level products are evaluated, namely signal significance, skymap, energy spectrum and lightcurve (LC) for the source under investigation.

The **signal significance** is computed by the MARS program `odie`, which generates the so-called θ^2 distribution plots starting from melibea data. These plots make use of the θ parameter, defined as the angular distance between the expected and recon-

structed source positions for each event. The $\gamma-$ray signal events should accumulate at small values of θ^2, while hadronic background events are isotropically distributed. Thus, the θ^2 distribution should be peaked close to zero if containing a signal. Possible exceptions are extended sources or additional $\gamma-$ray sources in the FoV, for which it is possible to have high numbers of events also for large θ^2 values. However, this does not apply in standard analyses, where the peak is expected to appear only for small θ^2 values. For this reason a cut on θ^2 is placed, defining the so-called signal region (or ON region). In the same way, one or more OFF regions are defined in order to evaluate the amount of background events inside the ON region. They are defined as circles with the same radius θ of the ON region, centered at a position of the camera where no $\gamma-$ray signal is expected (see Fig. 1.17). Moreover, $\gamma-$ray signal events show smaller hadronness values than hadronic ones, so a set of cuts is applied to estimate the significance of the observation. The cut parameters considered for the standard analysis are θ^2, hadronness, size, and estimated energy. The cut on size is usually loose in order to include also low-energy events, at the expense of a high level of background events. The cut values are chosen to have the best sensitivity for Crab Nebula observations and they are optimized for different energy ranges. Defining N_{ON} the number of events in the source region and N_{OFF} the number of events in the OFF regions, the number of excess events N_{ex} is given by: $N_{ex} = N_{ON} - \alpha N_{OFF}$, with α the ratio between the number of OFF and ON regions. The signal significance if then estimated through Eq. 17 of Li & Ma [59]:

$$\sigma_{LiMa} = \sqrt{2\left\{N_{ON}\ln\left[\frac{1+\alpha}{\alpha}\frac{N_{ON}}{N_{ON}+N_{OFF}}\right] + N_{OFF}\ln\left[(1+\alpha)\frac{N_{OFF}}{N_{ON}+N_{OFF}}\right]\right\}}. \quad (1.12)$$

For both N_{ON} and N_{OFF} Poisson distributions are assumed. If the $\sigma_{LiMa} > 5\sigma$ the source detection can be claimed. An example of θ^2 plot for Crab Nebula data is shown in Fig. 1.22.

The significance of the observation can be evaluated also through the so-called **skymaps**. A skymap is a 2-dimensional histogram in sky coordinates which contains the arrival direction of all $\gamma-$rays surviving the analysis cuts and the background subtraction. The program responsible for the creation of skymaps in MAGIC is called `caspar`, which takes as input melibea data. The main challenge for the skymap creation is a correct estimation of the background, since it depends on factors like the zenith and azimuth angles of the observations, and inhomogeneities in the camera pixels response. For this reason the `caspar` program firstly generates a camera exposure model from which the OFF background map is created and then generates a ON map using the $\gamma-$ray events. The histogram of excess events is obtained by subtracting the background skymap from the signal one. This resulting skymap is then smoothed by the MAGIC PSF and a Gaussian kernel added in quadrature to suppress the level of noise and highlight the sources. The significance of the signal in the skymap is computed through the Test Statistic (TS), which in this case corresponds to the Li & Ma significance [59] applied on a smoothed background model. An example of skymap with Crab Nebula data is shown in Fig. 1.23, where the source is clearly identified.

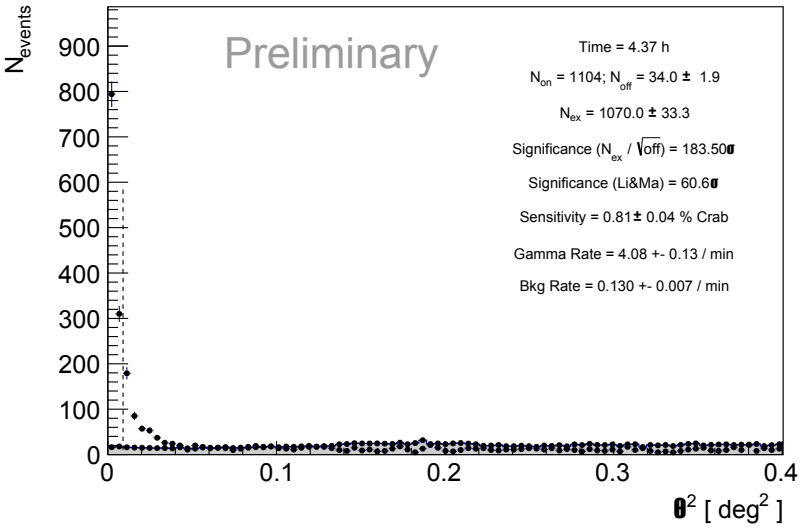

Figure 1.22: Example of θ^2 plot for the Crab Nebula. The grey shaded area represents the background distribution, while the black points are signal events. The cut on the signal region is given by the vertical dashed line.

Before proceeding with the description of spectrum and lightcurve computation, some quantities need to be defined. They are the instrument sensitivity, effective collection area, and effective observation time.

The **sensitivity** of an instrument is a measure of its performance. For IACTs the sensitivity is defined as the minimum $\gamma-$ray flux that can be detected with a significance of 5σ after 50 hours of observation. It can be used to compare the performance of different instruments and estimate the flux that can be detected from a given source for a certain amount of observation time. Let us consider a certain observation collecting a number of excesses N_{ex}, and a number of background events N_{OFF} in a time t_{OFF}. In the Gaussian approximation, the significance for an observation time t_{obs} is given by[14]

$$\sigma_{t_{obs}} = \sqrt{\frac{t_{obs}}{t_{OFF}}} \frac{N_{ex}}{\sqrt{N_{OFF}}}. \tag{1.13}$$

Since the sensitivity S of the instrument is defined as the minimum detectable flux for $t_{obs} = 50$ h and $\sigma_{t_{obs}} = 5\sigma$, it can be valuated as $S = 5\sigma/\sigma_{50}$. It is often expressed as a fraction of the Crab Nebula flux, also referred to as Crab Units (C. U.). Moreover, two conditions are imposed: $N_{ex} > 10$ and $N_{ex} > 0.05\, N_{OFF}$. The former allows the usage of the Gaussian approximation to the Poissonian event rate, while the latter eliminates statistically significant fluctuations of the background rate if it is large. The sensitivity can be computed in two ways:

[14]Note that the following formula is a Gaussian approximation of Eq. 1.12

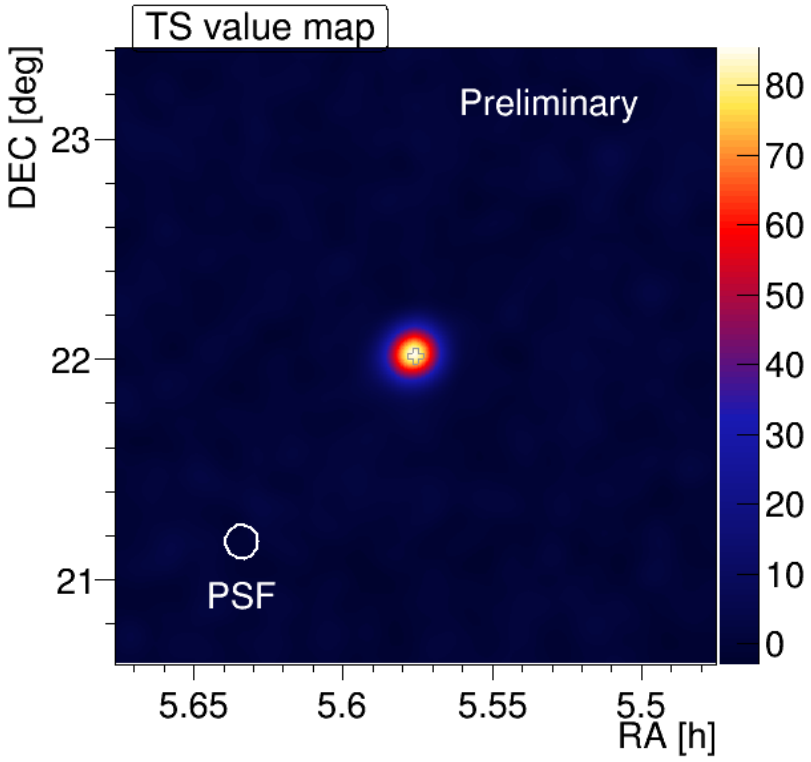

Figure 1.23: Example of skyamp for the Crab Nebula. The axes show the coordinates in the sky, while the colorbar indicates the TS value.

- *Integral sensitivity*: it is computed with global optimized cuts on hadronness and θ^2 above a specific energy threshold,
- *Differential sensitivity*: it is computed on small energy bins with cuts optimized on the considered bins (taking into account usually 5 energy bins per decade).

In 2012 a major upgrade of the system took place, from which we have its current performance. The current integral and differential sensitivity of the MAGIC telescopes for different zenith angles are shown in Fig. 1.24, in comparison with their sensitivities before the upgrade. Currently, the MAGIC integral sensitivity is 0.55% C. U. at few hundreds GeV for sources with a Crab-like spectrum, while the differential sensitivity is 6.7% C. U. in the lowest energy bin ($60 - 100$ GeV) and shows a general improvement in the whole energy range up to few TeV. Note that the differential sensitivity does not depend on the source spectrum since it is computed on narrow energy bins.

The **effective collection area** is defined as the area of an ideal instrument detecting the same rate of $\gamma-$rays as the real detector. It can be estimated as the size of the Cherenkov light pool, in first approximation. The effective collection area is computed from MC simulations by applying to MC data the same cuts used for real data. In an

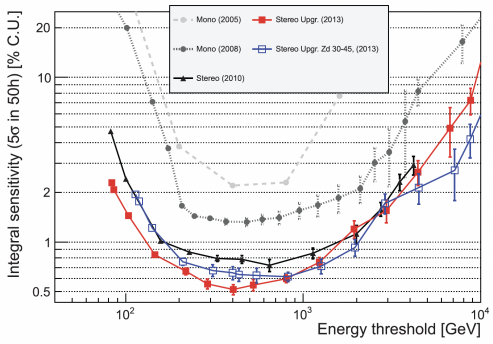

(a) MAGIC integral sensitivity

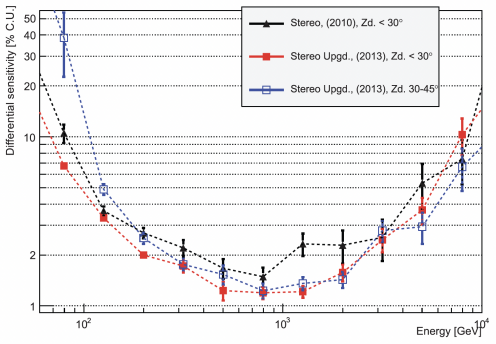

(b) MAGIC differential sensitivity

Figure 1.24: Integral (left) and differential (right) sensitivity of the MAGIC telescopes after the 2012 upgrade for $Zd < 30°$ (red filled squares) and $30° < Zd < 45°$ (blue empty squares). A comparison with the performance of the system in stereo mode (black filled triangles) and in mono mode with different readouts (grey and dark grey filled circles) before the upgrade is shown. Credits: [57]

energy range $[E, E + \mathrm{d}E]$ the effective area is given by :

$$A_{eff}(E, E + \mathrm{d}E) = A_{sim} \frac{N_{det}(E, E + \mathrm{d}E)}{N_{sim}(E, E + \mathrm{d}E)}, \tag{1.14}$$

where A_{sim} is the geometric simulated area of MC $\gamma-$rays, $N_{sim}(E, E + \mathrm{d}E)$ is the number of simulated $\gamma-$rays in the energy range $[E, E + \mathrm{d}E]$, and $N_{det}(E, E + \mathrm{d}E)$ is the number of γ-rays surviving the analysis cuts. It mainly depends on the zenith angle of the observation, as the Cherenkov light pool becomes larger with increasing zenith, and on the energy of the primary $\gamma-$ray, since with increasing energy, also the number of produced secondary particles increases, and hence the probability for them to be detected. This, in turn, increases the value of $N_{det}(E, E + \mathrm{d}E)$ and thus the effective collection area. The effective area of the MAGIC telescopes is shown in Fig. 1.25.

The **effective observation time** is the real time, during the observation, where the telescope is taking data. Indeed, after each trigger, there is a so-called dead time, in which the telescope is busy processing the triggered event. During this time data taking is stopped and and the system does not accept further events. For the MAGIC telescopes the dead time d is due to the DRS4 readout and corresponds to 26μs. Assuming the events arrival time to follow a Poissonian statistic, the effective observation time can be computed as $t_{eff} = \frac{t_{elapsed}}{1+\lambda d}$, where λ is the event rate and $t_{elapsed}$ is the time of the observation.

Given the above quantities, we can proceed with the computation of the source **spectrum** and **lightcurve**. Both these quantities and the previously mentioned ones are computed by the program `flute`, which takes as input the source data and the MC simulated $\gamma-$rays in melibea format. The former are used to compute the number of

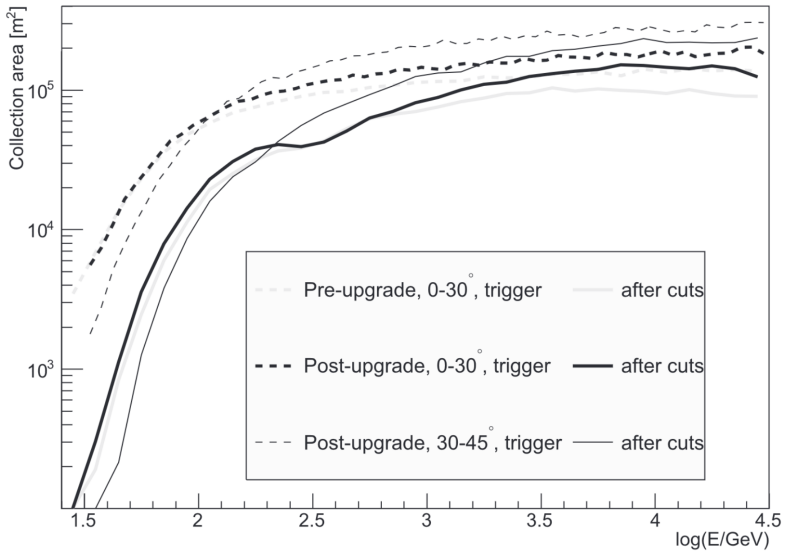

Figure 1.25: Effective collection area of the MAGIC telescopes before (thick dashed light-grey line) and after (thick dashed dark-grey line) the 2012 upgrade, and after all analysis cuts (solid lines) for different zenith ranges ($0° - 30°$ thick lines, $30° - 45°$ thin lines). Credits: [57].

excess $\gamma-$ray events (see below) and the effective observation time, while the latter is used to estimate the effective collection area of the observation. The $\gamma-$ray **differential energy spectrum** of a given source per unit energy, area and time is defined as:

$$\frac{\mathrm{d}\Phi}{\mathrm{d}E} = \frac{\mathrm{d}N_\gamma(E)}{\mathrm{d}E\,\mathrm{d}A_{eff}(E)\,\mathrm{d}t_{eff}}, \tag{1.15}$$

where A_{eff} is the effective area, t_{eff} the effective time, and $N_\gamma(E)$ the number of $\gamma-$rays emitted from the source at energy E. They are estimated as the number of excess events observed by the instrument, computed similarly to what is done in `odie`. The main difference is that in `flute` the hadronness and θ^2 cuts are optimized in each energy bin, according to a predefined efficiency value. For each bin, the corresponding θ^2 distribution is computed, from which the number of excess and background events are estimated. For the effective area calculation, a tentative spectrum for the MC sample has to be assumed in `flute`. It has to be as close as possible to the spectrum of the observed source, otherwise the computed energy bins become wider and the flux estimation less accurate.

Given the differential energy flux, the **integral flux** above a certain energy E_{th} is given by:

$$\Phi_{E>E_{th}} = \int_{E_{th}}^{\infty} \frac{\mathrm{d}\Phi}{\mathrm{d}E}\mathrm{d}E \qquad [\mathrm{cm}^{-2}\,\mathrm{s}^{-1}]. \tag{1.16}$$

If the integral flux is computed on time bins, we have the **lightcurve**, which shows the flux variations over time. Often, in order to have a better visualization of the spectral features, the **Spectral Energy Distribution** is used instead of the differential spectrum. It is defined as[15]:

$$E^2 \frac{\mathrm{d}\Phi}{\mathrm{d}E} = E \frac{\mathrm{d}\Phi}{\mathrm{d}(\log E)} \qquad [\mathrm{TeV\,cm^{-2}\,s^{-1}}]. \tag{1.17}$$

In IACT observations, the number of $\gamma-$rays in the obtained energy spectrum is computed in bins of estimated energy E_{est}, since the true energy of the events is not known. However, the effective area from simulated MC $\gamma-$rays is calculated in bins of true energy E_{true}. It is possible that events with E_{est} in the range $[\mathrm{E_1}, \mathrm{E_2}]$ have a corresponding E_{true} falling outside $[\mathrm{E_1}, \mathrm{E_2}]$, and so the source flux results wrongly reconstructed. This is known as *spillover effect* and becomes more important if the tentative flux used in the computation of the collection area does not approximate well the flux of the emitting source. It can be corrected through **unfolding** methods, which make use of the so-called *migration matrix*. It is computed by the least square minimization technique and maps events in bins of true energy into bins of estimated energy. Usually, the unfolding procedure gives unstable solutions, so regularization methods are needed to smooth the solution and produce acceptable results. A first basic unfolding approach is already implemented in `flute`, giving acceptable results in first approximation. It computes the number of events surviving the analysis cut for the effective area calculation in bins of estimated energy instead of true energy. More refined unfolding methods are described in [60]. However, they were not used in this work, since only flux upper limits were found, so the interested reader is referred to the given reference for more details about these methods.

Flux upper limits (UL) are computed by `flute` in energy bins where no significant signal is found. For this purpose the Rolke method [61] is used, which computes the maximum number of expected $\gamma-$ray events N_{UL} from the source. In MAGIC an UL is computed when a spectral point has a relative error on the estimated flux larger than 50%, and the calculation is done by assuming a 95% confidence level (CL) and a 30% systematic uncertainty in the detection efficiency of $\gamma-$rays after applying analysis cuts. The computation of N_{UL} in the Rolke method is based on the maximization of the likelihood and the application of the likelihood ratio test. In MAGIC, the likelihood used in the UL calculation is:

$$\mathcal{L}\,(g, b, \varepsilon; N_{\mathrm{ON}}, N_{\mathrm{OFF}}) = \frac{(\varepsilon g + b)^{N_{\mathrm{ON}}}}{N_{\mathrm{ON}}\,!} e^{-(\varepsilon g + b)} \cdot \frac{(\tau b)^{N_{\mathrm{OFF}}}}{N_{\mathrm{OFF}}\,!} e^{-(\tau b)} \cdot \frac{1}{\sqrt{2\pi}\sigma_\varepsilon} e^{-\frac{1}{2}\left(\frac{\varepsilon - \varepsilon_0}{\sigma_\varepsilon}\right)^2}, \tag{1.18}$$

where the first two terms, which are assumed to have a Poissonian distribution, describe the signal and the background, while the third one represents the detection efficiency, which is assumed to have a Gaussian distribution with mean $\varepsilon_0 = 1$ and standard deviation $\sigma_\varepsilon = 0.3$. The parameters appearing in Eq. 1.18 describe the following quantities: N_{ON} and N_{OFF} are the measured number of total events in the ON and OFF

[15] Note that the reported units are the ones used by MAGIC.

regions respectively, τ is the ratio between the OFF and ON exposure, g is the estimated number of $\gamma-$ray events in the ON region, b is the estimated number of background events in the OFF region, and ε is the efficiency of the detector. Note that the last factor takes into account the 30% global systematic uncertainty mentioned above. By considering τ, ε, and b as nuisance parameters, the profile likelihood ratio results to be $\lambda_p(g; N_{\rm ON}, N_{\rm OFF})$. Here, while applying the likelihood ratio test, the only parameter to be estimated by minimizing the quantity $-2\ln\lambda_p$, is g [61]. Once the number of expected $\gamma-$ray events g is computed through the Rolke method, an UL on the integral flux can be found. For this computation an assumption on the source spectrum is needed:

$$\frac{\mathrm{d}\Phi}{\mathrm{d}E} = K\,S(E), \tag{1.19}$$

where K is a normalization constant and $S(E)$ is the spectral shape. According to the measurements performed and the confidence level defined, the maximum number of expected events N_{UL} can be translated into an UL for the normalization K. In order to do this, we first recover the integral flux above an energy E_0 by integrating and equating Eqs. 1.15 and 1.19:

$$\int_{E_0}^{\infty}\frac{\mathrm{d}\Phi}{\mathrm{d}E}\mathrm{d}E = K\int_{E_0}^{\infty}S(E)\mathrm{d}E = \frac{N_{UL}}{\int_0^{t_{eff}}\int_{E_0}^{\infty}A_{eff}(E)\mathrm{d}E\mathrm{d}t}, \tag{1.20}$$

from which

$$K_{UL} = \frac{N_{UL}}{t_{eff}\int_{E_0}^{\infty}S(E)\,A_{eff}(E)\mathrm{d}E} \qquad [\mathrm{TeV\,cm^{-2}\,s^{-1}}]. \tag{1.21}$$

The computation of the integral flux UL is then:

$$\Phi_{UL}(E>E_0) = K_{UL}\int_{E_0}^{\infty}S(E)\mathrm{d}E = \frac{N_{UL}\int_{E_0}^{\infty}S(E)\mathrm{d}E}{t_{eff}\int_{E_0}^{\infty}S(E)\,A_{eff}(E)\mathrm{d}E}, \tag{1.22}$$

while for the differential flux UL we have:

$$\frac{\mathrm{d}\Phi_{UL}}{\mathrm{d}E} = \frac{N_{UL}\,S(E)}{t_{eff}\int_{E_0}^{\infty}S(E)\,A_{eff}(E)\mathrm{d}E}. \tag{1.23}$$

The differential flux ULs are computed on energy bins which should be narrow enough in order not to have effects due to the assumed spectral shape, but sufficiently wide in order to have enough events and therefore obtain meaningful limits.

1.3.5 A non-standard analysis: analysis of Sum-Trigger data

The Sum-Trigger-II system described in Sec. 1.3.2 is a particular type of trigger specifically designed for the detection of low-energy signals. Given its peculiarities and differences with respect to the standard trigger used in ordinary observations, the data taken with Sum-Trigger-II need a dedicated analysis procedure. The analysis of Sum-Trigger data undergoes a special low-energy focused cleaning algorithm called **MaTaJu**

cleaning, from the names of its developers: Maxim Shayduk (Ma), Takayuki Saito (Ta), and Julian Sitarek (Ju). The basic idea behind this algorithm is that the signal extraction and the image cleaning, which are usually performed in two different steps in the standard analysis (`sorcerer` and `star` programs, see Sec. 1.3.4), are now carried out together (both with `sorcerer`), with the aim of lowering the energy threshold of the observation.

The signal extraction, i. e. the extraction of intensity and arrival time of the pulses in each pixel, is performed in the same way as for the standard analysis (see Sec. 1.3.4), while the image cleaning is different and involves an additional extraction of the signal. In standard analysis, the image cleaning is performed by selecting clusters of pixels, with a summed charge exceeding a given threshold and an arrival time within a certain time window. Then, core and boundary pixels are selected from this cluster according to specific requirements on their individual charge and arrival time. The pixels that do not satisfy these requirements are discarded. In the MaTaJu cleaning, the selection of the cluster of pixels is performed in the same way, but with an optimized threshold for the observed source. Then, all the pixels in the cluster are considered as core pixels, and for each pixel adjacent to a core one, a new signal extraction is done with the same algorithm described in Sec. 1.3.4. The time interval of the waveform is now centered on the average arrival time of the adjacent core pixel in order not to take possible fluctuations in the pixel signal. After all pixels adjacent to a core one are analyzed, the procedure is repeated for pixels adjacent to the just analyzed ones, until covering 3 rings of pixels surrounding the core ones. The list of survived pixels is then written on output calibrated files from `sorcerer`.

The following step is performed by the `star` program, which in Sum-Trigger analysis only removes possible stars in the FoV, since the image cleaning has already been done. Indeed, if a star in the FoV is too bright, it can pass the low threshold of the MaTaJu cleaning, creating a new island on the camera and thus spoiling the image parametrization, stereo reconstruction and hadronness calculation. This effect is visible for stars up to magnitude 6 and they can be removed by just cutting out the pixels affected by the star signal. The number of cut pixels depends on the star magnitude.

After the low-level analysis is done, the stereo reconstruction and the following steps of the analysis can be performed. Here, the main difference with respect to the standard analysis is given by the cut on the size of the shower (size parameter, see Table 1.1), which is now set to 20 phe, instead of 50, since the showers are dimmer. This is important in order not ot discard low-energy events.

1.4 Multi-wavelength instruments and related analysis techniques

Besides VHE $\gamma-$ray data, also information about other wavelengths is of fundamental importance in order to have a complete view of the emission state of the studied objects. The multi-wavelength data used in this thesis work range from the optical/UV band to HE $\gamma-$rays and are publicly released by the observatories taking them. In the following

a brief description of the instruments used and the analysis techniques needed in these energy ranges is reported.

1.4.1 *Fermi/LAT*

HE $\gamma-$rays in the range from MeV to hundreds of GeV can be observed by space-based satellites. Currently, the most important of them for the astrophysical community is the *Fermi* Gamma-ray Space Telescope[16]. It was launched in June 2008 and is composed of two main instruments: the Gamma-ray Burst Monitor (GBM) [62], operating in the energy range 10 keV $-$ 25 MeV and designed for GRB studies, and the Large Area Telescope (LAT) [63], covering the energy range from 20 MeV to more than 300 GeV and designed for long term high sensitivity observations of $\gamma-$ray sources and transient phenomena. This thesis makes use of *Fermi/LAT* data, so, in the following, a description of the instrument and its analysis chain is reported.

Structure and hardware

The *LAT* instrument on board the *Fermi* satellite is a pair conversion telescope characterized by a very wide FoV of 2.4 sr, which allows to scan $\sim$ 20% of the sky at each instant and to expose the whole sky for $\sim$ 30 min every $\sim$ 3 hours.

It is composed by a converter tracker, a calorimeter, and an anti-coincidence detector. The converter tracker consists of 4×4 towers, each of which contains 18 planes of tungsten, alternating with 2 layers of perpendicular silicon strips. The role of the planes is the conversion of the incoming $\gamma-$ray into an electron-positron pair through its interaction with the tungsten, which is a high Z material. The silicon strip layers are then needed to record the position of the passing e^- and e^+ after each plane, in order to reconstruct the direction of the incident $\gamma-$ray. Moreover, the 18 planes are not all equal to each other but present different properties:

- The first 12 planes have a thin layer of tungsten in order to allow a better angular resolution, since for thin layers multiple scatterings inside the material itself are reduced;
- The following 4 planes are $\sim$ 6 times thicker than the previous ones in order to increase the interaction probability of the $\gamma-$ray with the material in case the production of the e^-e^+ pair did not happen in the previous planes. As a consequence the angular resolution of these planes is less precise because of the multiple scatterings which can take place inside the tungsten layer;
- The last 2 planes do not have any tungsten converter material, but only contain the silicon strips.

Below each tower, there is a calorimeter made of scintillators arranged in 8 layers. It is needed to estimate the energy deposited by each e^-e^+ pairs through a measure of

[16] https://fermi.gsfc.nasa.gov/

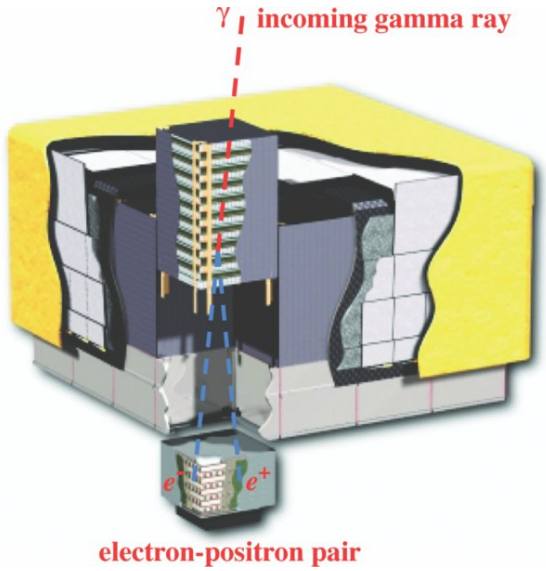

Figure 1.26: Schematic view of the *Fermi/LAT* instrument. One of the four towers is shown, with its 18 planes and the calorimeter. The golden layer surrounding the detector is the anti-coincidence shield. Credits: [63].

the scintillation light produced by the cascades developed inside the scintillators. Two photo-diodes per scintillator are used for this measure. Finally, plastic scintillation tiles are placed around the detector, used as anti-coincidence shields with the aim of recognizing and rejecting background events such as cosmic-rays. They record charged particles reaching the detector with a detection efficiency of 99.97%. A schematic representation of the *Fermi/LAT* instrument is shown in Fig. 1.26.

Data analysis pipeline

All data recorded by *Fermi/LAT* are automatically processed and publicly distributed. Data corresponding to observations around certain coordinates can be downloaded from the LAT Data Server[17] in the preferred observation dates and energy range. The *Fermi/LAT* instrument covers the energy range from 20 MeV to more than 300 GeV, but below 100 MeV the uncertainties in the arrival direction of photons are large, leading to a possible confusion between the emission of point-like sources and the diffuse Galactic background radiation [64]. For this reason, all the analyses presented in this thesis select data with energies $E > 100$ MeV. The analysis can be performed with the Fermi Science Tools[18] (Fermitools), specifically developed to treat *Fermi/LAT* data. However, other software programs were developed to optimize *Fermi/LAT* analysis, all based on

[17] https://fermi.gsfc.nasa.gov/cgi-bin/ssc/LAT/LATDataQuery.cgi
[18] https://fermi.gsfc.nasa.gov/ssc/data/analysis/software/

the Fermitools. Among them there is `Fermipy`[19] [65], an open-source python package automatizing large part of the functions of the Fermitools. In this thesis work, both these tools are used to perform the *Fermi/LAT* analysis.

The data needed for the analysis consist of two files: a photon and a spacecraft file. The photon file contains information on the observed $\gamma-$ray events from the source of interest, such as their reconstructed energy and direction, together with information on the event reconstruction quality and the observation time. The spacecraft file contains information on the *LAT* location and orientation during the observation, together with its detection efficiency.

Dedicated cuts on the downloaded data can be applied for a further **data selection** using the `gtselect` tool. Each event is characterized by an event class based on the quality of the event reconstruction depending on background cuts. From the purest $\gamma-$ray like events, these classes are ULTRACLEAN, CLEAN, SOURCE and TRANSIENT. In this thesis events from the SOURCE class are selected, which is the suggested class for point-like sources and moderately extended sources. Each class is in turn partitioned into three event types:

- FRONT and BACK selects events recorded in the first 12 thin planes of the converter tracker (FRONT) or the 4 thicker ones (BACK);
- PSF0 to PSF3 selects events based on the quality of the direction reconstruction, with PSF0 the lowest quality quartile and PSF3 the highest quality one;
- EDISP0 to EDISP3 selects events based on the quality of their energy reconstruction, with EDISP0 the lowest quality quartile and EDISP3 the highest quality one.

With `gtselect` it is possible to select the event class and type of interest and pose additional cuts on the downloaded data such as the energy and ranges, or the radius of the region of the sky we are interested in (also known as Region Of Interest, ROI), which is usually centered on the target. A quite important cut which is usually set is the zenith angle, which is used to exclude background $\gamma-$ray events coming from the Earth atmosphere. Cuts on time ranges can also be applied. For this purpose there is the `gtmktime` tool, which automatically selects time intervals where *LAT* data are not affected by spacecraft events and therefore have a good quality.

Fermi/LAT analysis is based on the **likelihood maximization method**, which provides the best parameters describing the observed data given an input source model. The functional form of the likelihood is based on Poisson distributions for the source counts and depends on the *LAT* response over the selected ROI, the number of observed photon counts, and the number of predicted ones according to the considered model. It results to be [20]:

$$\mathcal{L} = \prod_i \frac{m_i^{n_i}}{n_i!} e^{-m_i} = e^{-N_{exp}} \prod_i \frac{m_i^{n_i}}{n_i!}, \tag{1.24}$$

[19] https://fermipy.readthedocs.io/en/latest/

[20] See https://fermi.gsfc.nasa.gov/ssc/data/analysis/documentation/Cicerone/ for the derivation of this formula.

where n_i is the number of detected counts in the i-th bin, m_i is the number of predicted counts in the same bin according to the source model, and N_{exp} is the total number of expected counts. Note that the bins defined in *Fermi/LAT* analysis are multidimensional, depending on energy, direction and time. In Eq. 1.24, the expected counts depend on different quantities. They are:

- the **livetime cube**, computed with the `gtltcube` tool, which records the position and orientation of the instrument and calculates its response to the incident flux for each point in the sky;
- the **exposure map**, computed with the `gtexpmap` tool, which integrates the complete *LAT* response over the entire ROI under consideration, starting from the livetime cube and taking into account the Instrument Response Functions[21];
- the observed photon flux from the source under investigation.

The total number of expected counts is then computed by:

$$N_{exp} = \int S(E, \boldsymbol{p})\, \varepsilon(E, \boldsymbol{p})\, \mathrm{d}E \mathrm{d}\boldsymbol{p}, \tag{1.25}$$

where $S(E, \boldsymbol{p})$ is the assumed flux, $\varepsilon(E, \boldsymbol{p})$ is the exposure map, and E and $\boldsymbol{p}$ indicate the energies and directions respectively.

The model to be fit to the actual data through the likelihood maximization procedure is usually taken from published *Fermi* catalogs, like for example the Fourth Source Catalog (4FGL) [66], based on 8 years of *Fermi* data. Both spectral and spatial models[22] can be selected from the catalogs for the sources in the ROI. Within the mostly used spectral models there are the PowerLaw, defined as

$$\frac{dN}{dE} = N_0 \times \left(\frac{E}{E_b}\right)^{-\Gamma}, \tag{1.26}$$

with N_0 the normalization and Γ the photon index; and the LogParabola, defined as

$$\frac{dN}{dE} = N_0 \times \left(\frac{E}{E_b}\right)^{-[\alpha+\beta \ln(E/E_b)]}, \tag{1.27}$$

with N_0 the normalization, α and β the indexes related to the spectral shape, and E_b the scale parameter [67]. In addition, the contribution from the galactic and extragalactic diffuse background components can also be taken into account[23]. The galactic diffuse component takes into account the $\gamma-$ray radiation diffused by the interstellar gas in our galaxy, while the extragalactic one accounts for the contribution from extragalactic diffuse $\gamma-$rays, unresolved extragalactic sources, and residual cosmic-ray emission.

[21] https://www.slac.stanford.edu/exp/glast/groups/canda/lat_Performance.htm
[22] See https://fermi.gsfc.nasa.gov/ssc/data/analysis/scitools/source_models.htm
[23] https://fermi.gsfc.nasa.gov/ssc/data/access/lat/BackgroundModels.html

The contribution to the diffuse emission of each source in the ROI, including extended sources and background components, can be computed by the `gtdiffrsp` tool. This step is essential for the likelihood maximization process, as it requires accounting for all these contributions.

The maximization of the likelihood can be performed in the whole selected energy and time ranges, in energy bins, or in time bins. In the first case the integral flux of the source is recovered, while the other two cases are used to compute the source flux values in the spectrum and lightcurve bins respectively. The significance of the observation can be obtained for each source using the **Test Statistic (TS)**:

$$\mathrm{TS} = -2 \log \frac{\mathcal{L}_{max,0}}{\mathcal{L}_{max,1}}, \tag{1.28}$$

where $\mathcal{L}_{max,0}$ is the maximum likelihood for the null hypothesis, namely for a model without the additional source, while $\mathcal{L}_{max,1}$ is the maximum likelihood for the alternative hypothesis, namely for a model with the additional source at the specified location. The TS can then be converted into a significance level through the relation

$$\text{Significance} \simeq \sqrt{TS}\,\sigma. \tag{1.29}$$

From the fit also the best parameters of the source model describing the observed data can be recovered.

1.4.2 *Swift*

Besides $\gamma-$rays, space-based satellites can also observe in other bands like for example the optical/UV or X-ray ones. An instrument performing observations in these energy ranges is the *Neil Gehrels Swift observatory* [68]. It is a multiwavelength satellite observatory initially designed to study GRBs and their afterglows. It was launched in 2004 and is equipped with three modules: the Burst Alert Telescope (BAT) [69], operating in the energy range $15 - 150$ keV and dedicated to GRB observations, the X-ray Telescope (XRT) [70], operating in the energy range $0.2 - 10$ keV and covering a FoV of 23.6 arcmin^2, and the Ultraviolet/Optical Telescope (UVOT) [71], operating in the spectral range 170–600 nm and covering a FoV of 17 arcmin^2. In this thesis, data from *Swift/XRT* and *Swift/UVOT* are used. In the following a brief description of these two instruments is given.

Swift/XRT

The *XRT* instrument on board the *Swift* observatory is an X-ray telescope in a Wolter-1 configuration composed by a parabolic and a hyperbolic coaxial and confocal mirrors. It exploits the grazing incidence of X-rays to redirect them into a CCD detector used for both imaging and photon counting. The analyses performed in this thesis work make use of the photon counting mode [72], which provides photon counts within specific energy ranges defined by the instrument channels.

Data of the needed observations from the sources of interest can be downloaded from the UK Swift Science Data Centre[24] and analyzed using the `HEASOFT` and `xspec`[25] software packages. The **spectral analysis** can be performed by taking into account that the telescope measures photon counts within specific instrument channels, rather than the real source spectrum. The observed and real spectra are related by:

$$C(I) = \int f(E)R(I,E)\mathrm{d}E\,, \tag{1.30}$$

where $C(I)$ are the observed counts in the I channel, $f(E)$ is the source real spectrum at the energy E, and $R(I,E)$ is the instrument response in the I channel and at the energy E. In most cases it is not possible to invert Eq. 1.30 to obtain $f(E)$ for a given set of counts $C(I)$. Thus, a model spectrum $M(E, p_1, p_2, ...)$, depending on a set of parameters p_j, is usually defined and fit to the observed data in order to find the actual source spectrum. Thanks to the fit, a predicted count spectrum $C_{fit}(I)$ can be obtained and compared to the observed counts $C(I)$. The accuracy of the fit is quantified by the fit statistic. Usually, the χ^2 and Cash [73] statistics are used, with the latter more suitable in case of few photon counts.

Often, at the beginning of the analysis, it is useful to re-bin the spectrum of each source in energy through the `grppha` tool of `HEASOFT` in order to have a minimum number of counts per bin (usually $\simeq 20-25$) to apply the χ^2 test. If the detected counts are not enough, the Cash statistic can be used.

The model can be defined within the ones implemented in `xspec`. The model used for all sources in this thesis is an absorbed power-law, taking into account processes at play in the absorption of light in its way from the source to the observer. The model is initialized by the command `mo tbabs * pow`, multiplying the absorption term by the power-law term, and is defined as:

$$N(E) = K\,E^{-\Gamma_X}\,E^{-n_H\sigma_{abs}}, \tag{1.31}$$

where K is the normalization at 1 keV, Γ_X is the photon index in the X-ray band, σ_{abs} is the cross section related to all relevant absorption processes in the interstellar medium, and n_H is the Galactic column density, measured according to [74]. After the fit, both the fitted spectrum and the ratio between the expected and measured counts can be obtained. However, the derived results do not describe the intrinsic source spectrum, since the absorption only depends on the matter lying between the emitting object and the observer. In order to obtain the intrinsic spectrum of the source, it is necessary to re-build the model by putting $n_H = 0$ and leaving the parameters unchanged.

The procedure just described can be used for analyzing both the source spectrum and lightcurve: in the first case the flux in each energy bin is computed, while in the second case the fit has to be repeated in each time bin and the results integrated in the whole energy range considered.

[24] https://www.swift.ac.uk/user_objects/index.php
[25] https://heasarc.gsfc.nasa.gov/docs/xanadu/xspec/index.html

Filter	λ_c [nm]	FWHM [nm]
v	546.8	76.9
b	439.2	97.5
u	346.5	78.5
$w1$	260.0	69.3
$m2$	224.6	49.8
$w2$	192.8	65.7

Table 1.3: Central wavelength λ_c and FHWM of *Swift/UVOT* filters. Values from [75].

Swift/UVOT

The *UVOT* instrument on board the *Swift* observatory is an optical/UV telescope employing a Ritchey-Chrétien optical design with a 30 cm parabolic primary mirror and a 7.2 cm hyperbolic secondary mirror. This optical configuration is chosen for its ability to minimize optical aberrations, providing high-quality imaging across a broad field of view. The incoming light is reflected by the secondary mirror into a 45°-inclined mirror, which redirects it to a CCD detector. The detector is located behind a filter wheel equipped with six broad-band filters, three of which in the visible band (v, b, u) and three in the ultraviolet one ($w1$, $m2$, $w2$). The central wavelength and Full Width at Half Maximum (FWHM) of each filter are reported in Table 1.3

Both spectroscopic and photometric data can be downloaded from the High Energy Astrophysics Science Archive Research Center[26] (HEASARC). In this thesis we exploited the imaging mode of the telescope and photometry techniques to recover the magnitude and flux of the interested sources in each filter. In case an integral flux of a spectrum covering more observation dates is needed, data from each single pointing in each filter have to be merged and summed with the `fappend` and `uvotimsum` task respectively, at the very beginning of the analysis. A technique called **aperture photometry** can then be applied to the summed images with the `uvotsource` task in order to recover the instrumental magnitude of the source in the considered filter. For a given filter, the instrumental magnitude is defined as:

$$m_\lambda = Z_\lambda - 2.5 \log_{10} \left(\frac{\sum_{i=1}^{N} C_{*_i}}{t} \right) = Z_\lambda - 2.5 \log_{10} \left(\frac{\sum_{i=1}^{N} C_i - n C_{sky}}{t} \right), \qquad (1.32)$$

where the subscript λ denotes the considered filter or waveband, $C_{*,i}$ are the counts from the source only in the i-th pixel of the CCD, C_i are the counts from both the source and the background in the i-th pixel, C_{sky} are the average counts from the background, N is the number of pixels in a region containing the source only, n is the number of pixels in a source-free region, t is the observation time, and Z_λ is the photometric zero point, defined as the magnitude of an object producing 1 count per second. It is a specific property of the telescope, measured during the instrument calibration phase.

[26] https://heasarc.gsfc.nasa.gov/cgi-bin/W3Browse/w3browse.pl

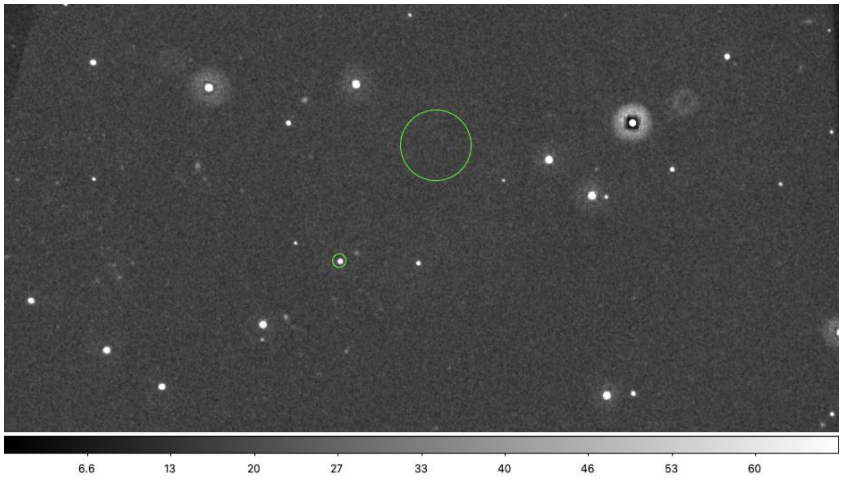

Figure 1.27: *UVOT* image in B band for the source PKS 0048-09, analyzed in Chap. 4. The source region is represented by the green contour around the target, while the background region is given by the green contour in the source-free area. The grey levels indicate the number of detected counts from the observed area in the sky.

The values of Z_λ in each filter for the *UVOT* telescope are measured in [75] and reported in Table 1.4, together with the conversion factors needed at the end of the analysis to recover the source flux from the observed counts. An example of a *UVOT* image showing selected regions for the source and the background is shown in Fig. 1.27.

However, the magnitude recovered through aperture photometry is not the intrinsic brightness of the source because of absorption and scattering of light by dust and gases between the emitting source and the observer, the so-called extinction. This contribution is called extinction and a correction taking it into account has thus to be applied to the obtained results. For *UVOT* the so-called extinction coefficient can be computed as [76]:

$$A_\lambda = E(B-V)[a_\lambda R_v + b_\lambda], \tag{1.33}$$

where the subscript λ indicates the filter, $E(B-V)$ is the colour excess, taking into account the differences between the intrinsic and measured magnitudes, R_v is a coefficient with a value $R_v = 3.1$ in the interstellar medium, and a_λ and b_λ are coefficients specific of the telescope. They are measured in [76] as described in [77] and reported in Table 1.5 for each filter.

For each filter, the analysis gives one spectral point to build the source SED. The same procedure can also be used to compute the source lightcurve, but in this case the analysis has to be repeated not only for each filter but also for each observation date.

Filter	Zero point	Conversion factor [erg cm^{-2} s^{-1} Å^{-1}]
v	17.89 ± 0.013	$(2.614 \pm 0.009) \times 10^{-16}$
b	19.11 ± 0.016	$(1.472 \pm 0.006) \times 10^{-16}$
u	18.34 ± 0.020	$(1.630 \pm 0.025) \times 10^{-16}$
$w1$	17.49 ± 0.03	$(4.00 \pm 0.01) \times 10^{-16}$
$m2$	16.82 ± 0.03	$(8.50 \pm 0.06) \times 10^{-16}$
$w2$	17.35 ± 0.03	$(6.20 \pm 0.14) \times 10^{-16}$

Table 1.4: Photometric zero point and conversion factor of the *Swift/UVOT* telescope in each filter.

	v	b	u	$w1$	$m2$	$w2$
a_λ	1.0015	0.9994	0.9226	0.4346	0.0773	-0.0581
b_λ	0.0126	1.0171	2.1019	5.3286	9.1784	8.4402

Table 1.5: Values of the a_λ and b_λ coefficients needed to compute *UVOT* extinction factor [76].

Chapter 2

Active Galactic Nuclei and blazars

The astrophysical objects mainly considered in this thesis are blazars, a particular subclass of Active Galactic Nuclei (AGNs). AGNs are extremely energetic and compact regions located in the core of galaxies. Their total luminosity typically ranges from $10^{44}\,\mathrm{erg\,s^{-1}}$ to $10^{48}\,\mathrm{erg\,s^{-1}}$, making them the most luminous persistent objects in the universe. Such high luminosity largely exceeds the output of the host galaxy. Moreover, the emission of AGNs covers the whole electromagnetic spectrum, from radio wavelengths to VHE $\gamma-$rays. Therefore, the output of AGNs cannot be attributed to stellar emission only.

The mechanism which is thought to power these peculiar objects is the accretion of matter onto a Super Massive Black Hole (SMBH) residing in the center of the host galaxy and showing a typical mass between $10^6\,\mathrm{M_\odot}$ and $10^{10}\,\mathrm{M_\odot}$, where $\mathrm{M_\odot}$ denotes the solar mass. The gravitational infall of matter inside the accreting structure is thought to radiate a large amount of energy through the dissipation of the heat stored in the accretion process. Besides the SMBH and the accretion structure, called accretion disk, other components characterize AGNs. Within them two collimated plasma outflows, commonly referred to as jets, are responsible for an intense non-thermal radiation, which is often the dominant emission component, in $\sim$ 10% of AGNs. The jet emission is given by accelerated particles which move along the jet at relativisitc velocities and emit non-thermal radiation through the different processes described in Sect. 2.4.

The capability of these objects to emit radiation at high energies makes them interesting candidates for neutrino emission, since $\gamma-$rays and high-energy neutrinos are thought to be produced in the same interactions of CRs with proton targets or photon fields, as described in Sect. 1.1. In addition, this interest grew in 2017, thanks to the first observation of a flaring blazar in coincidence with an astrophysical neutrino event detected by IceCube [3] (see Sect. 3.1 for more information about this event).

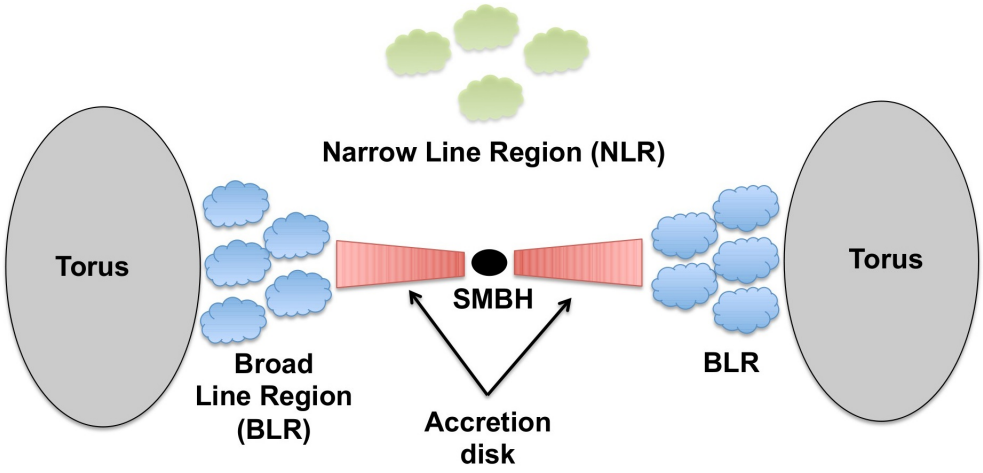

Figure 2.1: Schematic representation of AGNs structure, showing the components common to all AGNs. Image adapted from http://www.isdc.unige.ch/∼ ricci/.

2.1 AGNs structure

Given their peculiar structure, AGNs were initially challenging to classify, leading to the creation of various phenomenological classes. However, it was later established that observational differences between the various classes can be explained by different viewing angles of a single class of objects [78].

In terms of structure, all AGNs share the same components, schematically illustrated in Fig 2.1. The basic features characterizing an AGN include a central Super Massive Black Hole accreting material around itself, an accretion disk formed by matter spiraling towards the black hole, two distinct regions of ionized plasma known as the Broad Line Region (BLR) and Narrow Line Region (NLR), responsible for spectral lines in the optical spectrum, and an obscuring dusty torus absorbing the radiation emitted by the disk and the BLR and re-emitting it in the infrared band [79]. Additionally, about 10% of AGNs exhibit oppositely directed jets of plasma, streaming at relativistic velocities and emitting radiation up to the $\gamma-$ray band. The precise composition of these jets remains a subject of debate [80]. If hadrons are present, neutrino emission would be possible, adding astrophysical interest on these sources. In the following we report detailed information on the aforementioned components.

2.1.1 Super Massive Black Hole and accretion disk

The main source of power in AGNs is the accretion process. This phenomenon consists in matter to spiral towards the central SMBH because of gravitational effects, forming a flattened structure called accretion disk. This structure forms from the dissipation

of energy of the moving material through radiation and shocks, while conserving its angular momentum, and makes matter to spiral towards inner orbits. The matter composing the accretion disk emits radiation until it reaches a minimum radial distance beyond which the infalling material falls into the SMBH in a time shorter than the time needed for radiating, making it non-visible.

An important quantity describing the efficiency of the accretion mechanism onto the SMBH is the accretion rate $\dot{m}$, related to the accretion luminosity L_{acc} of the system. In computing L_{acc}, we have to take into account that the black hole radius is not a proper radius like in compact objects, but it is given by its event horizon. Therefore, part of the accretion energy is not radiated, but it just disappears into the black hole adding to its mass. This behaviour can be parametrized by introducing the quantity η, giving a measure of the radiative efficiency of accretion. In this way the accretion luminosity of the black hole can be written as [81]:

$$L_{acc} = \eta \dot{M} c^2, \tag{2.1}$$

where $\dot{M} = \frac{\mathrm{d}M}{\mathrm{d}t}$ is the rate at which matter is accreted. The accretion rate $\dot{M}$ can be written in terms of the accretion rate at the Eddington luminosity $\dot{M}_{Edd}$, obtaining

$$\dot{m} = \frac{\dot{M}}{\dot{M}_{Edd}}. \tag{2.2}$$

The Eddington luminosity is the maximum achievable accretion luminosity before the radiation pressure exceeds the inward gravitational force. It is obtained by balancing these two forces and it is given by:

$$L_{Edd} = \frac{4\pi c m_p G M}{\sigma_T} \simeq 1.3 \times 10^{38} \frac{M}{M_\odot} \frac{\mathrm{erg}}{\mathrm{s}}. \tag{2.3}$$

In terms of $\dot{M}_{Edd}$, it can be written as:

$$L_{Edd} = \dot{M}_{Edd} c^2. \tag{2.4}$$

The accretion process depends on the accretion rate, and has been modeled for both high and low values of $\dot{m}$. For high accretion rates, a standard thin accretion disk, known as the Shakura-Sunyaev Disk [82], is formed. It is geometrically thin, optically thick, and radiates efficiently, primarily in thermal emission, producing X-rays in the inner regions and UV/optical emission in the outer regions.

In contrast, low accretion rates lead to the formation of Advection-Dominated Accretion Flows [83], characterized by a particle density much lower compared to the geometrically thin case. Here, the energy exchange time scale between electrons and protons becomes larger than the accretion time scale. This results in geometrically thick, optically thin disks where a significant fraction of energy is not radiated away, making them little efficient. In this case the electrons and ions in the disk are thermally decoupled, and a non-thermal radiation through synchrotron, inverse Compton and Bremsstrahlung processes from the electrons can be observed, leading to a spectrum spanning from radio to soft X-rays. The transition between these accretion modes is thought to happen at $\dot{m} \sim 0.01$ [84].

2.1.2 Broad Line and Narrow Line Regions

Surrounding the central structure, there are two regions composed of clouds of partially or totally ionized plasma, called Broad Line Region (BLR) and Narrow Line Region (NLR) respectively, responsible for the emission lines in AGNs optical spectra. They are located at a distance from the central SMBH of $0.1 - 1$ pc and ~ 100 pc respectively. Being the BLR closer to the central SMBH, the plasma composing it moves at higher velocity in its keplerian motion around the SMBH with respect to the plasma composing the NLR. The typical velocities of these two regions are $10^3 - 10^4$ km s^{-1} for the BLR and $300 - 500$ km s^{-1} for the NLR.

Spectral lines are produced by the radiation emitted through the de-excitation of atoms and ions in the plasma clouds after they are excited by the photons emitted from the accretion disk. The radiation produced undergoes a Doppler shift in frequency which increases with the plasma velocity. For this reason the BLR shows broader lines than the NLR. In AGN spectra, both permitted and forbidden lines are observed within narrow lines, while only permitted lines are present in broad lines. Permitted lines arise from atomic transitions with non-zero probabilities at first order in quantum perturbation theory, while forbidden lines involve suppressed transitions that occur over a longer timescale. This implies a lower density of the NLR, so that recombination can happen by spontaneous de-excitation, rather than by collision events. In some cases, also semiforbidden lines are observed, coming from transitions with a probability about a thousand times higher than that for forbidden ones. The presence of these emission lines allows to estimate the density of the plasma clouds in the BLR and NLR, as respectively $10^9 - 10^{11}$ cm^{-3} and $10^3 - 10^4$ cm^{-3}.

2.1.3 Dusty Torus

At the distance of $1 - 10$ pc from the central black hole, there is a dusty toroidal structure, extending up to about 100 pc. This structure, commonly referred to as dusty torus, is usually described as a geometrically and optically thick torus of gas, placed between the BLR and the NLR. Some models [85, 86] expect it to be composed by a clumpy distribution of dust and gas clouds arranged in high-density clumps and low-density interclump material, rather than by a uniform distribution.

The presence of the tours can lead to the obscuration of the optical emission from the innermost structures, like the BLR and the disk. The extent of obscuration depends on the viewing angle of the observer with respect to the AGN axis. The obscured radiation is absorbed and then re-emitted in the infrared band, with estimated emission frequencies below 10^{14} Hz due to the temperature limit of the dust. Regardless of the viewing angle, the emission from the NLR remains always visible in the spectrum, since the NLR is located outside the dusty structure.

2.1.4 Relativistic jets

Approximately 10% of AGNs exhibit jet structures composed of oppositely directed, highly collimated outflows, a jet and counter-jet, originating perpendicularly to the disk and at distances < 1 pc from the SMBH. They are usually associated with intense radio emission, reason for which these kinds of AGNs are classified as radio-loud AGNs. The jets can have a size ranging from few tens of kpc to Mpc, and can terminate with two extended structures called lobes, where the jet plasma decelerates likely because of its interaction with the surrounding matter [80].

The exact composition and formation mechanisms of the jets are still unknown and debated. The two main considered processes involve the extraction of energy and angular momentum from the accretion disk [87] or the extraction of rotational energy from the spinning SMBH [88]. Moreover, as observed by high resolution measurements in the radio band, they are not composed by a coherent stream of particles but they present regions with increased density called knots (see e. g. [89]), whose origin is still not understood. The most likely cause is the formation of shocks traveling down the jet (see Sect. 2.4.1).

The local emission observed in the jets is attributed to particles moving at relativistic velocities, emitting radiation at all frequencies, from radio to VHE $\gamma-$rays. Both leptonic and hadronic processes can be taken into account to interpret the jet emission. More details on the main processes considered in AGNs and blazar emission are described in Sect. 2.4.

2.2 The unified model of AGNs

The AGNs class includes a large variety of objects characterized by variations in luminosity, spectral features, and temporal behaviour [90]. These differences can be explained within the framework of a unification scenario, which interprets the different observational properties as an effect of the jet orientation with respect to the observer.

For example, a first classification was made through the observation of AGNs optical spectra: we have a **Type I Seyfert galaxy** if it shows both broad and narrow emission lines and bright continua, while a **Type II Seyfert galaxy** if it shows only narrow emission lines and weak continua. This can be explained in terms of the viewing angle of the observer with respect to the normal to the disk: jet axis: for small viewing angles the emission from both the BLR and the NLR can be observed, while for large angles the emission from the BLR becomes not visible because of the absorption from the dusty torus, which, in this case, is located along the line of sight.

Another division is based on their radio emission. In this case, the dominance of the observed radio flux at $\nu \simeq 5$ GHz over the optical one in the blue B band ($250 - 500$ MHz) is considered. We have a **Radio-loud AGN** if the ratio $R = f_{5\,\mathrm{GHz}}/f_B > 10$, otherwise we have a **Radio-quiet AGN**. Radio-loud AGNs represent only 10% of the whole class and they are typically characterized by a powerful jet component contributing to

significant radio emissions through the synchrotron radiation. The radio emission is thus a good tracer of the presence of the jet.

In addition, a further radio division historically introduced by Fanaroff and Riley [91] is based on the position of the extended radio emission on the source radio skymap. We have a **FR-I** object if it shows a rather compact radio emission dominating the core, while we have a **FR-II** object if it shows a radio emission mainly coming from the end of the jet, dominating the lobes. These two classes present a different radio luminosity, which is the reason why a dividing luminosity, $L_R = 10^{32}\,\mathrm{erg\,s^{-1}\,Hz^{-1}\,sr^{-1}}$ at a frequency of 175 MHz, was defined to distinguish between FR-I (with $L < L_R$) and FR-II (with $L > L_R$). The differences in morphology and luminosity between the two classes suggest these objects to be governed by different physical scenarios. FR-I sources typically exhibit low accretion rates, suggesting them to be powered by inefficient accretion flows, while FR-II sources are believed to possess a more efficient engine. Moreover, also for radio-loud AGNs we observe different properties based on their inclination angle with respect to the observer. For large viewing angles we have a *radio-galaxy*, while for small angles we have a *blazar*.

The unification scenario, taking into account both the optical and radio classifications, is shown in Fig. 2.2. Within all the shown classes, we highlight the blazar sources, which are the main topic of this thesis. Given their orientation with respect to Earth and the relativistic velocities of the particles composing the jet, they show an emission characterized by a strong Doppler boosting, connected to a direct observation of the jet itself and responsible for peculiar features. The main properties of blazars are described in the next section.

2.3 Blazars

Blazars are a particular subclass of radio-loud AGNs with the jet inclined at small observation angles ($\theta \leq 10^\circ$). They represent only the 1% of radio-loud AGNs, which in turn are just the 10% of all AGN sources.

This class of objects is characterized by a high flux variability, on time scales from years to less than one day, making them the most variable AGN subclass. Moreover they show a high bolometric luminosity, which can reach up to 10^{45} erg $\mathrm{s^{-1}}$, and an emission covering the whole electromagnetic spectrum, from radio frequencies to TeV energies. These features can be physically explained by the presence and inclination of the relativistic jet, which dominates their emission.

Their jet behaves as a natural accelerator of particles, such as electrons and protons, at high energies. For this reason blazars are currently considered as possible sources of high-energy CRs and neutrinos. The broad-band emission they show can be investigated by plotting their energy flux νF_ν [erg $\mathrm{cm^{-2}\ s^{-1}}$] as a function of the energy E or frequency ν in logarithmic scale. This plot is called **Spectral Energy Distribution (SED)** and allows to compare the source emission in the different bands. The SED of blazars is characterized by two broad bumps, typically peaking in the optical/UV and in the $\gamma-$ray bands. Their origin can be attributed to different non-thermal radiative

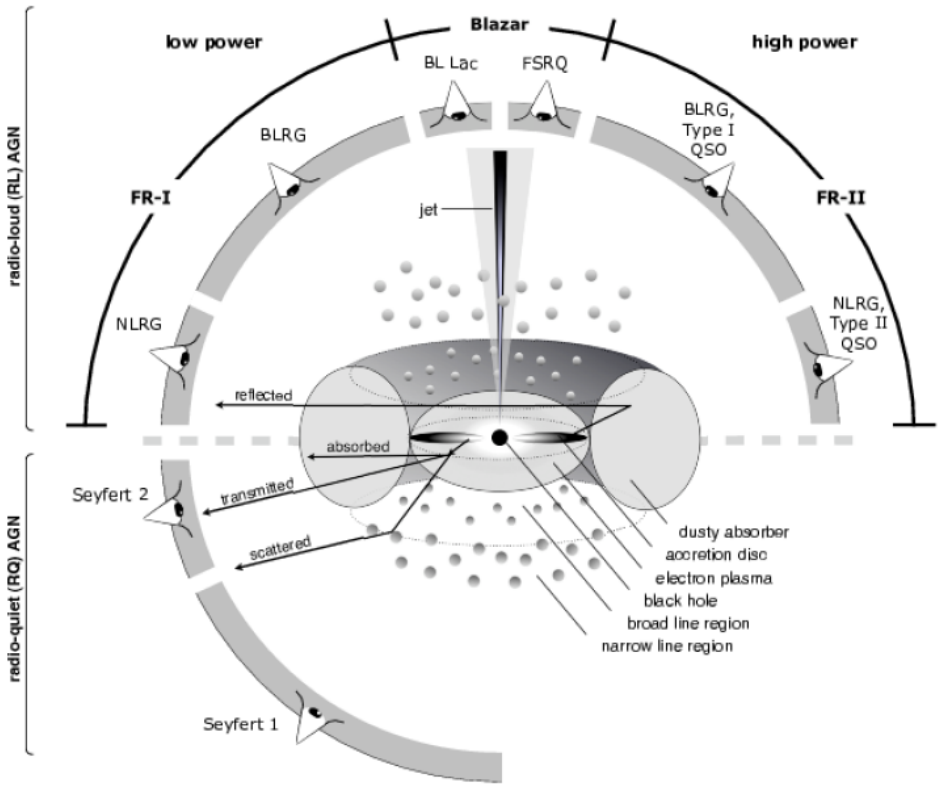

Figure 2.2: Unified models of AGNs. Radio-quiet AGNs are shown in the lower part of the image, while radio-loud AGNs in the upper part. They are in turn divided into the FR-I and FR-II classes. Credits [92].

processes. For example the optical emission can be explained in terms of synchrotron radiation from relativistic electrons, while the X-ray band can show the contribution from different processes, of both leptonic and hadronic origin. More details on the different processes at work in blazars emission are given in Sect. 2.4.

2.3.1 Classification of blazars

Blazars are generally divided into two sub-classes: Flat-Spectrum Radio-Quasars (FSRQ) and BL Lacertae objects (BL Lacs). This division comes from observational properties of sources optical spectra. It considers as FSRQs those sources showing bright emission lines, while as BL Lacs those with very faint or even absent spectral lines. A dividing value of the Equivalent Width (EW) of the broad lines was set to distinguish between the two classes: sources showing $EW > 5$ Å are classified as FSRQs, while those showing $EW < 5$ Å are classified as BL Lacs [93].

However, this classification does not consider the physical properties of the sources. Taking into account the high variability of the jet emission, it can happen that a source

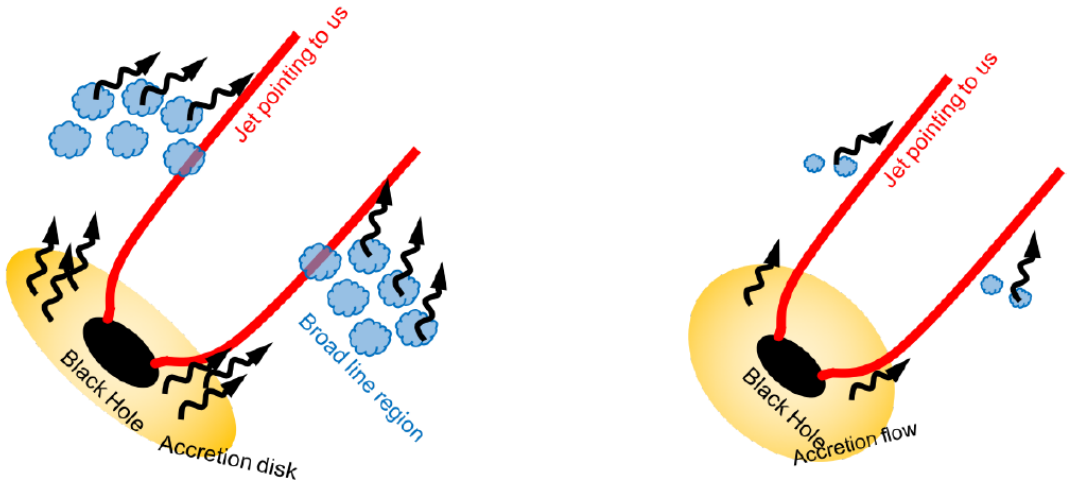

Figure 2.3: Schematic representation of blazar subclasses. FSRQs (left) are thought to have an efficient accretion disk and a rich BLR, while BL Lacs (right) are thought to have an inefficient disk and a poor or absent BLR. Credits: [94]

with intrinsically prominent lines can be misclassified as a BL Lac if the non-thermal continuum given by the jet emission is particularly enhanced at the time of the observation. Viceversa, a source with intrinsically faint lines can be misclassified as a FSRQ if the jet emission shows a low state of activity when the measurement is performed. For this reason a new classification was proposed by [84]. It is based on the luminosity of the BLR, normalized to the source Eddington luminosity: for $L_{BLR}/L_{Edd} \geq 5 \times 10^{-4}$ we have a FSRQ, otherwise, for $L_{BLR}/L_{Edd} \leq 5 \times 10^{-4}$ we have a BL Lac. This division is related to the efficiency of the accretion flow onto the SMBH. Indeed, given that the broad emission lines originate in the BLR due to the plasma clouds photoionized by radiation from the accretion structure, there is direct relation between the disk luminosity L_{disk} and the BLR luminosity L_{BLR}. Moreover, as we know from Sect. 2.1.1, the accretion rate $\dot{m}$ depends on the disk luminosity through the relation

$$\dot{m} = \frac{\dot{M}}{\dot{M}_{Edd}} = \frac{1}{\eta}\frac{L_{disk}}{L_{Edd}}. \tag{2.5}$$

For the last equivalence we used Eqs.2.2 and 2.4. An application of this relation can be found in Chap. 4.

Since the differences between FSRQs and BL Lacs are related to the accretion efficiency, they can explain differences in the intrinsic properties of the sources environment. The strong emission lines characterizing FSRQs imply these sources to have a radiatively efficient accretion process, such as the Shakura-Sunyaev disk [82], and a BLR rich of dust and gas. Differently, the weakness or absence of emission lines from BL Lacs suggests them to be powered by radiatively inefficient accretion flows,

like the Advection-Dominated Accretion Flow [83], and to have a poor or absent BLR. A schematic representation of the environment characterizing the blazar subclasses is shown in Fig. 2.3.

2.3.2 The blazar sequence

One of the first comprehensive studies of blazars SED was performed by [95], where the authors proposed the SEDs of known blazars to form a sequence, the so-called *blazar sequence*. This work included a sample of 126 blazars, of which only 33 were detected in the $\gamma-$ray band. They were divided according to their radio luminosity, and for each radio luminosity bin an average SED was built. The main results of this analysis report a homogeneous SED shape for all the considered blazars, characterized by two bumps, peaking respectively in the ranges $10^{13} - 10^{17}$ Hz and $10^{21} - 10^{24}$ Hz. Moreover, a trend on the peak frequencies is observed: sources with higher radio luminosity show the peaks at lower energies, while, as the luminosity decreases, the peaks shift to higher energies. For any case, the peak frequencies in a single SED seem to be correlated, meaning that a lower energy of the first peak corresponds to a lower energy of the second one and viceversa. Moreover, the ratio between the luminosity of high- and low-energy peaks, so-called Compton dominance, increases with increasing radio luminosity. The bins of higher luminosity are mostly composed of FSRQs, while BL Lacs show lower radio luminosities and peaks shifted to higher energies.

The blazar sequence found by [95] has been confirmed by [96], a more recent work which considers a much larger sample of 747 objects and divides them according to their $\gamma-$ray luminosity. In this case the sources are selected from the third catalog of AGNs released by the Fermi Collaboration (3LAC) [28], so they all show data in the $\gamma-$ray band. The main results are shown in Fig. 2.4 and described in the following for FSRQ and BL Lacs separately, as well as for the whole sample:

- Considering the whole sample, although the different selection in luminosity between the two analyses (radio luminosity bins vs $\gamma-$ray luminosity bins), a trend consistent with the results of [95] is found. This confirms and reinforces the existence of the blazar sequence.

- Considering FSRQs only, the overall SED shape is mostly unchanged. They do not exhibit shifts in the peak frequencies with changing luminosity. The main trend is observed in the Compton Dominance, which increases with increasing $\gamma-$ray luminosity from a value of 0.5 to 15. Another trend is observed in the slope of the X-ray spectrum, becoming harder with increasing luminosity, as a consequence of the increasing Compton dominance.

- Considering BL Lacs only, a remarkable trend in the entire SED shape is observed, with the peak frequencies shifting towards lower energies while the $\gamma-$ray luminosity increases. In particular, the low-energy peak is observed to move from $\sim 10^{17}$ Hz to $\sim 10^{12}$ Hz with increasing luminosity of 4 orders of magnitude. The Compton dominance for BL Lacs changes by one order of magnitude only in the

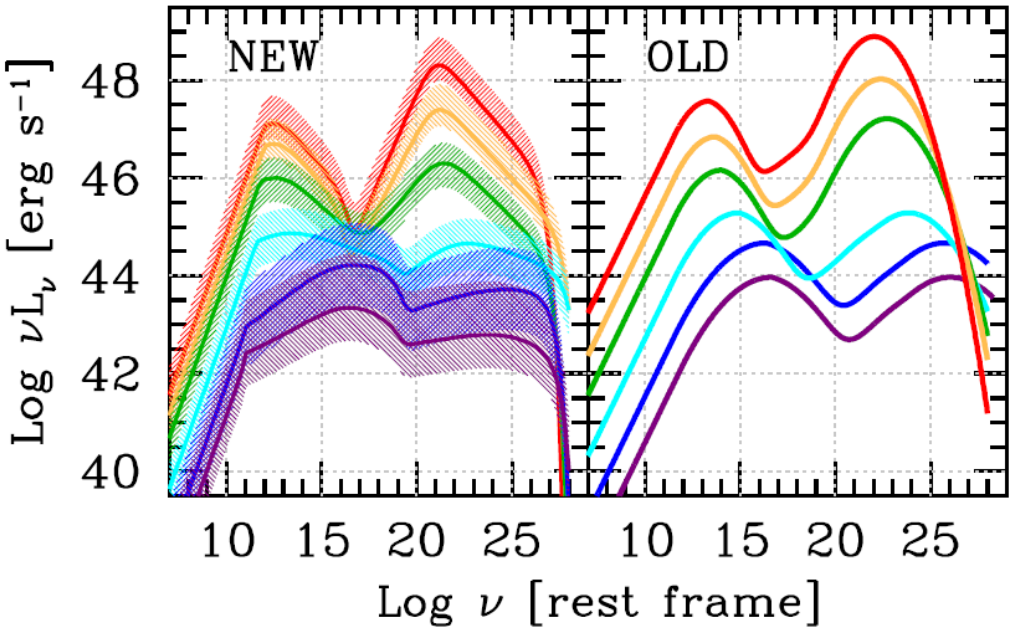

Figure 2.4: Comparison between the most recent [96] and the original [95] blazar sequence. Credits: [96].

entire luminosity range, showing that the low- and high-energy components are almost equal. Given their broad frequency interval, BL Lacs are further classified into low frequency-peaked (LBL), intermediate frequency-peaked (IBL) and High frequency-peaked (HBL) BL Lac objects, based on the location of their synchrotron peak frequency ($\nu_S \leq 10^{14}$ Hz, 10^{14} Hz $\leq \nu_S \leq 10^{15}$ Hz, $\nu_S \geq 10^{15}$ Hz respectively) [97].

The differences observed between FSRQs and BL Lacs emission can be related to different physical processes powering it. For example, the efficient disk and rich BLR expected in FSRQs make their environment rich of target photons which can play a role in the so-called external Compton (EC) process (see Sect. 2.4.2 for more details). This, together with a possible decrease of the magnetic energy density with luminosity, can explain the higher Compton dominance in these objects [96]. Differently, for BL Lacs, we do not expect external photon fields, so the main radiative process can be the Synchrotron Self Compton (SSC), which depends on the synchrotron radiation energy density. It increases with luminosity, implying a more severe cooling for more luminous BL Lacs, thus limitating the maximum energy of the electrons emitting at the SED high-energy peak.

2.4 Interpretation of blazars Spectral Energy Distribution

As already mentioned, the jet of blazars, and radio-loud AGNs in general, is a natural accelerator of particles. Its emission is assumed to come from one or more specific emitting regions, filled with a population of relativistic particles, assumed at a certain distance from the central SMBH (usually < 1 pc), and characterized by different properties such as for example a Lorentz factor Γ and a magnetic field B. The particles composing the emitting region are out of equilibrium, usually following a power-law distribution (see next section), and emitting non-thermal radiation.

The two bumps characterizing blazars SED can be explained as originating from the emission of these emitting zones. The low-energy bump in the SED is unanimously attributed to the synchrotron emission from a population of relativistic electrons, while the origin of the high energy one is still unclear and debated. It can be interpreted in terms of both leptonic and hadronic emission models. The former assume the emitting region to be filled with a population of relativistic electrons and positrons, while the latter require the presence of accelerated protons too. Also in the first case protons can be present, but they are considered not to be accelerated to sufficiently high energy to significantly contribute to the emission. Within leptonic models, the inverse Compton scattering of relativistic electrons with soft photons can usually well describe the high-energy bump. The target soft photons can be the ones originated through the synchrotron radiation at low energies (SSC), or come from external radiation fields such as the disk, BLR or torus (EC). Within hadronic models, the most relevant processes in blazars emission are the proton synchrotron radiation or the photo-meson interactions, namely interactions between accelerated protons and soft photons, from which high-energy neutrinos can arise. Mixed lepto-hadronic models are also taken into account. An example is provided in Chap. 4.

Blazars show also thermal emission components in their environments, associated to particles in thermal equilibrium. This is the case for example of the emission coming from the disk, or torus. However, the thermal emission from the inner regions is often subdominant with respect to the non-thermal jet emission, and thus not visible.

2.4.1 Particle acceleration

In astrophysical objects, particle acceleration is usually determined by plasma perturbations in the source environment, known as shocks. In the jet of AGNs, these components stream relativistically along the jet. The most efficient acceleration mechanism in shocks is the so-called **First order Fermi acceleration mechanism** [98], which occurs when particles cross the shock front multiple times. This is possible thanks to the high magnetic fields close to the shock front, which cause particles to gyrate along the field lines.

Let us consider an initial number of particles N_0, with energy E_0 each, and define with P the probability these particles have to remain in the acceleration region after a round trip across the shock front. After n round trips the total number of particles

becomes:

$$N = N_0 P^n \Rightarrow \ln\left(\frac{N}{N_0}\right) = n \ln P. \tag{2.6}$$

If we also assume that the energy gained by each particle after a round trip is proportional to a factor ξ, the total energy after n round trips is

$$E = E_0(1+\xi)^n \Rightarrow \ln\left(\frac{E}{E_0}\right) = n \ln(1+\xi), \tag{2.7}$$

By solving for n and equating the two expressions, it is possible to obtain:

$$N = N_0 \left(\frac{E}{E_0}\right)^{\ln P / \ln(1+\xi)}. \tag{2.8}$$

which gives the typical power-law shape Particles accelerated through the Fermi mechanism are therefore described by a power-law distribution. It is typically observed, for example, in the case of cosmic-rays. Here the spectral index depends on the containment probability and the energy gain. In the First order Fermi mechanism, the energy gained by the particle at each passage of the shock front in both directions results to be [98]:

$$\xi = \left\langle \frac{\Delta E}{E} \right\rangle \simeq \frac{4}{3}\beta, \tag{2.9}$$

where $\beta = v/c$, with v the relative velocity between the shock front and the particle, and c the speed of light.

2.4.2 Leptonic models

In the following, the relevant leptonic processes at work in blazar emission are described.

Synchrotron emission

The synchrotron radiation is produced by particles accelerating in a magnetic field B. In blazar SED, this process is responsible for the origin of the low-energy bump, usually peaking in the optical/UV band.

If we consider a relativistic electron in a uniform magnetic field B, it will gyrate along the magnetic field lines with a frequency [99]

$$\nu_B = \frac{eB}{2\pi\gamma m_e c}, \tag{2.10}$$

where e is the electron charge, B is the magnetic field, γ is the electron Lorentz factor, m_e is the electron mass, and c is the speed of light. The power emitted during its motion is given by

$$P_{syn} = \frac{4}{3}\sigma_T U_B c \gamma^2 \beta^2, \tag{2.11}$$

where $U_B = B^2/(8\pi)$ is the magnetic field energy density, c is the speed of light, γ is the particle Lorentz factor, β is the particle velocity in units of c, and σ_T is the Thomson cross-section, given by $\sigma_T = 8\pi r_0^2/3$, with $r_0 = e^2/(m_e c^2)$ the classical electron radius. Given the dependence $P_{syn} \propto m^{-2}$, we can deduce that light particles like electrons and positrons emit more efficiently than heavier particles like protons. Thus in a relativistic jet, if protons and electrons are accelerated to the same energy E, the dominant contribution of the synchrotron emission is given by the electrons.

When the spectrum is converted from the electron frame to the observer frame, the radiation appears to be concentrated within an opening angle of $\theta \simeq 1/\gamma$, along the motion of the electron. Through mathematical calculations [99], it is possible to obtain the spectral power emitted by a single electron through synchrotron radiation (see also Sect. 6.2.1):

$$P(\nu, \theta) = \frac{\sqrt{3} e^3 B \sin\alpha}{m_e c^2} F\left(\frac{\nu}{\nu_c}\right), \tag{2.12}$$

where α is the electron pitch angle, and $F(x) = x \int_x^\infty K_{5/3}(\tau) \mathrm{d}\tau$, with $K_{5/3}(\tau)$ the modified Bessel function of order 5/3.

However, in blazars and astrophysical environments in general, the emission is given by a distribution of particles, rather than a single particle. If we consider an energy distribution given by a power-law (see Sect.2.4.1), we have that the number density of particles with energies between E and E + dE results

$$N(\gamma)\mathrm{d}\gamma = K\gamma^{-p}\mathrm{d}\gamma \quad \text{for} \quad \gamma_{min} < \gamma < \gamma_{max}. \tag{2.13}$$

The total power radiated per unit solid angle, volume, and frequency, is given by the integral of the product $N(\gamma)P(\nu, \theta)$ over the possible energies, leading to

$$P(\nu) \propto \nu^{-\frac{p-1}{2}}. \tag{2.14}$$

Therefore, from the spectral index of synchrotron spectrum, it is possible to obtain an indication on the spectral index of the radiating electrons. Additional details on the synchrotron process can be found in Sect. 6.2.1.

Inverse Compton scattering

The inverse Compton scattering is a process occurring when a relativistic electron interacts with a photon transferring energy to it, allowing, for example, the creation of X-ray or $\gamma-$ray emission from a soft photon of energy spanning from radio to UV. In blazar SED, this process can explain the high-energy bump, peaking at the aforementioned energies.

If the energy of the incoming photon in the electron rest frame is much smaller than the electron rest energy, namely $h\nu \ll m_e c^2$, the regime in which the scattering happens is defined as Thomson regime, otherwise, for $h\nu \gg m_e c^2$ we are in Klein-Nishina regime. In the first case there is no transfer of energy between the photon and

the electron, and the cross-section of the interaction is given by [99, 100]:

$$\sigma_T = \frac{8}{3}\pi r_0^2 = \frac{8}{3}\pi \left(\frac{e^2}{m_e c^2}\right)^2, \tag{2.15}$$

with r_0 the classical electron radius. In the second case, the cross-section is given by [99, 100]:

$$\sigma_{KN} = \frac{3}{4}\sigma_T \left\{ \frac{1+x}{x^3}\left[\frac{2x(1+x)}{1+2x} - \ln(1+2x)\right] + \frac{\ln(1+2x)}{2x} - \frac{1+3x}{(1+2x^2)} \right\}, \tag{2.16}$$

where the variable x denotes $x = h\nu/(m_e c^2)$. If we consider the asymptotic limits, we can note that for low photon energies ($x \ll 1$), the cross-section approximates σ_T:

$$\sigma_{KN} \simeq \sigma_T \left(1 - 2x + \frac{26x^2}{5} + ...\right), \tag{2.17}$$

while for very high energies ($x \gg 1$) we have that the cross-section is strongly suppressed:

$$\sigma_{KN} \simeq \frac{3}{8x}\sigma_T \left(\ln(2x) + \frac{1}{2}\right). \tag{2.18}$$

Here, we concentrate on the Thomson regime. For the Klein-Nishina regime a quantitative treatment can be found in [101]. In Thomson regime, the total power emitted by the electron during the process is given by [99]

$$P_{IC} = \frac{4}{3}\sigma_T U_{rad} c \gamma^2 \beta^2, \tag{2.19}$$

similarly to the result obtained for synchrotron radiation. The only difference is the energy density, now given by the incoming radiation rather than the magnetic field. The spectral power released during the interaction with a photon with energy $E_0 = h\nu_0$ is given by [99]

$$I(\nu)\mathrm{d}\nu = \frac{3\sigma_T c N(\nu_0)}{16\gamma^4 \nu_0^2}\nu \left[2\nu \ln\left(\frac{\nu}{4\gamma^2\nu_0}\right) + \nu + 4\gamma^2\nu_0 - \frac{\nu^2}{2\gamma^2\nu_0}\right]\mathrm{d}\nu, \tag{2.20}$$

where $N(\nu_0)$ is the number density of photons. If we consider a power-law distribution of electrons as in the synchrotron case, the radiated power becomes

$$P_{tot}(\langle\nu\rangle) = \frac{1}{8\pi}\left(\frac{4}{3}\right)^{\alpha} \sigma_T c K \frac{U_{rad}}{\nu_0}\left(\frac{\langle\nu\rangle}{\nu_0}\right)^{-\alpha}, \tag{2.21}$$

where $\langle\nu\rangle$ is the average frequency at which the total power is emitted, and $\alpha = \frac{p-1}{2}$.

Synchrotron Self Compton

Two different kinds of inverse Compton scatterings are usually considered in blazar emission. When the produced synchrotron photons giving origin to the low energy component of the blazar spectra serve as a target field for Inverse Compton scattering we have the SSC process. This is the most common model applied to BL Lacs, given that they do not have external target photons fields. An example of BL Lac SED fitted with a SSC model is shown in Fig. 2.5a. The relation between the synchrotron and inverse Compton emission in this process implies the two peaks of the SED to be strongly related. Moreover, this link allows the model to be characterized by few free parameters, allowing to put constraints on some physical properties like the magnetic field B or the Doppler factor δ. Indeed, by measuring the frequencies of the two peaks, it is possible to obtain the values of δ and B [92]:

$$\delta = \left(\frac{3}{4}\frac{e}{2\pi mc}\right)^{1/2}\left(\frac{\nu_{IC}}{\nu_S^2}\right)^{1/2}\left(\frac{2L_S^2}{c^3 L_{IC} t_{var}^2}\right)^{1/4} \tag{2.22}$$

$$B = (1+z)\left(\frac{4}{3}\frac{2\pi mc}{e}\right)^{3/2}\left(\frac{\nu_S^2}{\nu_{IC}}\right)^{3/2}\left(\frac{c^3 L_{IC} t_{var}^2}{2L_S^2}\right)^{1/4}, \tag{2.23}$$

where ν_S and ν_{IC} are the frequencies of the synchrotron and inverse Compton peaks respectively, similarly L_S and L_{IC} are the luminosities of the peaks, and t_{var} is the observed variability time scale.

External Compton

Differently from the SSC, the EC considers external target photon fields for the inverse Compton scattering. The mainly considered soft photons are those coming from the central regions of the AGN. They can be directly emitted from the disk, or reprocessed by the BLR and the torus before interacting with the relativistic electrons in the jet. Given that the target photon fields are in this case independent from the jet emission, this model involves a larger number of free parameters making the mathematical treatment more complex.

In any case, this scenario works well in the interpretation of the emission of FSRQ. Firstly, the rich environment which is thought to characterize FSRQs, provides different source of external photons, justifying the usage of such target fields. Moreover, the energy density of this external radiation is amplified by a factor Γ^2, with Γ the bulk Lorentz factor of the jet, in the rest frame of the emitting region, allowing to explain the larger Compton dominance observed in the blazar sequence for this kind of sources.

$\gamma\gamma$ absorption

In blazars emission, also the photon-photon pair production can play a relevant role. This process can arise both internally to the source environment and externally. In the

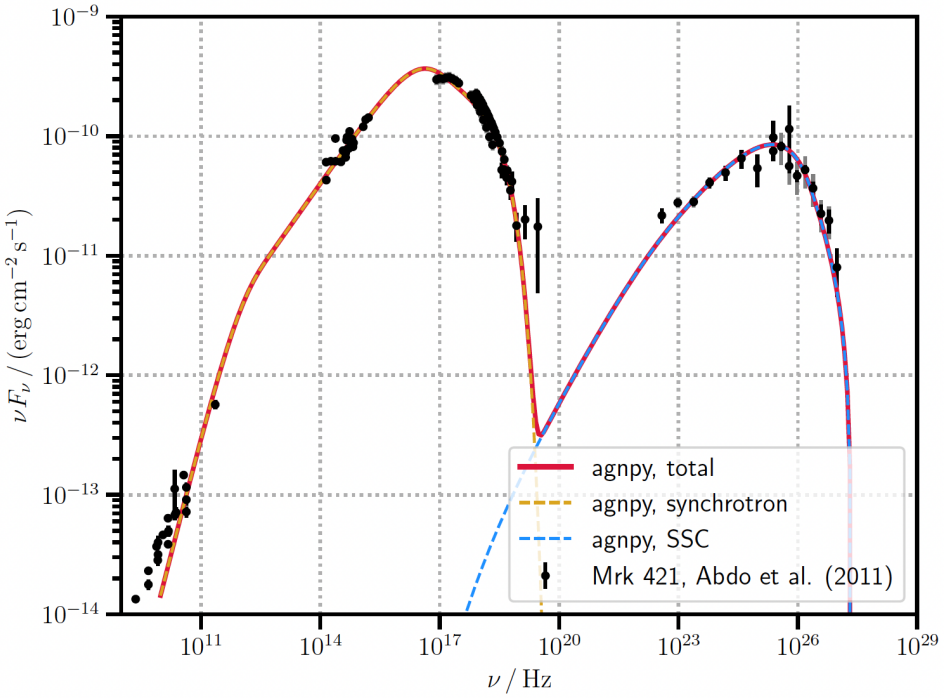

(a)

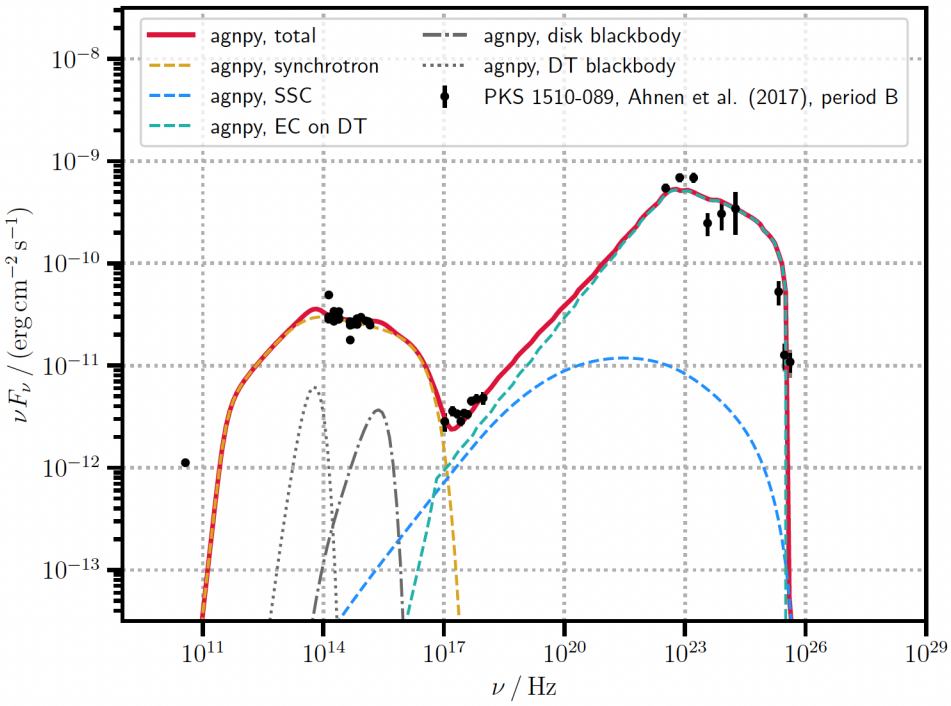

(b)

Figure 2.5: Examples of blazars SEDs fitted with leptonic models. (a) SED of the BL Lac Mrk 421, modeled with the SSC process, (b) SED of the FSRQ PKS 1510-089, modeled with the EC process on the dusty torus. In (b) also the thermal emission from the disk and the dusty torus is shown. Credits: [102].

first case we have that the $\gamma-$rays produced in the inverse Compton emission interact with low-energy photons ($E \sim$ eV) from the disk, BLR and torus, leading to the production of an electron-positron pair through the relation $\gamma\gamma \rightarrow e^- e^+$. In the second case, the emitted photons interact with the EBL in their way to Earth, creating a pair through the same process. The effect of this process is an attenuation of the source flux at high energies.

If two photons of energies ε_1 and ε_2 moving along trajectories forming an angle θ, have a total energy available for the interaction fulfilling the condition $\varepsilon_1\varepsilon_2(1-\cos\theta) \gg 2m_e^2c^4$, then an e^-e^+ pair is produced. The effect of this process on a photon flux can be quantified through the $\gamma\gamma$ opacity or optical depth $\tau_{\gamma\gamma}$, depending on the $\gamma-$ray energy, the target photon energy, and on the path traversed in the absorbing field. If we consider our high-energy photon of energy ε_1 interacting with a uniform isotropic radiation field with a number density $n_{ph}(\varepsilon_2)$, the optical depth is given by [103]:

$$\tau_{\gamma\gamma}(\varepsilon_1) = R \int_0^\infty \mathrm{d}\varepsilon_2 \sigma_{\gamma\gamma}(\varepsilon_1\varepsilon_2) n_{ph}(\varepsilon_2), \tag{2.24}$$

where R is the source dimension, while $\sigma_{\gamma\gamma}$ is the pair-production cross-section, given by [104]

$$\sigma_{\gamma\gamma}(s) = \frac{3}{8}\sigma_T(1-\beta_{cm}^2)\left[(3-\beta_{cm}^4)\ln\left(\frac{1+\beta_{cm}}{1-\beta_{cm}}\right) - 2\beta_{cm}(2-\beta_{cm}^2)\right], \tag{2.25}$$

where $\beta_{cm} = \sqrt{1-s^{-1}}$, with $s = \gamma_{cm}^2 = \varepsilon_1\varepsilon_2(1-\cos\theta)$ the squared value of the Lorentz factor the produced e^-e^+ pair has in the center-of-momentum frame. The source flux seen by the observer is attenuated by a factor $\exp(-\tau_{\gamma\gamma})$ with respect to the intrinsic flux.

2.4.3 Hadronic models

In the leptonic scenario, the emission is dominated by relativistic electrons, while protons in the jet are assumed to have an energy not high enough to emit a significant radiation. Differently, hadronic models consider the presence of both ultrarelativistic electrons and protons in the jet. In this case, while the low-energy peak of the SED is still attributed to the electron synchrotron process, the high-energy one can be dominated by hadronic processes such as proton synchrotron emission, photo-meson interactions, Bethe-Heitler pair production or secondary products originated by particle decay or pair cascades initiated by these processes.

Since the low-energy bump is still attributed to the synchrotron emission of electrons, pure hadronic models are usually not taken into account. Their occurrence is also made improbable by the fast variability at high energies observed in some blazars. Since the cooling time of protons is characteristically long, such variability cannot be explained by hadronic models alone. Lepto-hadronic scenarios as thus those usually considered when dealing with protons. Besides those describing the high-energy bump in terms of pure hadronic emission, there are some still interpreting both SED peaks in

terms of leptonic processes. In these cases the hadronic component arises as a subdominant component, in between these two major bumps, as for example in the X-ray band, when representing the valley between the two peaks. This is the case, for example, of the model presented in Chap. 4.

In the following, the main hadronic processes taken into account in blazars emission are described.

Proton synchrotron radiation

The synchrotron radiation from ultrarelativistic protons in the emitting region is considered as one of the main processes responsible for the origin of the SED high-energy peak. However, since the synchrotron radiation from protons is highly suppressed with respect to that from electrons, intense magnetic fields ($B \geq 10$ G) or high proton densities are necessary in order to make it effective. More details on the description of this process and its mathematical treatment can be found in Sect. 6.2.1.

Photo-meson interactions

The photo-meson process involves the interaction of relativistic protons with low energy radiation. As for the inverse Compton, the target photon fields considered for the interaction can be internal to the jet [105] or external, provided by the disk [106] or reprocessed from the BLR [107]. Through photo-meson interactions, secondary particles such as pions and muons are produced. The initial process produces the Δ resonance, which decays into hadrons and pions (see also Eq. 1.1):

$$p + \gamma \rightarrow \Delta^{+} \rightarrow \begin{cases} p + \pi^{0} \\ n + \pi^{+} \end{cases} . \tag{2.26}$$

The produced pions subsequently decay following (see also Eqs. 1.4−1.8):

$$\pi^{+} \rightarrow \mu^{+} + \nu_{\mu} \rightarrow e^{+} + \nu_{e} + \bar{\nu}_{\mu} + \nu_{\mu} \tag{2.27}$$

$$\pi^{-} \rightarrow \mu^{-} + \bar{\nu}_{\mu} \rightarrow e^{-} + \bar{\nu}_{e} + \nu_{\mu} + \bar{\nu}_{\mu} \tag{2.28}$$

$$\pi^{0} \rightarrow \gamma + \gamma. \tag{2.29}$$

Through these decays, both photons and neutrinos are produced. The photons originated from the π^0 decays are highly energetic. This is the reason why $\gamma-$rays and astrophysical neutrinos are thought to be produced in the same interactions in blazar emission. Moreover, both the photons and the leptons produced, can initiate electromagnetic cascades, which develop until the energy of the produced photons does not reach the threshold for pair production. If the magnetic field in the emission region is very intense, as in the case of proton synchrotron, also the synchrotron emission from the secondary pions and muons can play a relevant role in the final output. In addition, also the electrons and positrons generated in the pair production process can undergo synchrotron emission, giving origin to photons which can originate other $e^{-}e^{+}$ pairs. A detailed treatment of the photo-meson process is described in Sect. 6.2.2, where the spectrum of the secondary particles directly produced in pion decay is computed.

Bethe-Heitler pair production

At low energies, the interactions between relativistic protons and soft photons is dominated by the Bethe-Heitler process, which gives:

$$p + \gamma \rightarrow p + e^- + e^+ \,. \tag{2.30}$$

The process is energetically allowed when [108]

$$\gamma_p \varepsilon > m_e c^2, \tag{2.31}$$

with γ_p the proton Lorentz factor, ε the soft photon energy, and m_e the electron mass. The pairs produced in the Bethe-Heitler process are usually energetic enough to initiate electromagnetic cascades. The maximum energy of the produced electron (or positron) is given by the kinematics of the process and results [108]:

$$E_{max,e} = \begin{cases} 4\gamma_p^2 \varepsilon & \text{for } m_e c^2 \ll \gamma_p \varepsilon \ll m_p c^2 \\ \gamma_p m_p c^2 & \text{for } \gamma_p \varepsilon \gg m_p c^2 \end{cases} \,. \tag{2.32}$$

These relations are valid for $\gamma_p \gg 1$ and $\varepsilon \ll \gamma_p m_p c^2$. Moreover, we can see that in the case of $\gamma_p \varepsilon \gg m_p c^2$, the whole energy of the proton is transferred to one of the produced leptons.

If we now consider a distribution of ultrarelativistic protons ($\gamma_p \gg 1$) colliding with a distribution of soft photons, rather than the interaction between single particles, we have that the energy spectrum of the produced electrons (or positrons) is given by [108]:

$$\frac{\mathrm{d}N}{\mathrm{d}E_e} = \frac{1}{2\gamma_p^3} \int_{\frac{(\gamma_p + E_e)^2}{4\gamma_p^2 E_e}}^{\infty} \mathrm{d}\varepsilon \, \frac{f_{ph}(\varepsilon)}{\varepsilon^2} \int_{\frac{(\gamma_p + E_e)^2}{2\gamma_p E_e}}^{2\gamma_p \varepsilon} \mathrm{d}\omega \, \omega \int_{\gamma_p^2 + \frac{E_e^2}{2\gamma_p E_p}}^{\omega - 1} \frac{\mathrm{d}E_-}{p_-} W(\omega, E_-, \xi), \tag{2.33}$$

where E_e is the electron (or positron) energy in the laboratory frame, γ_p is the proton Lorentz factor, $f_{ph}(\varepsilon)$ is the energy distribution of the target soft photons, ε is the energy of the target photons, E_- is the electron (or positron) energy in the proton reference frame, $p_- = \sqrt{E_-^2/c^2 - m_e^2 c^2}$ is the is the momentum modulus of electron in the rest frame of the proton, and $W(\omega, E_-, \xi) = \frac{\mathrm{d}^2\sigma}{\mathrm{d}E_- \mathrm{d}\cos\theta}$ is the cross section of the interaction, given by Eq. 10 of [109], with $\xi \equiv \cos\theta_- = \frac{\gamma_p E_p - E_e}{\gamma_p p_p}$. Finally, $\omega = \mathbf{u_p} \cdot \mathbf{k} = \varepsilon \gamma_p (1 - \cos\theta)$ is the energy of the photon in the the rest frame of the proton. Here θ is the angle between the 4-velocity of the proton $\mathbf{u_p}$ and the 4-momentum of the photon $\mathbf{k}$.

Chapter 3

Monitoring of the blazar TXS 0506+056 with MAGIC and multi-wavelength partners

This chapter focuses on the long-term multi-wavelength monitoring of the blazar TXS 0506+056, which represents a key object in the astrophysical and multi-messenger communities. Indeed, on September 2017, a high-energy neutrino detected by IceCube was found to be spatially and temporally coincident with a long-term flaring activity from this object. This event represents the first association between an astrophysical neutrino and an extragalactic source, boosting the interest in blazars as candidate neutrino emitters and cosmic-ray accelerators.

Before the 2017 event, TXS 0506+056 was a quite unknown object, so very little information is available from previous observations. The only available data prior to 2017 come from survey instruments only, like *Fermi/LAT* or OVRO. The study presented in this chapter collects long-term multi-wavelength data of the source for the first time. The monitoring campaign involves several different instruments operating in all energy bands. It covers the period from November 2017 to February 2020 for the VHE and HE $\gamma-$ray bands, and from November 2017 to February 2021 for X-ray, optical/UV, and radio bands. During the monitored period the source resulted to be mostly in a low state of activity, with two flaring episodes at VHE. Results from this work are published in the conference proceeding [110]. In this project I had an important role in the MAGIC and *Fermi/LAT* data analyses, and writing of the proceeding.

3.1 The blazar TXS 0506+056

The blazar TXS 0506+056 is a BL Lac object located in the Orion constellation at a redshift of $z = 0.336$ [111]. It was discovered by the Texas survey of radio sources [112] in 1983 but has been a poorly studied object until 2017, September 22, when IceCube reported the detection of a high-energy neutrino coming from the direction of the source[1] [3].

The neutrino event, called IceCube-170922A, consisted of a muon track (see Sect. 1.2.1 for more details) traversing the whole detector and depositing an energy of (23.7 ± 2.8) TeV, from which the initial neutrino energy was estimated. It resulted to be 290 TeV, with a 90% confidence level lower limit of 183 TeV, assuming a power-law spectrum for the diffuse astrophysical neutrino flux, with a spectral index of 2.13. The track reported a high probability of being of astrophysical origin, with a signalness of 56.5%. The reconstructed direction points to a region of the sky consistent with the position of the blazar TXS 0506+056, located at 0.1° from the best-fit neutrino arrival direction. The event display of IceCube-170922A is shown in Fig. 3.1a as seen by IceCube DOMs. Thanks to its real-time alert system, IceCube sent a public alert to the whole astrophysical community in the form of a GCN circular[2] encouraging prompt follow-up observations.

Triggered by the neutrino alert, intense multi-wavelength observations from different instruments were performed across the entire electromagnetic spectrum. The source showed an enhanced emission in all energy bands. In particular, the *Fermi/LAT* Collaboration reported a long-term flaring activity with a duration of 6 months. The highest *Fermi* flux above an energy of 100 MeV, integrated on a 7-days bin during the long-term flare, is $(5.3 \pm 0.6) \times 10^{-7}\,\mathrm{cm}^{-2}\,\mathrm{s}^{-1}$, which is almost one order of magnitude larger than the average flux on 9.5 years of observations: $(7.6 \pm 0.2) \times 10^{-8}\,\mathrm{cm}^{-2}\,\mathrm{s}^{-1}$. In VHE $\gamma-$rays, the MAGIC telescopes were the first instruments to detect the source, reporting a 6.2σ excess over the background in 13 hours of observation, and a maximum flux above 90 GeV of $(8.0 \pm 2.0) \times 10^{-11}\,\mathrm{cm}^{-2}\,\mathrm{s}^{-1}$ observed on 2017, October 4, in 0.65 hours. The significance obtained in the latter date is 5.4σ. The MAGIC skymap above 90 GeV is shown in Fig. 3.1b. Several multi-wavelength instruments observed the source finding a high state of emission. Details on the multi-wavelength observations can be found in [3].

With this event, enhanced $\gamma-$ray activity from an astrophysical object was detected for the first time in coincidence with the arrival of a high-energy neutrino. The probability of a chance coincidence between the neutrino detection and the flaring activity of TXS 0506+056 was evaluated and was found to be disfavoured at the 3σ level thanks to the precise determination of the neutrino direction. In addition, the IceCube collaboration performed an archival search on 9.5 years of data, finding an excess of high-energy neutrinos at the position of the blazar between September 2014 and March 2015 [113].

Thus, this events increased the interest of the astrophysical community in blazars

[1] Note that the redshift measurement of the source was performed after 2017 neutrino event.
[2] https://gcn.nasa.gov/circulars

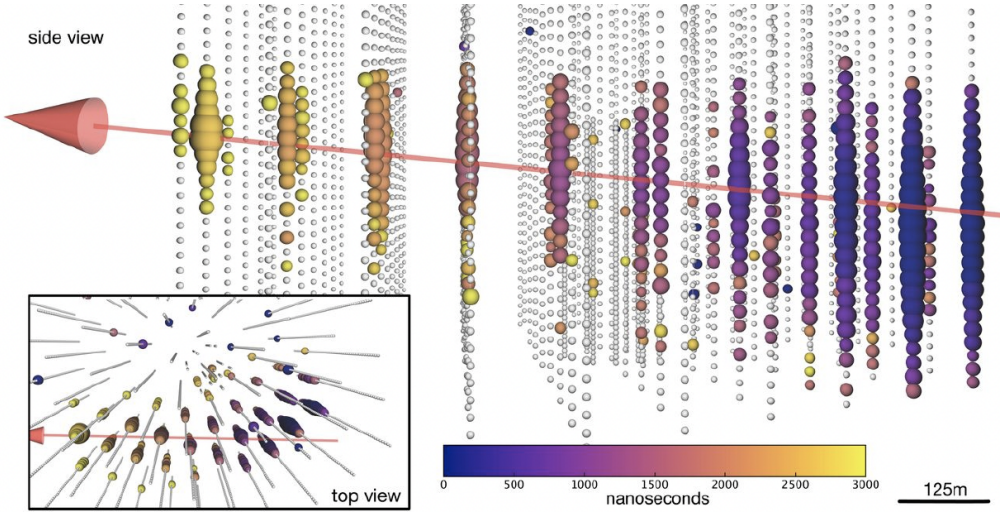

(a)

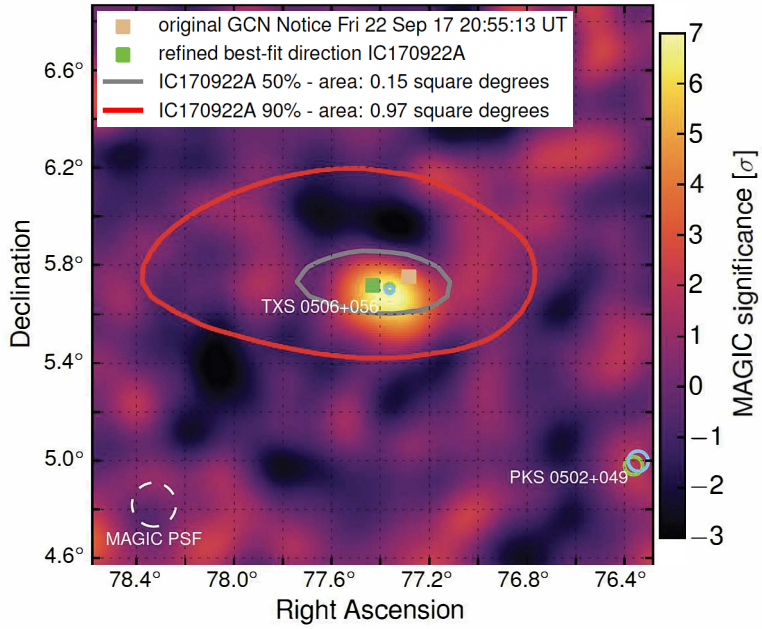

(b)

Figure 3.1: (a) Visualization of the event IceCube-170922A as seen by the IceCube DOMs. Colors indicate the time where they detected the signal, with darker colors corresponding to earlier times, while the dimension of the DOMs indicates the amount of light detected, with larger spheres corresponding to larger signals. (b) MAGIC skymap above 90 GeV for the observation of TXS 0506+056 in October 2017. Credits: [3].

as candidate neutrino emitters. Many models were developed to interpret this multi-messenger observation [114–120]. The MAGIC Collaboration proposed a lepto-hadronic model, based on the so-called *spine-layer structure* [121, 122], considering the jet as composed of a fast moving spine containing accelerated protons and electrons, and an external slower sheath of low-energy photons serving as targets for $p\gamma$ interactions. Indeed, differently from FSRQs, which are usually considered good candidate neutrino emitters thanks to the presence of high-density target photon fields in their environments (e. g. disk, BLR, torus), BL Lacs usually present an environment poor of target photon fields for $p\gamma$ interactions. Therefore, in order to efficiently produce neutrinos, these sources are required to have a high proton power, or, alternatively, a different source of target soft photons.

A working scenario is found by considering a structured jet as described above. Such a structure is also supported by radio observations [123, 124]. The model built in this scenario was in good agreement with the observational data and found that the SED can be mostly described with leptonic processes. In particular, the low-energy bump can be described by the synchrotron emission of relativistic electrons in the spine, while the high-energy peak can be interpreted as inverse Compton emission of the same electrons with the synchrotron radiation emitted by the layer. The hadronic emission is mainly subdominant but it can have a significant contribution in the X-ray and VHE $\gamma-$ray bands, through Bethe-Heitler pair production or photo-meson cascades in the first case and photo-meson cascades only in the second case. Hence, data in these bands became fundamental in distinguishing between leptonic or hadronic emission. Moreover, by assuming a maximum proton energy of $E_{p,max} = 10^{16}$ eV, the model predicts a 90% confidence level lower and upper limits to the neutrino energy consistent with the observed event, and an expected detection rate in the same interval in agreement with the detection of a single neutrino during the period of enhanced $\gamma-$ray activity [114]. In more recent years, the spine-layer structure was observed also for TXS 0506+056, further indicating the neutrino and $\gamma-$ray emission to have a cospatial origin, and strengthening the model built to interpret the data [125, 126].

However, the excess of neutrino event found by IceCube in 2014-2015 data, was not coincident with a flaring $\gamma-$ray activity from *Fermi/LAT* data, so the coincidence of the neutrino and $\gamma-$ray events, as well as the details of the emission are still not fully clear. Therefore, long-term observations of this source are essential to deeply understand the radiative processes at work in the emission, the source duty cycle, and the exceptionality of the 2017 flare.

In this work we show results from a first multi-wavelength monitoring of the source in the long term, collecting 27 months of data in VHE and HE $\gamma-$rays, and 39 months of data from X-rays to radio frequencies. The first 16 months of this dataset were also used in the publication [127], where the authors characterized the low-state of the source for the first time, and found an anti-correlation between flux and spectral index from *Swift/XRT* data in the $2-10$ keV energy band, which is lost when considering the the whole $0.3-10$ keV band observed by *XRT*. This suggests a transition between different radiation mechanisms in X-rays, which is translated into the transition from syn-

	Nov 2017 - Feb 2020	Sep 2019 - Feb 2020
MC periods	ST.03.09 - ST.03.12	ST.03.12
Zenith	$22^\circ - 50^\circ$	$22^\circ - 36^\circ$
Total obs. time	123 h	33 h
Good-quality data	109 h	30.4 h

Table 3.1: Details on monitoring observations of TXS 0506+056. Both the whole dataset from November 2017 to February 2020 and the dataset taken with Sum-Trigger-II, from September 2019 to February 2020, are shown. For each of them we report the Monte Carlo periods involved in the analysis, the zenith angle of the observations, the total observation time, and the observation time obtained after the application of data-quality cuts. The good-quality data thus obtained were then used in the analysis.

chrotron emission by primary electrons to Bethe-Heitler pair production in the considered model. Here, we mainly concentrate on the behaviour of the source emission over time from the longer term observational results.

3.2 Observations and data analysis

In the following, the instruments used in the observations and the techniques used in the analysis are described.

3.2.1 MAGIC data

The MAGIC telescopes took part in the observation campaign for the VHE $\gamma-$ray band. The source is visible from the site of the MAGIC telescopes from September to February, so the observations are concentrated in these months for each year of the monitoring campaign. Data were taken from November 2017, just after the neutrino event, up to February 2020 in wobble mode, with both the standard [30, 37] and Sum-Trigger-II [38, 39] triggers (see Sect. 1.3.4 for more details), and were split into different MC periods, based on the seasonal and technical conditions of the telescopes as described in Sect. 1.3.4. Details on these periods, as well as on the observation time and the zenith angle of the observations are reported in Table 3.1.

I performed the analysis of the data taken from September 2019 to February 2020. The observations in this period were performed with the Sum-Trigger-II system, optimized for low energies, while in the previous periods the standard trigger was used.

All data were analyzed with the MAGIC analysis package MARS, described in Sect. 1.3.4. The data between September 2019 and February 2020, belong to the same MC period, reporting a worsening of the PSF of the telescopes with respect to the previous periods. Since the datataking was performed with the Sum-Trigger-II system, the data had to undergo the MaTaJu cleaning described in Sect. 1.3.5. Good-quality data were then selected by applying a cut on the atmospheric transmission value provided

Cut	Value
Selection	
Transmission	> 0.75
Average current	$> 3000\,\mu$A
Analysis	
size	> 20 phe
hadronness	< 0.28

Table 3.2: Cuts used in data-quality selection and data analysis of TXS 0506+056 during the period from September 2019 to February 2020.

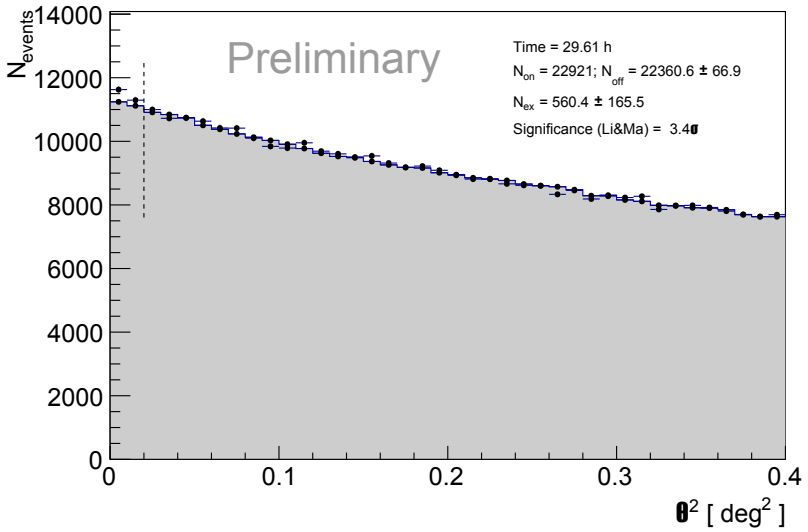

Figure 3.2: θ^2 plot of TXS 0506+056 data, taken in the period between September 2019 and February 2020. The resulting significance is 3.4σ.

by the LIDAR, and a cut on the average current in MAGIC-I camera in order to suppress the NSB. The used cut values are reported in Table 3.2. These selection cuts resulted in a total of 30.4 hours of good-quality data, which were used for the later analysis.

The Sum-Trigger-II analysis follows the procedure described in Sect. 1.3.5, which mainly corresponds to the standard analysis with a lower cut of the images size in order to keep faint signals. After applying the RF, which was previously built using MC data, to the source data, the θ^2 plot on this dataset in the low-energy regime was computed. The signal significance is computed according to [59], as described in Sect. 1.3.4, and it resulted to be 3.4σ for this dataset, suggesting a hint of detection. The cuts used in the analysis are reported in Table 3.2, while the θ^2 plot is shown in Fig. 3.2.

Following, the lightcurve of the source was computed with a night-wise binning,

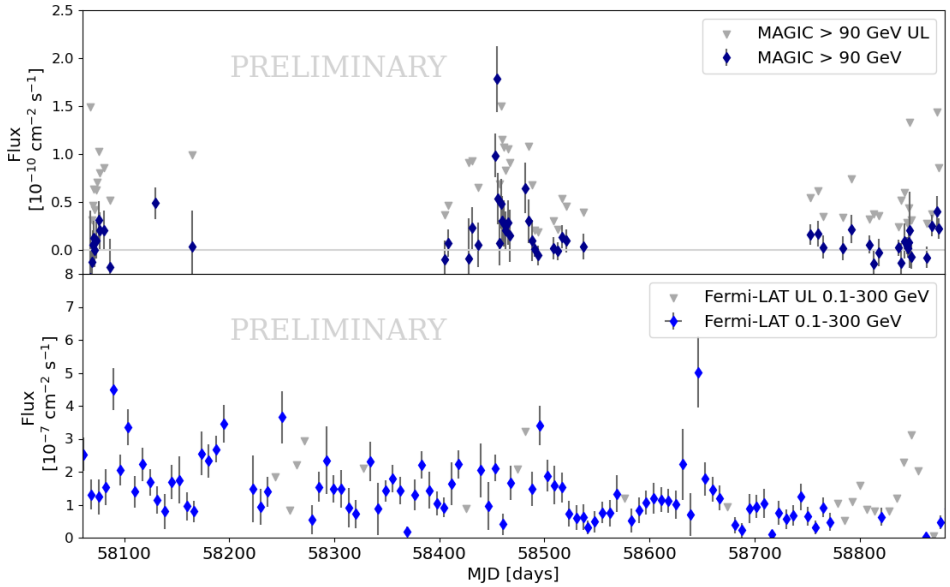

Figure 3.3: Lightcurve from November 2017 to February 2020 for the source TXS 0506+056 from MAGIC (VHE $\gamma-$rays, top panel) and *Fermi-LAT* (HE $\gamma-$rays, bottom panel) instruments. The MAGIC lightcurve is computed in nightly bins, while the Fermi lightcurve in weekly bins.

above an energy threshold of 90 GeV. (see Fig. 3.3). The source spectral shape assumed for the lightcurve computation is a simple power-law with spectral index 3.8, value found from previous observations [114]. For time bins where no significant $\gamma-$ray emission was observed, an UL was computed at the 95% confidence level using the Rolke method [61] (see Sect. 1.3.4). Results show the source to be in a low-state of activity during the analyzed period (upper plot of Fig. 3.3, data from MJD 58753), with an integral flux of $(7.1 \pm 2.7) \times 10^{-12}\,\mathrm{cm}^{-2}\,\mathrm{s}^{-1}$ above an energy threshold of 90 GeV.

Looking at the whole dataset, a total of 109 hours of good-quality data were used in the analysis. The resulting LC shows the source to be in low state of activity during most of the monitored period (about 105 hours), with an enhanced emission on 2018, December 1 and 3 (MJD 58453 and 58455). The VHE fluxes computed in these dates and on the long-term low-state period are reported in Table 3.3.

3.2.2 *Fermi/LAT* data

In HE $\gamma-$rays public data from the *LAT* instrument on board the *Fermi* satellite [63] (see Sect. 1.4.1 for more details) were used. Since *Fermi/LAT* scans the entire sky every three hours, the observations cover the whole monitoring period.

Obs. period	Flux
2018, Dec 1	$(9.8 \pm 2.2) \times 10^{-11}\,\mathrm{cm}^{-2}\,\mathrm{s}^{-1}$
2018, Dec 3	$(1.8 \pm 3.4) \times 10^{-10}\,\mathrm{cm}^{-2}\,\mathrm{s}^{-1}$
Nov 2017 - Feb 2020	$< 1.0 \times 10^{-11}\,\mathrm{cm}^{-2}\,\mathrm{s}^{-1}$

Table 3.3: Results of MAGIC observations on TXS 0506+056 during the whole period, from November 2017 to February 2020. The reported fluxes are computed above an energy threshold of 90 GeV.

I took care of the data taken between January 2019 and February 2020. Data were analyzed using the Fermi Science Tools[3] v.1.2.23 and PASS8 response function (P8R3) [128]. We considered Source class events from all layers of the detector. The selection was made on all data in an energy range of $100\,\mathrm{MeV} - 300\,\mathrm{GeV}$ contained in a ROI of 15° radius centered on TXS 0506+056 position. In addition, a cut of 90° on the zenith angle was put in order to avoid contamination by background $\gamma-$rays coming from the Earth's limb [129]. Good-quality data were then prepared by selecting only those time intervals where *LAT* was in a standard data-taking mode, and excluding those related to particular spacecraft events which could affect the data quality.

A maximum likelihood analysis was performed, providing the best parameters approximating the observed data given an input source model. The model is taken from the *Fermi/LAT* Fourth Source Catalog (4FGL) [66], based on 8 years of data, and includes all point-like and extended sources in the ROI. A contribution to the model is also given by the galactic and isotropic background diffuse emission, which are added thanks to the templates provided by *Fermi*[4]. In order to limit the number of degrees of freedom, during the fitting process we concentrated on the optimization of TXS 0506+056 parameters, leaving them free to vary, together with those modeling the diffuse background components. The spectral functions used to model the sources are those reported in the 4FGL catalog, where, in particular, TXS 0506+056 is described with a LogParabola:

$$\frac{dN}{dE} = N_0 \times \left(\frac{E}{E_b}\right)^{-[\alpha+\beta\ln(E/E_b)]}, \tag{3.1}$$

with the spectral parameters defiend in Sect. 1.4.1. Results from the analysis show an integral flux of $(3.6 \pm 0.3) \times 10^{-8}\,\mathrm{cm}^{-2}\,\mathrm{s}^{-1}$ and a test statistic of 1918 ($\sim 44\sigma$) on the period under consideration.

The source lightcurve was then computed in weekly bins, by applying the same procedure as before in each time bin For those bins where no significant signal is observed, an upper limit is computed. The *Fermi/LAT* lightcurve is shown in Fig. 3.3, together with the MAGIC one.

[3]https://fermi.gsfc.nasa.gov/ssc/data/analysis/software/

[4]https://fermi.gsfc.nasa.gov/ssc/data/access/lat/BackgroundModels.html

3.2.3 Multi-wavelength dataset

The monitoring of TXS 0506+056 involved a lot of other instruments spanning the radio to X-ray bands, in order to have a complete picture of the behaviour of the source over time.

In the **X-ray** band observations were performed with the *XRT* telescope [70] on board the *Neil Gehrels Swift observatory* [68] (see Sect. 1.4.2) and the *NuSTAR* telescope [130], which provided data in the ranges $2 - 10$ keV and $3 - 78$ keV respectively. The observations of both telescopes were organized in order to ensure simultaneity with MAGIC pointings.

In the **ultraviolet** band observations were performed by the *UVOT* telescope [71], another instrument on board the *Swift* satellite. It observed the source simultaneously to XRT in all the available filters (v, b, u, $w1$, $m2$, $w2$), which cover a total range of $1700 - 6500$ Å.

In the **optical** band several instruments observed the source. In particular, public data are taken from the All-Sky Automated Survey for Supernovae project (ASAS-SN) [131], which automatically monitors the entire visible sky every night up to a magnitude of 17 in the V band. ASAS-SN observed the source in the g and V bands. Data were taken and analyzed through their automatic online tool[5]. The source was also monitored by the KVA telescope [132] and the Astronomical Observatory of the University of Siena. Both telescopes coordinated their observations with MAGIC in order to have contemporaneous data. Finally, additional observations with the Rapid Eye Mount telescope (REM) [133, 134] were triggered after the MAGIC flare in December 2018. All the three telescopes took data in the r band. Apart from KVA, which took observations during the whole monitoring period, the other instruments observed in the period from November 2017 to the beginning of 2019.

Also in the **radio** band a lot of different instruments were involved. Since the neutrino event in 2017, observations in this band were intensified. The 40 m telescope at the Owens Valley Radio Observatory (OVRO) took data of TXS 0506+056 at 15 GHz as part of its blazar monitoring program, which started in 2008 [135]. The Australia Telescope Compact Array[6] (ATCA) has been observing the source at multiple frequencies between 5 GHz and 40 GHz since 2009 [136]. Finally, since August 2020, the Effelsberg 100 m radio telescope started a monitoring of the source in the ranges between 19 GHz and 25 GHz, and between 36 GHz and 44 GHz [137].

Results from multi-wavelength observations are shown in Fig. 3.4, from X-ray (top panel) to radio (bottom panel), in the period from November 2017 to February 2021.

[5] https://asas-sn.osu.edu/

[6] It is a radio interferometer composed of 6 radio telescopes with a diameter of 22 m, which can reach baseline lengths up to a maximum of 6 km.

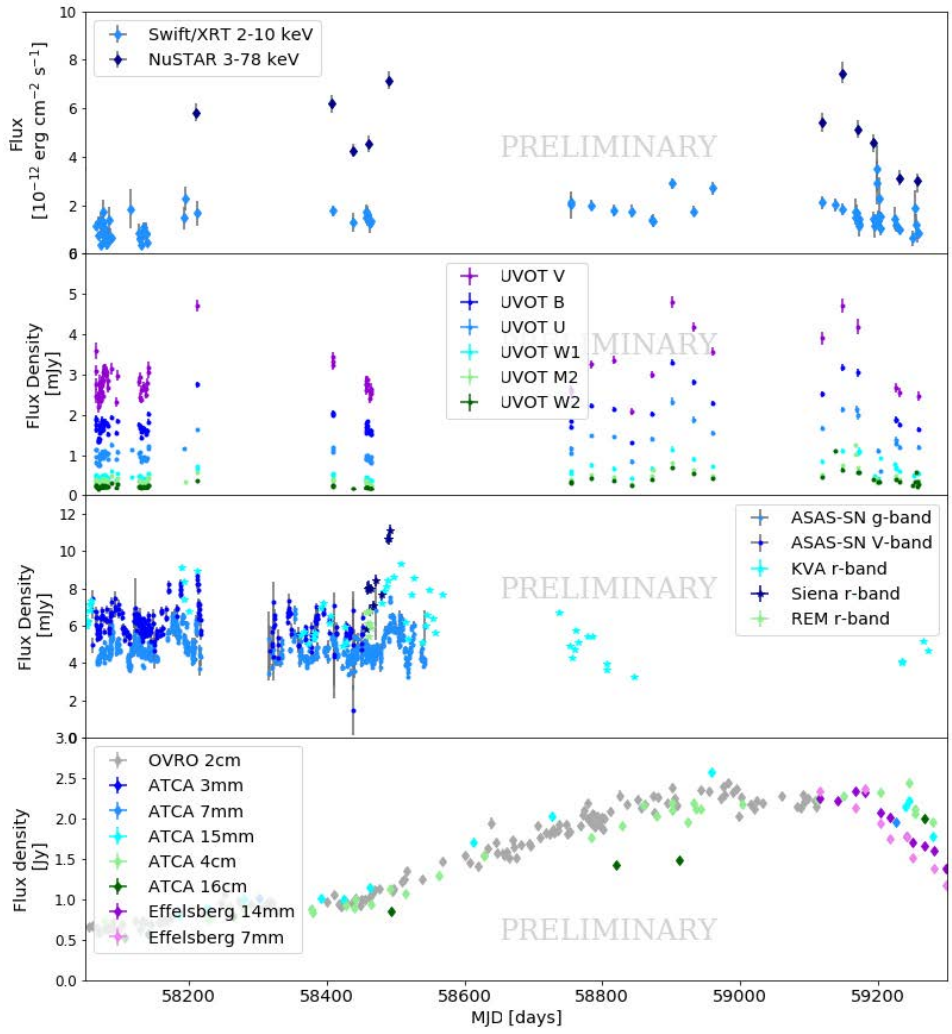

Figure 3.4: Multi-wavelength lightcurve of TXS 0506+056 from Nov 2017 to Feb 2021. From top to bottom the panels show X-ray data (*Swift/XRT*, *NuSTAR*), ultraviolet data (*Swift/UVOT*), optical data (ASAS-SN, KVA, Siena observatory, REM), and radio data (OVRO, ATCA, Effelsberg).

3.3 Results and outlook

This work presents a long-term multi-wavelength campaign on the candidate neutrino blazar TXS 0506+056, which plays a crucial role in establishing connections between high-energy neutrinos and astrophysical objects. TXS 0506+056 was a poorly studied source before the 2017 neutrino event, and this work, complementing the paper [127], is one of the most complete monitoring campaigns of the source.

In VHE $\gamma-$rays (Fig. 3.3, top), TXS 0506+056 shows an emission consistent with a low-state of activity during most of the observations. A flaring activity is registered on 2018, December 1 and 3, where a flux level consistent with the September 2017 flare is detected. However, this more recent flare is not accompanied by any detected neutrino emission.

In HE $\gamma-$rays (Fig. 3.3, bottom), the source appears to be in a very different state with respect to September 2017. During the neutrino emission, the source was experiencing a long-term brightening which lasted multiple months, while results from this campaign show several short flares and a lower average flux from November 2017 until the last months of 2019. In the last period of the campaign the source emission changed to a low-state of activity, the duration of which could be proved only with additional observations.

In the other bands (Fig. 3.4) we observe a moderate variability, with a decay trend in X-rays and UV in 2020-2021. However, in these bands, no significant flares are detected. In radio a long-term rising trend is observed, starting from the period around the 2017 neutrino event and lasting more than two years. During this phase the radio flux density increased from $\sim$ 600 mJy to more than 2000 mJy in all the observed bands but the low-frequency 16 cm band observed by ATCA, where the rising trend is slower and never reached the same absolute maximum of the other frequency ranges. This behaviour transitioned into a plateau at the end of 2019, which lasted until the end of 2020, when the source experienced a steep flux decay continuing until February 2021, namely the end of the monitoring program.

To conclude, this work represents one of the most complete monitoring campaigns of the source TXS 0506+056, collecting more than two years of data from radio to VHE. However, since this object started to be deeply studied only after the 2017 neutrino event, we are far from understanding its duty cycle and the precise processes at work in the emission, for which additional observations in the coming years are needed. In particular, collecting more data can provide insights into multi-wavelength correlations, the investigation of which would be of great help in shedding light on the zones where the emission in the various bands comes from. For example, the radio trend seems to be completely uncorrelated from the behaviour in the other bands, but, the physical zones related to radio emission are usually different from the ones contributing to higher energies. Thanks to intra-band correlations, similar conclusions can be drawn on the emission in other frequency ranges.

Chapter 4

Candidate neutrino-emitting blazars sharing physical properties with TXS 0506+056

TXS 0506+056 is the first potential neutrino-blazar ever detected. This source is classified as a BL Lac object of the IBL type, making it neither one of the most powerful blazars, nor one with the peaks at the highest energies and placing it in the middle of the blazar sequence [95, 96]. As already introduced in Sect. 3.1, although the developed emission models are in agreement with the 2017 observational data, the details of the neutrino production and the nature of the source are not yet fully understood. Moreover, despite the observational differences between FSRQs and BL Lacs[1], the division between the two sub-classes is not sharp and the classification of a single blazar is often not straightforward. Indeed, TXS 0506+056, which is usually referred to as a BL Lac object, was suggested to have a potential FSRQ nature in the last years [138].

The work presented in this chapter aims at investigating the properties of a sample of blazars with observational features similar to TXS 0506+056, especially regarding their accretion flow and jet emission. The objective is a better understanding of their nature as FSRQs or BL Lacs and their multi-messenger role as potential neutrino emitters. Our results suggest most of the candidates to potentially be masquerading BL Lacs, presenting VHE and neutrino fluxes not detectable by the current and future instruments in an average emission state.

Results from this project have been published in the proceeding [139] and a paper is currently in preparation [140]. In this work I had a central role on different aspects.

[1]For example the presence of lines in their optical spectra, the position of the peaks in their SED, or their Compton dominance.

I performed the selection of the candidate sources, investigated the reliability of their redshift, discarding those objects with an unreliable redshift, and further filtered the sample based on information on the emission lines in their optical spectra. Then I worked on the estimation of the sources accretion rate, based on the information on spectral lines above cited, and on the *Swift* analysis of all publicly available data. Finally, I also had an important role in the project organization, and writing of the paper. The following chapter is adapted from the aforementioned paper.

4.1 Selection of candidates

The candidates have been selected from the second release of the Fourth Catalog of *Fermi/LAT* Active Galactic Nuclei (4LAC-DR2) [141, 142], based on the second release of the Fourth *Fermi/LAT* catalog (4FGL-DR2) [66, 143]. The 4FGL-DR2 contains γ-ray sources detected in the energy range from 50 MeV to 1 TeV in the first 10 years of Fermi activity, from 2008 to 2018. The 4LAC catalogs have been developed to identify counterparts to 4FGL γ-ray sources, the position of which is associated with objects showing AGN-type spectral features in different wavebands. The new catalogue contains 285 additional AGNs with respect to the first release, the majority of which are blazars. In particular, the 4LAC-DR2 contains 689 FSRQs, 1111 BL Lacs, 1277 blazar candidates of unknown type and 70 non-blazar AGNs.

By taking into account all blazars in the catalog with a known redshift, the luminosity of each object was derived using the relation:

$$L_\gamma = 4\pi d_L^2 \frac{S_\gamma(\nu_1, \nu_2)}{(1+z)^{1-\alpha_\gamma}}, \tag{4.1}$$

where $(1+z)^{1-\alpha_\gamma}$ is the redshift correction, with z the redshift and $\alpha_\gamma = \Gamma_\gamma - 1$ the spectral index in the $\gamma-$ray band; d_L is the luminosity distance[2], depending on the redshift [144, 145] and computed through `astropy`[3]. Both z and α_γ are measured values taken from the 4LAC-DR2 catalog. The term $S_\gamma(\nu_1, \nu_2)$ in Eq. 4.1 is the $\gamma-$ray energy flux between the frequencies ν_1 and ν_2 and it is computed as in [146] through the relation:

$$S_\gamma(\nu_1, \nu_2) = \begin{cases} \frac{\alpha_\gamma h \nu_1 F_\gamma}{1-\alpha_\gamma} \left[\left(\frac{\nu_2}{\nu_1} \right)^{1-\alpha_\gamma} - 1 \right] & \text{if } \alpha_\gamma \neq 1 \\ h \nu_1 F_\gamma \ln \left(\frac{\nu_2}{\nu_1} \right) & \text{if } \alpha_\gamma = 1 \end{cases}, \tag{4.2}$$

where F_γ is the photon flux between ν_1 and ν_2. In this specific case, the computation was done using the value of F_γ reported in the catalog for each source, which is estimated in the energy range $1 - 100$ GeV, so the values of ν_1 and ν_2 considered here are the corresponding frequencies of this energy range.

[2]It is defined by the relation $f = L/(4\pi d_L^2)$, where f is the bolometric flux of the source and L its bolometric luminosity.

[3]https://docs.astropy.org/en/stable/cosmology/index.html

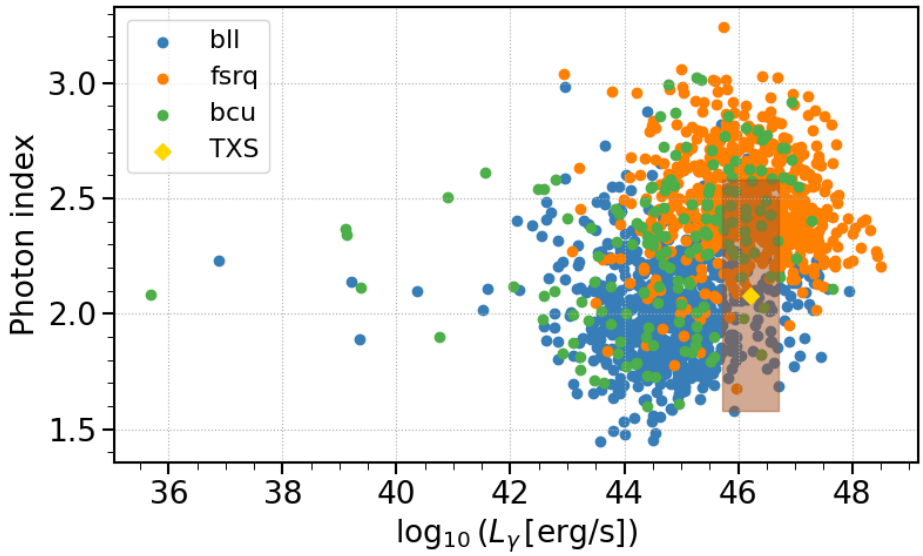

Figure 4.1: Photon index Γ_γ versus γ-ray luminosity L_γ of all sources in 4LAC-DR2 with known redshift. The legend reports: BL Lacs (bll), FSRQs (fsrq), blazar candidate of unknown type (bcu) and TXS 0506+056 (TXS). The brown box indicates the range used for the selection parameters Γ_γ and L_γ. Error bars have been omitted for clarity.

The luminosity distribution of the blazars in the catalog is shown in Figures 4.1 and 4.2, displaying the photon index Γ_γ of the sources as a function of their $\gamma-$ray luminosity and the luminosity histogram of the candidates. From these plots a clear division between the two blazar subclasses can be observed, with FSRQs tending to have higher values of both Γ_γ and L_γ with respect to BL Lacs. In both plots, TXS 0506+056 lies in the overlapping region of the FSRQ and BL Lac distributions, suggesting a complex classification of the source, although in the catalog it is classified as a BL Lac object. Indeed the nature of this source is not firmly established and it was also suggested to be an FSRQ in the work of [138]. Thus, its nature is not fully understood and it may have transitional properties between the two subclasses of blazars.

Motivated by these arguments, we performed a selection based on parameters directly related to the physics governing the sources and, consequently, on their classification into FSRQs and BL Lacs. The chosen parameters are the γ-ray photon index, the integral luminosity in $1 - 100$ GeV range and the frequency of the synchrotron peak. The photon index and the synchrotron peak frequency were extracted directly from the catalog, while the luminosity was derived as described above. Note that, since the luminosity was chosen as a selection parameter, all sources without a known redshift are excluded a priori from the selection. The chosen parameters were constrained to be

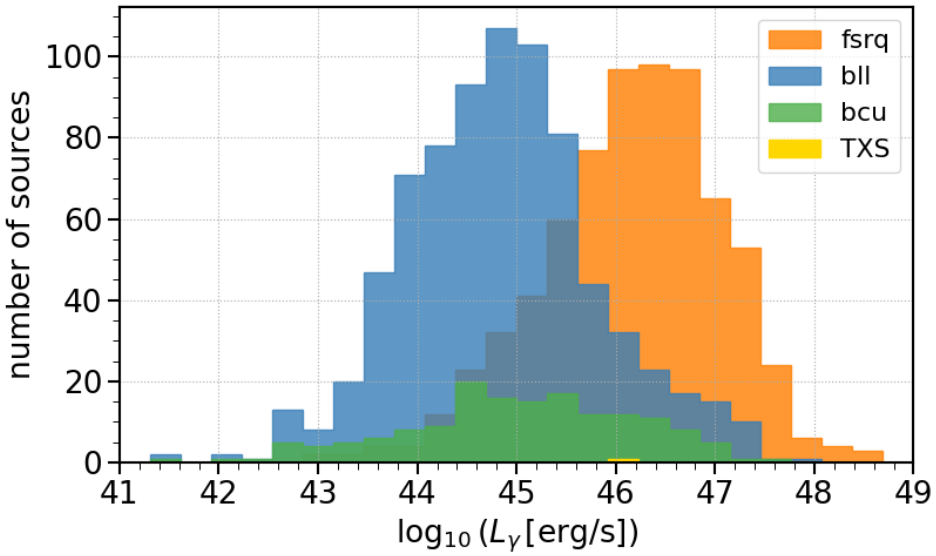

Figure 4.2: Luminosity histogram of all sources in the 4LAC-DR2 catalog with known redshift. The legend is the same as in Fig. 4.1. The bin width is 0.3.

close to those of TXS 0506+056 within the following defined ranges:

$$\Gamma_{\gamma,TXS} - 0.5 < \Gamma_\gamma < \Gamma_{\gamma,TXS} + 0.5,$$
$$\log_{10}(\mathrm{L}_{\gamma,TXS}) - 0.5 < \log_{10}(\mathrm{L}_\gamma) < \log_{10}(\mathrm{L}_{\gamma,TXS}) + 0.5,$$
$$\log_{10}(\nu_{S,TXS}) - 0.7 < \log_{10}(\nu_S) < \log_{10}(\nu_{S,TXS}) + 0.7,$$

where $\Gamma_{\gamma,TXS} = 2.079 \pm 0.014$, $\nu_{S,TXS} = 3.55 \times 10^{14}$ Hz, and $\mathrm{L}_{\gamma,TXS} = (1.62 \pm 0.04) \times 10^{46}$ erg/s are referred to TXS 0506+056[4]. The ranges for Γ_γ and L_γ are displayed in Fig. 4.1. The sample resulting from this selection contains 27 sources, most of which are blazars and, in particular, BL Lac objects. The full list of the selected sources can be found in Table 4.1.

4.1.1 Resulting sample

Since the aim of this work is to find a sample of sources with similar physical properties to TXS 0506+056, we intend to give an estimation of the accretion rate of the candidates. For the computation of this quantity we need not only the redshift value of the candidates but also information on the emission lines in their optical spectra, in particular the luminosity of the lines.

Starting from the sources in Table 4.1, we thus applied a further selection aimed at keeping only the objects with a detailed spectral analysis in the optical and/or ultraviolet band. For each object we performed a search in the literature to inspect the reliability

[4]Note that the 4LAC-DR2 catalog does not report an error on the synchrotron peak frequency.

4LAC-DR2 name	Photon Flux [10^{-10} cm^{-2}s^{-1}]	Photon index	Type	Redshift	SED class	ν_S [10^{14} Hz]	L_γ [10^{46} erg/s]	Spectral analysis	Refs.
4FGLJ0004.0+0840	1.9 ± 0.4	2.04 ± 0.13	bll	2.057	ISP	3.02	4.3 ± 0.8	z ll	[147]
4FGLJ0035.2+1514	11.6 ± 0.7	1.9 ± 0.04	bll	1.090	ISP	9.71	5.9 ± 0.4	z ll	[148]
4FGLJ0050.7-0929	$\mathbf{39.27 \pm 1.12}$	$\mathbf{2.016 \pm 0.018}$	**bll**	**0.635**	**ISP**	**1.32**	$\mathbf{4.77 \pm 0.15}$	**yes**	[147]
4FGLJ0114.8+1326	$\mathbf{11.1 \pm 0.6}$	$\mathbf{2.11 \pm 0.04}$	**bll**	**0.583**	**ISP**	**6.31**	$\mathbf{1.02 \pm 0.06}$	**yes**	[149]
4FGLJ0153.9+0823	16.2 ± 0.8	1.95 ± 0.03	bll	0.681	ISP	8.91	2.45 ± 0.14	z only	[150]
4FGLJ0253.2-0124	2.9 ± 0.4	2.07 ± 0.10	bll	1.480	ISP	2.24	2.8 ± 0.4	no	—
4FGLJ0434.1-2014	3.4 ± 0.4	2.27 ± 0.08	bll	0.928	ISP	1.12	0.92 ± 0.11	z only	[150]
4FGLJ0509.4+0542	$\mathbf{80.2 \pm 1.6}$	$\mathbf{2.079 \pm 0.014}$	**bll**	**0.3365**	**ISP**	**3.55**	$\mathbf{2.00 \pm 0.05}$	**yes**	[111, 147]
4FGLJ0528.7-5920	2.8 ± 0.3	2.06 ± 0.09	bll	1.13	HSP	15.85	1.39 ± 0.17	no	—
4FGLJ0849.5+0456	5.4 ± 0.5	2.08 ± 0.07	bll	1.06959	ISP	2.45	2.30 ± 0.24	no	—
4FGLJ0908.9+2311	4.8 ± 0.5	1.82 ± 0.07	bll	1.184	ISP	5.07	3.1 ± 0.3	z only	[150]
4FGLJ0921.7+2336	3.6 ± 0.4	2.06 ± 0.09	bll	1.062	ISP	2.00	1.54 ± 0.18	no	—
4FGLJ1003.4+0205	1.5 ± 0.3	2.03 ± 0.15	bcu	2.075	ISP	5.72	3.5 ± 0.7	no	—
4FGLJ1103.0+1157	12.2 ± 0.6	2.41 ± 0.03	fsrq	0.914	ISP	1.27	3.04 ± 0.16	no	—
4FGLJ1107.8+1501	5.8 ± 0.5	1.95 ± 0.06	bll	0.6	ISP	3.63	0.65 ± 0.06	z only	[150]
4FGLJ1155.8+6137	0.87 ± 0.21	1.85 ± 0.16	bll	1.525	ISP	2.66	1.00 ± 0.26	no	—
4FGLJ1213.6+1306	6.1 ± 0.5	2.47 ± 0.05	fsrq	1.14	LSP	0.87	2.73 ± 0.24	z only	[151]
4FGLJ1215.1+5002	3.9 ± 0.4	1.88 ± 0.07	bll	1.545	ISP	7.94	4.5 ± 0.4	no	—
4FGLJ1245.1+5709	3.6 ± 0.3	2.13 ± 0.07	bll	1.545	ISP	7.94	3.8 ± 0.3	no	—
4FGLJ1253.8+6242	4.1 ± 0.3	1.99 ± 0.06	bll	0.867	LSP	0.09	1.10 ± 0.10	z only	[150]
4FGLJ1309.4+4305	$\mathbf{16.4 \pm 0.7}$	$\mathbf{1.90 \pm 0.03}$	**bll**	**0.691**	**ISP**	**5.19**	$\mathbf{2.68 \pm 0.13}$	**yes**	[147]
4FGLJ1459.0+7140	2.94 ± 0.28	2.50 ± 0.06	css	0.91	ISP	3.83	7.12 ± 0.07	z only	[151]
4FGLJ1509.7+5556	3.4 ± 0.3	1.88 ± 0.07	bll	1.68	ISP	1.41	4.9 ± 0.5	no	—
4FGLJ1530.9+5736	2.23 ± 0.28	2.06 ± 0.09	bll	1.1	ISP	2.00	1.04 ± 0.14	no	—
4FGLJ2116.2+3339	34.3 ± 1.1	1.900 ± 0.021	bll	0.35	ISP	7.94	1.13 ± 0.04	z ll	[152]
4FGLJ2145.5+1006	1.0 ± 0.3	1.79 ± 0.18	bll	2.826	ISP	1.82	5.1 ± 1.7	no	—
4FGLJ2156.9-0854	2.7 ± 0.4	2.09 ± 0.10	bll	1.017	ISP	1.74	1.03 ± 0.16	no	—

Table 4.1: Parameters of the 27 selected sources. All parameters except the luminosity are directly extracted from the 4LAC-DR2 catalog. The columns report: name of the source from the catalog, photon flux, photon index, source type (bll = BL Lac object, fsrq = Flat Spectrum Radio Quasar, bcu = blazar candidate unknown, css = Compact Steep Spectrum radio source), redshift, SED class, frequency of the synchrotron peak, luminosity in 1 - 100 GeV energy range, information on spectral analysis in the literature (z ll = redshift lower limit, z only = only redshift value provided, yes = both redshift and information on spectral lines provided), and related references. The sources highlighted in bold represent those included in the final sample (see Sect. 4.1.1).

of the redshift value reported in the 4LAC-DR2 catalog and the presence of information on the emission lines. Details are reported in the last column of Table 4.1 and listed in the following. We found that almost half of the sources in the sample (13 objects) do not report any optical/UV spectral analysis in the literature; 7 sources have a reliable redshift but no detailed information on their spectral lines is reported. In particular, one of them went out of the selection after the redshift inspection (4FGL J0908.9+2311): the redshift reported in the catalog for this source is $z = 1.184$, while the one provided in the reference [150] is $z = 0.431$. With this new value, the luminosity of the source does not lie anymore in the range defined for the selection. Within the remaining 7 sources, 3 just provide a redshift lower limit given by the absorption lines of the host galaxy. Finally, there are 4 sources, including TXS 0506+056, showing a detailed optical/UV spectral analysis. All of them are classified as BL Lac objects. Our work is then based on these 4 sources, namely 4FGL J0509.4+0542, 4FGL J0050.7-0929, 4FGL J1309.4+4305, 4FGL J0114.8+1326. In Table 4.2, for each of them, we report the selection parameters (photon index Γ_γ, synchrotron peak frequency ν_S, luminosity L_γ) as derived from the 4LAC-DR2 catalog, together with the information on their redshift and spectral lines and the related references. We also report the associated counterpart. Throughout the chapter, we will refer to each of them using the counterpart name.

4.2 Estimation of accretion rate

From the optical/UV spectral observations, we are interested in the luminosity of the emission lines, which can be exploited to recover different useful quantities such as the photon energy density in the broad line region (BLR) and in the torus (see Sect 4.4), or the accretion rate. In this section we give an estimate of the accretion rate of the candidates in order to understand if they could share the same accretion mechanism and the same nature as typical BL Lac type objects.

Starting from the luminosity of the lines we extrapolated the luminosity of the BLR of the source through the use of the lines ratios reported in Table 1 of [153], where the authors estimate the strength of the emission lines with respect to the lyα line (to which a reference value of 100 is assigned) in a composite spectrum of > 700 quasars. These ratios are used to estimate L_{BLR} through the relation

$$L_{BLR} = \sum_i L_{i,obs} \frac{\langle L^*_{BLR} \rangle}{\sum_i L_{i,est}}, \tag{4.3}$$

reported in Eq. 1 of [154], where $L_{i,obs}$ is the observed luminosity, $L_{i,est}$ is the line ratio and $\langle L^*_{BLR} \rangle$ is the sum of the ratios. Since one of our sources shows Hα emission, we added this contribution (not included in the list of [153]) to the line ratios, as it was done in [154]. The BLR luminosity is a reliable tracer of the disk emission, since the broad emission lines observed in the spectrum arise from the plasma directly ionized by the disk radiation. Thus, we estimated the luminosity of the accretion disk assuming a that the BLR reprocesses about 10% of the disk emission: $L_{disk} \simeq 10\, L_{BLR}$. Finally, from the disk luminosity, we recovered the accretion rate, defined as the quantity of matter

Source	Alias	Γ_γ	ν_S [10^{14} Hz]	L_γ [10^{46} erg s^{-1}]	z_{ref}	Emission lines	L_{lines} [10^{41} erg s^{-1}]	Refs.
4FGL J0509.4+0542	TXS 0506+056	2.079 ± 0.014	3.55	2.00 ± 0.05	0.3365	[O II] [O III] [N II]	1.0 0.05 0.05	[111, 147]
4FGL J0050.7-0929	PKS 0048-09	2.016 ± 0.018	1.32	4.77 ± 0.15	0.635	[O II] [O III] Hα	1.0 0.94 1.6	[147]
4FGL J0114.8+1326	GB6 J0114+1325	2.11 ± 0.04	6.31	1.02 ± 0.06	0.685	Hβ [O III]	124 245	[149]
4FGL J1309.4+4305	B3 1307+433	1.90 ± 0.03	5.19	2.68 ± 0.13	0.693	[O II] [O III]	20.0 5.5	[147]

Table 4.2: Final sample of selected sources with information on selection parameters as extracted or derived from the 4LAC-DR2 catalog, their redshift and emission lines. The columns are: source name, associated counterpart name, photon index, synchrotron peak frequency, luminosity, redshift found in the literature, emission lines observed in the optical spectrum, luminosity of each line, and references. Note that the luminosity is derived using the redshift reported in 4LAC-DR2 catalog.

Source	L_{BLR} [erg s^{-1}]	L_{disk} [erg s^{-1}]	$\dot{m}_{low}$	$\dot{m}_{high}$
TXS 0506+056	2.55×10^{43}	2.55×10^{44}	1.96×10^{-2}	1.96×10^{-1}
PKS 0048-09	2.42×10^{42}	2.42×10^{43}	1.86×10^{-3}	1.86×10^{-2}
GB6 J0114+1325	3.66×10^{44}	3.66×10^{45}	2.82×10^{-1}	2.82
B3 1307+433	3.39×10^{44}	3.39×10^{45}	2.61×10^{-1}	2.61

Table 4.3: Estimated values of BLR luminosity, disk luminosity and accretion rate.

accreted by the black hole per unit of time and given by $\dot{M} = L_{disk}/(\eta c^2)$, with η the accretion efficiency. In terms of the Eddington luminosity, the accretion rate becomes:

$$\dot{m} = \frac{1}{\eta}\frac{L_{disk}}{L_{Edd}}, \tag{4.4}$$

where $L_{Edd} = 1.3\times10^{38}\frac{M}{M_\odot}\frac{\text{erg}}{\text{s}}$, and η is assumed to be $\eta = 0.1$ for black holes. Since we do not know the exact value of the black hole mass, we assumed the two reasonable values $M_{BH} = 10^8$, $10^9\,M_\odot$ in order to define a possible range in which the accretion rate can lie. The results we found are summarized in Table 4.3.

Despite the expectations, we can see that the recovered accretion rates are quite different from source to source. Taking into account the division proposed by [84], we suppose a separating value between FSRQs and BL Lacs of $\dot{m}_d \sim 5\times10^{-3}$, assuming that the FSRQs have a higher $\dot{m}$ value while BL Lacs have a lower one. From our results, we can see that the values found for B3 1307+433 and GB6 J0114+1325 lie well above the dividing value, suggesting a radiatively efficient accretion regime. The same applies for TXS 0506+056, for which we found values slightly larger than the one found in Padovani et al. [138] and being thus in line with the results of this work. The recovered values are one order of magnitude lower than the ones of the two previous sources but still consistent with an efficient accretion regime. For PKS 0048-09 the situation seems more complex, since the recovered values for this source lie around $\dot{m}_d$, so we cannot make any strong conclusion about the possible classification of this object.

4.3 Instruments involved and analysis

For each source, public data from *Swift/UVOT*, *Swift/XRT* and *Fermi/LAT* were analyzed. The aim is to build and then model the SED of each candidate by using data taken contemporaneously. For this reason, we firstly computed the candidates lightcurves in order to identify eventual quiescent and flaring states of activity. Then, identified them, we chose periods for both low and high states which present contemporaneous multi-wavelength data. Having contemporaneous data is necessary in order to build a SED where the emission comes from the same mechanisms in the source environment. In the following, a description of the instruments involved and the analysis techniques used, together with results for each single source is reported.

4.3.1 *Fermi/LAT* data

In HE $\gamma-$rays public data from *Fermi/LAT* were analyzed [63]. A dedicated analysis was performed for each selected source using 12 years of LAT observations taken between 2008, August 4 and 2020, August 4. Following, the analysis was repeated on the smaller time intervals we identified based on the $\gamma-$ray and multi-wavelength activity of the selected sources as explained above.

The analysis was performed with `Fermipy`[5] v1.0.1 [65], the Fermi Science Tools[6] v.2.0.8 and PASS8 response function (P8R3). The data selection was made by using P8R3 (v3) Source class events [128], in the energy range $100\,\mathrm{MeV} - 1\,\mathrm{TeV}$, in a ROI of 15° radius centered on the source position. Different cuts were applied on the zenith angle in order to limit the contamination from background γ-rays from the Earth's limb [129]. In particular, for energies $E < 300\,\mathrm{MeV}$ events with zenith $z_d > 85^\circ$ were excluded, for energies $300\,\mathrm{MeV} - 1\,\mathrm{GeV}$ the cut is put on $z_d > 95^\circ$, while for $E > 1\,\mathrm{GeV}$ on $z_d > 105^\circ$.

A count map with a pixel size of 0.1° was created. A model is also created to describe the sky, which includes al point-like and extended sources in the 4FGL-DR2 [66, 143] catalog located within 15° from the source position, and the galactic and isotropic diffuse emission[7]. In the analysis, the spectral parameters of the sources located within 3° from the target and the normalization of the background emission were left free to vary, while for the sources within $3^\circ - 5^\circ$ distance only the normalization was allowed to vary. The parameters of the source at a larger distance from the target were kept fixed. The spectrum of the sources was modeled with the same functions as in 4FGL-DR2. For GB6 J0114+1325 a PowerLaw was used:

$$\frac{dN}{dE} = N_0 \times \left(\frac{E}{E_b}\right)^{-\Gamma}, \tag{4.5}$$

while for the others a LogParabola was adopted:

$$\frac{dN}{dE} = N_0 \times \left(\frac{E}{E_b}\right)^{-[\alpha+\beta\ln(E/E_b)]} \tag{4.6}$$

(see Sect. 1.4.1 for parameters definition). This procedure was applied firstly to create the sources lightcurve, with time bins of two months, for each time bin, and then to compute their SEDs is the chosen time periods.

4.3.2 *Swift/XRT* data

In X-ray public data from *Swift/XRT* [70] were analyzed in the energy range $0.2 - 10\,\mathrm{keV}$. Firstly, a dedicated analysis of each selected source using all available observations was performed in order to compute their daily lightcurve. Then, the analysis was repeated

[5]http://fermipy.readthedocs.io/en/latest/, it is a python library which makes use of the Fermi Science Tools.

[6]https://fermi.gsfc.nasa.gov/ssc/data/analysis/software/

[7]https://fermi.gsfc.nasa.gov/ssc/data/access/lat/BackgroundModels.html

Source	$E(B-V)$
PKS 0048-09	0.0274 ± 0.0008
GB6 J0114+1325	0.0261 ± 0.0016
B3 1307+433	0.0168 ± 0.0006

Table 4.4: Values of the colour excess for each candidate.

on smaller time intervals selected based on the activity of the source, integrating all observations in the chosen interval in order to recover the sources spectrum. Data from the sources were analyzed by using the `HEASOFT` v. 6.29 and `XSPECv.12.12.0g` software packages.

All *XRT* observations were performed in photon counting mode [72] and each spectrum was rebinned in energy in order to have at least 25 counts per bin to apply the χ^2 test. In one case, namely for the source GB6 J0114+1325, the counts were not sufficient, so the spectrum was rebinned with 4 counts per bin and the Cash statistic [73] was used. All *XRT* spectra were then modeled with an absorbed power-law, defined by $N(E) = K\,E^{-\Gamma_X}\,E^{-n_H\sigma_{abs}}$ (see Sect. 1.4.2 for the definition of the spectral parameters), where the Galactic column density was measured according to [74] and kept fixed in the fit.

4.3.3 *Swift/UVOT* data

In the optical/UV band simultaneous *UVOT* observations were performed during the *XRT* pointings. *UVOT* observed in all available filters (v, b, u, $w1$, $m2$, $w2$), covering the range $1700 - 6500$ Å, for each source. Data were analyzed using the 20201215 CALDB-UVOTA release of the calibration database.

For each filter, we summed the available images and applied the aperture photometry technique in order to recover the magnitude of the candidates. This was done firstly for images taken in single observation dates to build the source lightcurve and then on all those taken in the selected periods to build the sources SED, contemporaneous to the other multi-wavelength data.

For each candidate, the source counts were extracted from a circular region centered on the source, with a radius of 5 arcsec; while background counts were obtained from a circular region of $40 - 60$ arcsec radius located in a source-free area. The magnitudes were computed in the Vega system and then corrected for Galactic extinction, given by the relation $A_\lambda = E\,(B-V)\,[a_\lambda R_v + b_\lambda]$ [76] as described in Sect. 1.4.2. The colour excess $E(B-V)$ was recovered according to [155] and is reported in Table 4.4 for each source, while the other coefficients are measured in [76] and reported in Table 1.5. The corrected magnitudes were finally converted into energy fluxes by using the parameters in [75], reported in Table 1.4.

4.3.4 Analysis results

In the following we report the results from our *Swift* and *Fermi* analyses. As already mentioned, we firstly recovered the sources multiwavelength emission over time and then built their SED in specific time intervals defined by the candidates state of activity. Among our sources, B3 1307+433 and GB6 J0114+1325 do not show clear low and flaring states in their lightcurves, so for these sources we just created a SED in their average state. The source PKS 0048-09 is the only one for which we defined both a low and a high state period, given that it is the only source in our sample showing signs of flaring activity. For all sources, the spectral results from *Fermi/LAT* and *Swift/XRT* analyses have been collected in Tables 4.5 and 4.6 respectively, while the magnitudes obtained from *UVOT* analysis in Table 4.7. The recovered multi-wavelength SEDs for each source in the selected periods are shown in Fig. 4.4.

PKS 0048-09

The source has been observed by *Swift* 9 times between 2008, June 4 and 2012, January 13 with both *XRT* and *UVOT*. The multiwavelength lightcurve of the source is quite peculiar, since it shows three flares in the three analyzed bands (*Fermi/LAT*, *Swift/XRT*, *Swift/UVOT*) which are not coincident in time. Indeed they happened in different periods and do not correspond to the brightest activity on the other bands, so it is not easy to define a unique high state of activity for the source. The *Fermi/LAT* flare has no coincident *Swift* simultaneous observations, so we cannot say anything about the source activity in the other bands in that period and cannot consider it to build the simultaneous high-state SED of the source. Regarding the brightest *XRT* flare, it happened in May−June 2009 and is not coincident with the brightest activity in *UVOT* band. The same happens for the *UVOT* flare in December 2011−January 2012: it corresponds to a relatively high activity of the source in the X-ray band, but not to the brightest X-ray flare.

We finally decided to consider as high state a period of few months coincident with the *UVOT* flare because of the slightly higher LAT flux in that period. The full period we considered for *Fermi-LAT* analysis in the high state ranges from 2011, November 15 to 2012, January 24. Instead, for the low state we considered the period between 2009 September 26 and 2011 February 8, containing two *Swift* pointings. Given the peculiarity of the source emission over time, we also report its full multi-wavelength lightcurve (see Figure 4.3).

For *XRT* and *UVOT* analyses, we summed all data from observations in the chosen periods. For both the high and low states, the spectral parameters obtained from *XRT* analysis, together with the n_H value and the total exposure time of the observation are reported in Table 4.6, while the magnitudes recovered through *UVOT* analysis are reported in Table 4.7. For *Fermi/LAT* analysis, data in the selected periods were integrated and the obtained spectral parameters can be found in Table 4.5. This table shows also the results for the analysis on 12 years of *Fermi/LAT* data, which was used to build the lightcurve. In this period, the source significantly detected (TS $=$ 7500, corresponding

Source	Period	MJD	TS	Flux	Spectral values
PKS 0048-09	12 years	54682 − 59065	7500	3.31±0.15	$N_0 = 4.97 \pm 0.12$; $\alpha = 1.91 \pm 0.02$; $\beta = 0.062 \pm 0.010$
	quiescent	55100 − 55600	610	2.04±0.34	$N_0 = 8.11 \pm 1.14$; $\alpha = 1.97 \pm 0.11$; $\beta = 0.044 \pm 0.005$
	high	55880 − 55950	230	6.00±1.22	$N_0 = 3.30 \pm 0.26$; $\alpha = 1.92 \pm 0.09$; $\beta = 0.089 \pm 0.040$
B3 1307+433	12 years	54682 − 59065	2930	0.76±0.07	$N_0 = 0.76 \pm 0.03$; $\alpha = 1.74 \pm 0.04$; $\beta = 0.093 \pm 0.017$
	average	59488 − 59759	80	0.65±0.30	$N_0 = 0.76 \pm 0.19$; $\alpha = 1.59 \pm 0.23$; $\beta = 0.090 \pm 0.085$
GB6 J0114+1325	12 years	54682 − 59065	1260	1.39±0.10	$N_0 = 0.56 \pm 0.03$; $\Gamma = 2.09 \pm 0.03$
	average	55450 − 55600	95	2.54±0.66	$N_0 = 0.86 \pm 0.15$; $\Gamma = 2.18 \pm 0.13$

Table 4.5: *Fermi/LAT* results. For PKS 0048-09 and B3 1307+433 a log-parabola function has been used for fitting their spectra using a E_b of 924 MeV and 1.39 GeV, respectively. A power-law function with $E_b = 1.4$ GeV has been used for GB6 J0114+1325. The reported flux values are in unit of 10^{-8} ph cm^{-2} s^{-1}, while normalization values are in unit of 10^{-12} MeV^{-1} cm^{-2} s^{-1}.

Source	State of activity	n_H [cm^{-2}]	Γ_X	K [keV^{-1} cm^{-2} s^{-1}]	Exp. time [ks]
PKS 0048-09	high	3.10×10^{20}	2.16 ± 0.17	$(7.0 \pm 0.5) \times 10^{-4}$	2.94
	quiescent		2.12 ± 0.07	$(8.7 \pm 0.4) \times 10^{-4}$	6.69
GB6 J0114+1325	average	3.27×10^{20}	4.0 ± 0.7	$(7.7 \pm 3.6) \times 10^{-5}$	1.18
B3 1307+433	average	1.85×10^{20}	2.38 ± 0.18	$(6.9 \pm 0.6) \times 10^{-5}$	21.29

Table 4.6: Values of the parameters obtained from the fit and total exposure time for each source.

Source	State of activity	v [mag]	b [mag]	u [mag]	$w1$ [mag]	$m2$ [mag]	$w2$ [mag]
PKS 0048-09	high	16.4 ± 0.04	16.81 ± 0.03	15.99 ± 0.02	16.02 ± 0.03	16.05 ± 0.03	16.18 ± 0.02
	quiescent	14.85 ± 0.03	15.22 ± 0.02	14.39 ± 0.02	14.41 ± 0.02	14.41 ± 0.03	14.69 ± 0.02
GB6 J0114+1325	average	16.85 ± 0.1	17.21 ± 0.07	16.29 ± 0.05	16.29 ± 0.05	16.27 ± 0.06	16.28 ± 0.04
B3 1307+433	average	17.31 ± 0.04	17.72 ± 0.03	16.86 ± 0.03	16.86 ± 0.03	16.9 ± 0.03	17.01 ± 0.02

Table 4.7: Recovered magnitudes in Vega system for each source in the selection. For PKS 0048-09 we report both the magnitudes obtained in the chosen low state (upper line) and high state (lower line).

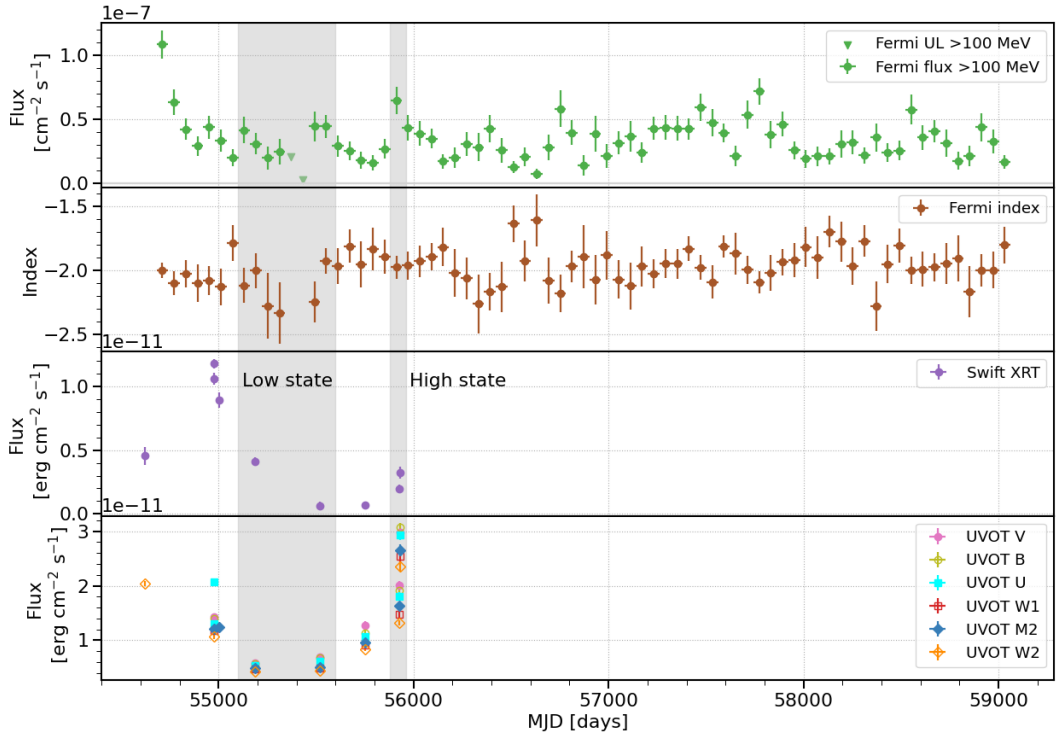

Figure 4.3: Multi-wavelength lightcurve of the source PKS 0048-09. From top to bottom, the panels show: *Fermi-LAT* flux in 60-days bins, values assumed by the $\gamma-$ray spectral index in the same bins, *Swift/XRT* flux in daily bins, *Swift/UVOT* flux in daily bins. The shaded areas identify the boundaries of the low and high state periods chosen to build the SED.

to a significance $> 85\sigma$) and presents flux and spectral parameters in agreement with the values reported in the 4FGL-DR2 catalog, which are $\alpha = 1.92 \pm 0.03$, $\beta = 0.06 \pm 0.01$. During the high-state period the source presents a slightly higher flux (about twice the one derived in the 12-years analysis) while the log-parabola indexes are compatible within the statistical uncertainties.

GB6 J0114+1325

The source has been observed by *Swift* only 4 times between 2010, November 22 and 2020, July 17, with both the *XRT* and *UVOT* modules. As for the other sources, we firstly built the lightcurve of the candidate in order to identify suitable low and high states of activity, finding no a clear variation in the source flux. However, since the data are so few and so sparse in time, it is not possible to select a time interval with a large number of *Swift* pointings for the construction of the SED. Moreover for this source we did not identify any clear high state in the lightcurve, so we just considered

the average-state SED.

We decided to consider an interval of a few months around the first *Swift/XRT* observation (on 2010, November 22), which is one of the most significant ones. The *Fermi/LAT* analysis is then computed on the whole period, defined from 2010, September 11 to 2011, February 8.

The *XRT* observations show a low total exposure (see Table 4.6). For this reason the number of counts obtained in each energy bin is not enough to apply the χ^2 statistic, so in this case the Cash statistic is used (see Sect. 1.4.2). The values of the spectral parameters resulting from the fit, the value used for n_H, and the total exposure time are reported in Table 4.6. *UVOT* performed observations in the same day in all photometric bands. The values found for each filter are reported in Table 4.7. In *Fermi/LAT*, GB6 J0114+1325 presents a significant emission (TS $= 1260$, $> 35\sigma$) on the 12 years of data and the obtained spectral parameters (see Table 4.5) in agreement with the 4FGL-DR2 results ($\Gamma = 2.11 \pm 0.04$) for this source. During the selected period the source present a slightly higher flux (less than twice the one derived in the 12-years analysis) and a power-law index compatible within the statistical uncertainties.

B3 1307+433

This source has been observed by *Swift* 18 times between 2010, September 2 and 2021, December 10, with the majority of the pointings in 2021, thanks to a dedicated observation proposal we submitted. In particular, we have 13 observations in the period from 2021, October 4 to 2021, December 10.

We firstly generated the lightcurves of the source in all bands, which do not show changes in the average emission state of the source in the period from October to December 2021. Taking into account this result and given the large number of observations in this period, we chose these data to build the SED of the source in its average state. *Fermi/LAT* analysis was performed in the whole period from 2021, October 1 to 2021, December 31.

For both *XRT* and *UVOT*, we summed all the available observations in this period. With *UVOT* we obtained the detection in all photometric bands. Results from the analyses are reported in Tables 4.6 and 4.7 In *Fermi/LAT* the source shows a significant excess (TS $= 2931$, $> 50\sigma$) on the 12-years analysis, with spectral parameters in agreement with the 4FGL-DR2 ($\alpha = 1.77 \pm 0.05$ and $\beta = 0.08 \pm 0.02$) For the selected average-state period the source presents a similar emission with flux and spectral parameters compatible within the uncertainties with the one obtained using 12 years.

4.4 Modeling

During the 2017 multi-messenger campaign, the most likely emission scenario found to interpret the SED of TXS 0506+056 is a mixed lepto-hadronic model with a dominant leptonic component and a subdominant hadronic one. The former describes both

[8] See https://www.cta-observatory.org for data on CTA sensitivity.

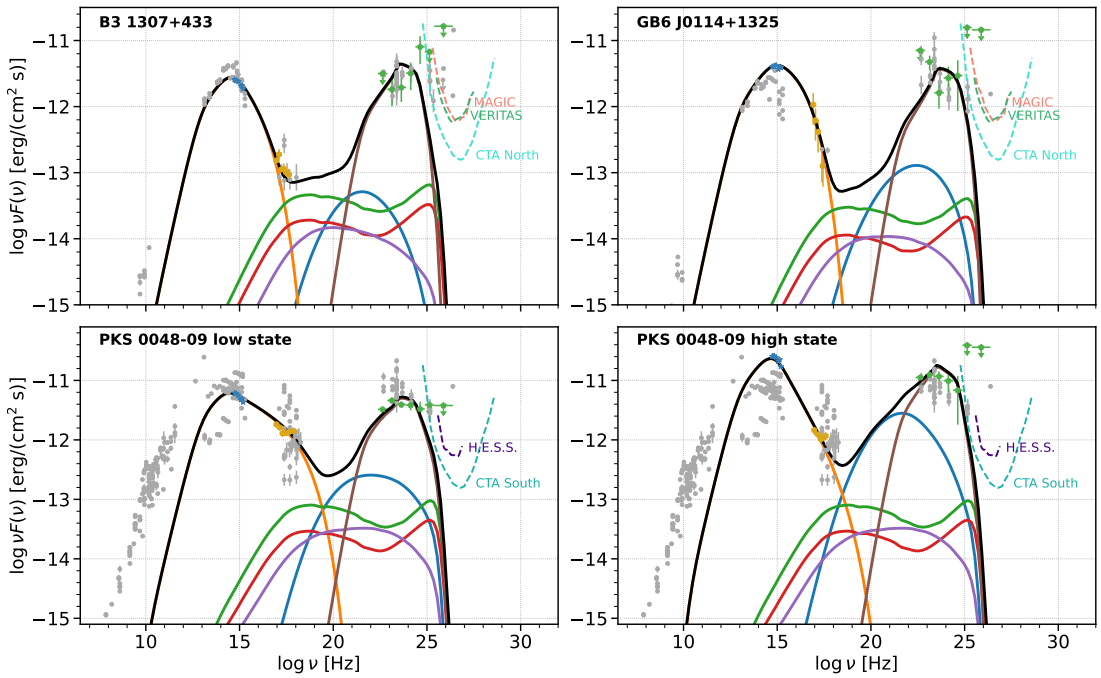

Figure 4.4: Multi-wavelength SED of the candidates in the selected periods and modeling in lepto-hadronic context. Grey points show the archival data from ASI ASDC [156], while light-blue stars, gold hexagons, and green pentagons show *Swift/UVOT*, *Swift/XRT* and *Fermi/LAT* data in the selected periods, respectively. The model lines show: electron synchrotron emission (orange), synchrotron self Compton emission (blue), external Compton emission (brown), Bethe-Heitler cascades (violet), cascades from π^0 (green), and $\pi^{\pm}$ (red) decay. For the two sources lying in the northern emisphere (GB6 J0114+1325, B3 1307+433) a comparison with the sensitivity of MAGIC (salmon dashed line, [30]), VERITAS (light-green dashed line, [157]), and CTA Northern array[8](cyan dashed line) for 50 hours of observation, is also shown, while for the only source in the southern emisphere (i. e. PKS 0048-09), the comparison is done with H.E.S.S. (purple dashed line, [158]) and CTA Southern array (seagreen dashed line).

Source	L_{torus} [erg s^{-1}]	R_{BLR} [cm]	R_{torus} [cm]
PKS 0048-09	9.68×10^{42}	1.56×10^{16}	3.89×10^{17}
GB6 J0114+1325	1.46×10^{45}	1.91×10^{17}	4.78×10^{18}
B3 1307+433	1.36×10^{45}	1.84×10^{17}	4.60×10^{18}

Table 4.8: Estimated values of torus luminosity, BLR radius and torus radius.

bumps of the SED in therms of synchrotron and inverse Compton emission by primary electrons, while the latter arises in X-rays and VHE $\gamma-$rays as the result of $e^{\pm}$ cascades initiated by pion decay and Bether-Heitler pair production. In this model, the target photon field for $p\gamma$ interactions was considered to be external to the jet, as suggested by energetic constraints, and relativistically boosted in the reference frame of the emitting region, which is schematized as a spherical blob moving along the jet with radius R', Doppler factor δ, and average magnetic field B'.

The three selected targets are here modeled under the same framework and using the same code already applied to TXS 0506+056, i e. *LeHa* [159]. It is a stationary code able to calculate the photon and neutrino emission from a spherical emitting region in the jet. The main difference between the model used for TXS 0506+056 and the one applied here is that in the first case a spine-layer structured jet was considered, with the layer providing the main target photon field, while now we consider external target photon fields from the BLR and the torus, as suggested by our results on the accretion rate. This is possible since *LeHa* accepts arbitrary target photons fields as input for both $p\gamma$ and $\gamma\gamma$ interactions. The energy distributions of the primary electrons and protons filling the emitting region are parametrized as a broken power-laws the former and a power-law the latter, both with exponential cut-offs at the maximum energy.

For the purposes of this work, the important parameter is the radiation energy density of the broad emission line photons. In order to compute this quantity we need information on the luminosity and radius of the BLR. We gave an estimation for the former in Sect. 4.2 thanks to our study on the spectral lines, while the latter can be recovered from the disk luminosity by assuming a simple scaling relation: $R_{BLR} = 10^{17} L_{disk,45}^{1/2}$ cm [160], where $L_{disk,45}$ is the luminosity of the disk in units of 10^{45} erg s^{-1}. The recovered values for each source are listed in Table 4.8. This relation implies that, within the BLR, the energy density of the line photons is constant and equal for all sources. The value obtained in the observer's frame is

$$u_{ph,BLR} = \frac{L_{BLR}}{4\pi c R_{BLR}^2} 2.24 = 5.95 \times 10^{-2} \,\mathrm{erg\,cm^{-3}}, \tag{4.7}$$

where the factor 2.24 in the formula comes from geometrical considerations of a uniform spherical emitter [161]. The photon energy density in the jet frame ($u'_{ph,BLR}$) relates to what is measured in the observer's frame ($u_{ph,BLR}$) as $u'_{ph,BLR} = \Gamma^2 u_{ph,BLR}$, where Γ is the bulk Lorentz factor.

A similar procedure can be done in order to obtain the luminosity and photon energy density in the torus. In this case we assume that the accretion luminosity reprocessed by the torus is about 40%, so $L_{torus} = 0.4\, L_{disk}$. As in the case of the BLR, we assume a scaling relation between the luminosity of the disk and the radius of the torus: $R_{torus} = 2.5 \times 10^{18}\, L_{disk,45}^{1/2}$ cm [160]. The results for both L_{torus} and R_{torus} for each source can be found in Table 4.8.

In the numerical modeling, the energy densities of the BLR and the torus photon fields (u'_{BLR} and u'_{torus} respectively) are considered as free parameters in the fit. They are parametrized as functions of the location of the emitting region r and the Lorentz factor Γ following the approach of [162] with slight modifications in order to consider a full shell between $0.9\, R_{BLR}$ and $1.1\, R_{BLR}$ instead of an opening angle of $\pi/4$ as in the original version (see [163] for details), as well as a torus reprocessing fraction of 0.4. We assume the the emitting region to be always within R_{torus}, which gives thus $u'_{torus} = 0.028$ erg cm^{-3}. This result, together with the results obtained for u'_{BLR} for each source, will be compared with the values obtained by estimations and discussed in Sect. 4.5.

The modeling of the SEDs is provided in Fig. 4.4, the expected neutrino spectrum is shown in Fig. 4.5, and the detailed list of model parameters in Table 4.9. For all sources, we start by performing a leptonic modeling with a fixed value of $\delta = 30$. Once the leptonic component is able to reproduce the data, we then add a hadronic contribution, increased up to a level that does not overshoot the constraints in the X-rays. We do not perform an extensive study of the parameter space, nor perform a minimization. In particular, the hadronic component here is not constrained by the data. With these results we show that a lepto-hadronic modeling inspired by the ones developed for TXS 0506+056, and assuming as target photon field the radiation from the BLR and the torus, can reproduce the SED, and provide an estimate of the neutrino spectrum.

4.5 Discussion and Conclusions

In this work we searched for sources with similar observational properties to TXS 0506+056, aiming at identifying potential similarities in their accretion mechanism and non-thermal processes at work in the jet emission.

We selected the sources from the 4LAC Fermi catalog of AGNs, based on their $\gamma-$ray luminosity, $\gamma-$ray photon index and synchrotron peak frequency. These selection criteria excluded a priori all sources without an established value of their redshift, which represent $\sim$ 63% of the BL Lac population in the catalog. The initial sample we obtained consisted of 27 objects. However, the need for precise information on the spectral emission lines for the determination of the candidates accretion rate led to only 4 blazars, including TXS 0506+056, all classified as BL Lacs. Indeed, the great majority of the selected objects lacks a detailed spectral analysis in the literature, and almost half of them lacks any measurement of their optical/UV spectra. Therefore, we strongly support detailed spectroscopic measurements of the blazars which we had to exclude from the sample, as well as campaigns aimed at measuring the redshift of *Fermi/LAT*

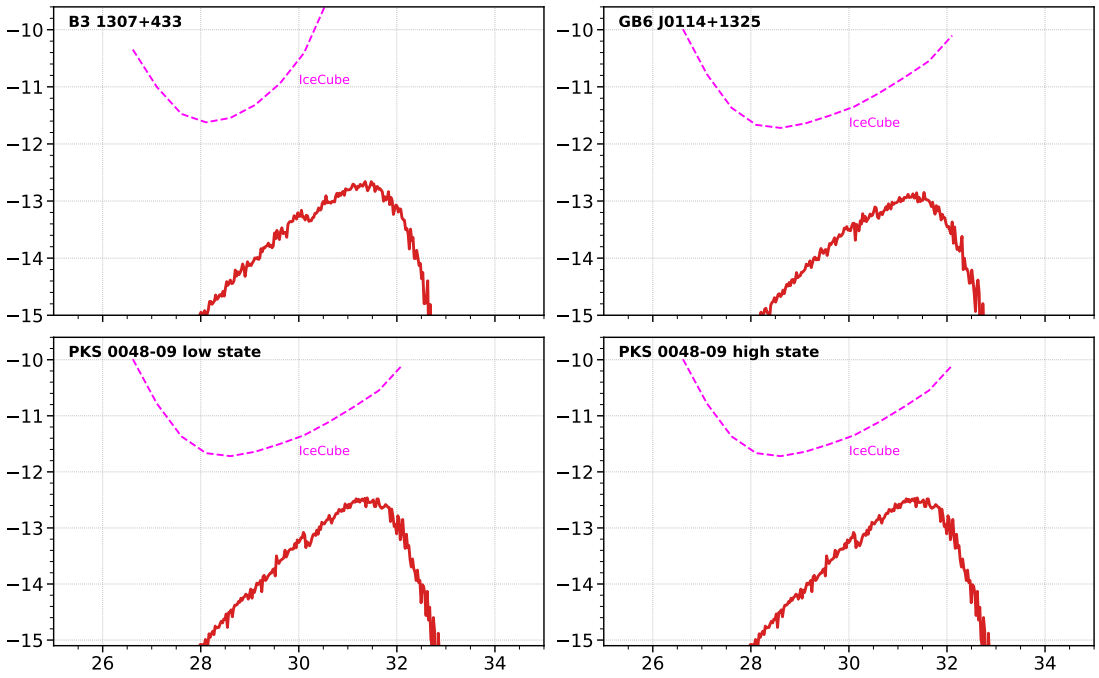

Figure 4.5: Neutrino spectrum expected from the model in Fig. 4.4 of the sources under consideration, compared with the IceCube 5σ sensitivity for point-source searches in for 8 years of exposure [164]. The sensitivity is shown for a declination of 30° in the upper left panel and of 0° in the other panels, based on the proximity to the source declination.

blazars. These measurements will be essential for the knowledge of the luminosity of the sources in the catalog and a deeper investigation of the selected objects, allowing us to enlarge the sample and potentially perform statistical studies.

For three sources in the selection, namely TXS 0506+056, B3 1307+433, and GB6 J0114+1325, the obtained values for the accretion rate suggest an efficient accretion process around the supermassive black hole and the presence of a BLR rich of gas (see [84]), which is also supported from the modeling performed on the sources. For one source, i. e. PKS 0048-09, the situation seems more uncertain, since the estimated values lie around the proposed dividing value between FSRQs and BL Lacs. The accretion rate depends on the unknown black hole mass and, in this work, for all selected sources, the ranges we found for the accretion rate are computed assuming two typical mass values for AGNs. The obtained values are consistent with typical accretion rate estimates in AGNs. However, the lack of a black-hole mass estimate adds an additional uncertainty, preventing a more precise estimation of the accretion rate. This fact is particularly relevant for the case of PKS 0048-09, for which a further investigation is needed for a better understanding of its nature.

Public multiwavelength data from the selected sources were analyzed, searching for

Source	PKS 0048-09 low	PKS 0048-09 high	GB6 J0114+1325	B3 1307+433
z	0.635	0.635	0.685	0.693
δ	30	30	30	30
Γ	20	20	20	20
R' [10^{16} cm]	1.25	1.25	1.25	1.25
B' [G]	1	1	1	1
$^\star u'_B$ [erg cm^{-3}]	0.04	0.04	0.04	0.04
$\gamma'_{e,min}$	300	300	300	300
$\gamma'_{e,break}$	1.6×10^3	2.6×10^3	3.0×10^3	2.2×10^3
$\gamma'_{e,max}$	2×10^5	2×10^5	1.6×10^4	1.5×10^4
$\alpha_{e,1} = \alpha_{p,1}$	2.0	2.0	2.0	2.0
$\alpha_{e,2}$	3.35	4.1	3.0	3.5
K'_e [cm^{-3}]	1.6×10^3	4.5×10^3	8.0×10^2	8.0×10^2
$^\star u'_e$ [erg cm^{-3}]	1.0×10^{-3}	9.6×10^{-3}	1.8×10^{-3}	1.5×10^{-3}
$\gamma'_{p,min}$	1	1	1	1
$\gamma'_{p,max}[10^8]$	1	1	1	1
K'_p [cm^{-3}]	130	130	56	56
$^\star u'_p$ [erg cm^{-3}]	3.4	3.4	1.5	1.5
$u'_{\rm BLR}$ [erg cm^{-3}]	7.0×10^{-2}	7.0×10^{-2}	0.12	0.20
$u'_{\rm torus}$ [erg cm^{-3}]	2.8×10^{-2}	2.8×10^{-2}	2.8×10^{-2}	2.8×10^{-2}
$^\star r[R_{BLR}]$	2.0	2.0	1.9	1.7
$^\star L$ [10^{46} erg s^{-1}]	2.7	2.7	1.2	1.2

Table 4.9: Parameters of the lepto-hadronic models. The quantities flagged with a star (⋆) are derived quantities, and not model parameters. The jet luminosity has been calculated as $L = 2\pi R'^2 c\Gamma^2(u'_B + u'_e + u'_p)$, where u'_B, u'_e, and u'_p are the energy densities of the magnetic field, the electrons, and the protons, respectively, in the jet frame.

contemporaneous high and low emission activity in the different bands. A flaring state could be identified for PKS 0048-09 only, while for the other sources simultaneous periods of average activity were selected. The SED of the candidates in the selected periods was built with the available multiwavelength data and modeled in the same framework used for TXS 0506+056, assuming a lepto-hadronic emission. Results from the modeling show that standard leptonic scenarios can reproduce the SED of the selected sources, with a dominant component at high energies given by the external Compton (EC) process on the BLR and the torus. These features are typical of FSRQs. The model is thus in agreement with the results found for the accretion rate, suggesting the selected sources to have a non-inefficient accretion disk and a rich BLR, and hence potentially be masquerading BL Lacs. PKS 0048-09 is the only source showing a flaring behaviour and for which we modeled two different flux states. A successful modeling of the high state is achieved by changing only the energy distribution of primary electrons in the emitting region, without modifying the parameters of the jet, nor of the external photon

field (see Table 4.9). This change explains the higher SSC contribution in the SED of the flaring state of PKS 0048-09 compared to the other sources.

The hadronic component, responsible for the neutrino emission, emerges in X-rays as the contribution of pion decay and Bethe-Heitler pair production, coming from photo-meson interactions. For B3 1307+433 the observations we took thanks to our *Swift* proposal play relevant role in constraining the contribution of the hadronic component. Therefore, additional measurements in this band are essential for a more precise characterization of the X-ray emission of these sources and to rule out the possibility of a purely leptonic emission. In particular, additional data from *Swift/XRT* for the objects with few observations would provide a better characterization of the $0.2 - 10$ keV band, while data from e. g. *NuSTAR* are essential to characterize the higher energies, since no data in this band are available at the moment for the selected sources.

The models were computed assuming both the BLR and the dusty torus as target photon fields, the photon energy densities of which were free model parameters. The target photon field energy density in the reference frame of the emitting region depends on its position with respect to the accretion disk, the BLR, and the torus. It can thus be used to infer the position of the emitting region in the jet. The values used in the models constrain the emitting region to be just outside the BLR, at a few R_{BLR}, as confirmed by the fit values (see Table 4.9). Indeed the value obtained for u'_{BLR} results to be lower than the one estimated thanks to our study on the emission lines, which assumes a region located inside the BLR. The value obtained from our estimation is: $u'_{BLR} = u_{BLR}\,\Gamma^2 = 23.8\,\mathrm{erg\,cm^{-3}}$, where u_{BLR} is given by Eq. 4.7 and Γ has the same value used in the fit. In addition the value of r computed from the fit is $\geq 1.7\,\mathrm{R_{BLR}}$ for all sources, further confirming the results.

The obtained SEDs and models of the sources were compared with the sensitivities, for 50 hours of observation, of Imaging Air Cherenkov Telescopes (IACT) − H.E.S.S., MAGIC, VERITAS, and the upcoming CTA array − in order to provide perspectives for VHE observations (see Fig. 4.4). The selected sources appear to be out of reach for IACTs in their average state. One of the selected sources, B3 1307+433, was observed by VERITAS with an exposure time of 9.4 hours, obtaining a flux upper limit of $17.8 \times 10^{-12}\,\mathrm{cm^{-2}\,s^{-1}\,TeV^{-1}}$ at 256 GeV [165]. This is in line with their potential nature as masquerading BL Lacs, for which we expect a stronger absorption at VHE from the source environment with respect to standard, bare, BL Lacs. These objects could be detected by the upcoming Cherenkov Telescope Array only during bright flaring states. The same comparison was also made for the obtained neutrino spectra with the sensitivity of the IceCube Neutrino Observatory for 8 years of data-taking at a declination of 0° or 30° (we chose the closest to the source declination). This comparison is reported in Fig. 4.5 and shows that the expected neutrino fluxes are not detectable by the current IceCube Neutrino Observatory.

Finally, a comparison with the blazar PKS 0735+17 is worth to be mentioned, since this object was proposed as the counterpart of the neutrino event IceCube-211208A[9], which was coincident with flaring activity of the source in several wavebands, and was

[9]See https://www.astronomerstelegram.org/?read=15099.

shown to have a SED very similar to the one of TXS 0506+056 in the work of [166] (see Fig. 5). After an inspection of the source parameters reported in the 4LAC-DR2 catalog, we found that the $\gamma-$ray luminosity and spectral index lie in the ranges we defined in Sect. 4.1. Regarding the synchrotron peak frequency ν_S, it was found to be quite close to TXS 0506+056 value during the period of the flare ($\log \nu_S = 15.17$) and shortly after ($\log \nu_S = 14.13$) [166]. However, in the catalog this blazar is classified as a BL Lac of the LSP type and the reported value results to be too low to include the source in the selection ($\log \nu_S = 13.43$). The value in the 4LAC-DR2 refers to an average emission state of the source. Therefore, the similarities observed in its flaring state are due to the variability of ν_S with the source activity and the SED in its average state results to be not as similar as suggested. A further investigation of this object is needed for a better understanding of its similarities and differences with TXS 0506+056.

Chapter 5

Follow-up observations of IceCube neutrino alerts in Very High Energy γ-rays

In 2013, the IceCube Neutrino Observatory [15] announced the observational evidence for the existence of high-energy neutrinos of cosmic origin. Additional measurements performed in the following years [167] confirmed this discovery. The observed astrophysical neutrino flux has an isotropic distribution, which suggests high-energy neutrinos to have mostly an extragalactic origin. This is supported by the evidence for neutrino emission from the blazar TXS 0506+056 [3], already described in Sect. 3.1. However, the blazar contribution to the astrophysical neutrino flux was estimated to be at the level of 7% maximum [168, 169], hence also objects other than blazars have to be investigated in order to find neutrino and CR sources. Given the recent evidence of neutrinos from the Seyfert galaxy NGC 1068 [4] and from the Galactic plane [5], good candidates are represented by other kind of AGNs or by galactic sources, in addition to other potential candidates, like Tidal Disruption Events [170].

In order to shed light on the composition and multi-messenger emission from these objects, simultaneous observations in the electromagnetic spectrum need to be performed. In particular, $\gamma-$rays are expected to be produced together with neutrinos in the same interactions of hadrons with ambient matter (proton-proton interactions) or radiation fields (photo-meson interactions). These processes lead to the generation of charged and neutral pions, which decay into neutrinos and $\gamma-$rays respectively, following the relations 1.4$-$1.8. The coincident observation of neutrinos and $\gamma-$rays from the same source can thus pinpoint to genuine neutrino emitters and cosmic-ray accelerators. However, $\gamma-$rays of high energy may interact with the source environment or

the EBL in their path to Earth, reducing the VHE $\gamma-$ray flux and leading to possible non-detections by $\gamma-$ray telescopes. For this reason, also simultaneous observations in other wavebands are essential to define the state of activity of the source at the time of the neutrino arrival and provide information on the source emission mechanisms.

The four major IACTs currently operating, namely FACT [171], H.E.S.S. [27], MAGIC [30, 57], and VERITAS [26], operate real-time follow-up observational programs in cooperation with IceCube aiming at identifying $\gamma-$ray counterparts to neutrino events. This strategy turned out to be successful in the 2017 IceCube-170922A event related to TXS 0506+056, allowing to identify the first evidence for a neutrino source. In this case, the multi-wavelength follow-up of the neutrino alert was essential for establishing the coincidence and interpreting the source emission.

In this chapter, we present the extensive real-time follow-up programs operated by the four aforementioned IACTs to neutrino events, the data analysis, and the obtained results. The followed-up neutrino events are of two main types: singlets and multiplets (see Sect. 1.2.1 and the next section for more details). The observations are related to the period ranging from October 2017, just after the IceCube-170922A event, to January 2021, and collect data from counterparts of 11 singlets and 7 multiplets. VHE $\gamma-$ray observations are complemented by multi-wavelength observations in optical, UV, X-ray, and HE $\gamma-$ray bands. At VHE, no detection was achieved in most of the observed alerts and for each of them integral flux ULs constraining the VHE emission were computed.

Results from this project are published in the proceedings [172, 173] and a paper is currently in preparation [174]. In this project I was responsible for the MAGIC data analysis of the source OP 313, counterpart of different multiplet alerts, and for the comparison of emission models of the source PKS 1502+106, counterpart of the singlet alert IceCube-190730A, with our results. I also had an important role in the project organization and writing of the paper. The following chapter is adapted from the aforementioned paper. Additionally, it contains a novel analysis performed by myself evaluating the MAGIC detectability at very high energies of the sources monitored by IceCube for multiplet alerts (see Sect. 5.6).

5.1 IceCube neutrino alerts

The IceCube alerts considered in this work can be divided into two broad categories: single high-energy track events, referred to as singlets, and clusters of neutrinos with typical lower energies, referred to as multiplets. In this work we report observations of singlet alerts issued between October 2017 and January 2021, and multiplet alerts issued between May 2019 (i. e. when IceCube real-time infrastructure was updated, see Sect. 1.2.1) and January 2021.

Neutrino **singlets** are individual events with typical energies of hundreds of TeV, since for this channel the alert system is mostly sensitive to neutrinos with $E > 100$ TeV. Based on their probability of being of astrophysical origin (the so-called *signalness*, see Sect. 1.2.1), they are divided in to BRONZE and GOLD events, showing a probabil-

Name (GCN Circular)	Energy [TeV]	Signalness	FACT [h]	H.E.S.S. [h]	MAGIC [h]	VERITAS [h]	Potential counterpart	MWL
IceCube-171106A	230	0.75	19.0	—	4.5	2.5	7GB 223537.9+070825	
IceCube-181023A	120	0.28	1.0	—	—	—		
IceCube-190503A	100	0.36	—	—	0.5	—		
IceCube-190730A	299	0.67	—	—	3.1	—	PKS 1502+106	*Swift*
IceCube-190922B	187	0.50	2.0	—	2.2	—	AT2019pqh	
IceCube-191001A	217	0.59	5.4	—	—	1.0	AT2019dsg	
IceCube-200107A	—	—	—	—	2.7	9.5	4FGL J0955.1+3551	*Swift*
IceCube-200926A	670	0.44	—	1.3	1.0			
IceCube-201007A	683	0.88	—	3.0	0.5	—		
IceCube-201114A	214	0.56	—	14.3	6.0	7.0	4FGL J0658.6+0636	*Swift*
IceCube-201222A	186	0.53	—	—	—	1.0		

Table 5.1: List of IceCube singlet alerts issued between October 2017 and January 2021 which were followed-up by at least one IACT. The alert name links to the corresponding GCN circular released by IceCube. The columns show: energy and signalness of the neutrino events, observation time of each IACT (FACT, H.E.S.S., MAGIC, and VERITAS), name of potential counterpart, and available multi-wavelength data. Note that energy and signalness are not available for the singlet event IceCube-200107A.

Source	Duration [days]	Pre-trials significance	H.E.S.S [h]	MAGIC [h]	VERITAS [h]	MWL
MG1 J181841+0903	Multiple alerts	$> 3.3\,\sigma$	—	1.6	—	*Swift*
1ES 1312-423	0.26	$3.4\,\sigma$	2.6	—	—	*Swift*, ATOM
PMN J2016-09	0.01	$3.6\,\sigma$	—	0.9	—	
OP 313	Multiple alerts	$> 3.0\,\sigma$	—	3.2	—	*Swift*
OC 457	0.30	$3.3\,\sigma$	—	2.5	—	*Swift*
GB6 J0316+0904	2.25	$3.1\,\sigma$	6.0	1.9	1.0	
All-sky PMN J0325-1843	3.67	$5.1\,\sigma$	—	2.0	—	

Table 5.2: List of IceCube multiplet alerts issued in the years 2019-2020 which were followed-up by at least one IACT. The columns show: duration and significance of the neutrino flare, observation time of each IACT (H.E.S.S., MAGIC, and VERITAS), and available multi-wavelength data.

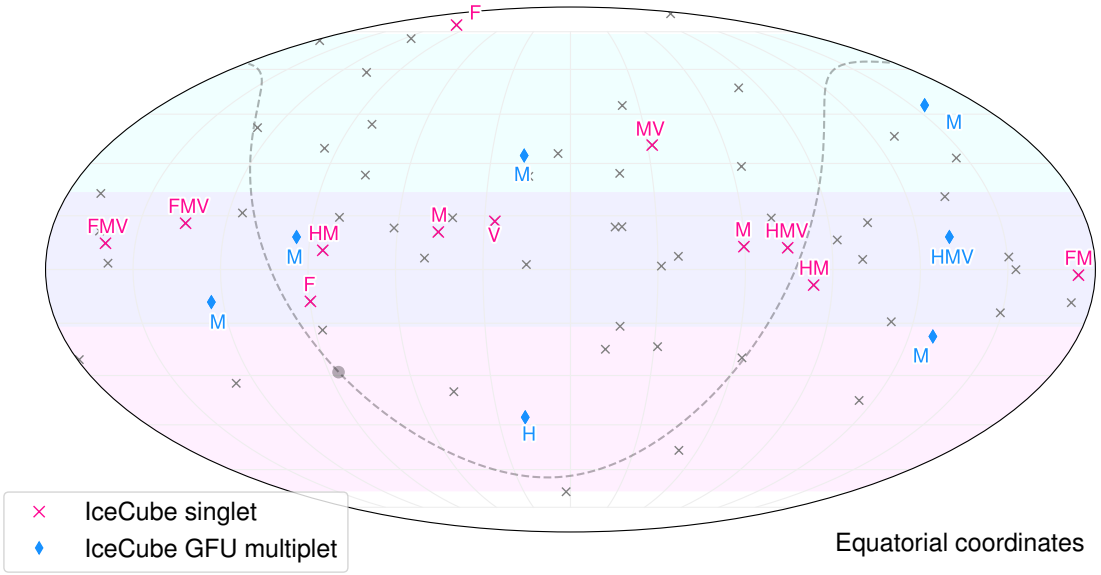

Figure 5.1: Skymap in equatorial coordinates showing the locations of IceCube neutrino alerts issued between October 2017 and January 2021. Singlets are labeled by crosses, while multiplets by diamonds. Grey alerts indicate those which were not followed-up. Letters indicate which telescopes participated in the observations (F - FACT, H - H.E.S.S., M - MAGIC, V - VERITAS). Light cyan and magenta bands indicate regions of the sky potentially observable at a zenith angle less than 45° from the Northern (FACT, MAGIC, VERITAS) and Southern (H.E.S.S.) IACTs, respectively. The visibility windows for instruments in both hemispheres overlap around the celestial equator, where the IceCube sensitivity to neutrinos in the $\sim$ 100 TeV energy range is maximal.

ity $>$ 30% and $>$ 50% respectively. The typical localization uncertainty for these events is of $\sim 1^{\circ}$, which well matches the $3.5^{\circ} - 5^{\circ}$ FoV of current IACTs. The single-event alerts are publicly distributed under the GCN, with a typical latency of $\sim$ 30 s, allowing independent real-time observations by the multi-wavelength observatories around the world. For this kind of alerts the aim of the follow-up is the identification of the electromagnetic counterpart to the neutrino event. Usually, one or more candidate neutrino sources can be found inside the alert localization error region. They can be identified through the use of *Fermi/LAT* or IACT catalogs, or thanks to targeted electromagnetic observations. When more than one candidate is found inside the IceCube error region, the observations focus on the most interesting candidate and can be based, for example, on the state of activity of the source. When no candidate sources are found inside the IceCube error region, IACTs usually point to the best-fit neutrino position.

Neutrino **multiplets** include clusters of neutrinos (also referred to as flares) with typical energies around $\sim$ 1 TeV coming from a list of known $\gamma-$ray emitters. The flare duration is not constrained a priori and can range between few seconds up to 180 days. The multiplet alerts are privately distributed by IceCube to the partner IACTs

Source	Start date	Trigger date	ΔT [days]	-$\log_{10}(p)$
MG1 J181841+0903	2019-01-19	2019-05-27	127.4	3.36 (3.3 σ)
	2019-01-19	2019-05-27	127.7	3.36 (3.3 σ)
	2019-01-19	2019-05-27	127.9	3.38 (3.3 σ)
	2019-01-19	2019-06-05	136.8	3.79 (3.6 σ)
	2019-01-19	2019-06-05	137.0	3.79 (3.6 σ)
1ES 1312-423	2019-03-12	2019-03-12	0.26	3.46 (3.4 σ)
PMN J2016-09	2019-11-29	2019-11-29	0.01	3.73 (3.6 σ)
OP 313	2020-02-12	2020-04-10	57.5	2.97 (3.1 σ)
	2020-02-12	2020-05-01	78.8	2.93 (3.0 σ)
	2020-02-12	2020-05-17	94.7	2.91 (3.0 σ)
	2020-03-13	2020-08-27	166.7	2.97 (3.1 σ)
OC 457	2020-08-04	2020-08-04	0.3	3.24 (3.3 σ)
GB6 J0316+0904	2021-01-13	2021-01-15	2.3	3.02 (3.1 σ)
All-sky (α=51.2°, δ=-18.6°)	2019-09-15	2019-09-19	3.7 d	6.77 (5.1 σ)

Table 5.3: Detailed information related to the multiplet alerts followed-up by at least one IACT. For each alert the source name, the date of the first event in the multiplet (Start date), the trigger date, the duration of the multiplet time window (ΔT), and the alert pre-trials significance (-$\log_{10}(p)$) [22] are given. Note that for MG1 J181841+0903 and OP 313 multiple alerts were issued.

(currently H.E.S.S., MAGIC, and VERITAS) aiming at determining possible changes in the emission state of the source, both in terms of temporal or spectral variations. A system update in 2019 introduced the implementation of the same analysis also in the search for neutrino clusters in the whole sky. In both cases, the alert is sent to partner IACTs only if a pre-defined significance threshold is reached. It corresponds to 3σ for pre-defined $\gamma-$ray sources and 4.2σ for the all-sky search. More details on the singlets and multiplets alerts can be found in Sect. 1.2.1.

IceCube issued 62 singlet alerts between October 2017 and January 2021, and 27 neutrino multiplets from 17 sources, between May 2019 and January 2021. Within these multiplets, one is an all-sky alert. The location in the sky of all alerts sent is shown in Fig. 5.1, while basic information on the alerts followed-up by IACTs are listed in Tables 5.1 and 5.2 (second and third columns) for singlets and multiplets, respectively. This information includes the energy and signalness for singlets, and the alert duration and pre-trials significance for multiplets[1]. In addition, detailed information about the

[1]The pre-trial significance is the probability of observing a given test statistic from an online trigger in a background only hypothesis. It does not take into account specific time scales in the computation, except for the maximum 180 days considered in the analysis. For this reason, it can be quickly computed and thus be a suitable quantity to define the alert threshold in a real-time analysis. Differently, the post-trial significance adds time constraints, taking into account a background only hypothesis in the full exposure time from the beginning of instrument operations up to the time of the interested event. Thus, it makes a

IACT	n° tel.	Diameter [m]	FoV [deg]	Energy range [TeV]	Rep. speed [deg s^{-1}]	Location
FACT	1	3.5	4.5	$0.4 - 10$	12	La Palma, Spain
H.E.S.S.	4 1	12 28	5.0 3.5	$0.03 - 100$	3	Khomas, Namibia
MAGIC	4	17	3.5	$0.05 - 50$	7	La Palma, Spain
VERITAS	4	12	3.5	$0.1 - 30$	1	South Arizona, USA

Table 5.4: Technical information about current IACT systems. The columns are: number of telescopes, reflector diameter, camera field of view (FoV), energy range[2], repositioning speed, and location.

followed-up multiplet alerts, such as the number of alerts for each source and their start and end dates, are reported in Table 5.3.

5.2 IACTs follow-up strategy

All current IACT systems (FACT, H.E.S.S., MAGIC, and VERITAS), operate real-time follow-up programs of IceCube neutrino alerts to search for VHE $\gamma-$rays in association with astrophysical neutrinos. Basic technical information about the current IACT systems, like the number of telescopes of each system, the telescopes diameter, the system FoV, energy range, repositioning speed, and location, are listed in Table 5.4. Note that the H.E.S.S. system is the only one in the southern hemisphere.

The specific observation strategy, as well as the total time allocated for follow-up of neutrino alerts is different for each IACT. For example, MAGIC allocates approximately 40 hours of dark time and 20 hours of moon time per year, while VERITAS allocates about 45 hours of dark time per year. The final decision to perform follow-up observations is taken by each IACT independently and relies typically on a combination of several factors like the intrinsic parameters of the neutrino alert (e. g., signalness, duration of the flare, etc.), the available visibility window, weather conditions, or the presence of a candidate electromagnetic counterpart. Usually, for the most interesting cases, as for example the identification of a new source in IceCube error region, or a $\gamma-$ray source with flux enhancement in other wavebands, deep long-exposure observations are performed in order to detect and better characterize the interested object.

In addition, all four IACTs have an automatic repointing system allowing to reduce the delay between the detection of the neutrino at the South Pole and the start of observations. In this context, a crucial role is played by the telescopes repositioning speed,

more precise estimate. This quantity is usually computed in an offline analysis to find the final significance level.

[2]In this table the energy range reported for MAGIC considers the use of the standard stereo trigger [37] for observations. If the Sum-Trigger-II analog trigger [38, 39] is used the energy threshold can be lowered to ~ 20 GeV. The energy threshold reported for H.E.S.S. considers all five telescopes in the system.

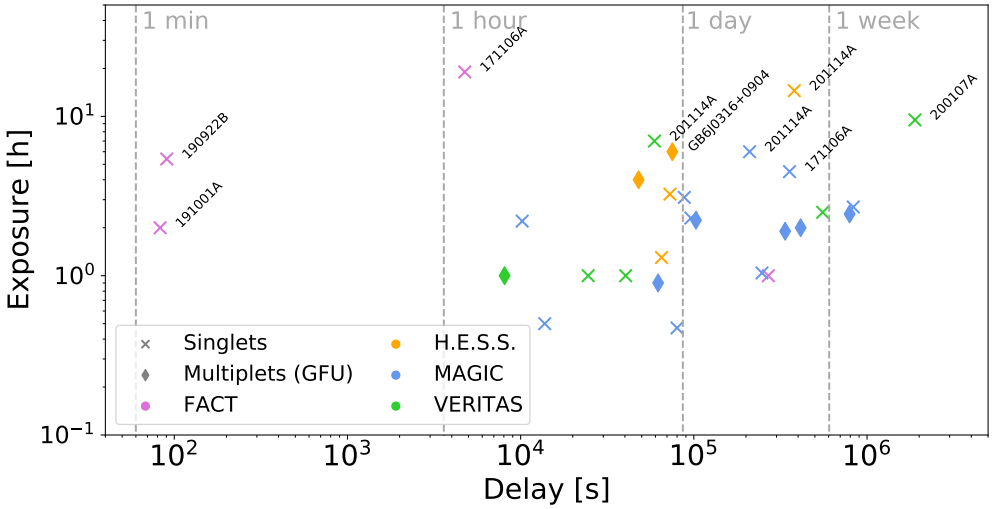

Figure 5.2: Exposure time of IACT observations as a function of the delay for followed-up alerts. The delay is calculated from the neutrino event arrival time (singlets) or the flare threshold-crossing time (multiplets) up to the start of the IACT observation. Observations performed with a start delay less than 100 s or with a total exposure longer than 4 h are Highlighted. Marker color represents the IACT observing facility (violet - FACT, orange - H.E.S.S., blue - MAGIC, green - VERITAS) while the marker type represents the alert type (cross - singlets, diamond - multiplets).

reported in Table 5.4, where we can observe that FACT and MAGIC are the fastest systems, the former reaching a speed of even 12 deg s^{-1}. Currently, FACT, MAGIC, and VERITAS automatically repoint to alerts received by GCN (i. e. singlets), while H.E.S.S. has an alert system allowing a fully automatic response also to multiplets [175]. The automatic reaction is triggered if the alert is received at night and fulfills specific requirements, independently set by each IACT. For example, MAGIC repoints automatically to singlet GOLD alerts visible during the night, with a 50% angular resolution $< 1°$, a zenith angle $< 60°$, and an angular distance to the Moon $> 30°$. The initial exposure for the alerts automatically followed-up is of 2.5 hours. In MAGIC, singlet BRONZE and multiplet alerts are evaluated case-by-case and scheduled manually.

In detail, the IACTs observed 11 out of the 62 single-event alerts sent by IceCube between October 2017 and January 2021, and 7 out of the 27 multiplet alerts sent between May 2019 and January 2021, including the only all-sky alert issued. Seven of the single-event alerts and one neutrino multiplet were observed by more than one IACT. The location in the sky of the alerts followed-up by at least one IACT is highlighted in color in Fig. 5.1. Information on the observation time spent by each IACT on each alerts is reported in Tables 5.1 and 5.2 for singlets and multiplets respectively. In these tables the instruments performing multi-wavelength observations are also reported for each alert.

The IACT delay and exposure for all single-event alerts and neutrino multiplets dis-

cussed here are presented in Figure 5.2. The delay is calculated from the neutrino event arrival time, in the case of singlets, or the time at which the significance threshold is exceeded, in the case of multiplets, up to the start of the IACT observation. Already from this broad overview, we can deduce some general trends in the follow-up strategies. Reaction within one day is achieved in 50% of the cases and observations performed more than one week after the trigger are rare. In two cases, the automatic reaction previously mentioned allowed to reduce the delay to few tens of seconds. Both observations were performed by FACT. The total time spent on public IceCube alerts follow-ups is very similar for all collaborations ($\sim$20 hours), but the approaches are different. In general, FACT, H.E.S.S., and VERITAS concentrated longer exposures on a few alerts, while MAGIC performed the highest number of follow-ups but with a shorter average exposure. Similar trends are observed for neutrino multiplet alerts.

5.3 IACTs observations and analysis

As already mentioned, IACT observations are concentrated in the period October 2017 − January 2021 for singlet alerts and May 2019 − January 2021 for multiplets. All observations were performed in wobble mode [43], allowing a simultaneous background measurement in the telescopes FoV. H.E.S.S. collected data using the four 12-m telescopes for all alerts except for the multiplet alert associated with the source 1ES 1312-423 where data from all five telescopes are included. MAGIC observed most of the alerts using the standard stereo trigger [37]. An exception is the AGN OP 313, associated with a multiplet alert. The observations of this source were performed using the Sum-Trigger-II analog trigger [38, 39] which delivers improved sensitivity at low energies.

The analysis was performed by each IACT independently using different packages [45, 176–179]. The procedure is the same described in Sect. 1.3.4 for all IACTs. In MAGIC, the data taken with Sum-Trigger-II had to undergo the MaTaJu cleaning (see Sect. 1.3.5) and be analyzed with lower cuts on the image size in order to keep faint signals (size$>$ 20 phe instead of the standard size$>$ 50 phe). Good-quality data were selected based on atmospheric conditions and hardware performance. The signal significance was computed through Eq. 1.12 [59]. In the flux computation, the sources spectral shape is assumed to be a simple power-law,

$$\frac{\mathrm{d}N}{\mathrm{d}E} = K\,E^{-\Gamma},$$

with an index $\Gamma = 2.5$, corresponding to the slope of the IceCube spectrum of the astrophysical neutrino flux. In MAGIC analysis, when necessary, the flux values were corrected for atmospheric extinction due to clouds and aerosols, using data from the LIDAR system at the MAGIC site [40].

No significant $\gamma-$ray emission has been detected from any of the targets under study, with the only exception of the source 1ES 1312-423, observed by H.E.S.S. and detected with a significance of 4σ above an energy threshold of 140 GeV. For all other

alerts, both differential and integral-flux upper limits above a given energy threshold (different for each alert and observatory) were calculated assuming the aforementioned spectrum. For the ULs calculation, we used the Rolke method [61, 180] with a confidence level set to 95%, and including a 30% global systematic uncertainty in the efficiency of the applied cuts, as described in Sect. 1.3.4. When an alert is observed by more than one IACT, we used the combined exposure to calculate joint ULs [181]. The calculation uses a profile maximum likelihood method with a likelihood functional form as the one reported in Eq. 1.18 and applies the likelihood ratio test for each telescope. Since different instruments provide independent observations, the test statistics of individual experiments, $-2\ln\lambda_i$, can be summed to compute a combined upper-limit value [174]:

$$-2\ln\lambda_{comb} = \sum_{i=1}^{N} -2\ln\lambda_i, \tag{5.1}$$

where N is the number of experiments involved in the follow-up of the same event. Note that in order to apply this method, all IACTs had to adopt the same energy binning. As an example, in Sect. 5.5.2, we report combined ULs for one source[3]. The analysis for the remaining sources will be available in the upcoming paper [174].

5.4 Multi-wavelength observations and analysis

In the following, we report information on the complementary observations performed by instruments operating in different bands of the electromagnetic spectrum.

5.4.1 *Fermi/LAT*

In HE $\gamma-$rays, observations were performed by *Fermi/LAT*, which operates a real-time monitoring program of public IceCube neutrino alerts, based on a systematic analysis of the region around the neutrino arrival direction, looking for possible counterparts [182]. This program showed its potential in the 2017 detection of the flaring blazar TXS 0506+056 in coincidence with the event IceCube-170922A, since the prompt observations carried out by *Fermi/LAT* triggered a rich campaign involving several instruments operating in the whole electromagnetic spectrum.

All observations follow the same analysis procedure. The analysis was performed with `Fermipy`[4] [65] and PASS8 response function [128]. The settings used in the data selection and analysis are reported in Table 5.5. For all sources the ROI is centered at the target position, and a cut on the zenith angle is applied in order to minimize the contamination of background $\gamma-$rays produced in the Earth atmosphere. For singlets a time range of one month centered at the neutrino arrival time is considered, while

[3]Note that FACT, H.E.S.S. and VERITAS allow statistical fluctuations of the number of γ-ray events in the signal region to go below the estimated background. These fluctuations are reduced by the combination of data sets from different instruments. The resulting, combined upper limits on the γ-ray flux can therefore be higher, i. e. less constraining, than the ones derived by the individual instruments.

[4]3http://fermipy.readthedocs.io/en/latest/

Setting	Value
Energy range	$0.1 - 800\,\mathrm{GeV}$
ROI	$15^\circ \times 15^\circ$
Zenith	$< 90^\circ$
Spatial bins	0.1°
Energy bins	10 per decade

Table 5.5: Settings applied on the data selection and analysis of neutrino counterparts with *Fermi/LAT*. The reported quantities are: energy range, ROI dimension, zenith range, width of spatial bins, number of energy bins.

for multiplets a period contemporaneous to the flare duration and IACTs observations is considered. For singlets, the analysis is centered at the coordinates of the candidate counterpart if present, otherwise the IceCube alert best-fit position is considered. A maximum likelihood analysis is applied to estimate the flux and spectrum of each target. It makes use of a model which includes all 4FGL sources [66] located within 20° from the ROI center as well as the Galactic and isotropic background diffuse emission. The sources spectral shape is taken directly from the 4FGL catalog. For energy bins with a low significance ($< 2\sigma$), flux upper limits are computed.

5.4.2 *Swift*

The *Neil Gehrels Swift observatory* [68] observed neutrino counterparts of 3 singlets (PKS 1502+106, NVSS J095508+355102, and NVSS J065844+063711, possible counterparts of IceCube-190730A, IceCube-200107A, and IceCube-201114A respectively) and 7 multiplets (MG1 J181841+0903, 1ES 1312-423, PMN J2016-0903, OP 313, GB6 J0316+0904, PMN J0325-1843, and OC 457) in the X-ray and optical/UV bands thanks to their *XRT* [70] and *UVOT* [71] telescopes on board.

The **X-ray** spectral analysis was performed in the $0.3 - 10$ keV energy range, using the `XSPECv12.9.1` software package. All *XRT* observations were performed in photon counting mode [72]. The spectrum was rebinned in energy and the Cash statistic [73] was used in the analysis. All XRT spectra are fitted with an absorbed power-law model and a fixed Galactic column density value in the direction of the source.

In the **optical/UV** band, *UVOT* observed the sources in all its filters (the optical v, b, u and the ultraviolet $w1$, $m2$, $w2$) during *XRT* pointings. Data were analyzed using the 20201215 CALDB-UVOTA release of the calibration database. The magnitude of the candidates is estimated through the aperture photometry technique. For each candidate, source counts were extracted from a circular region with a radius of of 5 arcsec centered on the source, while background counts were derived from a circular region of 20 arcsec radius in a nearby source-free region. Magnitudes were corrected for the Galactic extinction [76] and then converted into energy fluxes [75].

5.5 Results

In this section we report observational results on few interesting followed-up alerts. For each of them we give a description of the issued alert, summarize the results from VHE and multi-wavelength observations, and show the source SED. The SED was built with simultaneous multi-wavelength data, compared with archival data obtained from ASI ASDC [156] to have a visual representation of the possible changes in the source emission state. When possible, the VHE spectrum reporting instruments combined ULs is also shown. All the remaining alerts will be available in the upcoming paper [174]. Given that most of the results are flux ULs, a detailed modeling of the observed sources is out of the scope of this project, which is meant to be a reference catalog paper summarizing the status of the neutrino follow-up campaigns and the effort done in VHE $\gamma-$rays. In one case, the obtained flux ULs are put in context of already existing models in order to check if additional constraints on the VHE emission can be put.

5.5.1 Neutrino singlets

In this section, the main results on the follow-up of neutrino singlets are reported. Information on the tracks and a summary of observations at VHE can be found in Table 5.1.

IceCube-190730A / PKS 1502+106

The distant blazar PKS 1502+106 ($z = 1.84$ [183]) has been proposed as a potential electromagnetic counterpart to the IceCube-190730A GOLD alert in several publications (e. g. [184, 185]), as it is located within the 50% neutrino uncertainty region, precisely at 0.31° from the best-fit neutrino location.

Within IACTs, only MAGIC participated in the follow-up of the alert, observing at the source position for 3.1 hours on July 31st, a day after the alert was issued, within a zenith angle range of $29^\circ - 50^\circ$. The source was not detected. The integral-flux upper limit computed at the location of the source, above an energy threshold of 150 GeV, is $8.09 \times 10^{-12}\text{cm}^{-2}\text{s}^{-1}$.

Swift/XRT observations performed during 2019 found the source in a low activity state at the time of the neutrino flare, showing index and flux values consistent with archival data. The recovered flux in the $0.3 - 10$ keV energy range for observation dates close to the neutrino detection is reported in Table 5.6.

Since PKS 1502+106 was found to be in a quiet state in optical to γ-ray bands at the time of detection, the authors of [184] concentrated on the low-state long-term period of the source, compiling data from *WISE*, *Swift*/UVOT, *Swift*/XRT and *Fermi*-LAT telescopes in $2010 - 2014$. The SED of the candidate was modeled within a lepto-hadronic framework. Several different emitting region locations were tested to explain the multi-wavelength and neutrino emission. The authors favor the one placing the emitting region of PKS 1502+106 beyond the BLR but inside the dust torus. In Figure 5.3a we present this model together with the VHE γ-ray ULs obtained from the MAGIC observations and multi-wavelength data.

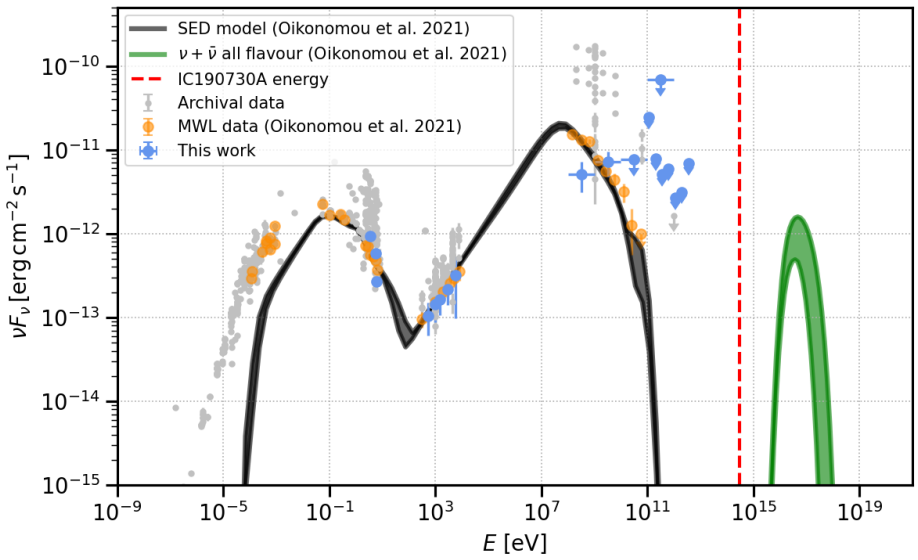

(a)

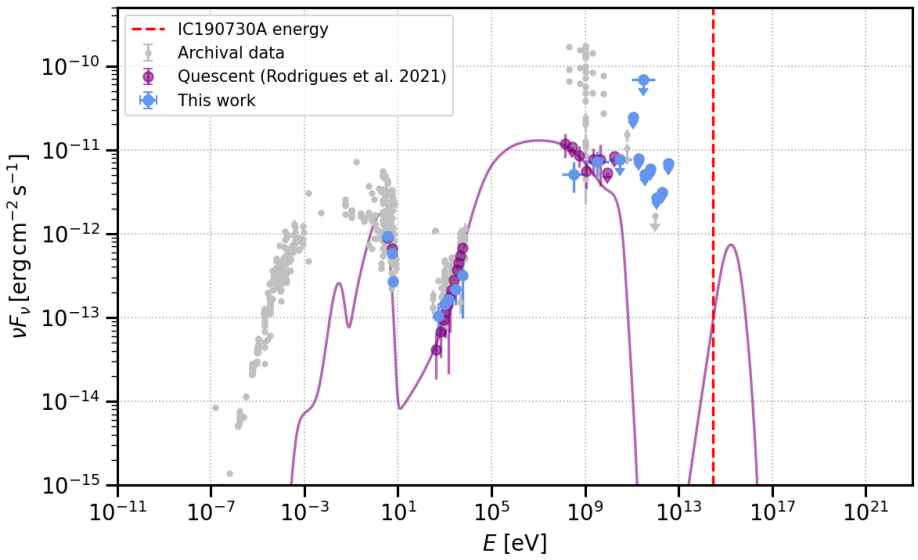

(b)

Figure 5.3: Multi-wavelength SED of PKS 1502+106 compared with model from [184] (a), and [185] (b).

Observation date	Exposure Time [s]	Γ	Flux 0.3-10 keV [$\times 10^{-12}$ erg cm^{-2} s^{-1}]
2019-01-03/31	5442	1.46 ± 0.26	1.14 ± 0.23
2019-06-20/27	2103	1.09 ± 0.52	1.38 ± 0.65
2019-07-04/30	4308	1.11 ± 0.37	1.10 ± 0.36
2019-08-01/09-20	3396	1.01 ± 0.42	1.17 ± 0.43
2019-12-20/27	2415	1.36 ± 0.41	1.20 ± 0.40
2020-01-03/31	4423	1.40 ± 0.34	0.89 ± 0.24

Table 5.6: Results of *Swift/XRT* observations on PKS 1502+106 around the time of the neutrino alert in 2019-2020.

Another work modeling the emission of this source in a lepto-hadronic context is the one from Rodrigues et al. [185], where authors selected three different emission states of the source starting from the 11-year *Fermi* light curve. Their model considers a single emitting region placed at the boundaries of the BLR, which allowed external inverse Compton emission from the BLR. This component dominates the hard X-ray and soft γ-ray emission, while soft X rays and hard $\gamma-$rays are dominated by photons originated in Bethe-Heitler processes and subsequent cascades. A comparison between the low state considered in Rodrigues et al. [185] and the results obtained in this work is shown in Fig. 5.3b.

Compared with both works, VHE γ-ray data do not provide strong constraints on either of these models. Moreover, from both Figures 5.3a and 5.3b a different trend in high energy (HE) γ-ray data from the paper and those from this work can be observed, while UV and X-ray data show a behavior consistent with the one reported in the two mentioned papers. Differences in HE γ-rays emission can derive from the non-simultaneity of the analyzed data, although each of the period considered coincides with a low state of activity of the source. Indeed we note that both Oikonomou et al. [184] and Rodrigues et al. [185] consider a long-term low-state period of activity of the source, while here we analyzed only one month of *Fermi* data centered on the neutrino arrival time. A detailed modeling of the source emission is beyond the scope of this work. However, we suggest our results as a possible starting point for further modeling.

5.5.2 Neutrino multiplets

In the following, the main results on the follow-up of neutrino multiplets are shown. A summary of observations can be found in Table 5.2, while details on the issued alerts are listed in Table 5.3.

Observation date	Exposure Time [s]	Γ	Flux $0.3-10$ keV $\times 10^{-12}$ erg cm^{-2} s^{-1}
2007-04-03	2130	1.47 ± 0.17	4.31 ± 0.66
2007-04-07	2793	1.52 ± 0.15	3.99 ± 0.50
2007-06-27	465	1.63 ± 0.34	4.59 ± 1.20
2007-07-31	852	1.82 ± 0.30	2.97 ± 0.65
2007-08-01	4409	1.53 ± 0.15	3.09 ± 0.36
2007-08-05	4181	1.49 ± 0.12	4.61 ± 0.43
2008-05-12	7911	1.58 ± 0.11	2.58 ± 0.23
2008-08-20	4755	1.48 ± 0.13	3.76 ± 0.40
2009-12-12	2303	1.66 ± 0.26	1.70 ± 0.33
2010-04-15	1975	1.47 ± 0.33	2.40 ± 0.62
2011-04-17	3249	1.61 ± 0.28	1.16 ± 0.25
2011-07-03	4722	1.90 ± 0.21	1.21 ± 0.17
2014-05-04	3486	1.65 ± 0.16	2.72 ± 0.40
2014-06-29	3494	1.60 ± 0.18	2.22 ± 0.30
2019-06-20	1870	2.03 ± 0.31	1.35 ± 0.28
2019-12-27	2035	1.55 ± 0.24	2.82 ± 0.48
2019-12-29	1865	1.53 ± 0.23	2.79 ± 0.52
2019-12-31	1249	1.47 ± 0.28	3.09 ± 0.69
2020-03-11	1641	1.70 ± 0.22	3.41 ± 0.55
2020-03-16	2238	1.67 ± 0.23	2.56 ± 0.45
2020-03-21	2218	1.50 ± 0.22	2.85 ± 0.51
2020-05-21	2492	1.61 ± 0.22	2.25 ± 0.38
2020-05-25	2230	1.59 ± 0.25	2.22 ± 0.40
2020-05-29	2048	1.70 ± 0.23	2.44 ± 0.41
2020-06-02	2794	1.48 ± 0.23	2.36 ± 0.42
2020-06-06	2899	1.51 ± 0.20	2.44 ± 0.39
2020-06-10	3037	1.56 ± 0.22	2.02 ± 0.35
2020-06-14	2737	1.68 ± 0.20	2.29 ± 0.35

Table 5.7: Results of *Swift/XRT* observations on OP 313 between 2007 and 2020.

OP 313

OP 313 is a flat-spectrum radio quasar with redshift $z = 0.996$ [186] located at RA: 13° 10′ 28″.66, Dec: +32° 20′ 43″.78. Between April and August 2020, IceCube reported the detection of four multiplet events from this object, with a duration ranging from 57 to 167 days, and a significance slightly above the trigger threshold of 3σ (more details on Table 5.3).

The MAGIC telescopes observed the source on June 19th, 20th and 23rd within a low zenith range of $16° - 34°$ using the the Sum-Trigger-II analog trigger in order to reach low energies. The observations were performed in good weather conditions, allowing 3.2 hours of good quality data to be collected. The source was not detected at VHE and an integral-flux upper limit of 5.20×10^{-11} cm^{-2} s^{-1}, above an energy threshold of

Obs. date	v mag	b mag	u mag	$w1$ mag	$m2$ mag	$w2$ mag
2007-04-03	16.91 ± 0.08	17.39 ± 0.07	16.56 ± 0.07	16.58 ± 0.08	16.66 ± 0.08	16.96 ± 0.07
2007-04-07	17.58 ± 0.09	18.20 ± 0.08	17.25 ± 0.07	17.20 ± 0.08	17.22 ± 0.09	17.57 ± 0.07
2007-06-27	-	-	-	-	17.46 ± 0.10	-
2007-07-31	16.56 ± 0.16	16.98 ± 0.12	16.20 ± 0.07	16.28 ± 0.06	16.15 ± 0.14	16.66 ± 0.12
2007-08-01	16.73 ± 0.06	17.24 ± 0.06	16.45 ± 0.06	16.55 ± 0.06	16.66 ± 0.04	16.93 ± 0.06
2008-05-12	-	-	-	-	17.32 ± 0.06	-
2008-08-20	-	-	-	-	16.70 ± 0.06	-
2009-12-12	-	-	-	-	-	18.59 ± 0.08
2010-04-15	-	-	-	-	-	18.39 ± 0.08
2011-04-17	18.85 ± 0.31	19.82 ± 0.31	18.22 ± 0.14	18.12 ± 0.14	18.08 ± 0.14	18.68 ± 0.13
2011-04-17	-	-	18.40 ± 0.07	-	-	18.53 ± 0.12
2011-07-03	18.10 ± 0.15	18.71 ± 0.13	17.72 ± 0.11	17.64 ± 0.11	17.74 ± 0.11	18.21 ± 0.07
2014-05-04	18.27 ± 0.08	17.91 ± 0.10	18.03 ± 0.16	18.16 ± 0.17	19.31 ± 0.26	18.28 ± 0.25
2014-06-05	-	19.48 ± 0.26	18.20 ± 0.15	18.09 ± 0.15	-	18.57 ± 0.08
2014-06-10	> 19.09	19.50 ± 0.24	19.58 ± 0.18	18.29 ± 0.16	18.08 ± 0.08	18.65 ± 0.14
2014-06-29	18.91 ± 0.33	19.79 ± 0.31	18.20 ± 0.15	18.22 ± 0.15	18.15 ± 0.17	18.50 ± 0.08
2019-06-20	16.52 ± 0.07	17.05 ± 0.07	16.31 ± 0.07	16.35 ± 0.08	16.35 ± 0.08	16.70 ± 0.07
2019-12-27	16.51 ± 0.07	16.99 ± 0.07	16.16 ± 0.06	16.35 ± 0.08	16.34 ± 0.08	16.57 ± 0.07
2019-12-29	16.52 ± 0.08	16.89 ± 0.06	16.20 ± 0.06	16.27 ± 0.08	16.27 ± 0.08	16.58 ± 0.07
2019-12-31	16.43 ± 0.07	16.80 ± 0.06	16.20 ± 0.06	16.16 ± 0.07	16.44 ± 0.08	16.87 ± 0.08
2020-03-11	-	-	-	15.84 ± 0.06	-	-
2020-03-16	-	-	16.08 ± 0.05	-	-	-
2020-03-21	-	-	-	-	-	16.32 ± 0.06
2020-05-21	17.18 ± 0.09	17.87 ± 0.08	17.07 ± 0.08	17.14 ± 0.09	17.17 ± 0.09	17.45 ± 0.08
2020-05-25	17.16 ± 0.09	17.76 ± 0.08	16.99 ± 0.08	17.03 ± 0.09	17.24 ± 0.10	17.52 ± 0.09
2020-05-29	17.14 ± 0.09	17.68 ± 0.08	16.94 ± 0.08	16.94 ± 0.09	16.96 ± 0.11	17.28 ± 0.08
2020-06-02	17.29 ± 0.09	17.73 ± 0.07	16.88 ± 0.07	17.00 ± 0.08	17.04 ± 0.09	17.24 ± 0.08
2020-06-06	17.28 ± 0.09	17.90 ± 0.08	17.03 ± 0.07	17.06 ± 0.09	17.16 ± 0.09	17.34 ± 0.08
2020-06-10	17.64 ± 0.11	18.08 ± 0.09	17.21 ± 0.08	17.30 ± 0.09	17.43 ± 0.10	17.72 ± 0.08
2020-06-14	17.56 ± 0.11	18.03 ± 0.09	17.37 ± 0.08	17.30 ± 0.09	17.37 ± 0.10	17.59 ± 0.08

Table 5.8: Results of *Swift/UVOT* observations on OP 313 between 2007 and 2020.

55 GeV, was computed.

Multi-wavelength observations by *Swift* were carried out 32 times between April 3rd, 2007 and March 17th, 2021. The $0.3 - 10$ keV spectrum can be fitted with an absorbed power-law model with N_H fixed to $1.23 \times 10^{20}\,\mathrm{cm}^{-2}$. After a period of high activity in 2007, the X-ray flux of OP 313 decreased during $2008 - 2014$. A new increase of activity has been observed starting from 2019, December 27th up to 2020, March 21st, period which is partly contained in the time window of the neutrino multiplet (starting on 2020, February 12th). An increase of activity has been observed also in optical and UV bands during December 2019−March 2020, similar to what is observed in X-rays. Results from *Swift/XRT* and *Swift/UVOT* analyses are reported in Tables 5.7 and 5.8 respectively, while the multi-wavelength SED comparing simultaneous observations to archival data is shown in Fig. 5.4.

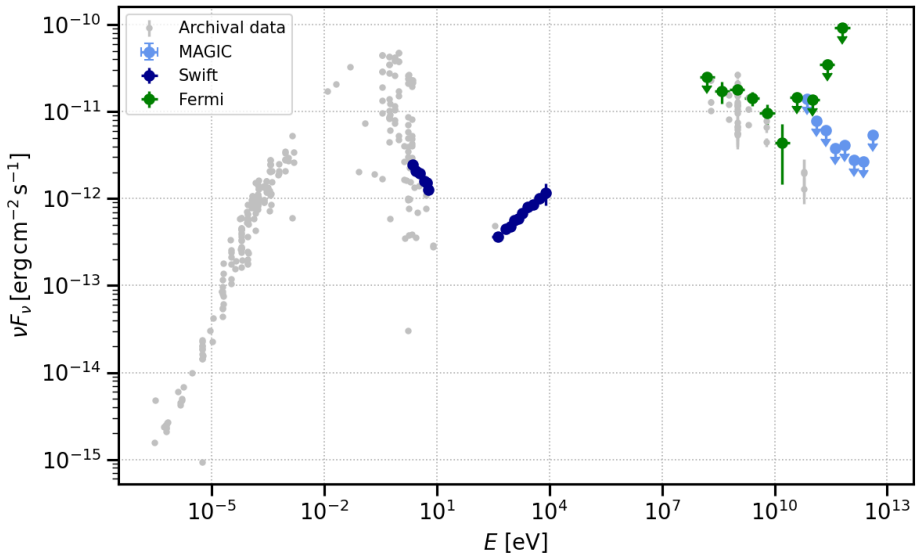

Figure 5.4: Multi-wavelength SED of OP 313 showing archival observations and observations obtained during the period following the multiplet neutrino alert.

GB6 J0316+0904

GB6 J0316+0904 is a BL Lac type object with redshift z = 0.372 [187] located at RA: 03° 16′ 12″.733, Dec: +09° 04′ 43″.283. It was selected as a potential target for the neutrino multiplet program for all three participating IACTs. A multiplet flare was reported by IceCube on January 15th, 2021, with a short duration of ∼2.5 days and a significance of 3.1 σ just above the trigger threshold (more details on Table 5.3).

The VERITAS telescopes were first on target thanks to their automatic response and collected data on the same night of the alert issuing. H.E.S.S. pointed to the source within the following 24 hours and extended the observations over the three following days. MAGIC started observing three days after the alert; earlier observations were not possible due to high humidity on site. The total observation time spent by each IACT on the source is reported in Table 5.2. No detection was achieved by any of the IACTs. Figure 5.5a shows the differential-flux ULs at VHE, obtained by combining the data from all three IACTs and computed with the method described in Sect. 5.3.

Swift observed the source 5 times between 2009, March 9th and 2015, January 9th, i. e. before the neutrino alert. The $0.3 - 10$ keV spectrum can be fit with an absorbed power-law model with N_H = 1.27 $\times 10^{21}$ cm^{-2}. Observations carried out on July 3rd and 4th, 2011 are summed together in order to improve the statistics for the spectral fit. Results show a significant variability in both the X-ray and optical/UV bands (see Tables 5.9 and 5.10 for X-rays and optical/UV respectively). However, a comparison with the source activity at the time of the neutrino alert is not possible since there are no *Swift* observations in that period. The source SED showing simultaneous multi-

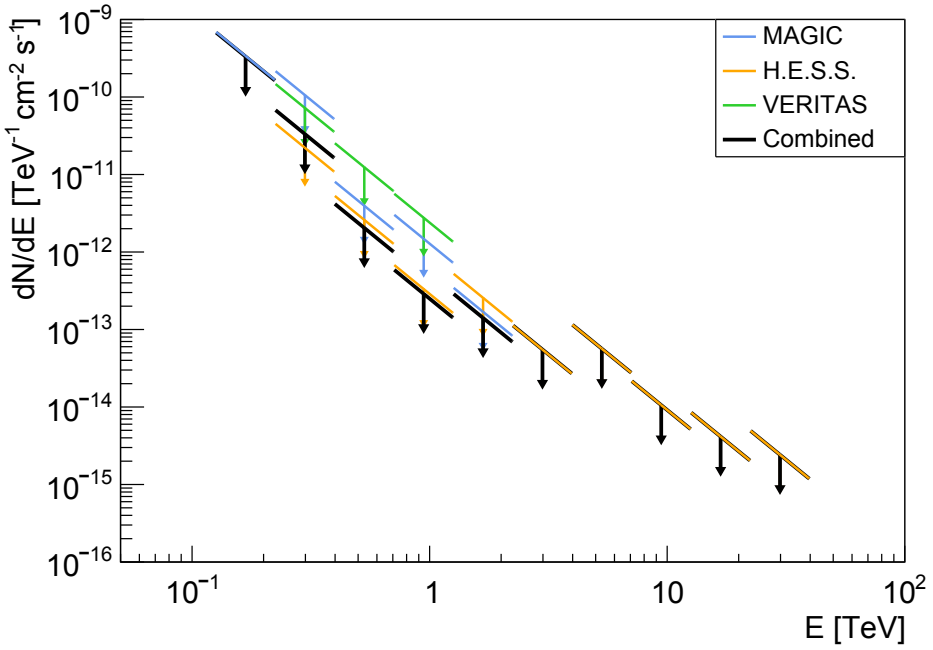

(a)

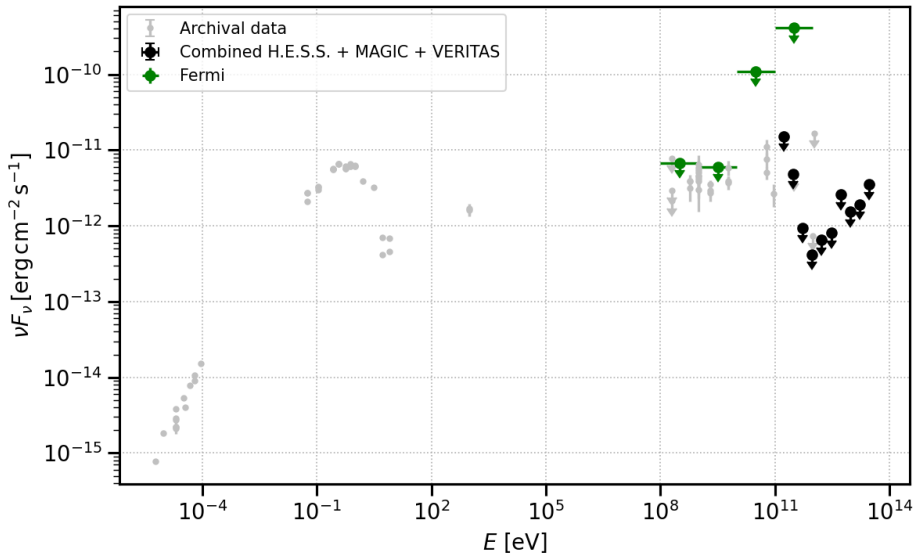

(b)

Figure 5.5: Combined differential flux UL at VHE (a), and multi-wavelength SED (b) for GB6 J0316+0904.

Observation date	Exposure Time second	Γ	Flux $0.3-10$ keV $\times 10^{-12}$ erg cm^{-2} s^{-1}
2009-03-09	2487	1.94 ± 0.10	16.0 ± 1.2
2010-11-23	974	2.23 ± 0.85	1.17 ± 0.45
2011-07-03/04	3259	2.27 ± 0.33	1.05 ± 0.23
2015-01-09	2645	1.97 ± 0.24	2.34 ± 0.39

Table 5.9: Results of *Swift/XRT* observations on GB6 J0316+0904 between 2009 and 2015.

Obs. date	v mag	b mag	u mag	$w1$ mag	$m2$ mag	$w2$ mag
2009-03-09	15.91 ± 0.12	16.47 ± 0.05	15.79 ± 0.05	16.37 ± 0.06	> 16.57	16.89 ± 0.07
2010-11-23	16.64 ± 0.11	17.54 ± 0.10	17.02 ± 0.11	17.59 ± 0.14	18.32 ± 0.20	18.10 ± 0.13
2011-07-03	16.38 ± 0.12	17.32 ± 0.12	16.53 ± 0.10	17.08 ± 0.12	17.74 ± 0.16	17.78 ± 0.08
2011-07-04	16.62 ± 0.13	17.10 ± 0.10	16.55 ± 0.09	17.35 ± 0.13	17.73 ± 0.11	17.73 ± 0.11
2015-01-09	17.63 ± 0.12	18.33 ± 0.12	17.81 ± 0.11	18.39 ± 0.16	18.95 ± 0.19	19.04 ± 0.15

Table 5.10: Results of *Swift/UVOT* observations on GB6 J0316+0904 between 2009 and 2015.

wavelength data is reported in Fig. 5.5b.

5.6 An investigation of the detection chances on individual sources with MAGIC

The sources monitored for the identification of neutrino clusters were selected from the 3LAC [28] and 3FHL [29] *Fermi* catalogs based on their $\gamma-$ray energy flux, expected to correlate with a state of enhanced neutrino emission, and additional selection criteria, aimed at maximizing their detectability prospects at VHE (see Sect. 1.2.1). The VHE detectability of the sources was computed starting from their average *Fermi* flux reported in the catalogs, multiplied by a factor of 10 in order to simulate a flare. The resulting spectrum was then extrapolated at $E > 100$ GeV in order to evaluate the significance of the observation for a defined amount of observation time. For MAGIC the considered time is 2 hours. Only the sources exceeding a significance of 5σ are kept in the selection. The final list comprises 179 sources for MAGIC and a total of 339 objects if we consider also those monitored for H.E.S.S. and VERITAS.

However, performing the selection based on the average flux does not take into account possible temporal changes of the sources flux over time, which is an important factor since AGNs are known to be variable objects. In order to have a more precise estimation of their detectability chances with MAGIC, we re-performed the same analysis on the sources lightcurves, making the extrapolation on the flux observed by *Fermi*

in each time bin, rather than on the average flux. In this case we did not simulate any flare on the source fluxes, considering the actual flux values observed.

We concentrated our work on the list of 179 objects monitored by IceCube for MAGIC, selecting only those for which we received at least one neutrino alert in the past. These include both the set of sources related to the previous sections, as well as those sources showing at least one multiplet alert in the archival search performed by [22]. The selection comprises three sets of sources reporting respectively:

- only one alert;
- more than one alert, with all alerts showing the same start date of the neutrino flare, meaning that they can be potentially related to the same flare;
- more than one alert, with some of them showing a different start date of the neutrino flare, meaning that they can potentially come from different neutrino flares.

Within these three sets, the last one comprises the most interesting sources under the point of view of neutrino emission, since it is possible that these objects underwent different neutrino flares in the past. Besides the sources in the list, we also added the possible counterpart to the all-sky flare mentioned in Sec. 5.1, which was observed by IceCube in September 2019. The potential counterpart is the source PMN J0325-1843, a blazar candidate of unknown type without a redshift estimation[5]. In order to make the extrapolation also for this source, we assumed as redshift the median value of all sources in the catalogs, which is $z = 0.4$.

For all the considered sources, the lightcurves were built over 9.5 years of data, starting from August 2008, with time bins of 28 days and an integral flux per bin computed above an energy threshold of 1 GeV. For the extrapolation at VHE, we used the spectral shape and parameters reported in the 3FGL [188] and 3FHL catalogs for each single source. When a source shows a redshift $z > 0.01$, the effect of EBL absorption is taken into account in the computation of the spectral shape. For example, in the case of a LogParabola, the spectral functional form used is:

$$\frac{dN}{dE} = N_0 \times \left(\frac{E}{E_b}\right)^{-[\alpha+\beta\ln(E/E_b)]} e^{-\tau}, \tag{5.2}$$

where the term $e^{-\tau}$ is the absorption factor, with τ the optical depth, tabulated in [189] for different energy bins and redshift values.

In order to estimate the significance of an observation in the VHE band, Eq. 1.12 is used, where the number of signal events is recovered according to Eqs. 1.15 and 1.16 for each time bin in the lightcurve. In the computation, we used the effective area of the MAGIC telescopes, the source spectrum previously defined, scaled with the flux observed in the interested time bin, and an assumed observation time. In the following we report the results for observations of 2 hours, 10 hours and 50 hours for all sources

[5]Note that the unknown redshift prevents it to be part of the list of 179 monitored sources.

showing at least one alert in the past [22]. They are shown in Table 5.11. From this table we can observe that very few objects are bright enough to be probably detected by MAGIC with just 2 hours of observation. Those showing a non-zero number of bins with a detection significance $> 5\sigma$ for this amount of time are $\sim$ 20% of the total number of sources here considered. If we consider only those objects showing a $> 5\sigma$ significance in at least 30% of the total bins, this number reduces to just $\sim$ 8% of the sources in the table. Moreover, a large fraction of the sources would have never been detected even with 50 hours of observation in the 9.5 years considered for the analysis. They represent 47% of the full sample reported in the table. This result suggests that such bright flares as the ones simulated to select the whole list of monitored sources are very rare and that 47% of the objects considered here has never undergone a bright-enough flare in $\gamma-$rays allowing the MAGIC telescopes to detect them with even 50 hours of observation.

	3FGL name	Alias	Det. bins 2h	Det. bins 10h	Det. bins 50h
One alert	3FGL J0112.8+3207	4C +31.03	0%	0%	0%
	3FGL J0128.5+4430	GB6 J0128+4439	0%	0%	0%
	3FGL J0221.1+3556	S3 0218+35	0%	0%	1.7%
	3FGL J0316.1+0904	GB6 J0316+0904	0%	6.7%	43%
	3FGL J0342.2+3857	GB6 J0342+3858	0%	0%	0%
	3FGL J0349.2-1158	1ES 0347-121	0.8%	14%	34%
	3FGL J0424.7+0035	PKS 0422+00	0%	0%	2.5%
	3FGL J0608.0-0835	PKS 0605-08	0%	0%	0%
	3FGL J0750.6+1232	OI 280	0%	0%	0%
	3FGL J0809.8+5218	1ES 0806+524	8.4%	42%	84%
	3FGL J0909.0+2310	RX J0908.9+2311	0%	3.4%	30%
	3FGL J1031.0+7440	S5 1027+74	0%	0%	2.5%
	3FGL J1015.0+4925	1ES 1011+496	40%	98%	100%
	3FGL J1028.5-0235	PMN J1028-0237	0%	0%	0%
	3FGL J1105.9+2814	MG2 J110606+2812	0%	0%	0%
	3FGL J1127.8+3618	MG2 J112758+3620	0%	0%	0%
	3FGL J1217.8+3007	1ES 1215+303	24%	76%	98%
	3FGL J1218.0-0029	PKS 1215-002	0%	0%	0%
	3FGL J1221.3+3010	1ES 1218+304	50%	90%	98%
	3FGL J1224.5+2436	MS 1221.8+2452	0%	9.2%	24%
	3FGL J1230.9+1224	M 87	0%	4.2%	50%
	3FGL J1312.7+4828	GB 1310+487	0%	0.8%	2.5%
	3FGL J1416.0+1325	PKS B1413+135	0%	0%	0%
	3FGL J1419.9+5425	OQ 530	0%	0%	0%
	3FGL J1555.7+1111	PG 1553+113	97%	100%	100%
	3FGL J1628.2+7703	6C B163030.4+771303	0%	0%	0.8%
	3FGL J1728.5+0428	PKS 1725+044	0%	0%	0%
	3FGL J1734.3+3858	B2 1732+38A	0%	0%	0%
	3FGL J1743.9+1934	1ES 1741+196	0%	8.4%	40%
	3FGL J1849.2+6705	S4 1849+67	0%	0%	0%

	3FGL J2016.4-0905	PMN J2016-0903	0%	0%	7.6%
	3FGL J2250.1+3825	B3 2247+381	6.7%	38%	60%
>1 alert, same flare	3FGL J0217.2+0837	ZS 0214+083	0%	0.8%	3.4%
	3FGL J0319.8+1847	RBS 0413	0.8%	18%	40%
	3FGL J0423.2-0119	PKS 0420-01	0%	0%	0%
	3FGL J0521.7+2113	VER J0521+211	56%	96%	100%
	3FGL J1058.6+5627	TXS 1055+567	0%	5.0%	50%
	3FGL J1442.8+1200	1ES 1440+122	0%	11%	41%
	3FGL J1818.6+0903	MG1 J181841+0903	0%	0%	0%
	3FGL J1829.6+4844	3C 380	0%	0%	0%
	3FGL J2143.5+1744	OX 169	0%	0%	0%
>1 alert, more flares	3FGL J0137.0+4752	OC 457	0%	0%	0%
	3FGL J0141.4-0929	PKS 0139-09	0%	0%	0%
	3FGL J0232.8+2016	1ES 0229+200	0%	10%	29%
	3FGL J0416.8+0104	1ES 0414+009	0%	3.4%	33%
	3FGL J0509.4+0541	TXS 0506+056	0.8%	5.9%	38%
	3FGL J0937.7+5008	GB6 J0937+5008	0%	0%	0%
	3FGL J1310.6+3222	OP 313	0%	0%	0%
	3FGL J1647.4+4950	SBS 1646+499	0%	0%	0.8%
	3FGL J1955.1+1357	87GB 195252.4+135009	0%	0%	0%
all-sky	3FGL J0326.0-1842	3PMN J0325-1843	0%	0%	0%

Table 5.11: Detectability at VHE of IceCube monitored sources for which at least one multiplet alert was received by MAGIC. The sources are divided based on the number and type of alerts received: only one alert, >1 alert, with all alerts showing the same start date (i. e. potentially coming from the same flare), and >1 alert, with some of them showing a different start date of the neutrino flare (i. e. potentially coming from different flares). In addition, the last line shows the detectability of the source associated with the only all-sky alert received. The columns show the 3FGL name of the sources, their associated counterpart, and the percentage of time bins for which the sources are detected by MAGIC with 2 hours, 10 hours and 50 hours of observation. These last values were computed by dividing the number of time bins where the significance of the observation resulted to be $> 5\sigma$ by the total number of time bins, which is 119 for each source.

As already mentioned before, the sources in the third group are so far the most interesting ones under the neutrino-emission point of view. However, according with the table, most of them are very faint. Indeed, only 4 objects out of 9 show a non-zero probability of being detected with 50 hours of observation time. Within them, TXS 0506+056 results to be the one with the highest number of detected time bins, although they are only the $\sim 38\%$ of the total number of bins. If we consider 2 hours of

observation, only the 0.8% of the bins is detected, corresponding to 1 bin out of the total 119 and being it the period of the famous 2017 flare. Besides the 2017 neutrino event, this source resulted to be associated also with 4 neutrino multiplets in the past (see Sect. 3.1): three of them in 2015, all showing the same flare start date, and one in 2016, with a different start date of the neutrino flare. All these events make TXS 0506+056 an interesting object under the neutrino-emission point of view.

Other interesting candidates regarding the received neutrino alerts are OP 313 and SBS 1646+499. The former shows 4 neutrino multiplet alerts in the past, all happening in 2020 and three of them reporting the same start date (see also Table 5.3 and Sect. 5.5.2). It may also be the possible counterpart of the singlet event IceCube-120515A ($\sim$ 200 TeV). The latter shows 4 neutrino multiplet alerts in the past (one in 2013, one in 2014, two in 2016), all possibly related to different neutrino flares. However, the detectability prospect at VHE for these objects are very low, since for 50 hours of observation, OP 313 results to be non-detectable in each of the considered time bins, while SBS 1646+499 results to be detectable in only the 0.8% of the cases.

5.7 Discussion and outlook

In this work, we have presented results from the neutrino follow-up programs of the FACT, H.E.S.S., MAGIC, and VERITAS experiments. These programs have evolved significantly over the years as more has been learned about the properties of the astrophysical neutrino flux and its potential sources, and as new alert streams have been made available by IceCube through the upgrade of the GFU program (see Sect. 1.2.1). Within this context, each IACT collaboration implemented its own observing priorities, and the resulting observations turn out to be highly complementary to each other (see Sect. 5.2). These efforts are an integral part of the current long-term science programs of the IACT observatories. The significant observation times allocated to the follow-up of neutrino events allow for the coverage of a large parameter range in terms of observed events, delay times between the neutrino event(s), and duration of the observations.

The IACTs performed follow-up observations of six multiplets and one all-sky alert from May 2019 to January 2021. The sources monitored for the search of multiplet events are mostly composed of BL Lac objects and FSRQs, expected to be potential neutrino emitters and selected based on their detectability prospects at VHE. In order to computed their detectability, the selection criteria include a simulated flaring state based on their average flux in HE $\gamma-$rays. However, as already mentioned in Sect. 5.6, this simulation does not account for variations of the source flux over time, leading to a possible overestimation of the detection chances of the selected objects. This is confirmed by the subsequent study performed on a selection of the sources monitored for MAGIC, where the monthly fluxes recovered in their 9.5-years lightcurve were considered. The $\sim$ 47% of the selected objects results to be non-detectable even with 50 hours of observation, suggesting that a revision of the list of monitored source based on their actual flux variations over time may be beneficial in the selection of candidates with higher detectability chances. However, although most of the followed-up sources

would need a larger amount of observation time, the differential flux upper limits given by the IACTs in the TeV $\gamma-$ray regime together with the X-ray observations can be used to constrain maximum contributions from photo-hadronic interactions, and the combined upper limits from all IACTs increase our constraints on SED models.

Furthermore, the IACTs performed follow-up observations of eleven IceCube singlet events between September 2017 and January 2021. These events have a relatively high signalness (compared to low energy events) and small uncertainty region (of the order of 1°). In addition, potential counterpart sources are found within the uncertainty region of six events. It is an ideal data sample for IACTs to search TeV $\gamma-$ray signals from the photo-hadronic interactions. The main purpose of this work is to serve as a legacy data set. While a detailed SED modeling for all sources is beyond the scope of this project, we used PKS 1502+106 (Sec. 5.5.1) as an example to discuss the potential effects as well as the limitation of our results on the current modeling works, and suggest our results as a possible starting point for further modeling.

Looking to the future, the geographical distribution of the observatories in latitude has enabled full-sky coverage across Northern and Southern hemispheres, and their location in longitude expands the total sky observable area of the combined IACT network, increasing the likelihood of a prompt follow-up observation in cases where the visibility from one observatory site is constrained by weather, sunlight, bright moonlight, or technical issues. This aspect is critically important to enable VHE γ-ray observations of rare transient neutrino candidate events, or in the search for other time-domain or multi-messenger triggers, as has been demonstrated recently by follow-up observations of gravitational wave events (e.g., GW170817A [190]) and γ-ray bursts detectable in the VHE range (see [191] for an overview of recent detections). This underlines the value of conducting analyses combining all available IACT data as presented in this project. All follow-up programs are ongoing and further analyses of this kind will prove highly beneficial in the search for VHE counterparts to neutrino events.

In the absence of a clear association of multi-wavelength signatures with neutrino alerts, these broad searches need to continue in the future. The upcoming Cherenkov Telescope Array has included neutrino follow-up observations as part of the Key Science Projects to be conducted with high priority in the early years of the observatory [192]. The significant increase in sensitivity and the full-sky coverage provided by its installation on both hemispheres promise exciting breakthroughs [193] in these searches. Further improvements are also expected in the near future with the onset of science operations of the KM3NeT neutrino telescope in the Mediterranean Sea [194], further extensions to the Gigaton Volume Detector (GVD) installation in Lake Baikal [195], and other proposed neutrino telescopes such as P-ONE [196] and the TRIDENT [197]. These facilities will be able to identify more astrophysical neutrino candidate events, improve the angular resolution of the overall dataset and due to their location in the Northern hemisphere, they will offer a view of the Galactic Plane complementary to that provided by IceCube. The next-generation IceCube detector, IceCube-Gen2 [198], will provide significantly increased sensitivity to high-energy neutrinos in the next decade due to its larger volume, and will therefore improve multi-messenger searches like the

ones presented here.

Chapter 6

Development of hadronic emission models into the open-source python package agnpy

The emission of jetted AGNs and blazars is usually interpreted by means of software tools implementing the radiative processes of non-thermal, relativistic particles (both leptons and hadrons) accelerated in their jets. This approach is very effective in advancing the theoretical understanding of the field. Indeed, modeling the broadband SED of such astrophysical objects allows to infer the non-thermal energy distribution of the emitting particles, the location of the emission sites, and to investigate the jet composition, with the ultimate aim of identifying the long-sought sources of cosmic-rays. However, the currently available modeling software programs including also a hadronic description of AGNs emission are private (see e. g. [159, 199–204]). This limits their usage by the astrophysical community at large and makes it difficult to reproduce or verify the obtained results.

Open-source software programs do also exist. Among them, `naima`[1,2] [205] is the first python package aimed at modeling the non-thermal emission of astrophysical objects made publicly available. It assumes comoving densities of interacting particles, hence being more appropriate to interpret the radiation from unbeamed sources, like for example supernova remnants.

`JetSet`[3,4] is a `C/Python` package developed to reproduce radiative and accelera-

[1] https://github.com/zblz/naima
[2] https://naima.readthedocs.io/en/latest/
[3] https://github.com/andreatramacere/jetset
[4] https://jetset.readthedocs.io/en/latest/index.html

tion processes acting in galactic and extragalactic jetted sources. It is a time-dependent code evolving the particle distribution according to its acceleration and cooling, and computing the emitted non-thermal spectra due to radiative processes. However, this package mainly considers leptonic processes. The only hadronic process it implements consists of proton-proton (pp) interactions, which do not have a relevant contribution in the emission of jetted AGNs, since the environment of these objects is mainly constituted of photon fields. The role of pp interactions becomes important only in the case of a proton target (like e. g. a star [206] or a red giant [207]) entering the jet.

In this chapter, we describe the implementation of two hadronic processes relevant in AGNs and blazars emission into `agnpy` [102], an open-source python package specifically designed to model the broadband SED of jetted AGNs. The package was initially built including only leptonic processes, thus not capable of estimating a possible neutrino flux from the sources under study. With the development of hadronic processes, we made `agnpy` the first open-source software able of a lepto-hadronic interpretation of AGNs emission. The processes I took care of implementing are the synchrotron emission from relativistic protons in the jet and the radiation of secondary particles from photo-meson interactions, with the latter being the most commonly considered in hadronic modeling scenarios. They will be described in detail in the next sections. Results from this project have been published in the proceeding [208]. The work here described was also conducted within the scope of a Master thesis [209], where I coworked with the student in the code development but also had an important advising role.

6.1 The `agnpy` package

As already mentioned, the package `agnpy` was created with the aim of providing an open-source software for the modeling of jetted AGNs. It is entirely written in the `python` programming language and built of the `Numpy` [210], `SciPy` [211], and `astropy` [212] packages.

Before our development, `agnpy` only provided leptonic radiative processes from an electron distribution accelerated in a spherical region, known as plasmoid or blob, streaming relativistically along the jet. These processes include synchrotron emission (implemented following [213]) and inverse Compton, either in the form of Synchrotron Self Compton [213] or External Compton [103, 104], both allowing the computation of the cross-section in the Klein-Nishina regime. Additionally, the package takes into account the absorption due to $\gamma\gamma$ pair production [214]. The latter is due to the interactions of high-energy photons with target photon fields provided for example by thermal and line emitters (as disk, broad line region or torus), synchrotron photons, the CMB, or the EBL. Regarding EBL, values of the absorption factor are computed as a function of energy and redshift from the optical depth tabulated in different works. The available models are [215–218], with the latter being implemented by myself into `agnpy`. These photon fields can be used as targets also for the external Compton scattering. Moreover, besides using them as targets for other processes, it is possible to directly

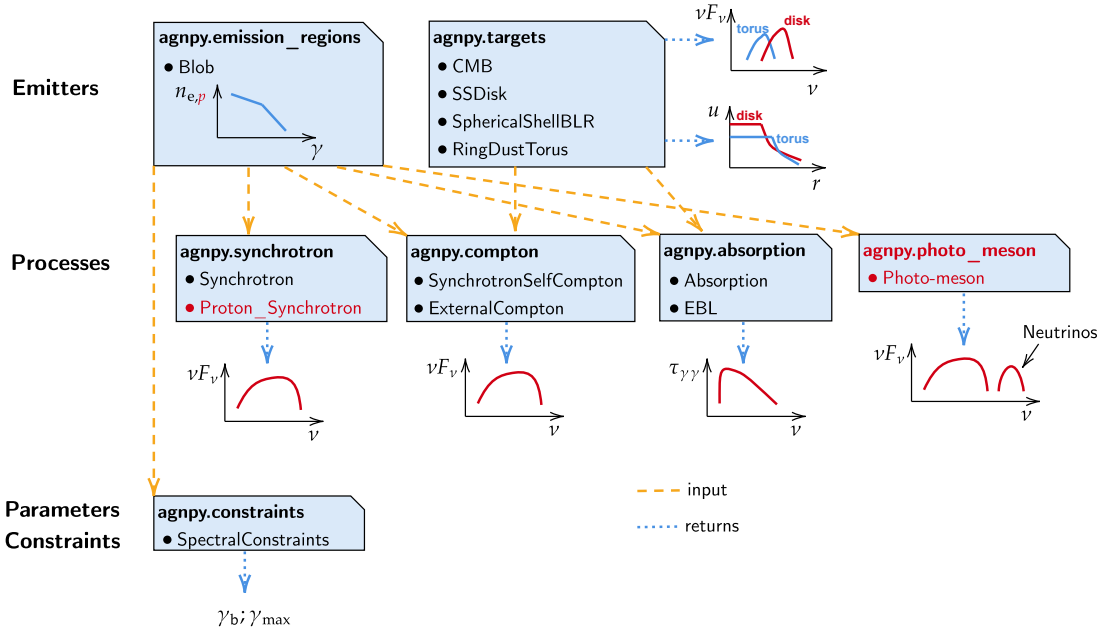

Figure 6.1: Schematic representation of agnpy structure. All modules implemented in the package and their functionality are shown. The emitters (emission regions and targets) are given as input to the radiative processes and parameter constraints (orange dashed lines). Plots represent the output that can be computed from each module (blue dotted lines). The new additions presented in this chapter are highlighted in red. Image adapted from: [102]

compute the thermal emission from the disk and the torus. In all physical processes implemented, the viewing angle between the observer and the jet axis is included within the parameters that can be set. In this way, agnpy allows to model also non-blazar jetted AGNs. The possibility of modeling the radiation from the inner components of AGNs is particularly relevant for these objects, being their emission at low energies not always dominated by the jet.

The agnpy package is time-independent, meaning that it does not solve the differential equation for the electrons energy distribution (see Eq. 7 of [219]), and thus does not consider its evolution over time. Though, it contains a module constraining spectral parameters of the electrons distribution according to a simplified parametrization of the available acceleration and radiative processes and the definition of specific time scales [102]. In addition, although it does not include utilities for data fitting, it contains wrappers to export its radiative models to data-analysis software such as `Gammapy` [220] and `sherpa` [221]. In addition, it does not include utilities for data fitting, but it can be interfaced with the fitting routines of other software tools such as `Gammapy` [220] and `sherpa` [221]. In this way it is possible to constrain the parameters of the model through

a proper statistical analysis.

Finally, each process implemented in agnpy has been validated by comparing its output with bibliographic references [103, 104] and with the open-source package JetSet [222–224], already introduced before, showing deviations within 30% when the same physical assumptions are considered. A schematic representation of the code can be found in Fig. 6.1. It indicates the name of each module implementing the components just described. In the former version of the package, hadronic models were not contemplated. Being this a limitation of the code, and given the still-unknown origin of cosmic-rays and high-energy neutrinos, we started the development of hadronic processes in the package. They are described in the following and are validated against bibliographic references and other software programs.

6.2 Implementation and validation of hadronic emission processes

The hadronic processes which we implemented to describe the high-energy emission of AGNs are the synchrotron radiation from accelerated relativistic protons filling the emission region and the photo-meson interactions between relativistic protons and low-energy radiation fields.

6.2.1 Proton synchrotron radiation

As already introduced in Sect. 2.4.2, synchrotron emission is the radiation produced by charged particles moving in a magnetic field. In the case of AGNs and blazars, synchrotron emission from accelerated electrons is unanimously accepted as the origin of the low-energy bump of the SED. However, in some cases, also the synchrotron radiation from relativistic protons becomes relevant, and its emission can reproduce the high-energy bump. This happens in case of a high proton density or a strong magnetic field. For example, if we consider a single particle, the average synchrotron power emitted is $P_{syn} \propto (B/m)^2$ (see Eq. 2.19), meaning that light particles as electron and positrons emit more efficiently than heavier particles like protons. In order to have a high emitted power also in the case of protons, a high magnetic field B is then required.

The new class agnpy.synchrotron.proton_synchrotron implements the proton synchrotron process in agnpy, allowing the computation of the corresponding spectrum by assuming the blob to be filled with a uniform magnetic field. For the implementation we followed the formalism in [103, 213, 225], as for the case of electrons, replacing the electron mass with the proton mass. The synchrotron spectral power of a single proton along a certain direction of a random magnetic field can be written as [99, 103]:

$$P(\nu, \theta) = \frac{\sqrt{3} e^3 B \sin\theta}{m_p c^2} F\left(\frac{\nu}{\nu_c}\right), \tag{6.1}$$

where e is the electron charge, B is the magnetic field strength, ν_c is a critical frequency defined by

$$\nu_c = \frac{3eB}{4\pi m_p c}\gamma_p^2 \tag{6.2}$$

with γ_p the proton Lorentz factor, and $F(\nu/\nu_c)$ is a function of the form

$$F(x) = x\int_x^\infty K_{5/3}(\tau)\mathrm{d}\tau, \tag{6.3}$$

with $K_{5/3}(\tau)$ the modified Bessel function of order 5/3. If we integrate the function $F(x)$ over the possible magnetic field directions, it is modified into the following form, in terms of Bessel functions [225]:

$$G(x) = \frac{x}{20}[(8+3x^2)(K_{1/3}(x/2))^2 + xK_{2/3}(x/2)(2K_{1/3}(x/2) - 3xK_{2/3}(x/2))]. \tag{6.4}$$

This function has been approximated in a simpler analytical form by [225], without the use of special functions and with an accuracy better than 0.2% over the entire range of the variable x:

$$\tilde{G}(x) \simeq \frac{1.808x^{1/3}}{\sqrt{1+3.4x^{2/3}}}\frac{1+2.21x^{2/3}+0.347x^{4/3}}{1+1.353x^{2/3}+0.217x^{4/3}}e^{-x}. \tag{6.5}$$

We used this approximation in the implementation in `agnpy`. If we consider a distribution of protons $f_p(\gamma_p)$ [cm^{-3}] instead of a single particle, we have to convolve the obtained results with the particle distribution:

$$P(\nu) = \frac{\sqrt{3}e^3 B}{m_p c^2}\int_1^\infty \mathrm{d}\gamma_p f_p(\gamma_p)\tilde{G}(x). \tag{6.6}$$

If we consider the radiation to be emitted by a spherical blob located at a redshift z, the emitted synchrotron flux is [103]:

$$\nu F_\nu^{syn} = \frac{\delta_D^4 \nu'}{4\pi d_L^2}P'(\nu'), \tag{6.7}$$

where δ_D is the Doppler factor accounting for the relativistic beaming effect [100], d_L is the luminosity distance of the source, and primed quantities refer to the comoving frame of the emitting region[5]. In `agnpy` this expression is implemented in terms of the dimensionless energy $\varepsilon = h\nu/(m_p c^2)$, with h the Planck constant, obtaining:

$$\nu F_\nu^{syn} = \frac{\delta_D^4}{4\pi d_L^2}\frac{\sqrt{3}e^3 B}{h}\varepsilon'\int_1^\infty \mathrm{d}\gamma_p' f_p(\gamma_p')\tilde{G}(x), \tag{6.8}$$

where in this case

$$x = \frac{4\pi\varepsilon' m_e^2 c^3}{3eBh\gamma'^2}. \tag{6.9}$$

[5]Remember that the frequency transforms as $\nu' = \delta_D\nu/(1+z)$ of a given beaming factor and redshift (see [100]).

Blob		Proton distribution	
z	0.044	$\gamma'_{p,min}$	1
δ	30	$\gamma'_{p,break}$	3.64×10^9
B [G]	62.89	$\gamma'_{p,cut}$	3.64×10^9
R [cm]	9.06×10^{14}	$\gamma'_{p,max}$	1×10^{20}
		$\alpha_{p,1}$	1.5
		$\alpha_{p,2}$	2.5
		k_p [cm^{-3}]	3.51×10^{-18}

Table 6.1: Model parameters used in the computation of the proton synchrotron spectrum in both agnpy and *LeHa*.

Validation

The implementation of the proton synchrotron emission was validated by comparing its results with those of the private code *LeHa* [159], already used in Chap. 4 to model the selected candidates. This code is a well-established tool used in several publications (examples are [116, 127, 226–228]). As agnpy, it is not meant for temporal evolution, providing the steady-state emission of photons and neutrinos produced in different leptonic and hadronic processes. Morevoer, it provides the same geometry as agnpy for the emitting region: a spherical plasmoid.

The model used in the validation considers the spherical blob to be filled with a distribution of relativistic protons only, following an exponential cut-off broken power-law:

$$N_p(\gamma_p) = \begin{cases} k_p \left(\frac{\gamma_p}{\gamma_{p,break}}\right)^{-\alpha_{p,1}} e^{-\gamma_p/\gamma_{p,cut}} & \text{for } \gamma_{p,min} \leq \gamma_p \leq \gamma_{p,break} \\ k_p \left(\frac{\gamma_p}{\gamma_{p,break}}\right)^{-\alpha_{p,2}} e^{-\gamma_p/\gamma_{p,cut}} & \text{for } \gamma_{p,break} \leq \gamma_p \leq \gamma_{p,max} \end{cases}, \tag{6.10}$$

where k_p is the normalization, $\alpha_{p,1}$ and $\alpha_{p,2}$ are the spectral indexes, $\gamma_{p,min}$ and $\gamma_{p,max}$ are the minimum and maximum Lorentz factors of the distribution, $\gamma_{p,break}$ is the break Lorentz factor, and $\gamma_{p,cut}$ is the cut-off Lorentz factor. The blob parameters and those used for the proton distribution are reported in Table 6.1, while the comparison of results from the two codes are shown in Fig. 6.2. The bottom panel of Fig. 6.2 shows the deviation between the codes, computed as $\frac{\nu F_{\nu,\text{agnpy}}}{\nu F_{\nu,LeHa}} - 1$. It results to be $< 5\%$, confirming a good agreement between the two implementations and validating the new process developed in agnpy.

6.2.2 Photo-meson interactions

Besides emitting synchrotron radiation, the relativistic protons filling the emission region can also interact with low-energy radiation fields, typically coming from the source environment, via the so-called photo-meson ($p\gamma$) interactions. Thanks to this process,

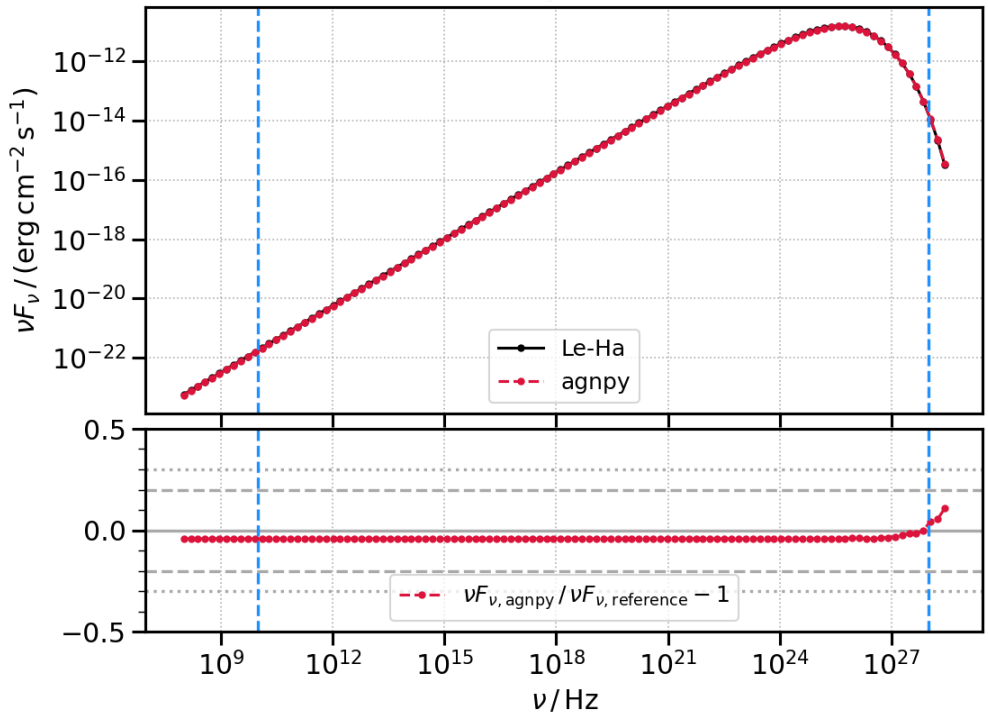

Figure 6.2: Comparison between `agnpy` (red) and *LeHa* (black) for proton synchrotron emission. The upper panel shows the obtained spectrum, while the bottom panel the deviation between the two codes.

charged ($\pi^{\pm}$) and neutral (π^0) pions are generated. They decay, further producing secondary $\gamma-$rays, electrons, positrons and neutrinos, following the relations 1.4 − 1.8. In AGNs and blazars the target photon fields usually taken into account in the interaction are the same considered for the external Compton process, e. g. radiation from disk, BLR, or torus.

Photo-meson interactions are implemented into the `agnpy` package through the addition of the new class `agnpy.photo_meson`. For the implementation we followed [108], where the authors provide analytical parametrizations of the energy distributions of the produced secondary particles. These approximations were obtained by running numerical simulations with the Monte Carlo code SOPHIA [229] and fitting the results. They provide a simple and accurate framework to compute the spectra of the decay products, posing an alternative scenario to the direct use of Monte Carlo simulations.

According to [108], the spectrum of each secondary particle produced can be written in the form:

$$\frac{dN}{dE} = \int_{\eta_0}^{\infty} H(\eta, E)\, d\eta, \tag{6.11}$$

where η is a quantity relating the energies of relativistic protons E_p and soft photons

ε_{ph}, while η_0 characterizes the interaction threshold. They are defined by the relations:

$$\eta = \frac{4\varepsilon_{ph} E_p}{m_p^2 c^4}, \quad \text{and} \quad \eta_0 \equiv 2\frac{m_\pi}{m_p} + \frac{m_\pi^2}{m_p^2} \simeq 0.313. \tag{6.12}$$

The function $H(\eta, E)$ is given by

$$H(\eta, E) = \int_E^\infty \frac{dE_p}{E_p^2} f_p(E_p) f_{ph}\left(\frac{\eta\, m_p^2 c^4}{4E_p}\right) \Phi_i\left(\eta, \frac{E}{E_p}\right), \tag{6.13}$$

where m_p is the protons mass, c is the speed of light, $f_p(E_p)$ is the energy distribution of the accelerated protons, $f_{ph}(\varepsilon_{ph})$ is the energy distribution of the target soft photons, and $\Phi_i\left(\eta, \frac{E}{E_p}\right)$ is a function containing the information on the kinematic and the cross section of the interaction. Defining $x = E_i/E_p$ the fraction of the parent proton energy carried by the output particle (which can be $\gamma-$rays, e^+, e^-, ν_μ, $\bar{\nu}_\mu$, ν_e, $\bar{\nu}_e$), its expression results:

$$\Phi_i(\eta, x) = \begin{cases} B_i (\ln 2)^{\psi_i} & \text{if } x < x_- \\ B_i \exp\left\{-s_i \left[\ln\left(\frac{x}{x_-}\right)\right]^{\delta_i}\right\} \left[\ln\left(\frac{2}{1+y^2}\right)\right]^{\psi_i} & \text{if } x_- < x < x_+ \\ 0 & \text{if } x > x_+ \end{cases}, \tag{6.14}$$

where x_+ and x_- represent the minimum and maximum energy of the output particle, depending on the particle type and the kinematics of the process, $y = \frac{x - x_-}{x_+ - x_-}$, and B_i, s_i, δ_i and ψ are functions of η. The values of B_i, s_i and δ_i are tabulated in Tables I, II, and III of [108] for different values of η/η_0. Since they are quite smooth functions of η, we performed a linear interpolation to compute their values for intermediate values of η, not reported in the tables. Differently, the function ψ has an analytical form. All the parameters in Eq. 6.14 are different based on the output particle considered.

For example, for the production of $\gamma-$**rays** we have:

$$x_\pm = \frac{1}{2(1+\eta)}\left[\eta + r^2 \pm \sqrt{(\eta - r^2 - 2r)(\eta - r^2 + 2r)}\right], \tag{6.15}$$

$$\psi = 2.5 + 0.4 \ln(\eta/\eta_0), \tag{6.16}$$

where $r = m_\pi/m_p \simeq 0.146$. For the other particles, the terms y and $x_\pm$ are replaced by the variables y' and $x'_\pm$, which are functions of y and $x_\pm$ in most of the cases. For the definitions of the variables for the other particles we refer the reader to the reference [108]. We just note that for the production of e^- and $\bar{\nu}_e$ at least two pions have to be produced (a π^+ and a π^-), which is possible only for values of $\eta > 2.14\eta_0$.

Validation

The implementation of the photo-meson interactions was validated by comparing the obtained results with those reported in the reference paper [108]. In the following we

Proton distributions, Fig. 13 [108]			
$\gamma'_{p,min}$	1	$\gamma'_{p,min}$	1
$\gamma'_{p,max}$	1×10^{15}	$\gamma'_{p,max}$	1×10^{15}
α_p	2.0	α_p	2.5
k_p [eV]	1	k_p [eV]	5.5

Table 6.2: Model parameters for the proton distribution used in the computation of $H(\eta, E_\gamma)$ in photo-meson interactions as extracted from the reference paper [108].

Proton distribution, Fig. 15 [108]	
$\gamma'_{p,min}$	1×10^3
$\gamma'_{p,cut}$	3.20×10^{11}
$\gamma'_{p,max}$	1×10^{20}
α_p	2.0
k_p [cm^{-3}]	2.74×10^{-8}

Table 6.3: Model parameters of the proton distribution used in the computation of the energy spectra of the output particles in photo-meson interactions as extracted from the reference paper [108].

report the reproduction of Figs. 13 and 15 of the reference. The former shows the function $H(\eta, E)$ for a fixed value of the energy of the produced particles ($\gamma-$rays in this case), while the latter shows the energy spectra of all output particles.

Both cases consider the interaction between a distribution of relativistic protons with the CMB radiation, described by a black body with a characteristic temperature $T = 2.7$ K. It is defined as:

$$f_{ph}(y) = \frac{8\pi}{h^3 c^3} \frac{m_p^2 c^4 y^2}{\exp\left(\frac{m_p c^2 y}{kT}\right) - 1}, \tag{6.17}$$

with $y = \varepsilon_{ph}/(m_p c^2)$, and ε the energy of the target photons. The units of the distribution are [cm^{-3}]. On the contrary, the proton energy distribution are different in the two considered cases. In the first case a power-law distribution is used:

$$f_p(\gamma_p) = k_p \gamma_p^{-\alpha_p} \quad \text{for } \gamma_{p,min} \leq \gamma_p \leq \gamma_{p,max}, \tag{6.18}$$

evaluated for different values of the spectral index α_p and the normalization k_p; while in the second case a power-law with exponential cut-off is considered:

$$f_p(\gamma_p) = k_p \gamma_p^{-\alpha_p} e^{-\gamma_p/\gamma_{p,cut}} \quad \text{for } \gamma_{p,min} \leq \gamma_p \leq \gamma_{p,max}. \tag{6.19}$$

The parameters used for these distributions are reported in Tables 6.2 and 6.3.

Results for the first case are reported in Fig. 6.3, for a single, fixed, value of the energy of produced $\gamma-$rays. The considered energy is $E_\gamma = 0.5E^*$, where E^* is the

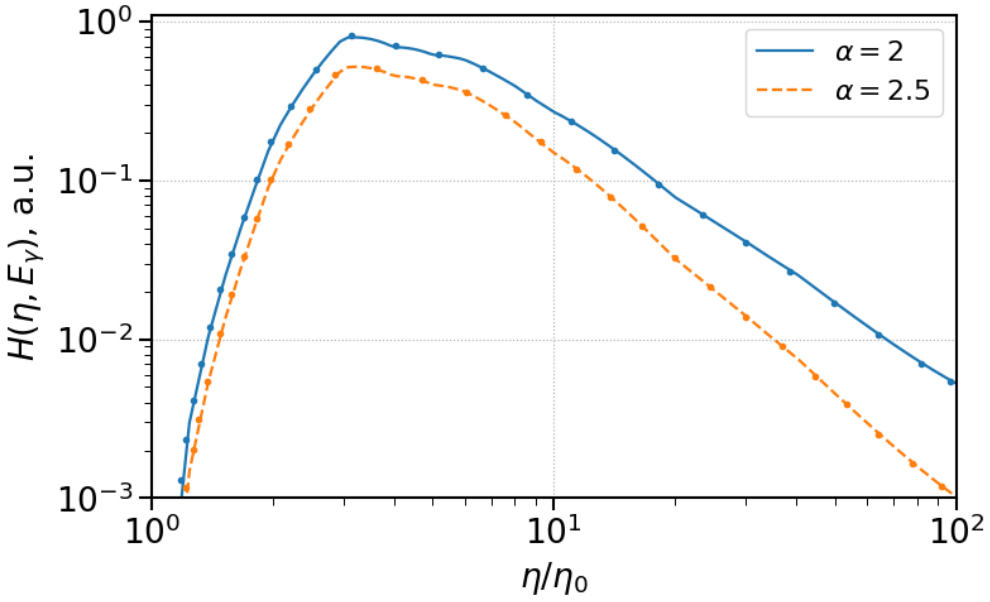

Figure 6.3: Reproduction of Fig. 13 of [108], showing the function $H(\eta, E_\gamma)$ for secondary $\gamma-$rays produced in photo-meson interactions. The points represent the data from the reference, while the lines represent the function computed with the implemented code. On the y axis the function $H(\eta, E_\gamma)$ is represented in arbitrary units. The computation is performed at the fixed energy of $\gamma-$rays $E_\gamma = 0.5E^*$ for a power-law distribution of protons with two different values of the spectral index.

characteristic energy of the proton, defined as

$$E^* = m_p c^2 \left(\frac{m_p c^2}{4kT} \eta_0 \right) \simeq 3.0 \times 10^{20}\,\text{eV}. \tag{6.20}$$

The comparison with data from [108] shows that the figure well reproduces the reference. We can observe that at low energies, the function $H(\eta, E)$ drops very quickly, while at high energies it becomes harder with decreasing the spectral index value.

Results for the second case are reported in Fig. 6.4 for all the output particles ($\gamma-$rays, e^+, e^-, ν_μ, $\bar{\nu}_\mu$, ν_e, $\bar{\nu}_e$). In this case the energy spectrum $E\,\mathrm{d}N/\mathrm{d}E$ of the secondary particles is shown. The value considered for the cut-off energy of the proton energy distribution is $E_{p,cut} = E^*$, also reported in Table 6.3 in terms of $\gamma_{p,cut}$. Also in this case we have a good agreement between the implemented code and the reference.

In both cases, the discrepancy between our development and the paper is $< 10\%$, thus validating the process newly implemented in `agnpy`.

Limitations

The formalism used in [108] considers the intermediate particles generated in the interaction (i. e. pions and muons) to decay instantaneously, neglecting their cooling

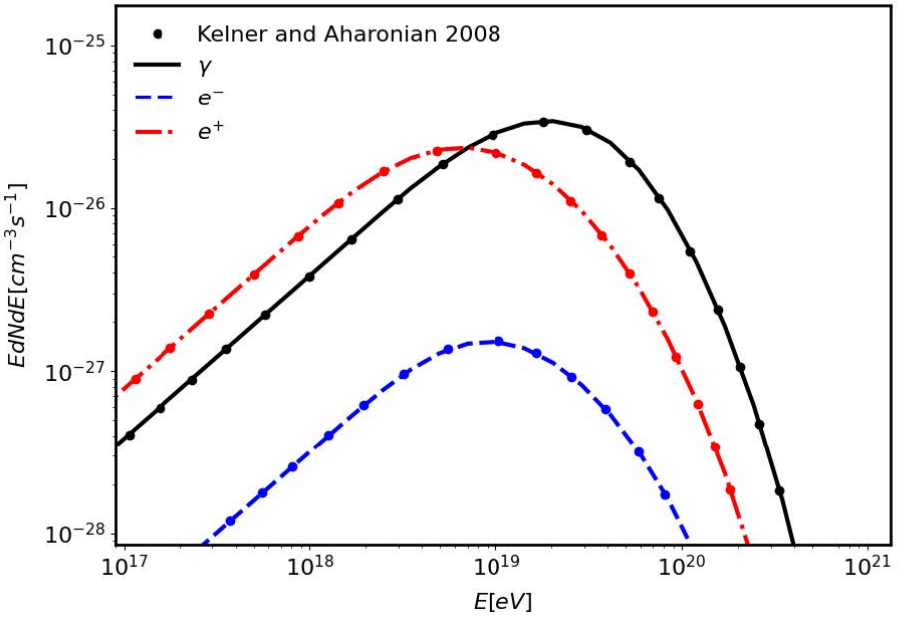

(a)

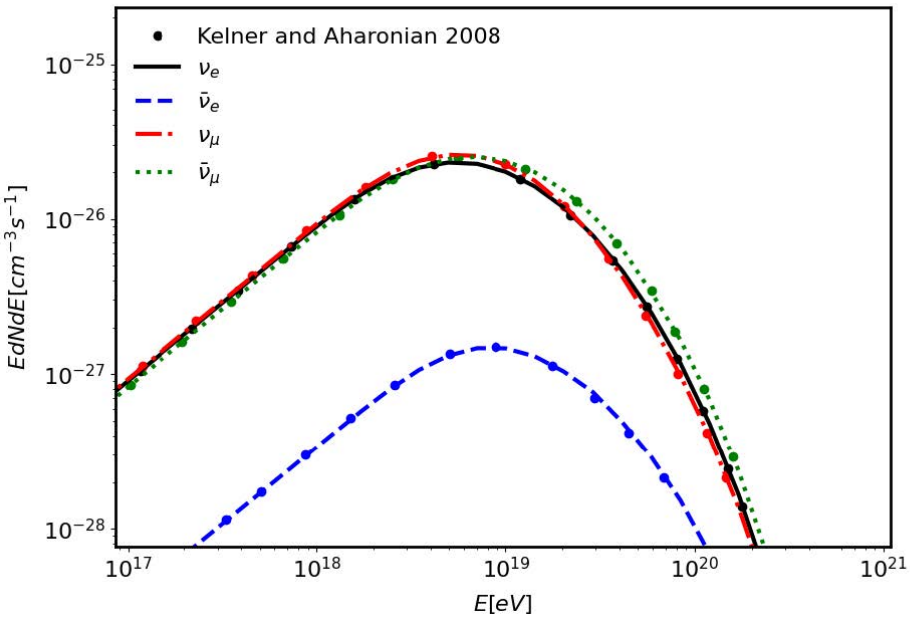

(b)

Figure 6.4: Reproduction of Fig. 15 of [108], showing the energy spectra for the secondary particles produced in photo-meson interactions. The points represent the data from the reference, while the lines represent the spectra computed with the developed code. In (a) we have $\gamma-$rays (black solid line), e^- (blue dashed line), e^+ (red dash-dotted line); while in (b) we have ν_e (black solid line), $\bar{\nu}_e$ (blue dashed line), ν_μ (red dash-dotted line), $\bar{\nu}_\mu$ (green dotted line).

through synchrotron emission and the possible inverse Compton radiation they can undergo. However, in some cases, these contributions can be relevant in the SED emission, as for example shown in [230, 231]. They can be neglected only if one of the following conditions is satisfied, as shown by [232]:

1. The proton-synchrotron losses are strongly dominant over the photo-meson losses,

2. The synchrotron cooling time scales of secondary muons and pions are much larger than their decay time scales. This condition leads to the following constraint on the magnetic field strength for a given proton Lorentz factor γ_p (or conversely, on the maximum proton Lorentz factor allowed for a given magnetic field):

$$B\gamma_p << \begin{cases} 7.8 \times 10^{11}\,\mathrm{G} & \text{for pions} \\ 5.6 \times 10^{10}\,\mathrm{G} & \text{for muons} \end{cases} . \tag{6.21}$$

With one of these conditions satisfied, the pion and muon synchrotron emission has a negligible contribution, hence the analytical parametrizations of [108] are valid and can be used in the modeling of sources emission.

6.3 Conclusions and outlook

In this work we have developed two of the most relevant hadronic processes for blazars emission into the open-source code `agnpy`. These processes include synchrotron radiation from a distribution of relativistic protons and photo-hadronic interactions between accelerated protons and low-energy radiation. The former becomes significant in the presence of high magnetic fields or high proton densities, while the latter is recognized as the primary source of neutrinos in the emission of AGNs and blazars. We implemented the aforementioned processes following the parametrizations of [103, 213, 225] and [108] for proton synchrotron and photo-meson interactions respectively. The results we obtained were compared with an existing private code and a theoretical reference, showing a deviation of less than 10% in both cases, thus validating the implementation.

The main drawback of the code is the assumption of instant decay of the intermediate pions and muons, specified in the main reference [108] we adopted. Since the synchrotron cooling of these particles is neglected, constraints on the magnetic field strength and the maximum proton Lorentz factor need to be imposed, as described in Sect. 6.2.2.

Future developments of this work include additional lepto-hadronic processes playing a relevant role in AGNs and blazars emission in order to allow a more complete description of their SED. Among them there are the Bethe-Heitler pair production (see Sect. 2.4.3), which dominates over photo-meson interactions at low energies; the synchrotron emission from secondary pions and muons, which becomes significant in case

of intense magnetic fields; and the development of pair cascades, initiated by the secondary particles produced in the aforementioned radiative processes. While rarely relevant in the description of AGNs emission, also pp interactions can play a role. This happens in case of a target entering the jet. Thus, also the implementation of such process shall be considered.

A crucial aspect of our work is its open-source nature. Our effort has the specific objective to offer to the broader astrophysical community the possibility to perform detailed modeling studies. This is highly relevant in pushing the advancement of the theoretical understanding of the sources emission, and easing the comparison of results. Moreover, it will be essential with the large amount of data that the next generation high-energy observatories will provide.

Chapter 7

Summary and future prospects

During my PhD I worked in the context of multi-messenger astrophysics, focusing in particular on the neutrino emission from blazars. Blazars are a particular subclass of AGNs showing a relativistic jet pointing in the direction of Earth. The jet is a natural accelerator of particles and thus a suitable environment for proton acceleration and neutrino production. The detection of high-energy photons and neutrinos from these sources, combined with detailed modeling of their emission mechanisms, can shed light on their internal composition and dynamics, and unravel the origin of cosmic rays, whose progenitors are still unidentified. The interest in blazars as candidate neutrino emitters grew in 2017 after the joint observation of a high-energy astrophysical neutrino event detected by IceCube with the flaring blazar TXS 0506+056. However, thanks to more recent studies by IceCube, other sources started to stand out, namely the Seifert-II galaxy NGC 1068 and potential galactic objects.

The projects I worked on in this thesis mainly concentrate on the investigation of blazars, but also presents an unbiased follow-up of IceCube neutrino events aiming at identifying possible new associations.

In Chapter 3 the first long-term multi-wavelength campaign of TXS 0506+056 is presented. Before the 2017 event, only little data was available from this source, making it difficult to interpret its emission. From November 2017, the MAGIC telescopes and multi-wavelength partners started long-term systematic observations of this neutrino source candidate with the objective of better characterizing its duty cycle and understanding the exceptionality of the $\gamma-$ray flare observed at the time of the neutrino detection. Results show a low state of activity during most of the observed period in VHE $\gamma-$rays, with two day-long flares consistent with the 2017 one. Remarkable differences with respect to the 2017 event are instead observed in HE $\gamma-$rays and radio frequencies. Although this work represents one of the most complete multi-wavelength monitoring campaigns of the source, its duty cycle and the precise processes responsible for

its emission are still not fully understood. Therefore, additional data are necessary in order to better characterize the source emission, as well as investigating the potential correlations of its state of activity in the different bands.

Chapter 4 focuses on the search of blazar sources showing similar properties to TXS 0506+056, with the objective of identifying similarities or differences in their accretion efficiency and radiative processes giving origin to their broadband emission. Such a project could have a high importance since it would identify a population of objects which, as TXS 0506+056, would be neither pure FSRQs, nor pure BL Lacs, and characterize their role in a multi-messenger context. The candidates were selected from the *Fermi* 4LAC-DR2 catalog of AGNs, according to observational properties, which can be directly related to physical processes governing their environments. From this selection we obtained a sample of 27 objects. However, the need of a detailed spectral analysis for each candidate brought us to reduce the sample to only 4 sources, all classified as BL Lacs. For all selected sources the accretion rate was estimated starting from spectral information, finding that three of them are suggested as possible masquerading BL Lacs, hosting an efficient accretion process and a rich BLR. For the fourth source we could not draw any strong conclusion on its accretion efficiency. Given the results on accretion, the external target photon fields from the BLR and the torus are taken into account when performing the modeling of simultaneous data from these objects. Results from the modeling show the high energy emission to be dominated by the external Compton process, while the hadronic contribution stands out in X-rays, further highlighting the importance of this band for hadronic processes, as it was already indicated by the modeling of TXS 0506+056 during the 2017 event [114]. Moreover, a comparison of the predicted candidates emission with the sensitivities of IceCube, and current and future IACTs was performed, showing that both the neutrino and $\gamma-$ray fluxes would be too faint for a detection during an average state of activity. Since a large number of potential candidates had to be ruled out due to a lacking spectral analysis, a future improvement of this study would be given by detailed spectroscopic measurements on the excluded sources, in order to enlarge the pool of candidates similar to TXS 0506+056 and allow a more detailed investigation. Moreover, given the hadronic contribution in X-rays, additional measurements in this band would be necessary to definitely confirm the hadronic emission and rule out the possibility of a purely leptonic one.

Besides TXS 0506+056, other sources may be relevant neutrino emitters. Given the success of the real-time multi-messenger approach in the 2017 event, the MAGIC Collaboration, together with the other currently active IACT Collaborations, performed real-time follow-up observations of neutrino events issued by IceCube. Observational results from this work are presented in Chapter 5. The campaign concentrates of the follow-up of two kinds of alerts, namely the single high-energy neutrino tracks and the lower-energy neutrino multiplets, with the latter coming from a list of pre-selected candidates or from the whole sky. Most of the observed alerts were not detected in VHE $\gamma-$rays. However, observations performed by more than one IACT allowed to put more constraining upper limits on the VHE emission of the observed sources through a combination of the single instruments results. These combined upper limits can be

used in the modeling of sources to add more stringent constraints on the hadronic emission. A detailed modeling of the observed sources is beyond the scope of this work, but in one case a comparison with already existing models was performed, suggesting our results as a possible starting point for further modeling. Finally, a study on the list of sources monitored by IceCube for the neutrino multiplet scan was performed. Here, we evaluated the detectability of these objects by MAGIC, through an extrapolation of their VHE flux starting from their 9.5-years *Fermi* lightcurves rather than their integral *Fermi* flux as it was done when the list was created. This study allowed to take into account temporal changes of the sources emission and produce a more precise estimation of their detectability. As a consequence, the need of a more careful selection process for these candidates emerged. Updated lightcurves and the most recent 4FGL-DR4 [233] *Fermi* catalog, based on 14 years of data, can be good starting points for such selection.

Finally, Chapter 6 presents the development of hadronic emission processes relevant in blazars emission into the open-source python package `agnpy`. This work is of fundamental importance since, to date, all the available software programs allowing a lepto-hadronic interpretation of blazars emission were private. The implementation of such processes in an open-source software allows the wider astrophysical community to independently model the emission of blazars of interest, further advancing the theoretical understanding of the field. The processes we implemented are the proton synchrotron radiation and the photo-meson interactions, both validated through the comparison with private already existing codes or with theoretical references. However, in order to make the code complete, additional processes would be needed. Within them, the Bethe-Heitler process, competing with the photo-meson channel at low energies, the sychrotron radiation from secondary pions and muons produced in photo-meson interactions, and electromagnetic pair cascades originating from the products of both leptonic and hadronic processes. In addition, proton-proton interactions can be taken into account. Although they are often subdominant in blazars emission because of the low matter density in the source environments, their role becomes relevant when a proton target, such as a gas cloud or a star, passes through the jet. The development of such mentioned processes is planned in the near future.

In conclusion, my PhD work contributed to two relevant open problems of multi-messenger astrophysics and astroparticle physics, namely the investigation of the emission processes characterizing the sources, and the search for new potential candidates neutrino emitters.

Taking into account the new discoveries by IceCube, the evidence for neutrino emission from the Seyfert-II Galaxy NGC 1068 [4] and the Galactic plane [5], future prospects in the field include the development of theoretical models predicting neutrino emission from the obscured environment around the core of AGNs, rather than from their jets. In these models, the acceleration conditions are provided by the super massive black hole in the AGN center, while the conditions for neutrino production and $\gamma-$ray absorption are provided by the accretion disk and a hot plasma surrounding it, known as corona.

In addition, given the success of the real-time follow-up strategy in the case of TXS 0506+056, follow-up of neutrino events needs to continue in the future, in order to

better understand the connection between electromagnetic and neutrino emission from the same objects. A promising approach can be the optimization of follow-up strategies based on list of objects of the same class, as those showing evidence of neutrino emission.

Finally, looking to future observations, upcoming new facilities will allow a better monitoring of the neutrino and $\gamma-$ray sky. Among them, the Cherenkov Telescope Array [192] will allow $\gamma-$ray observations up to 100 TeV. Thanks to its improved sensitivity with respect to current IACTs, it will also be of great help in discovering new sources and perform more precise measurements. In addition, the installation of two arrays of IACTs operating on both the Northern and Southern Hemispheres will ensure full-sky coverage. On the neutrino side, the KM3Net Neutrino Telescope [194], together with the next generation IceCube detector, IceCube-Gen2, will provide improved angular resolution and sensitivity, and a complementary view of the neutrino sky.

Bibliography

[1]IceCube Collaboration, "Evidence for High-Energy Extraterrestrial Neutrinos at the IceCube Detector", Science **342**, 1242856 (2013) (cit. on pp. iii, 4).

[2]IceCube Collaboration, "IceCube high-energy starting event sample: Description and flux characterization with 7.5 years of data", Phys. Rev. D **104**, 022002 (2021) (cit. on pp. iii, 4).

[3]The IceCube Collaboration et al., "Multimessenger observations of a flaring blazar coincident with high-energy neutrino IceCube-170922A", Science **361**, 10.1126/science.aat1378 (2018) (cit. on pp. iii, 57, 78, 79, 111).

[4]R. Abbasi et al., "Evidence for neutrino emission from the nearby active galaxy NGC 1068", Science **378**, 538–543 (2022) (cit. on pp. iii, 111, 151).

[5]R. Abbasi et al., "Observation of high-energy neutrinos from the Galactic plane", Science **380**, 1338–1343 (2023) (cit. on pp. iii, 111, 151).

[6]M. Spurio, *Probes of Multimessenger Astrophysics* (Springer International Publishing, Cham, Switzerland) (cit. on p. 2).

[7]C. Evoli, "The Cosmic-Ray Energy Spectrum", Zenodo, 10.5281/zenodo.2360277 (2018) (cit. on p. 3).

[8]K. Greisen, "End to the Cosmic-Ray Spectrum?", Phys. Rev. Lett. **16**, 748–750 (1966) (cit. on p. 2).

[9]G. T. Zatsepin and V. A. Kuz'min, "Upper Limit of the Spectrum of Cosmic Rays", Soviet Journal of Experimental and Theoretical Physics Letters **4**, 78 (1966) (cit. on p. 2).

[10]C. Spiering, "Towards high-energy neutrino astronomy", The European Physical Journal H **37**, 515–565 (2012) (cit. on p. 5).

[11] A. Saldana-Lopez, A. Domínguez, P. G. Pérez-González, J. Finke, M. Ajello, J. R. Primack, V. S. Paliya, and A. Desai, "An observational determination of the evolving extragalactic background light from the multiwavelength HST/CANDELS survey in the Fermi and CTA era", Mon. Not. R. Astron. Soc. **507**, 5144–5160 (2021) (cit. on p. 4).

[12] H. Abe et al., "MAGIC detection of GRB 201216C at z = 1.1", Mon. Not. R. Astron. Soc., stad2958 (2023) (cit. on p. 5).

[13] A. Moralejo Olaizola, "Búsqueda de fuentes cósmicas de radiación gamma de muy alta energía con el detector airobicc", PhD thesis (Universidad Complutense de Madrid, Spain, 2000) (cit. on p. 6).

[14] R. M. Wagner, "Measurement of Very High Energy Gamma-Ray Emission from Four Blazars Using the MAGIC Telescope and a Comparative Blazar Study", PhD thesis (Munich, Tech. U., Germany, 2006) (cit. on p. 7).

[15] M. G. Aartsen et al., "The IceCube Neutrino Observatory: instrumentation and online systems", J. Instrum. **12**, P03012 (2017) (cit. on pp. 8, 9, 111).

[16] M. Ahlers and F. Halzen, "Opening a new window onto the universe with IceCube", Prog. Part. Nucl. Phys. **102**, 73–88 (2018) (cit. on pp. 8, 10).

[17] M. Ahlers, K. Helbing, and C. Pérez de los Heros, "Probing particle physics with IceCube", Eur. Phys. J. C **78**, 1–51 (2018) (cit. on pp. 8, 12).

[18] P. A. Čerenkov, "Visible Radiation Produced by Electrons Moving in a Medium with Velocities Exceeding that of Light", Phys. Rev. **52**, 378–379 (1937) (cit. on p. 9).

[19] M. Ageron et al., "ANTARES: The first undersea neutrino telescope", Nucl. Instrum. Methods Phys. Res., Sect. A **656**, 11–38 (2011) (cit. on p. 9).

[20] S. Adrián-Martínez et al., "Letter of intent for KM3NeT 2.0", J. Phys. G: Nucl. Part. Phys. **43**, 084001 (2016) (cit. on p. 9).

[21] M. G. Aartsen et al., "The IceCube realtime alert system", Astropart. Phys. **92**, 30–41 (2017) (cit. on pp. 11, 12).

[22] T. Kintscher, "Rapid Response to Extraordinary Events: Transient Neutrino Sources with the IceCube Experiment", PhD thesis (Humboldt-Universität zu, Berlin, Germany, 2020) (cit. on pp. 11, 14–17, 115, 129, 130).

[23] J. G. Learned and K. Mannheim, "High-Energy Neutrino Astrophysics", Annu. Rev. Nucl. Part. Sci. **50**, 679–749 (2000) (cit. on p. 11).

[24] M. G. Aartsen et al., "Very high-energy gamma-ray follow-up program using neutrino triggers from icecube", Journal of Instrumentation **11**, P11009 (2016) (cit. on p. 13).

[25] R. Abbasi et al., "IceCat-1: the IceCube Event Catalog of Alert Tracks", arXiv, 10.48550/arXiv.2304.01174 (2023) (cit. on pp. 13, 14).

[26]J. Holder, "VERITAS: Status and Performance", in 4th Workshop on Science with the New Generation of High Energy Gamma-Ray Experiments (2007), pp. 69–76 (cit. on pp. 13, 112).

[27]F. Aharonian et al., "Observations of the Crab nebula with HESS", Astron. Astrophys. **457**, 899–915 (2006) (cit. on pp. 13, 112).

[28]F. Acero et al., "FERMI LARGE AREA TELESCOPE THIRD SOURCE CATALOG", Astrophys. J. Suppl. Ser. **218**, 23 (2015) (cit. on pp. 14, 65, 128).

[29]M. Ajello et al., "3FHL: The Third Catalog of Hard Fermi-LAT Sources", Astrophys. J. Suppl. Ser. **232**, 18 (2017) (cit. on pp. 14, 128).

[30]J. Aleksić et al., "The major upgrade of the MAGIC telescopes, Part I: The hardware improvements and the commissioning of the system", Astropart. Phys. **72**, 61–75 (2016) (cit. on pp. 18, 21, 23, 24, 81, 103, 112).

[31]F. E. Roach and J. L. Gordon, *The Light of the Night Sky* (Springer Netherlands, Dordrecht, The Netherlands) (cit. on p. 20).

[32]A. Berti, "Study of astrophysical transients with the MAGIC telescopes", PhD thesis (Università degli Studi di Trieste, Italy, 2018) (cit. on pp. 21, 28).

[33]T. Bretz, D. Dorner, R. M. Wagner, and P. Sawallisch, "The drive system of the major atmospheric gamma-ray imaging Cherenkov telescope", Astropart. Phys. **31**, 92–101 (2009) (cit. on p. 21).

[34]A. Biland, M. Garczarczyk, H. Anderhub, V. Danielyan, D. Hakobyan, E. Lorenz, and R. Mirzoyan, "The Active Mirror Control of the MAGIC Telescope", arXiv, 10.48550/arXiv.0709.1574 (2007) (cit. on p. 22).

[35]M. L. Ahnen et al., "Performance of the MAGIC telescopes under moonlight", Astropart. Phys. **94**, 29–41 (2017) (cit. on pp. 22, 29).

[36]M. Gaug, "Calibration of the MAGIC telescope and observation of gamma ray bursts", PhD thesis (Universitat Autònoma de Barcelona, Spain, 2006) (cit. on p. 22).

[37]R. Paoletti, R. Cecchi, D. Corti, F. Dazzi, M. Mariotti, R. Pegna, and N. Turini, "The Trigger System of the MAGIC Telescope", IEEE Trans. Nucl. Sci. **54**, 404–409 (2007) (cit. on pp. 23, 81, 116, 118).

[38]F. Dazzi, "A new stereoscopic 'Sum-Trigger-II' for the MAGIC Telescopes", PhD thesis (Università degli Studi di Udine, Italy, 2012) (cit. on pp. 24, 26, 81, 116, 118).

[39]F. Dazzi et al., "The Stereoscopic Analog Trigger of the MAGIC Telescopes", IEEE Trans. Nucl. Sci. **68**, 1473–1486 (2021) (cit. on pp. 24, 26, 27, 81, 116, 118).

[40]F. Schmuckermaier, M. Gaug, C. Fruck, A. Hahn, V. Acciari, J. Besenrieder, D. D. Prester, D. Dorner, D. Fink, L. Font, S. Mićanović, R. Mirzoyan, D. Müller, L. Pavletić, and M. Will, "Correcting MAGIC Telescope data taken under non-optimal atmospheric conditions with an elastic LIDAR", J. Phys. Conf. Ser. **2398**, 012011 (2022) (cit. on pp. 27, 118).

[41]D. Tescaro, A. López-Oramas, A. Moralejo, D. Mazin, and D. Hadasch, "The MAGIC telescopes DAQ software and the on-the-fly online analysis client", arXiv, 10.48550/arXiv.1310.1565 (2013) (cit. on p. 28).

[42]I. Oya, R. de los Reyes, J. L. Contreras, D. Nieto, J. A. Barrio, M. V. Fonseca, E. Carmona, M. Gaug, A. Moralejo, and J. Rico, "Data Quality Check and On-Site Analysis of the MAGIC Telescope", SpringerLink, 519 (2010) (cit. on p. 28).

[43]V. P. Fomin, A. A. Stepanian, R. C. Lamb, D. A. Lewis, M. Punch, and T. C. Weekes, "New methods of atmospheric Cherenkov imaging for gamma-ray astronomy. I. The false source method", Astropart. Phys. **2**, 137–150 (1994) (cit. on pp. 30, 118).

[44]R. Lopez-Coto, "Very-high-energy gamma-ray observations of pulsar wind nebulae and cataclysmic variable stars with MAGIC and development of trigger systems for IACTs", PhD thesis (Universitat Autònoma de Barcelona, Spain, 2015) (cit. on pp. 30, 34).

[45]R. Zanin, E. Carmona, J. Sitarek, P. Colin, K. Frantzen, M. Gaug, S. Lombardi, M. Lopez, A. Moralejo, K. Satalecka, V. Scapin, and V. Stamatescu, "MARS, the MAGIC analysis and reconstruction software", in 33rd International Cosmic Ray Conference (2013), p. 0773 (cit. on pp. 31, 118).

[46]R. Brun and F. Rademakers, "ROOT — An object oriented data analysis framework", Nucl. Instrum. Methods Phys. Res., Sect. A **389**, 81–86 (1997) (cit. on p. 31).

[47]A. Spolon, "Studio delle pulsars e del loro ambiente attraverso osservazioni gamma alle altissime energie", PhD thesis (Università degli studi di Padova, Italy, 2022) (cit. on p. 32).

[48]D. Heck, J. Knapp, J. N. Capdevielle, G. Schatz, and T. Thouw, "CORSIKA: A Monte Carlo code to simulate extensive air showers", (1998) (cit. on p. 31).

[49]P. Majumdar, "Monte Carlo simulation for the MAGIC telescope", in 33rd International Cosmic Ray Conference (2005) (cit. on p. 31).

[50]R. Mirzoyan, "On the Calibration Accuracy of Light Sensors in Atmospheric Cherenkov Fluorescence and Neutrino Experiments", in 25th International Cosmic Ray Conference, Vol. 7 (1997), p. 265 (cit. on p. 33).

[51]E. Aliu et al., "Improving the performance of the single-dish Cherenkov telescope MAGIC through the use of signal timing", Astropart. Phys. **30**, 293–305 (2009) (cit. on p. 34).

[52]A. M. Hillas, "Cerenkov Light Images of EAS Produced by Primary Gamma Rays and by Nuclei", in 19th International Cosmic Ray Conference, Vol. 3 (1985), p. 445 (cit. on p. 34).

[53]A. Fernández Barral, "Extreme particle acceleration in microquasar jets and pulsar wind nebulae with the MAGIC telescopes", PhD thesis (Universitat Autònoma de Barcelona, Spain, 2017) (cit. on pp. 35, 39).

[54]J. Albert et al., "Implementation of the Random Forest method for the Imaging Atmospheric Cherenkov Telescope MAGIC", Nucl. Instrum. Methods Phys. Res., Sect. A **588**, 424–432 (2008) (cit. on p. 37).

[55]C. Gini, "Measurement of inequality of incomes", The Economic Journal **31**, 124–126 (1921) (cit. on p. 38).

[56]V. P. Fomin, S. Fennell, R. C. Lamb, D. A. Lewis, M. Punch, and T. C. Weekes, "New methods of atmospheric Cherenkov imaging for gamma-ray astronomy. II. The differential position method", Astropart. Phys. **2**, 151–159 (1994) (cit. on p. 38).

[57]J. Aleksić et al., "The major upgrade of the MAGIC telescopes, Part II: A performance study using observations of the Crab Nebula", Astropart. Phys. **72**, 76–94 (2016) (cit. on pp. 38, 43, 44, 112).

[58]J. Aleksić et al., "Performance of the MAGIC stereo system obtained with Crab Nebula data", Astropart. Phys. **35**, 435–448 (2012) (cit. on p. 39).

[59]T. P. Li and Y. Q. Ma, "Analysis methods for results in gamma-ray astronomy.", Astrophys. J. **272**, 317–324 (1983) (cit. on pp. 40, 82, 118).

[60]J. Albert et al., "Unfolding of differential energy spectra in the MAGIC experiment", Nucl. Instrum. Methods Phys. Res., Sect. A **583**, 494–506 (2007) (cit. on p. 45).

[61]W. A. Rolke, A. M. López, and J. Conrad, "Limits and confidence intervals in the presence of nuisance parameters", Nucl. Instrum. Methods Phys. Res., Sect. A **551**, 493–503 (2005) (cit. on pp. 45, 46, 83, 119).

[62]C. Meegan, G. Lichti, P. N. Bhat, E. Bissaldi, M. S. Briggs, V. Connaughton, R. Diehl, G. Fishman, J. Greiner, A. S. Hoover, A. J. van der Horst, A. von Kienlin, R. M. Kippen, C. Kouveliotou, S. McBreen, et al., "THE FERMI GAMMA-RAY BURST MONITOR", Astrophys. J. **702**, 791 (2009) (cit. on p. 48).

[63]W. B. Atwood et al., "THE LARGE AREA TELESCOPE ON THE FERMI GAMMA-RAY SPACE TELESCOPE MISSION", Astrophys. J. **697**, 1071 (2009) (cit. on pp. 48, 49, 83, 97).

[64]G. Principe, D. Malyshev, J. Ballet, and S. Funk, "The first catalog of Fermi-LAT sources below 100 MeV", Astron. Astrophys. **618**, A22 (2018) (cit. on p. 49).

[65]M. Wood, R. Caputo, E. Charles, M. Di Mauro, J. Magill, and J. S. Perkins, "Fermipy: An open-source Python package for analysis of Fermi-LAT Data", in 35th international cosmic ray conference, Vol. 301 (2017), p. 824 (cit. on pp. 50, 97, 119).

[66]S. Abdollahi et al., "Fermi Large Area Telescope Fourth Source Catalog", Astrophys. J. Suppl. Ser. **247**, 33 (2020) (cit. on pp. 51, 84, 90, 97, 120).

[67]E. Massaro, M. Perri, P. Giommi, and R. Nesci, "Log-parabolic spectra and particle acceleration in the BL Lac object Mkn 421: Spectral analysis of the complete BeppoSAX wide band X-ray data set", Astron. Astrophys. **413**, 489–503 (2004) (cit. on p. 51).

[68]N. Gehrels et al., "The Swift Gamma-Ray Burst Mission", Astrophys. J. **611**, 1005 (2004) (cit. on pp. 52, 85, 120).

[69]S. D. Barthelmy, L. M. Barbier, J. R. Cummings, E. E. Fenimore, N. Gehrels, D. Hullinger, H. A. Krimm, C. B. Markwardt, D. M. Palmer, A. Parsons, G. Sato, M. Suzuki, T. Takahashi, M. Tashiro, and J. Tueller, "The Burst Alert Telescope (BAT) on the SWIFT Midex Mission", Space Sci. Rev. **120**, 143–164 (2005) (cit. on p. 52).

[70]D. N. Burrows et al., "The Swift X-Ray Telescope", Space Sci. Rev. **120**, 165–195 (2005) (cit. on pp. 52, 85, 97, 120).

[71]P. W. A. Roming et al., "The Swift Ultra-Violet/Optical Telescope", Space Sci. Rev. **120**, 95–142 (2005) (cit. on pp. 52, 85, 120).

[72]J. E. Hill et al., "Readout modes and automated operation of the Swift X-ray Telescope", in X-Ray and Gamma-Ray Instrumentation for Astronomy XIII, Vol. 5165 (2004), pp. 217 –231 (cit. on pp. 52, 98, 120).

[73]W. Cash, "Parameter estimation in astronomy through application of the likelihood ratio.", Astrophys. J. **228**, 939–947 (1979) (cit. on pp. 53, 98, 120).

[74]P. M. W. Kalberla, W. B. Burton, D. Hartmann, E. M. Arnal, E. Bajaja, R. Morras, and W. G. L. Pöppel, "The Leiden/Argentine/Bonn (LAB) Survey of Galactic HI - Final data release of the combined LDS and IAR surveys with improved stray-radiation corrections", Astron. Astrophys. **440**, 775–782 (2005) (cit. on pp. 53, 98).

[75]T. S. Poole, A. A. Breeveld, M. J. Page, W. Landsman, S. T. Holland, P. Roming, N. P. M. Kuin, P. J. Brown, C. Gronwall, S. Hunsberger, S. Koch, K. O. Mason, P. Schady, D. V. Berk, A. J. Blustin, et al., "Photometric calibration of the Swift ultraviolet/optical telescope", Mon. Not. R. Astron. Soc. **383**, 627–645 (2007) (cit. on pp. 54, 55, 98, 120).

[76]P. W. A. Roming, T. S. Koch, S. R. Oates, B. L. Porterfield, D. E. V. Berk, P. T. Boyd, S. T. Holland, E. A. Hoversten, S. Immler, F. E. Marshall, M. J. Page, J. L. Racusin, D. P. Schneider, A. A. Breeveld, P. J. Brown, et al., "THE FIRST SWIFT ULTRAVIOLET/OPTICAL TELESCOPE GRB AFTERGLOW CATALOG", Astrophys. J. **690**, 163 (2008) (cit. on pp. 55, 56, 98, 120).

[77]J. A. Cardelli, G. C. Clayton, and J. S. Mathis, "The Relationship between Infrared, Optical, and Ultraviolet Extinction", Astrophys. J. **345**, 245 (1989) (cit. on p. 55).

[78]C. M. Urry and P. Padovani, "UNIFIED SCHEMES FOR RADIO-LOUD ACTIVE GALACTIC NUCLEI", Publ. Astron. Soc. Pac. **107**, 803 (1995) (cit. on p. 58).

[79]H. Netzer, *The Physics and Evolution of Active Galactic Nuclei* (Cambridge University Press, Cambridge, UK, 2013) (cit. on p. 58).

[80]R. Blandford, D. Meier, and A. Readhead, "Relativistic Jets from Active Galactic Nuclei", Annual Review of Astronomy and Astrophysics **57**, 467–509 (2019) (cit. on pp. 58, 61).

[81]J. Frank, A. King, and D. Raine, *Accretion Power in Astrophysics* (Cambridge University Press, Cambridge, UK, Jan. 2002) (cit. on p. 59).

[82]N. I. Shakura and R. A. Sunyaev, "Black holes in binary systems. Observational appearance.", Astron. Astrophys. **24**, 337–355 (1973) (cit. on pp. 59, 64).

[83]R. Narayan and I. Yi, "Advection-dominated Accretion: A Self-similar Solution", Astrophys. J. **428**, L13 (1994) (cit. on pp. 59, 65).

[84]G. Ghisellini, F. Tavecchio, L. Foschini, and G. Ghirlanda, "The transition between BL Lac objects and flat spectrum radio quasars", Mon. Not. R. Astron. Soc. **414**, 2674–2689 (2011) (cit. on pp. 59, 64, 96, 106).

[85]M. Nenkova, Ž. Ivezić, and M. Elitzur, "Dust Emission from Active Galactic Nuclei", Astrophys. J. **570**, L9 (2002) (cit. on p. 60).

[86]M. Stalevski, J. Fritz, M. Baes, T. Nakos, and L. Č. Popović, "3D radiative transfer modelling of the dusty tori around active galactic nuclei as a clumpy two-phase medium", Mon. Not. R. Astron. Soc. **420**, 2756–2772 (2012) (cit. on p. 60).

[87]R. D. Blandford and D. G. Payne, "Hydromagnetic flows from accretion discs and the production of radio jets", Mon. Not. R. Astron. Soc. **199**, 883–903 (1982) (cit. on p. 61).

[88]R. D. Blandford and R. L. Znajek, "Electromagnetic extraction of energy from Kerr black holes", Mon. Not. R. Astron. Soc. **179**, 433–456 (1977) (cit. on p. 61).

[89]C. Müller, M. Kadler, R. Ojha, J. Wilms, M. Böck, P. G. Edwards, C. M. Fromm, H. Hase, S. Horiuchi, U. Katz, J. E. J. Lovell, C. Plötz, T. Pursimo, S. Richers, E. Ros, et al., "Dual-frequency VLBI study of Centaurus A on sub-parsec scales - The highest-resolution view of an extragalactic jet", Astron. Astrophys. **530**, L11 (2011) (cit. on p. 61).

[90]P. Padovani, D. M. Alexander, R. J. Assef, B. De Marco, P. Giommi, R. C. Hickox, G. T. Richards, V. Smolčić, E. Hatziminaoglou, V. Mainieri, and M. Salvato, "Active galactic nuclei: what's in a name?", Astron. Astrophys. Rev. **25**, 1–91 (2017) (cit. on p. 61).

[91]B. L. Fanaroff and J. M. Riley, "The Morphology of Extragalactic Radio Sources of High and Low Luminosity", Mon. Not. R. Astron. Soc. **167**, 31P–36P (1974) (cit. on p. 62).

[92]V. Beckmann and C. Shrader, *Active Galactic Nuclei* (Wiley, Weinheim, Germany, 2012) (cit. on pp. 63, 71).

[93]C. M. Urry and P. Padovani, "UNIFIED SCHEMES FOR RADIO-LOUD ACTIVE GALACTIC NUCLEI", Publ. Astron. Soc. Pac. **107**, 803 (1995) (cit. on p. 63).

[94]C. Righi, "Neutrino emission from Blazars.", PhD thesis (Università degli Studi dell'Insubria, Como, Italy, 2019) (cit. on p. 64).

[95]G. Fossati, L. Maraschi, A. Celotti, A. Comastri, and G. Ghisellini, "A unifying view of the spectral energy distributions of blazars", Mon. Not. R. Astron. Soc. **299**, 433–448 (1998) (cit. on pp. 65, 66, 89).

[96]G. Ghisellini, C. Righi, L. Costamante, and F. Tavecchio, "The Fermi blazar sequence", Mon. Not. R. Astron. Soc. **469**, 255–266 (2017) (cit. on pp. 65, 66, 89).

[97]P. Giommi and P. Padovani, "BL Lac reunification", Mon. Not. R. Astron. Soc. **268**, L51–L54 (1994) (cit. on p. 66).

[98]A. R. Bell, "The acceleration of cosmic rays in shock fronts – I", Mon. Not. R. Astron. Soc. **182**, 147–156 (1978) (cit. on pp. 67, 68).

[99]G. B. Rybicki and A. P. Lightman, *Radiative Processes in Astrophysics* (May 1985) (cit. on pp. 68–70, 138).

[100]G. Ghisellini, *Radiative Processes in High Energy Astrophysics* (Springer International Publishing, Cham, Switzerland) (cit. on pp. 70, 139).

[101]F. Tavecchio, L. Maraschi, and G. Ghisellini, "Constraints on the Physical Parameters of TeV Blazars", Astrophys. J. **509**, 608 (1998) (cit. on p. 70).

[102]C. Nigro, J. Sitarek, P. Gliwny, D. Sanchez, A. Tramacere, and M. Craig, "agnpy: An open-source python package modelling the radiative processes of jetted active galactic nuclei", Astron. Astrophys. **660**, A18 (2022) (cit. on pp. 72, 136, 137).

[103]C. D. Dermer and G. Menon, *High Energy Radiation from Black Holes* (Princeton University Press, Princeton, NJ, USA, Nov. 2009) (cit. on pp. 73, 136, 138, 139, 146).

[104]J. D. Finke, "EXTERNAL COMPTON SCATTERING IN BLAZAR JETS AND THE LOCATION OF THE GAMMA-RAY EMITTING REGION", Astrophys. J. **830**, 94 (2016) (cit. on pp. 73, 136, 138).

[105]K. Mannheim and P. L. Biermann, "Gamma-ray flaring of 3C 279 : a proton-initiated cascade in the jet ?", Astron. Astrophys. **253**, L21–L24 (1992) (cit. on p. 74).

[106]W. Bednarek and R. J. Protheroe, "Gamma-ray and neutrino flares produced by protons accelerated on an accretion disc surface in active galactic nuclei", Mon. Not. R. Astron. Soc. **302**, 373–380 (1999) (cit. on p. 74).

[107]A. M. Atoyan and C. D. Dermer, "Neutral Beams from Blazar Jets", Astrophys. J. **586**, 79 (2003) (cit. on p. 74).

[108]S. R. Kelner and F. A. Aharonian, "Energy spectra of gamma rays, electrons, and neutrinos produced at interactions of relativistic protons with low energy radiation", Phys. Rev. D **78**, 034013 (2008) (cit. on pp. 75, 141–146).

[109]G. R. Blumenthal, "Energy Loss of High-Energy Cosmic Rays in Pair-Producing Collisions with Ambient Photons", Phys. Rev. D **1**, 1596–1602 (1970) (cit. on p. 75).

[110]K. Satalecka, T. Aniello, E. Bernardini, W. Bhattacharyya, M. Cerruti, F. D'Ammando, E. Prandini, C. Righi, N. Sahakyan, I. Viale, P. Edwards, R. Ojha, J. Stevens, T. Hovatta, S. Kiehlmann, A. C. S. Readhead, F. Eppel, A. Gokus, J. Heßdörfer, M. Kadler, G. Paraschos, J. Sinapius, and F. Rösch, "Multi-epoch monitoring of TXS 0506+056 with MAGIC and MWL partners", in 37th International Cosmic Ray Conference PoS(ICRC2021), Vol. 395 (2021), p. 875 (cit. on p. 77).

[111]S. Paiano, R. Falomo, A. Treves, and R. Scarpa, "The Redshift of the BL Lac Object TXS 0506+056", Astrophys. J. Lett. **854**, L32 (2018) (cit. on pp. 78, 93, 95).

[112]J. N. Douglas, F. N. Bash, F. A. Bozyan, G. W. Torrence, and C. Wolfe, "The Texas Survey of Radio Sources Covering -35.5 degrees $<$ declination $<$ 71.5 degrees at 365 MHz", Astron. J. **111**, 1945 (1996) (cit. on p. 78).

[113]IceCube Collaboration, M. Aartsen, M. Ackermann, J. Adams, J. A. Aguilar, M. Ahlers, M. Ahrens, I. Al Samarai, D. Altmann, K. Andeen, T. Anderson, I. Ansseau, G. Anton, C. Argüelles, B. Arsioli, et al., "Neutrino emission from the direction of the blazar TXS 0506+056 prior to the IceCube-170922A alert", Science **361**, 147–151 (2018) (cit. on p. 78).

[114]S. Ansoldi et al., "The Blazar TXS 0506+056 Associated with a High-energy Neutrino: Insights into Extragalactic Jets and Cosmic-Ray Acceleration", Astrophys. J. Lett. **863**, L10 (2018) (cit. on pp. 80, 83, 150).

[115]K. Murase, F. Oikonomou, and M. Petropoulou, "Blazar Flares as an Origin of High-energy Cosmic Neutrinos?", Astrophys. J. **865**, 124 (2018) (cit. on p. 80).

[116]M. Cerruti, A. Zech, C. Boisson, G. Emery, S. Inoue, and J. P. Lenain, "Leptohadronic single-zone models for the electromagnetic and neutrino emission of TXS 0506+056", Mon. Not. R. Astron. Soc. Lett. **483**, L12–L16 (2019) (cit. on pp. 80, 140).

[117]A. Keivani, K. Murase, M. Petropoulou, D. B. Fox, S. B. Cenko, S. Chaty, A. Coleiro, J. J. DeLaunay, S. Dimitrakoudis, P. A. Evans, J. A. Kennea, F. E. Marshall, A. Mastichiadis, J. P. Osborne, M. Santander, et al., "A Multimessenger Picture of the Flaring Blazar TXS 0506+056: Implications for High-energy Neutrino Emission and Cosmic-Ray Acceleration", Astrophys. J. **864**, 84 (2018) (cit. on p. 80).

[118]N. Sahakyan, "Lepto-hadronic γ-Ray and Neutrino Emission from the Jet of TXS 0506+056", Astrophys. J. **866**, 109 (2018) (cit. on p. 80).

[119]S. Gao, A. Fedynitch, W. Winter, and M. Pohl, "Modelling the coincident observation of a high-energy neutrino and a bright blazar flare", Nat. Astron. **3**, 88–92 (2019) (cit. on p. 80).

[120]K. Wang, R.-Y. Liu, Z. Li, X.-Y. Wang, and Z.-G. Dai, "Jet Cloud–Star Interaction as an Interpretation of Neutrino Outburst from the Blazar TXS 0506+056", Universe **9**, 1 (2022) (cit. on p. 80).

[121]M. Georganopoulos and D. Kazanas, "Decelerating Flows in TeV Blazars: A Resolution to the BL Lacertae-FR I Unification Problem", Astrophys. J. **594**, L27 (2003) (cit. on p. 80).

[122]G. Ghisellini, F. Tavecchio, and M. Chiaberge, "Structured jets in TeV BL Lac objects and radiogalaxies - Implications for the observed properties", Astron. Astrophys. **432**, 401–410 (2005) (cit. on p. 80).

[123]M. Giroletti, G. Giovannini, W. D. Cotton, G. B. Taylor, M. A. Pérez-Torres, M. Chiaberge, and P. G. Edwards, "The jet of Markarian 501 from millions of Schwarzschild radii down to a few hundreds", Astron. Astrophys. **488**, 905–914 (2008) (cit. on p. 80).

[124]H. Nagai, T. Haga, G. Giovannini, A. Doi, M. Orienti, F. D'Ammando, M. Kino, M. Nakamura, K. Asada, K. Hada, and M. Giroletti, "LIMB-BRIGHTENED JET OF 3C 84 REVEALED BY THE 43 GHz VERY-LONG-BASELINE-ARRAY OBSERVATION", Astrophys. J. **785**, 53 (2014) (cit. on p. 80).

[125]E. Ros, M. Kadler, M. Perucho, B. Boccardi, H.-M. Cao, M. Giroletti, F. Krauß, and R. Ojha, "Apparent superluminal core expansion and limb brightening in the candidate neutrino blazar TXS 0506+056", Astron. Astrophys. **633**, L1 (2020) (cit. on p. 80).

[126]X. Li, T. An, P. Mohan, and M. Giroletti, "The Parsec-scale Jet of the Neutrino-emitting Blazar TXS 0506+056", Astrophys. J. **896**, 63 (2020) (cit. on p. 80).

[127]V. A. Acciari et al., "Investigating the Blazar TXS 0506+056 through Sharp Multi-wavelength Eyes During 2017–2019", Astrophys. J. **927**, 197 (2022) (cit. on pp. 80, 87, 140).

[128]P. Bruel, T. H. Burnett, S. W. Digel, G. Johannesson, N. Omodei, and M. Wood, "Fermi-LAT improved Pass 8 event selection", arXiv, 10.48550/arXiv.1810.11394 (2018) (cit. on pp. 84, 97, 119).

[129]A. A. Abdo et al., "Fermi large area telescope observations of the cosmic-ray induced γ-ray emission of the Earth's atmosphere", Phys. Rev. D **80**, 122004 (2009) (cit. on pp. 84, 97).

[130]F. A. Harrison et al., "THE NUCLEAR SPECTROSCOPIC TELESCOPE ARRAY (NuSTAR) HIGH-ENERGY X-RAY MISSION", Astrophys. J. **770**, 103 (2013) (cit. on p. 85).

[131]C. S. Kochanek, B. J. Shappee, K. Z. Stanek, T. W.-S. Holoien, T. A. Thompson, J. L. Prieto, S. Dong, J. V. Shields, D. Will, C. Britt, D. Perzanowski, and G. Pojmański, "The All-Sky Automated Survey for Supernovae (ASAS-SN) Light Curve Server v1.0", Publ. Astron. Soc. Pac. **129**, 104502 (2017) (cit. on p. 85).

[132]K. Nilsson et al., "Long-term optical monitoring of TeV emitting blazars - I. Data analysis", Astron. Astrophys. **620**, A185 (2018) (cit. on p. 85).

[133]R. M. Zerbi et al., "The REM telescope: detecting the near infra-red counterparts of Gamma-Ray Bursts and the prompt behavior of their optical continuum", Astron. Nachr. **322**, 275–285 (2001) (cit. on p. 85).

[134]S. Covino, M. Stefanon, G. Sciuto, A. Fernandez-Soto, G. Tosti, F. M. Zerbi, G. Chincarini, L. A. Antonelli, P. Conconi, G. Cutispoto, E. Molinari, L. Nicastro, and M. Rodono, "REM: a fully robotic telescope for GRB observations", Ground-based Instrumentation for Astronomy **5492**, 1613–1622 (2004) (cit. on p. 85).

[135]J. L. Richards et al., "BLAZARS IN THE FERMI ERA: THE OVRO 40 m TELESCOPE MONITORING PROGRAM", Astrophys. J. Suppl. Ser. **194**, 29 (2011) (cit. on p. 85).

[136]J. Stevens, P. G. Edwards, R. Ojha, M. Kadler, F. Hungwe, M. Dutka, S. Tingay, J. P. Macquart, A. Moin, J. Lovell, and J. Blanchard, "ATCA monitoring of gamma-ray loud AGN", arXiv, 10.48550/arXiv.1205.2403 (2012) (cit. on p. 85).

[137]M. Kadler et al., "TELAMON: Monitoring of AGN with the Effelsberg 100-m Telescope in the Context of Astroparticle Physics", in 37th international cosmic ray conference, Vol. 395 (2021), p. 974 (cit. on p. 85).

[138]P. Padovani, F. Oikonomou, M. Petropoulou, P. Giommi, and E. Resconi, "TXS 0506+056, the first cosmic neutrino source, is not a BL Lac", Mon. Not. R. Astron. Soc. Lett. **484**, L104–L108 (2019) (cit. on pp. 89, 91, 96).

[139]I. Viale, C. Righi, G. Principe, M. Cerruti, F. Tavecchio, and E. Bernardini, "Candidate neutrino-emitting blazars sharing physical properties with TXS 0506+056", in 38th International Cosmic Ray Conference PoS(ICRC2023), Vol. 444 (2023), p. 1526 (cit. on p. 89).

[140]I. Viale, C. Righi, G. Principe, M. Cerruti, F. Tavecchio, and E. Bernardini, *Candidate neutrino emitters sharing physical properties with TXS 0506+056*, in preparation (cit. on p. 89).

[141]M. Ajello et al., "The Fourth Catalog of Active Galactic Nuclei Detected by the Fermi Large Area Telescope", Astrophys. J. **892**, 105 (2020) (cit. on p. 90).

[142]B. Lott, D. Gasparrini, and S. Ciprini, "The Fourth Catalog of Active Galactic Nuclei Detected by the Fermi Large Area Telescope – Data Release 2", arXiv, 10.48550/arXiv.2010.08406 (2020) (cit. on p. 90).

[143]J. Ballet, T. H. Burnett, S. W. Digel, and B. Lott, "Fermi Large Area Telescope Fourth Source Catalog Data Release 2", arXiv, 10.48550/arXiv.2005.11208 (2020) (cit. on pp. 90, 97).

[144]S. Weinberg, *Gravitation and Cosmology: Principles and Applications of the General Theory of Relativity* (Wiley, Hoboken, NJ, USA) (cit. on p. 90).

[145]D. W. Weedman, *Quasar Astronomy* (Cambridge University Press, Cambridge, UK) (cit. on p. 90).

[146]G. Ghisellini, L. Maraschi, and F. Tavecchio, "The Fermi blazars' divide", Mon. Not. R. Astron. Soc. Lett. **396**, L105–L109 (2009) (cit. on p. 90).

[147]M. Landoni, R. Falomo, S. Paiano, and A. Treves, "ZBLLAC: A Spectroscopic Database of BL Lacertae Objects", Astrophys. J. Suppl. Ser. **250**, 37 (2020) (cit. on pp. 93, 95).

[148]S. Paiano, M. Landoni, R. Falomo, A. Treves, R. Scarpa, and C. Righi, "On the Redshift of TeV BL Lac Objects", Astrophys. J. **837**, 144 (2017) (cit. on p. 93).

[149]M. S. Shaw, R. W. Romani, G. Cotter, S. E. Healey, P. F. Michelson, A. C. S. Readhead, J. L. Richards, W. Max-Moerbeck, O. G. King, and W. J. Potter, "SPECTROSCOPY OF BROAD-LINE BLAZARS FROM 1LAC", Astrophys. J. **748**, 49 (2012) (cit. on pp. 93, 95).

[150]M. S. Shaw, R. W. Romani, G. Cotter, S. E. Healey, P. F. Michelson, A. C. S. Readhead, J. L. Richards, W. Max-Moerbeck, O. G. King, and W. J. Potter, "SPECTROSCOPY OF THE LARGEST EVER γ-RAY-SELECTED BL LAC SAMPLE", Astrophys. J. **764**, 135 (2013) (cit. on pp. 93, 94).

[151]A. Hewitt and G. Burbidge, "A New Optical Catalog of Quasi-stellar Objects", Astrophys. J. Suppl. Ser. **63**, 1 (1987) (cit. on p. 93).

[152]S. Paiano, M. Landoni, R. Falomo, A. Treves, and R. Scarpa, "Spectroscopy of 10 γ-Ray BL Lac Objects at High Redshift", Astrophys. J. **844**, 120 (2017) (cit. on p. 93).

[153]P. J. Francis, P. C. Hewett, C. B. Foltz, F. H. Chaffee, R. J. Weymann, and S. L. Morris, "A High Signal-to-Noise Ratio Composite Quasar Spectrum", Astrophys. J. **373**, 465 (1991) (cit. on p. 94).

[154]A. Celotti, P. Padovani, and G. Ghisellini, "Jets and accretion processes in active galactic nuclei: further clues", Mon. Not. R. Astron. Soc. **286**, 415–424 (1997) (cit. on p. 94).

[155]E. F. Schlafly and D. P. Finkbeiner, "MEASURING REDDENING WITH SLOAN DIGITAL SKY SURVEY STELLAR SPECTRA AND RECALIBRATING SFD", Astrophys. J. **737**, 103 (2011) (cit. on p. 98).

[156]G. Stratta, M. Capalbi, P. Giommi, R. Primavera, S. Cutini, and D. Gasparrini, "The ASDC SED Builder Tool description and Tutorial", arXiv, 10.48550/arXiv.1103.0749 (2011) (cit. on pp. 103, 121).

[157]N. Park, "Performance of the VERITAS experiment ", in 34th international cosmic ray conference, Vol. 236 (2016), p. 771 (cit. on p. 103).

[158]C. van Eldik, M. Holler, D. Berge, D. Zaborov, J.-P. Lenain, V. Marandon, T. Murach, H. Prokoph, M. de Naurois, and R. D. Parsons, "Observations of the Crab Nebula with H.E.S.S. phase II ", in 34th international cosmic ray conference, Vol. 236 (2016), p. 847 (cit. on p. 103).

[159]M. Cerruti, A. Zech, C. Boisson, and S. Inoue, "A hadronic origin for ultra-high-frequency-peaked BL Lac objects", Mon. Not. R. Astron. Soc. **448**, 910–927 (2015) (cit. on pp. 104, 135, 140).

[160]G. Ghisellini and F. Tavecchio, "The blazar sequence: a new perspective", Mon. Not. R. Astron. Soc. **387**, 1669–1680 (2008) (cit. on pp. 104, 105).

[161]A. M. Atoyan and F. A. Aharonian, "On the mechanisms of gamma radiation in the Crab Nebula", Mon. Not. R. Astron. Soc. **278**, 525–541 (1996) (cit. on p. 104).

[162]K. Nalewajko, M. C. Begelman, and M. Sikora, "CONSTRAINING THE LOCATION OF GAMMA-RAY FLARES IN LUMINOUS BLAZARS", Astrophys. J. **789**, 161 (2014) (cit. on p. 105).

[163]H. Abdalla et al., "H.E.S.S. detection of very high-energy γ-ray emission from the quasar PKS 0736+017", Astron. Astrophys. **633**, A162 (2020) (cit. on p. 105).

[164]M. G. Aartsen et al., "Search for steady point-like sources in the astrophysical muon neutrino flux with 8 years of IceCube data", Eur. Phys. J. C **79**, 1–19 (2019) (cit. on p. 106).

[165]S. Archambault et al., "UPPER LIMITS FROM FIVE YEARS OF BLAZAR OBSERVATIONS WITH THE VERITAS CHERENKOV TELESCOPES", Astron. J. **151**, 142 (2016) (cit. on p. 108).

[166]N. Sahakyan, P. Giommi, P. Padovani, M. Petropoulou, D. Bégué, B. Boccardi, and S. Gasparyan, "A multimessenger study of the blazar PKS 0735+178: a new major neutrino source candidate", Mon. Not. R. Astron. Soc. **519**, 1396–1408 (2023) (cit. on p. 109).

[167]R. Abbasi et al., "IceCube high-energy starting event sample: Description and flux characterization with 7.5 years of data", Phys. Rev. D **104**, 022002 (2021) (cit. on p. 111).

[168]M. G. Aartsen et al., "THE CONTRIBUTION OF FERMI-2LAC BLAZARS TO DIFFUSE TEV–PEV NEUTRINO FLUX", Astrophys. J. **835**, 45 (2017) (cit. on p. 111).

[169]IceCube Collaboration, "Search for high-energy neutrino emission from hard X-ray AGN with IceCube", in 38th International Cosmic Ray Conference, Vol. 444 (2023), p. 1032 (cit. on p. 111).

[170]R. Stein, S. V. Velzen, M. Kowalski, A. Franckowiak, S. Gezari, J. C. A. Miller-Jones, S. Frederick, I. Sfaradi, M. F. Bietenholz, A. Horesh, R. Fender, S. Garrappa, T. Ahumada, I. Andreoni, J. Belicki, et al., "A tidal disruption event coincident with a high-energy neutrino", Nat. Astron. **5**, 510–518 (2021) (cit. on p. 111).

[171]A. Biland et al., "Calibration and performance of the photon sensor response of FACT — the first G-APD Cherenkov telescope", J. Instrum. **9**, P10012 (2014) (cit. on p. 112).

[172]K. Satalecka and E. Bernardini and D. Dorner and G. Kukec Mezek and W. Jin, "Searching for VHE gamma-ray emission associated with IceCube neutrino alerts using FACT, H.E.S.S., MAGIC, and VERITAS", in 37th International Cosmic Ray Conference PoS(ICRC2021), Vol. 395 (2021), p. 960 (cit. on p. 112).

[173]F. Schüssler, H. Ashkar, E. Bernardini, A. Berti, F. Bradascio, S. Buson, D. Dorner, W. Jin, G. K. Mezek, M. Santander, K. Satalecka, B. Schleicher, M. Senniappan, and I. Viale, "Joint searches by FACT, H.E.S.S., MAGIC and VERITAS for VHE gamma-ray emission associated with neutrinos detected by IceCube", in 38th International Cosmic Ray Conference PoS(ICRC2023), Vol. 444 (2023), p. 1501 (cit. on p. 112).

[174]FACT, H.E.S.S., MAGIC, VERITAS, and IceCube Collaborations, *Prompt searches for Very-High-Energy Gamma-Ray Counterparts to IceCube Astrophysical Neutrino Alerts*, in preparation (cit. on pp. 112, 119, 121).

[175]C. Hoischen, M. Füßling, S. Ohm, A. Balzer, H. Ashkar, K. Bernlöhr, P. Hofverberg, T. L. Holch, T. Murach, H. Prokoph, F. Schüssler, S. J. Zhu, D. Berge, K. Egberts, and C. Stegmann, "The H.E.S.S. transients follow-up system", Astron. Astrophys. **666**, A119 (2022) (cit. on p. 117).

[176]T. Bretz and D. Dorner, "MARS - CheObs ed. – A flexible Software Framework for future Cherenkov Telescopes", in *Astroparticle, Particle and Space Physics, Detectors and Medical Physics Applications*, Vol. 5 (2010), pp. 681–687 (cit. on p. 118).

[177]M. de Naurois and L. Rolland, "A high performance likelihood reconstruction of γ-rays for imaging atmospheric Cherenkov telescopes", Astropart. Phys. **32**, 231–252 (2009) (cit. on p. 118).

[178]G. Maier and J. Holder, "Eventdisplay: An Analysis and Reconstruction Package for Ground-based Gamma-ray Astronomy", arXiv, 10.48550/arXiv.1708.04048 (2017) (cit. on p. 118).

[179]P. Cogan, "VEGAS, the VERITAS Gamma-ray Analysis Suite", arXiv, 10.48550/arXiv.0709.4233 (2007) (cit. on p. 118).

[180]J. Lundberg, J. Conrad, W. Rolke, and A. Lopez, "Limits, discovery and cut optimization for a Poisson process with uncertainty in background and signal efficiency: TRolke 2.0", Comput. Phys. Commun. **181**, 683–686 (2010) (cit. on p. 119).

[181]H. Abe, S. Abe, V. A. Acciari, T. Aniello, S. Ansoldi, L. A. Antonelli, A. Arbet Engels, C. Arcaro, M. Artero, K. Asano, D. Baack, A. Babić, A. Baquero, U. Barres de Almeida, J. A. Barrio, et al., "Gamma-ray observations of MAXI J1820+070 during the 2018 outburst", Mon. Not. R. Astron. Soc. **517**, 4736–4751 (2022) (cit. on p. 119).

[182]S. Garrappa, S. Buson, A. Franckowiak, M. Giroletti, I. Liodakis, and C. Nanci, "Fermi-LAT realtime follow-ups of high-energy neutrino alerts", in 37th International Cosmic Ray Conference, Vol. 395 (2021), p. 956 (cit. on p. 119).

[183]P. C. Hewett and V. Wild, "Improved redshifts for SDSS quasar spectra", Mon. Not. R. Astron. Soc. **405**, 2302–2316 (2010) (cit. on p. 121).

[184]F. Oikonomou, M. Petropoulou, K. Murase, A. Tohuvavohu, G. Vasilopoulos, S. Buson, and M. Santander, "Multi-messenger emission from the parsec-scale jet of the flat-spectrum radio quasar PKS 1502+106 coincident with high-energy neutrino IceCube-190730A", J. Cosmol. Astropart. Phys. **2021**, 082 (2021) (cit. on pp. 121–123).

[185]X. Rodrigues, S. Garrappa, S. Gao, V. S. Paliya, A. Franckowiak, and W. Winter, "Multiwavelength and Neutrino Emission from Blazar PKS 1502 + 106", Astrophys. J. **912**, 54 (2021) (cit. on pp. 121–123).

[186]K. Grasha, J. Darling, A. Bolatto, A. K. Leroy, and J. T. Stocke, "A Search for Intrinsic H i 21 cm and OH 18 cm Absorption toward Compact Radio Sources", Astrophys. J. Suppl. Ser. **245**, 3 (2019) (cit. on p. 124).

[187]M. Stadnik and R. W. Romani, "IMAGING REDSHIFT ESTIMATES FOR FERMI BL LAC OBJECTS", Astrophys. J. **784**, 151 (2014) (cit. on p. 126).

[188]Fermi-LAT Collaboration, "Fermi Large Area Telescope Third Source Catalog", arXiv, 10.48550/arXiv.1501.02003 (2015) (cit. on p. 129).

[189]A. Domínguez et al., "Extragalactic background light inferred from AEGIS galaxy-SED-type fractions", Mon. Not. R. Astron. Soc. **410**, 2556–2578 (2011) (cit. on p. 129).

[190]B. P. Abbott et al., "Multi-messenger Observations of a Binary Neutron Star Merger∗", Astrophys. J. Lett. **848**, L12 (2017) (cit. on p. 133).

[191]A. Berti and A. Carosi, "The Detection of GRBs at VHE: A Challenge Lasting for More than Two Decades, What Is Next?", Galaxies **10**, 67 (2022) (cit. on p. 133).

[192]The CTA Consortium, *Science with the Cherenkov Telescope Array* (World Scientific Publishing Company, Singapore, Feb. 2018) (cit. on pp. 133, 152).

[193]O. Sergijenko, A. Brown, D. Fiorillo, A. Rosales de Leon, K. Satalecka, C. F. Tung, R. Reimann, T. Glauch, and I. Taboada, "Sensitivity of the Cherenkov Telescope Array to emission from the gamma-ray counterparts of neutrino events", in 37th International Cosmic Ray Conference, Vol. 395 (2021), p. 975 (cit. on p. 133).

[194]A. Margiotta, "The KM3NeT infrastructure: status and first results", arXiv, 10.48550/arXiv.2208.07370 (2022) (cit. on pp. 133, 152).

[195]Baikal-GVD Collaboration, "Diffuse neutrino flux measurements with the Baikal-GVD neutrino telescope", Phys. Rev. D **107**, 042005 (2023) (cit. on p. 133).

[196]E. Resconi, "The Pacific Ocean Neutrino Experiment", in 37th International Cosmic Ray Conference, Vol. 395 (2021), p. 024 (cit. on p. 133).

[197]Z. P. Ye et al., "Proposal for a neutrino telescope in South China Sea", arXiv, 10.48550/arXiv.2207.04519 (2022) (cit. on p. 133).

[198]M. G. Aartsen et al., "IceCube-Gen2: the window to the extreme Universe", J. Phys. G: Nucl. Part. Phys. **48**, 060501 (2021) (cit. on p. 133).

[199]S. Gao, M. Pohl, and W. Winter, "On the Direct Correlation between Gamma-Rays and PeV Neutrinos from Blazars", Astrophys. J. **843**, 109 (2017) (cit. on p. 135).

[200]A. Mastichiadis and J. G. Kirk, "Self-consistent particle acceleration in active galactic nuclei.", Astron. Astrophys. **295**, 613 (1995) (cit. on p. 135).

[201]S. Dimitrakoudis, A. Mastichiadis, R. J. Protheroe, and A. Reimer, "The time-dependent one-zone hadronic model - First principles", Astron. Astrophys. **546**, A120 (2012) (cit. on p. 135).

[202]M. Böttcher, A. Reimer, K. Sweeney, and A. Prakash, "LEPTONIC AND HADRONIC MODELING OF FERMI-DETECTED BLAZARS", Astrophys. J. **768**, 54 (2013) (cit. on p. 135).

[203]S. Gasparyan, D. Bégué, and N. Sahakyan, "Time-dependent lepto-hadronic modelling of the emission from blazar jets with SOPRANO: the case of TXS 0506+056, 3HSP J095507.9+355101, and 3C 279", Mon. Not. R. Astron. Soc. **509**, 2102–2121 (2022) (cit. on p. 135).

[204]M. Cerruti, M. Kreter, M. Petropoulou, A. Rudolph, F. Oikonomou, M. Böttcher, S. Dimitrakoudis, A. Dmytriiev, S. Gao, S. Inoue, A. Mastichiadis, K. Murase, A. Reimer, J. Robinson, X. Rodrigues, W. Winter, A. Zech, and N. Żywucka, "The Blazar Hadronic Code Comparison Project", in 37th International Cosmic Ray Conference, Vol. 395 (2021), p. 979 (cit. on p. 135).

[205]V. Zabalza, "Naima: a Python package for inference of particle distribution properties from nonthermal spectra ", in 34th international cosmic ray conference, Vol. 236 (2016), p. 922 (cit. on p. 135).

[206]W. Bednarek and R. J. Protheroe, "Gamma-rays from interactions of stars with active galactic nucleus jets", Mon. Not. R. Astron. Soc. **287**, L9–L13 (1997) (cit. on p. 136).

[207]M. V. Barkov, F. A. Aharonian, and V. Bosch-Ramon, "GAMMA-RAY FLARES FROM RED GIANT/JET INTERACTIONS IN ACTIVE GALACTIC NUCLEI", Astrophys. J. **724**, 1517 (2010) (cit. on p. 136).

[208]I. Viale, D. K. Maniadakis, C. Nigro, J. Sitarek, and E. Bernardini, "Development of hadronic emission processes in the open-source python package AGNpy", in *38th International Cosmic Ray Conference PoS(ICRC2023)*, Vol. 444 (SISSA Medialab, July 2023), p. 1524 (cit. on p. 136).

[209]D. K. Maniadakis, "Development of a lepto-hadronic model of the high-energy emission of Active Galactic Nuclei", MA thesis (Università degli Studi di Padova, Italy, 2022) (cit. on p. 136).

[210]C. R. Harris et al., "Array programming with NumPy", Nature **585**, 357–362 (2020) (cit. on p. 136).

[211]P. Virtanen, R. Gommers, T. E. Oliphant, M. Haberland, T. Reddy, D. Cournapeau, E. Burovski, P. Peterson, W. Weckesser, J. Bright, S. J. van der Walt, M. Brett, J. Wilson, K. J. Millman, N. Mayorov, et al., "SciPy 1.0: fundamental algorithms for scientific computing in Python", Nat. Methods **17**, 261–272 (2020) (cit. on p. 136).

[212]T. P. Robitaille, E. J. Tollerud, P. Greenfield, M. Droettboom, E. Bray, T. Aldcroft, M. Davis, A. Ginsburg, A. M. Price-Whelan, W. E. Kerzendorf, A. Conley, N. Crighton, K. Barbary, D. Muna, H. Ferguson, et al., "Astropy: A community Python package for astronomy", Astron. Astrophys. **558**, A33 (2013) (cit. on p. 136).

[213]J. D. Finke, C. D. Dermer, and M. Böttcher, "Synchrotron Self-Compton Analysis of TeV X-Ray-Selected BL Lacertae Objects", Astrophys. J. **686**, 181 (2008) (cit. on pp. 136, 138, 146).

[214]R. J. Gould and G. P. Schréder, "Pair Production in Photon-Photon Collisions", Phys. Rev. **155**, 1404–1407 (1967) (cit. on p. 136).

[215]A. Franceschini, G. Rodighiero, and M. Vaccari, "Extragalactic optical-infrared background radiation, its time evolution and the cosmic photon-photon opacity", Astron. Astrophys. **487**, 837–852 (2008) (cit. on p. 136).

[216]J. D. Finke, S. Razzaque, and C. D. Dermer, "MODELING THE EXTRAGALACTIC BACKGROUND LIGHT FROM STARS AND DUST", Astrophys. J. **712**, 238 (2010) (cit. on p. 136).

[217]A. Domínguez et al., "Extragalactic background light inferred from AEGIS galaxy-SED-type fractions", Mon. Not. R. Astron. Soc. **410**, 2556–2578 (2011) (cit. on p. 136).

[218]A. Saldana-Lopez, A. Domínguez, P. G. Pérez-González, J. Finke, M. Ajello, J. R. Primack, V. S. Paliya, and A. Desai, "An observational determination of the evolving extragalactic background light from the multiwavelength HST/CANDELS survey in the Fermi and CTA era", Mon. Not. R. Astron. Soc. **507**, 5144–5160 (2021) (cit. on p. 136).

[219]M. Cerruti, "Leptonic and Hadronic Radiative Processes in Supermassive-Black-Hole Jets", Galaxies **8**, 72 (2020) (cit. on p. 137).

[220]A. Donath et al., "Gammapy: A Python package for gamma-ray astronomy", Astron. Astrophys. **678**, A157 (2023) (cit. on p. 137).

[221]P. Freeman, S. Doe, and A. Siemiginowska, "Sherpa: a mission-independent data analysis application", in *Astronomical Data Analysis*, Vol. 4477 (SPIE, Nov. 2001), pp. 76–87 (cit. on p. 137).

[222]E. Massaro, A. Tramacere, M. Perri, P. Giommi, and G. Tosti, "Log-parabolic spectra and particle acceleration in blazars - III. SSC emission in the TeV band from Mkn 501", Astron. Astrophys. **448**, 861–871 (2006) (cit. on p. 138).

[223]A. Tramacere, P. Giommi, M. Perri, F. Verrecchia, and G. Tosti, "Swift observations of the very intense flaring activity of Mrk 421 during 2006. I. Phenomenological picture of electron acceleration and predictions for MeV/GeV emission", Astron. Astrophys. **501**, 879–898 (2009) (cit. on p. 138).

[224]A. Tramacere, E. Massaro, and A. M. Taylor, "STOCHASTIC ACCELERATION AND THE EVOLUTION OF SPECTRAL DISTRIBUTIONS IN SYNCHRO-SELF-COMPTON SOURCES: A SELF-CONSISTENT MODELING OF BLAZARS' FLARES", Astrophys. J. **739**, 66 (2011) (cit. on p. 138).

[225]F. A. Aharonian, S. R. Kelner, and A. Yu. Prosekin, "Angular, spectral, and time distributions of highest energy protons and associated secondary gamma rays and neutrinos propagating through extragalactic magnetic and radiation fields", Phys. Rev. D **82**, 043002 (2010) (cit. on pp. 138, 139, 146).

[226]A. Zech, M. Cerruti, and D. Mazin, "Expected signatures from hadronic emission processes in the TeV spectra of BL Lacertae objects", Astron. Astrophys. **602**, A25 (2017) (cit. on p. 140).

[227]M. Cerruti, W. Benbow, X. Chen, J. P. Dumm, L. F. Fortson, and K. Shahinyan, "Luminous and high-frequency peaked blazars: the origin of the γ-ray emission from PKS 1424+240", Astron. Astrophys. **606**, A68 (2017) (cit. on p. 140).

[228]A. Acharyya et al., "Multiwavelength Observations of the Blazar PKS 0735+178 in Spatial and Temporal Coincidence with an Astrophysical Neutrino Candidate IceCube-211208A", Astrophys. J. **954**, 70 (2023) (cit. on p. 140).

[229]A. Mücke, R. Engel, J. P. Rachen, R. J. Protheroe, and T. Stanev, "Monte Carlo simulations of photohadronic processes in astrophysics", Comput. Phys. Commun. **124**, 290–314 (2000) (cit. on p. 141).

[230]A. Mücke, R. J. Protheroe, R. Engel, J. P. Rachen, and T. Stanev, "BL Lac objects in the synchrotron proton blazar model", Astropart. Phys. **18**, 593–613 (2003) (cit. on p. 146).

[231]M. Cerruti, A. Zech, C. Boisson, and S. Inoue, "A mixed lepto-hadronic scenario for PKS 2155-304", AIP Conf. Proc. **1505**, 635–638 (2012) (cit. on p. 146).

[232]M. Böttcher, A. Reimer, K. Sweeney, and A. Prakash, "LEPTONIC AND HADRONIC MODELING OF FERMI-DETECTED BLAZARS", Astrophys. J. **768**, 54 (2013) (cit. on p. 146).

[233]J. Ballet, P. Bruel, T. H. Burnett, and B. Lott, "Fermi Large Area Telescope Fourth Source Catalog Data Release 4 (4FGL-DR4)", arXiv, 10.48550/arXiv.2307.12546 (2023) (cit. on p. 151).

List of Figures

List of Tables

Acronyms

ADC Analog-to-Digital Converter

AGN Active Galatic Nuclei

ASAS-SN All-Sky Automated Survey for Supernovae

ATCA Australia Telescope Compact Array

BAT Burst Alert Telescope

BLR Broad Line Region

CC Charged Current

CCD Charged-Coupled Device

CH Counting House

CMB Cosmic Microwave Background

CR Cosmic Ray

DAQ Data AcQuisition

DOM Digital Optical Module

DT Discriminator Threshold

EAS Extensive Air Shower

EBL Extragalactic Background Light

EC External Compton

EHE Extreme High Energy

EW Equivalent Width

FoV Field of View

GCN General Coordinates Network

GFU Gamma-ray Follow-Up

GRB Gamma-Ray Burst

GW gravitational waves

HE High Energy

HESE High Energy Starting Event

HV High Voltage

IACT Imaging Atmospheric Cherenkov Telescope

LC LightCurve

LED Light-Emitting Diode

LIDAR LIght Detection and Ranging

LUT Look-Up Table

MARS MAGIC Analysis and Reconstruction Software

MC Monte Carlo

MWL Multi-wavelength

NC Neutral Current

NLR Narrow Line Region

NN Next Neighbour

NSB Night Sky Background

OVRO Owens ValleyRadio Observatory

phe photoelectron

PIC Port d'Informació Cientifica

PMT PhotoMultiplier Tube

PSF Point Spread Function

REM Rapid Eye Mount telescope

RF Random Forest

RMS Root Mean Square

ROI Region Of Interest

SED Spectral Energy Distribution

SMBH Super Massive Black Hole

SSC Synchrotron Self Compton

TS Test Statistics

UHECR Ultra High Energy Cosmic Rays

UL Upper Limit

UV UltraViolet

UVOT Ultraviolet/Optical Telescope

VCSEL Vertical Cavity Surface Emitting Laser

VHE Very High Energy

XRT X-ray Telescope